On The Interaction of Shock Waves With Contact Surfaces Between Gases of Different Densities

Thesis by

Martin Brouillette

In Partial Fulfillment
of the Requirements for the Degree of
Doctor of Philosophy

California Institute of Technology
Pasadena, California

1989
(Submitted May 19 1989)

To my parents

Nicole and Pierre

ACKNOWLEDGMENTS

First, I would like to thank my advisor, Professor Bradford Sturtevant, for his guidance and advice throughout the course of this work. His suggestions and enthusiasm have been instrumental to the success of this project. I have learned a great deal about research from my interaction with him.

I would like to express my gratitude to the entire GALCIT community, including students, faculty, secretaries, technicians and machinists, for their help. In particular, I would like to acknowledge the assistance of Riccardo Bonazza and David Lim with the design of the shock tube and test section and Rick Paniagua, Phil Wood and Jerry Landry for the machining and construction. Special thanks to Harry Hamaguchi for the help with the photography. This research was supported by the U.S. Department of Energy, Lawrence Livermore National Laboratory, under project agreement DOE W-7405-ENG-48.

I would also like to thank everybody I met at Caltech, especially the members of the sport community, for helping make my stay here so enjoyable. I would like to express my gratitude to my parents and my brother for their unequivocal moral support and encouragement throughout this adventure.

Finally, I would like to thank my love, Jocelyne, for making me the luckiest guy in the world.

ABSTRACT

The interaction of shock waves with a contact surface between gases of different densities has been studied experimentally and theoretically. The basic mechanism for the instability of perturbations at the interface is baroclinic vorticity generation resulting from the misalignment of the pressure gradient of the shock and the density gradient of the interface. In the present study, the effects of interface density contrast and initial thickness, and incident wave strength on the development of the instability at the interface are investigated. The experiments were performed in a new vertical shock tube facility where the interaction of a shock wave with either a discontinuous interface, formed by a thin (0.5 μm) plastic membrane, or a continuous interface, created by retracting a metal plate initially separating the two gases, was studied. Air was used on one side of the interface and either helium, carbon dioxide, refrigerant-22 or sulphur hexafluoride was used on the other side as the test gas.

Experiments to study the time evolution of quasi-sinusoidal perturbations on a continuous interface have shown that the growth rates are reduced as the interface thickness is increased. It has been observed that growth rates of perturbations of wavelength $\lambda \sim 25$ mm on interfaces of thickness $\delta \sim 10$ mm are about three times smaller than those predicted by the linear theory for the impulsive acceleration of discontinuous interfaces. A new model that accounts for the growth rate reduction caused by the presence of a finite density gradient on the interface has been proposed, and good agreement was obtained with the present experimental results.

Experiments were also performed to observe the schlieren visual thickness of plane discontinuous or continuous interfaces with random small-scale perturbations after interaction with the incident shock wave and its reverberations. The interface was initially located near the end wall of the shock tube to permit the observation of the development of the interface phenomena after the arrival of the incident shock and its reverberations. It is found that the interaction of a shock wave with a discontinuous interface causes the appearance of a turbulent mixing zone between the two gases, whose growth rate slows down as time increases, owing to a decrease in turbulence intensity and the action of viscosity. Because of the large uncertainty

associated with the measurements a short time after the interaction with the incident shock, the accurate determination of a possible universal power law governing the thickening of the interface is not feasible. Results for the interaction of the first reverberation of the primary wave with the already turbulent interface have demonstrated that this growth is sensitive to the initial pre-growth state of the interface. It also appears that the thickening of the turbulent mixing zone is accomplished by the merging of large structures within the interface. However, since the energy available for the turbulent motions at the impulsively accelerated interface remains constant after the interaction with the shock and also depends on the wavelength of the initial perturbation, it is not certain whether the development of mixing at the interface achieves an asymptotic stage of self-similar turbulence independent of initial conditions, as has been observed for the gravity-driven interfaces. Also, it has been found that the growth rates measured in the present experiments with discontinuous interfaces are nearly an order of magnitude lower than those reported by previous investigators. The continuous interfaces formed by the retracting plate are smoothed by molecular diffusion, and thus the combination of low density gradient and small initial perturbations is such that they exhibit growth only after being perturbed by acoustic noise introduced by the reverberation of waves between the interface, the side walls and the end of the shock tube.

The development of viscous boundary layers on the side walls of the test section can cause the bifurcation of waves reflected from the end wall of the shock tube, and, thereafter, the formation of wall bubbles and interface contaminating jets. Moreover, the generation of vortical structures by the baroclinic instability excited by the interaction of reflected waves with the distorted interface within the boundary layer has been demonstrated. Significant contamination of the test gas can by achieved by these structures, even if reflected-wave bifurcation is absent. Moreover, the strain induced by the vorticity in these wall structures tends to thin the interface; the magnitude of this effect on the growth rates in the present plane interface experiments is estimated to be of order 10% for discontinuous interfaces and 50% for continuous interfaces.

TABLE OF CONTENTS

LIST OF FIGURES

LIST OF TABLES

LIST OF SYMBOLS

Symbol	Description
a	Acceleration of membrane
A	Atwood ratio, $A \equiv (\rho_2 - \rho_1)/(\rho_1 + \rho_2)$
$\mathbf{A}$	Cross-sectional area of shock tube
$c_{1,2}$	Speed of sound in gas 1,2
C	Constant in approximation to growth reduction factor
d	Distance between wall vortex and side wall
d_{shock}	Shock formation distance
D	Molecular diffusion coefficient
$\mathbf{D}$	Test section width
E_k	Kinetic energy of perturbations, induced by the baroclinic instability
E_{turb}, $E_{turb\ tot}$	Turbulent kinetic energy per unit volume, area
f	Density dependence in linear growth regime of TMZ
F	Fraction of perturbation kinetic energy used for turbulent motions
g	Gravitational acceleration
k	Wavenumber
$k_{y,z}$	Wavenumber in y,z direction
L	Distance traveled by interface
m	Mass of a membrane
M	Mach number
M_{rel}	Maximum relative Mach number in compressibility analysis
M_s	Mach number of incident shock wave
$\mathbf{M}$	Molecular weight
p	Pressure
Δp	Pressure difference across membrane

Pr	Prandtl number
r	Wall vortex radius
$\dot{s}$	Vorticity-induced strain rate in middle of interface by a pair of wall vortices
$\dot{s}_{tot}$	Total vorticity-induced strain by vortices on all four side walls
S	Turbulent boundary layer parameter
t	Time
t_1	Time of arrival of first reflected shock
t^*	Time of transition from linear to 2/3 growth of inviscid TMZ
t^*_{vis}	Time of transition from linear to power law growth of viscous TMZ
T	Temperature
TMZ	Turbulent mixing zone
u	x-velocity
u_p	Wall vortex penetration speed
u_t	Tangential velocity at outer portion of a wall vortex
$u_{1,2}$	x-velocity in fluid 1,2 obtained from velocity potential
$[u]$	Interface velocity jump induced by incident shock
$[u]_i$	Interface velocity jump induced by ith wave
$U_{1,2}$	Velocity in air, test gas induced by incident shock
v	y-velocity
$v_{1,2}$	y-velocity in fluid 1,2 obtained from velocity potential
Δu_{max}	Maximum velocity jump at interface, in analysis of Appendix B
W	Shock velocity jump parameter
x	Space coordinate along shock tube length
x_i	x-coordinate of ith vortex
x_p	x-coordinate of interface perturbation
y	Space coordinate along shock tube width
y_i	y-coordinate of ith vortex
α	Exponent of the power-law growth of the TMZ

γ	Specific heat ratio
δ	Interface thickness
$\delta_D(t)$	Dirac delta function
δ_{diff}	Thickness of laminar molecular diffusion layer
δ_{ms}	Maximum slope thickness from concentration probe measurements
δ_{visual}	Visual thickness
δ^*	Thickness at which inviscid TMZ growth changes from linear to 2/3 power law
ε	Boundary layer thickness at interface
η	Amplitude of linear perturbation on interface
η_0	Initial amplitude of perturbation on interface
Γ	Vortex circulation
λ	Wavelength
μ	Dynamic viscosity
ν	Kinematic viscosity
Ω	Growth rate of perturbations under gravitational acceleration
ρ	Density
$\rho_{1,2}$	Density of fluid 1,2
$\bar{\rho}$	Average density across interface, $\bar{\rho} \equiv (\rho_1 + \rho_2)/2$
τ	Molecular diffusion time
$\phi_{1,2}$	Velocity potential in fluid 1,2
ψ	Growth reduction factor due to the presence of a finite density gradient
$(\,)'_i$	Conditions right after the refraction of wave i at the interface

Chapter 1

INTRODUCTION

When two fluids of different densities are impulsively accelerated into each other by a shock wave, if the interface separating them is not perfectly flat and parallel to the shock, a wide variety of fluid motions is generated. This class of problems is often referred to as the shock-excited Rayleigh-Taylor instability or as the Richtmyer-Meshkov instability. The basic mechanism for the amplification of perturbations at the interface is baroclinic vorticity generation resulting from the misalignment of the pressure gradient of the shock and the density gradient across the interface. As the interface between the two fluids becomes more distorted, secondary instabilities, such as the Kelvin-Helmholtz shearing instability, develop and a region of turbulence and intense mixing results. The intensity of the turbulent motions can be further increased by processing the interface with additional pressure waves.

In addition to the Richtmyer-Meshkov instability, other baroclinic instabilities include the Rayleigh-Taylor instability for an interface between two different fluids in a gravitational field, and the Landau-Darrieus instability (Landau & Lifshitz 1959) driven by mass transfer across the interface.

The instability resulting from the acceleration of a fluid into another one arises in the context of impulsively generated flows occurring both in man-made applications and in natural phenomena. For example, in the latter category, the Richtmyer-Meshkov instability is used to explain: (i) The overturn of the outer portion of the collapsing cores of supernovas (Smarr *et al.* 1981) and (ii) The instability of rapidly collapsing gas bubbles in liquids (Cole 1948, Plesset 1954 and Frost 1988).

Examples of familiar technological applications affected by the shock-induced instability are (i) The interaction of reflected shocks with the contact discontinuity between driver and driven gases in shock tubes (Stalker & Crane 1978), (ii) The interaction of pressure waves and flame fronts (Markstein 1957a), (iii) Supersonic combustion (Marble *et al.* 1987), (iv) Laser-matter interactions (Grun *et al.* 1984, Emery *et al.* 1982), and (v) Laser implosion of deuterium-tritium fusion targets (Lindl & Mead 1975, Afanas'ev *et al.* 1976). In most of these cases the

instability tends to cause undesirably violent and uncontrollable behavior even when the interface has initially only small-scale perturbations, although one proposed method to control the effects of the instability is to reduce the density gradient at the interface to decrease the baroclinic generation of vorticity. Since the basic underlying physical processes are very much the same for all the cases mentioned above, significant understanding can be achieved by performing simple laboratory experiments at more benign conditions.

1.1. Motivation.

This research project was initiated to investigate the Richtmyer-Meshkov instability and secondary instabilities generated by the interaction of one or more shock waves with an interface separating two gases of different densities. The current experiments were undertaken to: (i) determine the effects of a finite density gradient at the interface on the development of a single-scale perturbation on the interface, (ii) document the growth of a nominally flat interface between the two gases, since in most applications of interest the perturbations on the interface are small and have a random character, and (iii) identify and quantify the secondary effects introduced by the experimental apparatus. A vertical shock tube was built specially for the investigation of the shock-induced acceleration of an interface between two gases of different densities. The time evolution of the interface was studied using schlieren photography and high-speed cinematography, and fast response pressure measurements.

The most important accomplishment of the present work is the elucidation of the physical processes taking place when an interface between two gases of different densities is accelerated by one or many shock waves. The reduction in growth rate of single-scale perturbations by the decrease of the density gradient at the interface has been observed experimentally and has been confirmed by a new simple analytical model. Visual growth rates for the thickening of the interface region due to turbulent mixing between the two gases have been documented for various gas combinations, incident shock strengths and initial interface thicknesses. The various secondary effects introduced by the experimental apparatus have been identified and their influence on the development of the principal instability under consideration at the interface has been evaluated.

1.2. Previous Related Work.

The linear theory for the instability between two immiscible liquids of different densities under gravitational acceleration was first developed by Lord Rayleigh (1900). It was found that the instability occurs only if the light fluid accelerates into the heavy one, and that the initial growth of the perturbations is exponential in time. The theory has subsequently been modified to include effects of surface tension at the interface (Taylor 1950), viscosity (Bellman & Pennington 1956), molecular diffusion (Duff *et al.* 1962) and slight nonlinearity (Kiang 1969). All these effects have been found to reduce the growth rate of the instability. Sharp (1984) reviews the experimental and computational aspects of the nonlinear development and turbulent mixing resulting from the gravitational instability of an interface.

The incompressible theory for an interface under gravitational acceleration yields considerable insight into the processes taking place at an impulsively accelerated interface if the shock is weak. The first treatment of the shock-excited instability was the theoretical analysis of Richtmyer (1960). It was found that, for this case, unbounded growth of any perturbation initially present on the interface is predicted when the shock acceleration is directed either into the light or the heavy fluid. Effects of viscosity and molecular diffusion, although known to reduce the development of the instability, have not been incorporated in the theory. On the other hand, for strong shocks the entire process may be inherently compressible such that a significant amount of wave energy could be radiated from the interface even after the refraction of the incident shock. In addition, the difficulty of the problem of shock-generated turbulence has prevented any analytical treatment for the nonlinear development of the Richtmyer-Meshkov instability, and very little physical insight has been obtained so far from the various numerical computations in this field. The large Reynolds numbers typical of these types of flows generated in the laboratory suggest that the turbulent mixing zone developing at the shock-excited interface contains a wide range of scales. (For example, the Reynolds number is around 10^6, based on representative interface thicknesses, interface velocity jumps and average gas viscosities, in the experiments reported here). Previous experimental studies of the shock-excited instability have been performed by Meshkov (1970) for the growth of sinusoidal perturbations on a thin interface, and by Andronov *et al.* (1976, 1982) for the development of mixing at a nominally flat interface initially supported by a thin plastic membrane. Sturtevant

(1988) surveys the status of the experimental work performed in various other configurations.

1.3. Outline of Present Work.

The present work is an experimental investigation of the physical processes that take place when one or more shock waves interact with an interface between two gases of different densities. The experimental facility and instrumentation used to study this interaction are described in Chapter 2. Chapter 3 summarizes the theory on the growth of linear perturbations on an impulsively accelerated interface and presents a new model describing their growth on a thick diffusive interface. The basic features of the development of a turbulent mixing zone at a nominally flat interface are also reviewed.

Chapter 4 reports on experiments performed to study the growth of single-scale perturbations on a thick interface. It is observed that a finite density gradient at the interface causes a noticeable reduction of the growth rate of perturbations. Good agreement is obtained between the proposed model and the experimental results. Chapter 5 presents the results of the interaction of shock waves with a nominally flat interface. In this case, the seeds for the development of a turbulent layer between the two fluids are only the random small-scale perturbations initially present at the interface. The growth rates of thick interfaces are small and seem to be due more to perturbations introduced during the experiment than to initial inhomogeneities in the interfacial gas. Moreover, the thick interfaces are found to grow much more slowly than the thinner ones, which in turn exhibit much smaller growth than that previously reported by other authors. Because the development of the instability at the interface depends directly on the nature of the perturbation on it, it is not certain whether the turbulent mixing zone achieves a stage of self-similar development independent of initial conditions.

Wall effects, introduced by the experimental setup, are discussed in Chapter 6. It is seen that the propagation of shock waves into the boundary layers developing on the side walls of the facility can lead to secondary wave phenomena. Furthermore, the interaction of the waves reflected from the end of the shock tube with the distorted interface within the boundary layers causes the formation of wall vortices, which deform the interface and slow the development of the instability by vorticity-induced strain.

Chapter 2

EXPERIMENTAL FACILITY AND INSTRUMENTATION

A vertical shock tube has been built specially for the study of the Richtmyer-Meshkov instability. The facility is oriented vertically to take advantage of gravity forces in setting up an interface between a light and a heavy fluid. A test section at the bottom end of the tube incorporates a system to produce an interface between two gases of different densities. For each experimental run, a shock wave is launched from the top portion of the shock tube towards the interface below. After the passage of the shock, the development of the Richtmyer-Meshkov instability between the two gases is examined with schlieren photography and fast response pressure instrumentation.

2.1. Vertical Shock Tube.

A schematic of the GALCIT vertical shock tube is shown in figure 2.1. The vertical shock tube consists of a conventional cold gas driver section, a diaphragm section, and a driven section. The entire assembly is supported by a pin joint just below the diaphragm section and thus can be inverted or inclined at up to 7° from the vertical. The facility extends through three stories in the Guggenheim Laboratory. In the present configuration the driver is located on the ground floor and the test section, with most of the instrumentation, is in the sub-basement.

2.1.1. *Driver Section.* The driver section is comprised of a 1.83 m long piece of 16.5 cm I.D. type 321 stainless steel seamless tubing with a wall thickness of 1.27 cm. Connected to this tube is a 21 cm long transition section of the same inside diameter. The driver section assembly has been hydrotested to the design pressure of 102 atm without failure of O-Ring seals or joints. A picture of the driver section assembly is shown in figure 2.2. The driver tube is suspended from an H-beam directly above it using a cable-pulley-counterweight system so that a single operator can raise the entire driver section to change the diaphragm after each run. The driver vacuum line, the pressure gauge line and the driver gas inlet line are all connected to the top of the driver via high pressure flexible hoses.

To control the instant at which a shock wave is launched, the driver is filled to a pressure approximately 0.7 atm below diaphragm burst pressure, and a small volume of high pressure

gas is then rapidly dumped from a 2.3 liter boost tank, pressurized up to 81 atm, into the driver, causing the diaphragm to rupture. The boost tank is connected to the driver by a large diameter flexible hose and a high flow rate diaphragm solenoid valve (Skinner #R2HLB21252). It takes the place of a mechanical firing device, such as a diaphragm plunger or rupturing tool, without the added complexity. With the present setup, a shock wave can be fired within 500 ms of the actuation of the boost tank.

2.1.2. *Driven Section.* The driven section is square and has inside dimensions of 11.4 cm by 11.4 cm. It is made of 4140 cold-drawn steel tubing with 19 mm thick walls. The strength of the driven section was calculated from a solid model constructed with SDRC IDEAS software, and the stresses were obtained with the SUPERTAB finite element analysis program (Lim & Babcock 1984). The driven section assembly consists of a 30.5 cm driven transition section, two 2.13 m long segments and either two or three 60.5 cm pieces. The inside of the driven section was honed using a silica extrusion process to remove the scale produced during tube fabrication. However, the honing operation did not remove larger size pits of average depth 0.08 mm located randomly an all faces, and longitudinal grooves 15 mm wide and 0.4 mm deep running along the length of the tube on all four faces still remain. The inside corners of the driven section are not perfectly square but have fillets of 2.5 cm radius. The fillets account for a 2% reduction in area as compared to a perfectly square tube of same dimensions. After machining was completed, all sections were nickel plated to prevent corrosion. Selected driven section segments were hydrotested to the design pressure of 60 atm to verify structural and sealing capabilities.

Fourteen instrument ports of access diameter 18.5 mm are located along the driven section. They are mounted off center in the tube walls to avoid the above-mentioned longitudinal grooves. Five ports are machined to house PCB piezoelectric pressure transducers and the others are left blank.

When the distance between the flow visualization windows and the end wall of the tube has to be adjusted, plugs of various thicknesses are inserted in the shock tube or in the test section. Shock tube plugs were molded out of polyester resin, and test section plugs were molded out of RTV silicon rubber. Both sets of plugs follow closely the inside contour of the corresponding

tube.

2.1.3. *Diaphragm Section.* The diaphragm section is necessary to hold the diaphragm in place while the driver is being pressurized. It also provides the transition from the round driver to the square driven section. The vertical shock tube uses a diaphragm section modeled after that of the GALCIT 6" shock tube (see Smith *et al.* (1967) for more details). It was designed for a pressure of 200 atm and has been tested, along with the driver section, to 102 atm. It consists of an integral hydraulic piston that squeezes the diaphragm between two stainless steel flanges (figure 2.3). Both flanges are machined with mating chevron grooves that crimp the diaphragm in place under a hydraulic load of 460 kN. The design is such that the diaphragms need not be cut to perfectly circular shape, have holes drilled in them, or have been crimped prior to their use in the shock tube. Furthermore, it is not necessary to scribe the diaphragms beforehand since a set of knife blades, similar to those described by Roshko & Baganoff (1961), is mounted just below the diaphragm. The diaphragm cuts itself on the blades as it bulges under driver gas pressure. Control panels at both ends of the shock tube are used to monitor the gas filling operations (figure 2.1). The panels contain pressure gauges and valves necessary for supplying the gases to the driver, boost tank, driven and test sections. To monitor the driver pressure from the sub-basement, the driver is equipped with an electronic manometer (MKS Instruments Baratron Model 222CA25000B). The pressure across the interface can be measured with a differential pressure transducer (Baratron Model 221AD-01000A). All setup operations are performed from the sub-basement except for diaphragm change and tube evacuation which are accomplished on the ground floor.

2.2. Test Section.

The test section design was determined by two requirements: to set up an interface between two gases of different densities and to provide optical access to the development of the interaction between the interface and shock waves. Later, a short driven tube section was modified so that the two functions can be separated.

2.2.1. *Test Section.* The test section was designed to sustain an operating pressure of 13.5 atm. It is made out of four 5.1 cm thick 6160-T6 aluminum plates fastened together by dip brazing. It has been successfully hydrotested to 14 atm. Its inside section is square with a 11.4

cm side to match that of the driven section. The ends of the test section have also been machined down to the outside dimensions of the driven section. However, since the inside of the test section is perfectly square and the driven section has rounded corners, the transition between the two is made smoother by installing fillets in the test section corners, tapered over a distance of 7 cm. On opposing sides of the test section are two large access holes that house the viewing windows (figure 2.4). The optical grade glass windows are 38 mm thick and have a square aperture of 11.4 cm by 11.4 cm. Two rectangular slots (11.4 cm by 2.5 cm) are cut on the side of the test section to allow for the setup of interfaces, although only the slot in the field of view of the optical system is used in the present experiments. Thus, three out of four of the side walls of the test section are significantly weakened by cutouts. Therefore, the allowable pressure in the test section has been estimated assuming that the load is carried only by the material in the four corners. Since the test section is the weakest component of the shock tube assembly, the run conditions are such that a pressure of 14 atm is never exceeded in the driven and test sections.

2.2.2. *Interface Section.* To set up an interface at a location upstream of the windows, another section, the "interface section," was fabricated. The interface section consists of a modified 60.5 cm piece of driven tubing. A rectangular slot of the same dimensions as the one on the test section is cut on one of its sides to allow for the same interface setups. It is also equipped with gas inlet ports to permit the introduction of the test gases (figure 2.5). The interface section can be installed in two orientations, with the interface near the bottom or the top of the interface section, to change the initial distance between the interface and the flow visualization windows. All possible experimental configurations are outlined in Table 4.1 and in figure 2.8.

2.2.3. *Interfaces.* Two methods are used to initially form an interface between the two gases. To obtain an initially discontinuous interface, a thin (0.5 μm) nitrocellulose membrane is used. The mass of a membrane is 7.7×10^{-3} g. As it will be seen in Chapter 5, when a shock wave hits a membrane separating air on both sides, it stays in one piece while traveling down the shock tube. When the membrane initially separates two gases of different densities, the shock-excited instability of the interface causes the membrane to shatter in small pieces that are

subsequently entrained in the flow. The influence of the membrane's inertia on the refraction of a shock wave at the interface is discussed in Section 6.3.1.2.

When a membrane is installed in the interface section, it is initially held in a sandwich frame that slips into the interface section (figure 2.6). The inside contour of the sandwich frame perfectly matches that of the interface section to ensure that the flow disturbances are minimal. A special plug is inserted over the frame to close the rectangular access port.

When a membrane is installed in the test section, it is also held in a similar frame whose inside contour matches that of the test section. The frame is inserted in the test section through one of the window ports (figure 2.7). To accommodate the frame, windows equipped with a recess were built. These windows were made by joining together three sheets of 12.7 mm polycarbonate (General Electric MR-5 Margard^{TM}). The resulting assemblies lack the optical qualities of the glass windows but still allow for all measurements of interest to be performed. This setup is used with the end wall located at the bottom of the observing windows, in the so-called 'close end wall' configuration. Figure 2.8a shows the location of the membrane relative to the end wall of the shock tube and the field of view of the flow visualization system.

To form a continuous interface between a light and a heavy gas, the apparatus can be equipped with a system for withdrawing a thin (1.2 mm) metal plate initially separating the gases. With the light gas on top of the heavy one, the plate is withdrawn at speeds up to 10 cm/s leaving behind a region of smooth density change between the two fluids, free of the possible adverse effects of plastic membranes. Sealing around the plate is obtained by gluing small diameter (1 mm) O-Ring stock to its edges. The plate is inserted into a rectangular plug which closes the access port and also guides the motion of the plate. To prevent leaks from the inside to the outside of the tube at the point where the plate enters the test or interface section, an RTV rubber gasket was molded around the plate. This sub-assembly is shown in figure 2.9.

Figure 2.10 shows the sliding plate mechanism installed at the test section. The plate is driven, via a ball screw, by a DC stepping motor (Superior Electric Slo-Syn Model MO92-FF402). This motor can deliver the torque necessary to overcome the friction between the sliding plate and its various sealing components while maintaining motion accuracy at the

desired speed. The motor power is supplied by a motion control driver (Superior Electric Modulynx Model PDM155). This device translates TTL pulses from a 8085 microprocessor to driving power for the motor at a rate of one pulse per motor step. The microprocessor is programmed to supply the acceleration and deceleration commands, as well as the steady state information to ensure smooth plate retraction and prolonged motor life. The microprocessor also commands the operation of the boost tank. When the sliding plate is installed at the test section location, the end wall is brought to the bottom of the observing window, in the 'close end wall' configuration. Figure 2.8b shows the location of the interface with respect to the end wall and the field of view of the schlieren system.

2.3. Shock Tube Operation.

To perform a run, the operation starts at the driver station where the driver, boost tank and driven sections are evacuated to remove any undesired gas components from the previous run. After evacuation, the tube is opened to the atmosphere and a new diaphragm is put in. If helium is used as the driver gas, the driver and boost tank are evacuated again. The boost tank is filled with driver gas at 68 atm. The operation then moves to the sub-basement station.

For the discontinuous interface experiments, a new membrane is inserted in either the test section or the interface section. The driver is pressurized to about 0.7 atm below diaphragm burst pressure to prevent the accidental firing of the shock tube. In most experiments atmospheric air is used above the interface. The test gas is introduced below the interface by positive displacement: When the test gas is heavier than air, it is introduced from the bottom of the test section and pushes air out through an orifice below the interface. When the test gas is lighter than air, it flows in from the orifice below the interface and flushes the air out through the bottom of the test section. The test gas flow rate is monitored with a flowmeter. After about 3-5 test section volumes of gas have circulated, the gas purity is usually satisfactory. When the test gas is helium, leakage through the membrane can occur. The actual mean composition of the test gas below the interface is obtained from a comparison of the experimental $x-t$ diagram for the motion of the interface and waves with the $x-t$ diagram calculated from one-dimensional (1-D) gasdynamics theory (*cf.* Section 6.3.1). The holes necessary for gas introduction are closed flush with the shock tube wall to minimize flow

disturbances. The shock wave is then launched towards the interface by releasing the boost tank pressure into the driver.

For the experiments with a continuous interface, the tube is cleaned with the sliding plate in the retracted position. The driver is pre-pressurized, and the plate is inserted back into the tube. In these experiments the heavy gas is always located below the interface, and the gas filling operation is performed as described above. After the gases are introduced, the microprocessor control system then takes over to provide the sequence for retracting the plate and, after a preset delay, triggering the boost tank to fire the shock wave towards the interface below.

In the present experiments, the Mach number of the incident shock wave ranges from M_s = 1.12 to M_s = 1.66.

2.4. Description of Gases.

The choice of test gases was governed by both safety and convenience considerations. All fluids used are readily available commercial grade pressurized gases and they are non-combustible and non-poisonous. The gases chosen reflect an effort to cover the widest possible range of Atwood ratio A, defined as $(\rho_2 - \rho_1)/(\rho_1 + \rho_2)$, which is an important parameter in the development of the Richtmyer-Meshkov instability. For the light-heavy configurations, the light gas is atmospheric air and the heavy gases are either carbon dioxide (CO_2), refrigerant-22 ($CHClF_2$) or sulphur hexafluoride (SF_6). In the heavy-light configuration, helium (He) is used below air. All gases have a purity of 99.7% or better. Table 2.1 lists representative properties of the gases used in the experiments. Atwood ratios ranging from -0.76 to +0.67 can be achieved by pairing these gases with air.

The possible vibrational relaxation effects resulting from the propagation of shock waves in polyatomic gases are discussed in Section 6.3.1.1. It is found that relaxation can be ignored in the present experiments since the shock waves are neither very weak nor very strong.

2.5. Pressure Measurements.

Pressure transducers (Piezotronics PCB Model 113) are located along the tube for the measurement of the speed and strength of the pressure waves emanating from the refraction of the incident shock at the interface. The pressure transducers also provide trigger signals for the

Table 2.1. Gas Properties @ 25 °C, 1 atm

Property	Air	CO_2	R-22	SF_6	He
Molecular mass M (kg/kmol)	29.04	44.01	86.48	146.07	4.00
Density ρ (kg/m^3)	1.18	1.80	3.54	5.97	0.16
Atwood ratio with air A	0	0.20	0.50	0.67	-0.76
Specific heat ratio γ	1.40	1.29[1]	1.17[1]	1.09[1]	1.667
Kinematic viscosity ν (10^{-6} m^2/s)	15.7[2]	7.97[2]	3.60[3]	2.47[3]	117.3[2]
Prandtl number Pr	0.71[2]	0.77[2]	0.73[3]	0.90[4]	0.70[2]
Diffusion coefficient in air[5] D (cm^2/s)	0.204	0.151	0.104	0.097	0.711
Index of refraction (sodium D line)	1.000264[6]	1.000410[4]	1.000669[4]	1.000717[7]	1.000033[6]

1. Stull & Prophet (1971)
2. Kreith & Black (1980)
3. Baker & Mossman (1971)
4. Gray (1972)
5. Calculated using molecular theory from Hirschfelder *et al.* (1954)
6. Liepmann & Roshko (1957)
7. Marshall (1976)

flow visualization equipment. Their sensitivity ranges from 282 to 406 mV/bar.

The pressure transducers can be located at various positions along the shock tube. The pressure signals are recorded on an IBM PC-AT computer using Computerscope hardware and software from RC Electronics Inc.. The speed of a wave is determined by its time of flight between two adjacent transducers.

2.6. Flow Visualization.

Flow visualization of the development of the instability at the interface is achieved with a schlieren optical system. The setup can be used for individual high-resolution spark photographs or for high-speed cinematography.

Figure 2.11 shows the layout for the spark schlieren system. The spark gap is of a Caltech design, with a 10 kV 0.1 μF capacitor. A 20 cm clear aperture, 1.50 m focal length spherical mirror is used to collect the light from the spark gap and make it parallel through the test section. An identical mirror focuses the light emerging from the test section onto a knife edge, mounted on a high-precision two-dimensional positioner, to achieve the schlieren effect. The image is then recorded by a 35 mm camera (Nikon FE2) equipped with an 85 mm lens mounted on bellows. Ilford XP-1 (400 ASA) film is used. During a run, the camera is operated in the dark and its shutter is left open. A pressure transducer mounted upstream of the test section provides a trigger signal for the spark gap to illuminate the film after a preset delay. The trigger signal is recorded on the Computerscope, along with the pressure traces.

Figure 2.12 shows the setup used for high-speed schlieren cinematography. The mirrors and knife edge are at the same locations as for the single picture layout. The spark gap is replaced by a 100 W low pressure mercury vapor arc lamp (Ealing Stabilarc 250 lamphouse with Model 27-1015 power supply) to provide a continuous light source. The light is focused with a converging lens onto a 0.4 mm pinhole to reduce the effective source size. The time evolution of the interface is then recorded with a Cordin Model 374 camera, which has a framing rate of up to 100,000 frames per second (fps). The camera is equipped with a Canon 35-105 mm TV zoom lens. It records 500 16 mm frames on four parallel rows on a 1 m long strip of 70 mm wide film. Kodak Tri-X (400 ASA) and Plus-X (125 ASA) films are used. When a run is performed, the camera is operated in the dark with its shutter open. Upon a trigger signal from a pressure transducer, a fast electromagnetically-actuated shutter then exposes the film for a preset time duration.

The sensitivity of the schlieren system is adjusted so that the interface can easily be distinguished from the image of the shock wave-boundary layer interaction on the observing window (*cf.* Sections 4.2, 5.2 and 5.3). At the same time, the sensitivity is kept sufficient to record the random field of acoustic waves associated with the waves reverberating between the interface and the end of the tube.

Chapter 3

THEORETICAL CONSIDERATIONS

3.1. Introduction.

A wide variety of fluid motions can be generated when a shock wave is incident on an interface between two substances of different densities. In general, both the shock and the interface deform as a result of the interaction because the coupling between the pressure gradient of the shock and the density gradient across the interface is an efficient mechanism for generating vorticity. This can be demonstrated by considering the interaction of a plane shock wave with a sinusoidally perturbed thin interface (figure 3.1). For shock propagation from a light gas into a heavy gas, as seen in figure 3.1a, the misalignment of the pressure gradient of the shock and the density gradient of the interface (figure 3.1b) generates counterclockwise vorticity on the right portion of the perturbation and clockwise vorticity on the left (figure 3.1c). A vortex sheet of varying strength is thus created at the interface (figure 3.1d). The motions induced by this vorticity then lead to the deformation of the interface, causing an increase in amplitude of any perturbation initially present: the interface is unstable (figure 3.1e). For the interaction of a shock with a heavy-light interface (figure 3.1f), the density gradients are in the opposite direction from those on the light-heavy interface, and the vorticity generated by the shock thus has a different sense (figures 3.1g, h and i); the vorticity-induced motions cause the interface to flatten. However, since the vorticity deposited at the interface by the impulsive acceleration persists after the refraction of the incident shock wave, the interface reverses phase, and the distortions on the interface also grow without limit for this case (figure 3.1j).

The development of this instability can be evaluated theoretically if the amplitude of the perturbation is taken to be small compared to its wavelength. For a weak shock, the theory for the impulsive acceleration can be deduced from the analysis of the discontinuous interface between two incompressible fluids under constant acceleration. Furthermore, if the interface is continuous, the theory has to be modified to take into account the presence of the finite density gradient between the two fluids.

In this chapter the basic theory for the instability between two fluids of different densities is presented, and a simple model to predict the shock-induced growth of perturbations on a continuous interface is proposed. The basic physical mechanisms governing the nonlinear development of the interface into a turbulent mixing zone are also reviewed.

3.2. Linear Theory.

3.2.1. *Discontinuous Interface.*

3.2.1.1 Rayleigh-Taylor Instability. Lord Rayleigh (1900) and Taylor (1950) performed a detailed analysis of the evolution of a discontinuous interface separating two liquids of different densities under gravitational acceleration. Figure 3.2 shows the configuration being considered. Initially (time $t = 0$), two semi-infinite fluids of densities ρ_1 and ρ_2, respectively, are separated at $x = 0$ by a contact surface. Fluid **1** accelerates into fluid **2**, corresponding to an *upwards* gravitational field g. The perturbation on the interface is taken to be two-dimensional in the x–y plane and is described by $x_p(y) = \eta_0 \cos ky$, where η_0 and k are its initial amplitude and wavenumber, respectively. It should be noted that the growth of disturbances of arbitrary shape can be determined by decomposing them into a superposition of harmonic modes in the y and z directions, where each one would grow at a rate dependent on its wavenumber $k = \sqrt{k_y^2 + k_z^2}$.

The solution for the velocity potentials in the two liquids ϕ_1 and ϕ_2, subject to the conditions that velocities be negligible at $x \rightarrow \pm\infty$, and that pressure and normal velocity are continuous across the interface, is

$$\phi_1 = \frac{\Omega\eta_0}{k} e^{kx} \sinh\Omega t \cos ky \tag{3.1a}$$

$$\phi_2 = \frac{-\Omega\eta_0}{k} e^{-kx} \sinh\Omega t \cos ky \quad . \tag{3.1b}$$

The growth rate Ω is found to be

$$\Omega^2 = kg\frac{\rho_2-\rho_1}{\rho_1+\rho_2} = kgA \quad , \tag{3.2}$$

where A is the reduced density difference, also known as the Atwood ratio.

The time evolution of the amplitude of the perturbation is described by the Rayleigh-Taylor formula

$$\frac{d^2\eta(t)}{dt^2} = \Omega^2\eta(t), \tag{3.3}$$

which is valid as long as the perturbation stays in the linear regime, *i.e.*, for $k\eta \ll 1$. It can be seen from this equation that if $\rho_2 < \rho_1$, Ω^2 is negative, and thus $\eta(t) \propto e^{i\,t\sqrt{kgA}}$. The interface is therefore stable and waves persist on the interface. If $\rho_2 > \rho_1$ then $\eta(t) \propto e^{t\sqrt{kgA}}$. For this case, the growth is unbounded and exponential in time; the interface is unstable.

The total kinetic energy E_k of the motion of the perturbations can be evaluated from the perturbation velocities

$$u_1 = \frac{\partial\phi_1}{\partial x} \quad , \quad v_1 = \frac{\partial\phi_1}{\partial y} \tag{3.4a}$$

$$u_2 = \frac{\partial\phi_2}{\partial x} \quad , \quad v_2 = \frac{\partial\phi_2}{\partial y} \tag{3.4b}$$

as

$$E_k = \int_{-\infty}^{0} \frac{1}{2}\rho_1(u_1^2+v_1^2)\,dx \quad + \int_{0}^{\infty} \frac{1}{2}\rho_2(u_2^2+v_2^2)\,dx \quad . \tag{3.5}$$

The total perturbation kinetic energy per unit area is then

$$E_k = \frac{1}{2}\bar{\rho}\,g\,A\,\eta_0^2\sinh^2\Omega t \quad , \tag{3.6}$$

were $\bar{\rho} = (\rho_1+\rho_2)/2$ is the average density across the interface. It can be seen that, for the

unstable interface, E_k increases with time and is independent of the wavelength of the perturbation.

When the behavior is no longer linear, the crests and the troughs of the perturbations evolve asymmetrically and lead to the appearance of spikes of heavy fluid penetrating into the light one and bubbles of light fluid rising slowly into the heavy one, as it has been demonstrated, for example, by experiments of Lewis (1950) and Jacobs & Catton (1988), and numerical computations of Baker *et al.* (1980) and Menikoff & Zemach (1983). At this point the Kelvin-Helmholtz instability also becomes important, and the generation of small scale turbulence is observed. At the late stages of the evolution of the interface turbulent mixing between the two fluids is important. It is generally believed that, at this point, the evolution of the turbulent mixing region between the two liquids is independent of the initial perturbation after the initial scales disappear. These regimes of the evolution of the interface are illustrated in figure 3.3. Since part of the kinetic energy of the perturbation is available for the turbulent motions at the later stages of development, energy is continuously fed into the mixing process at the interface. In light of this and of the fact that the kinetic energy is not a function of the initial wavelength of the perturbations, the assumption that the turbulent mixing at the interface is independent of initial conditions seems reasonable. Read (1984) performed constant acceleration experiments with liquids and measured the asymptotic turbulent growth at the interface. Youngs (1984) reported results from numerical calculations that confirmed the existence of the asymptotic limit.

3.2.1.2 Richtmyer-Meshkov Instability. The case of a discontinuous interface under shock acceleration was considered by Markstein (1957b), although the first rigorous treatment of the shock-excited instability was the theoretical analysis of Richtmyer (1960). Richtmyer considered the linearized response of a discontinuous interface between two perfect gases to an incident shock wave propagating normal to the plane of the undistorted interface. The intensity of the motions at the interface depend on the strength of the incident wave. Richtmyer proposed that, for a weak shock, the velocities induced are relatively small, and the subsequent motion can be assumed to be incompressible. Taylor's formula (Eq. 3.3) can then be applied directly, replacing the constant acceleration g by an impulsive one $g = [u]\,\delta_D(t)$, to obtain the

growth rate relation

$$\frac{d\eta(t)}{dt} = k[u]A'\eta'_0 \ , \tag{3.7}$$

where $\delta_D(t)$ is the Dirac delta function, $[u]$ is the change of interface velocity induced by the shock and A' is the Atwood ratio across the interface based on post-shock densities. The analysis is valid as long as $\eta(t) \ll \lambda$, *i.e.*, for $t \ll \lambda^2/(\eta_0[u])$. From Eq. (3.7) it can be seen that the growth of the perturbations on an impulsively accelerated interface is linear in time, and that *both* light-heavy and heavy-light configurations are unstable. For the light-heavy or 'unstable' configuration the perturbation simply increases in amplitude. For the heavy-light or 'stable' configuration, the perturbation initially decreases in amplitude before reversing its phase and growing unboundedly.

Richtmyer solved the linearized problem numerically and found agreement within 5 - 10% with the impulsive incompressible formula (3.7), provided η'_0 and A', the post-shock amplitude and Atwood ratio, respectively, are used instead of the pre-shock values, η_0 and A. Experiments with curved gaseous interfaces under shock acceleration by Meshkov (1969) verified the linear growth law of single-scale perturbations for both the light-heavy and the heavy-light case. Sturtevant (1988) pointed out that by using the correct post-shock parameters the growth rates measured by Meshkov can be made to agree more closely with the values predicted by the theory of Richtmyer. The formula has also been checked numerically (Meyer and Blewett 1972) and experimentally in liquids (Benjamin *et al.* 1984, Benjamin & Fritz 1987).

After the refraction of the incident shock at the interface, the velocity potentials for both fluids in the reference frame of the interface are

$$\phi_1 = A'[u]\eta'_0 e^{kx} \cos ky \tag{3.8a}$$

$$\phi_2 = -A'[u]\eta'_0 e^{-kx} \cos ky \ . \tag{3.8b}$$

The total perturbation kinetic energy per unit area is obtained from the perturbation velocities as

$$E_k = \frac{1}{2}\bar{\rho}\, k\, [u]^2 A'^2 \eta_0'^2 \quad . \tag{3.9}$$

As opposed to the constant acceleration case, the kinetic energy for the impulsive case is dependent on the wavelength of the perturbation and remains constant after the passage of the shock.

The nonlinear development of the perturbations is similar to that for the constant acceleration case, leading ultimately to the appearance of a turbulent mixing zone at the interface. However, there is no experimental or theoretical evidence that it ever reaches an asymptotic stage of self-similar turbulent growth independent of initial conditions, as in the constant gravity case.

3.2.2. *Continuous Interface.*

3.2.2.1 Constant acceleration. The continuous interface under constant acceleration has first been considered in a rudimentary manner by LeLevier *et al.* (1955). The results have shown that the growth of the continuous interface is reduced as its thickness is increased. In the limit of a thickness that is large compared to the wavelength the growth is not totally suppressed but achieves a limiting value such that $\eta \sim \eta_0 \exp(t\sqrt{2gA/\delta})$, where δ is the thickness of the interface for the density profile considered by these investigators.

Duff *et al.* (1962) have considered the problem of the thick interface in more detail. The configuration of interest is shown in figure 3.4. Their approach involved the solution of the linear eigenvalue equation for the perturbation velocity u, for a sinusoidally distorted arbitrary density profile under constant acceleration (Chandrasekhar 1961, p. 433):

$$\frac{d}{dx}\left[\rho\frac{du}{dx}\right] = uk^2\left[\rho - \frac{g}{\Omega^2}\frac{d\rho}{dx}\right] \tag{3.10}$$

subject to $u \to 0$ as $x \to \pm\infty$. For a discontinuous interface, the eigenvalue Ω^2 reduces to kgA as before. By analogy with that solution, Duff *et al.* proposed for the continuous interface that the eigenvalue Ω^2 be replaced by

$$\Omega^2 = \frac{kgA}{\psi} \quad , \tag{3.11}$$

where ψ is the so-called growth reduction factor and is a function of interface thickness and Atwood ratio; $\psi > 1$ for the continuous interface and $\psi = 1$ for the discontinuous interface. Substituting Eq. (3.11) into Eq. (3.10), one then gets the following eigenvalue equation:

$$\frac{d}{dx}\left(\rho \frac{du}{dx}\right) = uk^2\left(\rho - \frac{\psi}{Ak}\frac{d\rho}{dx}\right) \quad , \tag{3.12}$$

where ψ is now the eigenvalue. Duff *et al.* computed the solution for a given density profile by solving the equation numerically.

The growth rate at the interface can then be obtained from

$$\frac{d^2\eta(t)}{dt^2} = \frac{kgA}{\psi}\eta(t) \quad , \tag{3.13}$$

where ψ can be a function of time if the thickness of the interface increases, by molecular diffusion for example, while the perturbation on the interface grows in amplitude. Duff *et al.* verified the validity of Eq. (3.13) experimentally .

The continuous interface problem was also considered analytically by Mikaelian (1982a, 1982b, 1983) by modeling the interface as a superposition of M discrete discontinuous interfaces. The results have shown that a smooth interface can be modeled accurately with M = 5, although the closed form expression for the growth rate becomes very complicated for M > 2.

3.2.2.2 Impulsive Acceleration. Mikaelian (1985a) also treated the continuous interface under impulsive acceleration by modeling it as a series of M discrete discontinuous interfaces. The growth rate is obtained from the eigenvalues of a system of M × M equations. Although M = 5 has been shown to model accurately a smooth continuous interface, this treatment is not amenable to a compact closed-form expression.

The approach that is considered here starts from the equation for the Rayleigh-Taylor instability of the continuous interface:

$$\frac{d^2\eta(t)}{dt^2} = \frac{kgA}{\psi}\eta(t) \quad . \tag{3.13}$$

As before, the constant acceleration g is replaced by an impulsive one $g = [u]\,\delta_D(t)$. Since, in this case, the thickening of the interface by molecular diffusion is much slower than the growth rate of the perturbation, the factor ψ can be considered constant, and the equation can be integrated directly to yield:

$$\frac{d\eta}{dt} = \frac{k\,[u]\,A'}{\psi}\eta'_0 \quad , \tag{3.14}$$

where the growth reduction factor ψ is now a function of Atwood ratio A' and interface thickness δ. Because the thickness of the interface is compressed as a result of the refraction of the incident shock at the interface, it is proposed that the interface thickness δ be taken as the average of the pre- and post-shock thicknesses, *i.e.*, $\delta = (\delta_0 + \delta'_0)/2$.

The growth reduction factor ψ is determined by solving (Eq. 3.12) numerically for the case of a diffusive profile between the two gases:

$$\rho(x) = \frac{1}{2}(\rho'_1+\rho'_2)\left[1+A'\,\mathrm{erf}\left[\frac{x}{\delta}\right]\right] \tag{3.15}$$

The characteristic thickness of the interface δ can be taken as the maximum slope thickness of the density profile at a time τ after molecular diffusion began to take place between the two gases, such that $\delta = 2\sqrt{\pi D\,\tau}$, where D is the molecular species diffusion coefficient. Figure 3.5 shows a plot of ψ as a function of thickness *vs.* wavelength ratio δ/λ for the gas combinations considered in the present experiments. One can see that, for a given δ/λ, the growth reduction factor ψ is higher for a lower Atwood ratio at the interface. In fact, the limit $A' = 0$ corresponds to the analysis of LeLevier *et al.* (1955), *i.e.*, $\psi = 1+\pi(\delta/\lambda)$. For a very thin interface, *i.e.*, $\delta/\lambda \sim 0$, ψ reduces to 1, and the discontinuous result is recovered. In the limit

that $A' = 1$, then $\psi = 1$ also.

If the wavelength of a perturbation on a continuous interface becomes small compared to its thickness, the ψ *vs* δ/λ curve becomes linear, and thus can be described by

$$\psi_\infty = 1 + C\,\frac{\delta}{\lambda} \quad . \tag{3.16}$$

It is found that this is a good approximation for $\delta/\lambda > 1$. For the case that $\delta >> \lambda$, the growth rate at the interface is not zero but reduces to

$$\frac{d\eta}{dt} = \frac{2\pi}{\delta}\,\frac{A'[u]\,\eta'_0}{C} \quad . \tag{3.17}$$

Table 3.1 lists the value of the constant C for the gas combinations of interest, obtained from a straight line fit to the curves of figure 3.5 at large δ/λ.

Table 3.1. Approximation to the Growth Reduction Factor -- $\psi = 1 + C\,\delta/\lambda$

Test Gas	A'	C
He	-0.76	2.36
Air	0	3.1416
CO_2	0.20	3.06
R-22	0.50	2.83
SF_6	0.67	2.59

For a typical interface under impulsive acceleration, say $[u]$ = 100 m/s, A' = 0.5, δ = 10 mm and C = 2.83, the growth rate would be about 1 m/s for η'_0 = 0.1 mm.

As long as the perturbation stays in the linear regime, it is proposed that, when the interface undergoes multiple impulsive accelerations caused by the arrival of many waves at the interface, the growth rate after $N + 1$ waves is given by

$$\left[\frac{d\eta}{dt}\right]_N = k \sum_{i=0}^{N} \frac{[u]_i A'_i \eta'_i}{\psi_i} \quad , \tag{3.18}$$

where $[u]_i$ is the interface velocity change caused by the ith wave; A'_i and η'_i are the Atwood ratio across the interface and the amplitude of the perturbation after the passage of wave i, respectively. The wave reduction factor ψ_i is computed from A'_i and δ'_i. The wave numbering convention is such that the first wave is wave 0, the first reflection interacting with the interface is wave 1, and so on. As before the formula is valid for $k\eta \ll 1$. Experiments to verify the validity of Eq. (3.17) are presented in Chapter 4.

By solving for the linearized equations of motion numerically, Saffman & Meiron (1989) have calculated the perturbation kinetic energy deposited by the impulsive acceleration of an interface with a finite density gradient. They found that a significant reduction in kinetic energy can be achieved by increasing the thickness of the interface. For the case in which the thickness is large compared to the wavelength of the perturbation, they obtain

$$E_k = \frac{1}{2}\bar{\rho} k [u]^2 A'^2 \eta'^2_0 \frac{\lambda}{3\pi\delta} = \frac{1}{3\delta}\bar{\rho}[u]^2 A'^2 \eta'^2_0 \quad , \tag{3.19}$$

which is different from Eq. (3.9) for the discontinuous interface by a factor $\lambda/3\pi\delta$. Since $k = 2\pi/\lambda$, the kinetic energy is independent of the wavelength of the perturbation for this limiting case, although it now depends on the thickness of the interface.

3.3. Richtmyer-Meshkov Instability of Plane Interfaces.

The basic processes taking place during the nonlinear development of the instability are presented here.

It has been seen in the previous section that the refraction of a shock wave at an interface between two gases of different densities causes the growth of any perturbation initially present on the interface. Afterwards, as the perturbations on the interface increase in amplitude, secondary instabilities such as the Kelvin-Helmholtz instability develop, leading to the

appearance of regions of turbulence and mixing between the two fluids. Further enhancement of the mixing between the two gases can be achieved when the already turbulent interface is processed by one or more additional pressure waves. The turbulence generated by shock interaction is highly anisotropic, with vorticity lying predominantly in the plane of the shock. Little is known about the processes by which shock-generated turbulence relaxes toward isotropy or about mixing in such turbulence, though it is likely that three-dimensionality develops from two-dimensional features.

In applications in which turbulent mixing is undesirable, such as in the design of laser-fusion pellets, interfaces are made as smooth as possible, and the configurations are arranged with the shocks parallel to the interfaces. In this case, random small-scale fluctuations (usually introduced during the manufacture of the interface) are the most important perturbations on the interface, since high-frequency perturbations grow most rapidly into the nonlinear regime, $\eta \sim \lambda$. The incident shock thus generates small-scale turbulence, presumably in the form of a random array of vortex rings (for suggestive pictorial evidence in a different setting see Detleff *et al.* (1979) and Thompson *et al.* (1988)), by the baroclinic vorticity production mechanism. Merging of the scales associated with the fluid motion and entrainment by the resulting large-scale structures then become the dominant mechanisms for mixing at the interface. Qualitative numerical evidence for this scenario is shown in figure 3.6. The 2-D calculation, performed by Mikaelian (1988) using an inviscid arbitrary Lagrangian-Eulerian (ALE) code, is for the development of random small-scale perturbations on an air/SF_6 interface interacting with a M_s = 1.30 shock. The emergence of large scale structures from the initially small scale fluctuations can clearly be seen. However, it is not known whether the development of the turbulent mixing zone (TMZ) becomes independent of the initial conditions, by analogy with results from constant acceleration Rayleigh-Taylor turbulent mixing (*e.g.*, Youngs 1984). Furthermore, for the impulsive case, since the energy responsible for the fluid motion is deposited at the interface only at the time of the impulsive acceleration, the turbulence intensity decays in time due to the thickening of the interface region, the action of viscosity and the possible radiation of wave energy.

To describe the initial motion of small-scale perturbations on an impulsively accelerated interface, the linear theory for the baroclinic instability can be used. As can be seen from Richtmyer's formula (Eq. 3.7), perturbations of small wavelength grow comparatively faster

into the nonlinear regime than longer ones. For example, an interface with a perturbation of wavelength λ = 1 mm and η_0/λ = 0.1, impulsively accelerated from rest to a velocity of 100 m/s, will grow out of the linear regime within 100 μs. Subsequently, a turbulent mixing zone between the two gases develops.

The total kinetic energy of the velocity perturbations introduced by the incident shock at the interface has been determined in Eq. (3.9). Part of this energy is available for the turbulent motions and ultimately all of it is dissipated into heat by the action of viscosity. It can be seen that the total kinetic energy depends on the initial configuration of the interface through η'^2_0/λ. Considering the influence of initial conditions on the energy available for the turbulent motions at the impulsively accelerated interface, and the fact that this energy remains constant after the refraction of the incident shock, it seems doubtful that the development of the turbulence achieves a self-similar regime independent of initial conditions, as it is observed for the constant gravity experiments.

Several authors have considered the time evolution of the TMZ, *e.g.*, Barenblatt (1983) and Leith (1985). The arguments can be summarized as follows: For small time the relevant dynamical parameters are the densities across the shocked interface, ρ'_1 and ρ'_2, the thickness of the TMZ, δ, and the velocity change of the interface $[u]$. As is customary, the motion is taken to be fully turbulent and of high Reynolds number, such that, to a first approximation, the effects of viscosity are negligible. The motion is assumed to be independent of the initial state, so there is no characteristic time and the flow develops conically in space-time,

$$\frac{\delta}{[u]\,t} = f(A') \,. \tag{3.20}$$

As has been discussed above, the TMZ evolves from the nonlinear development of small-scale perturbations on the interface which initially grow linearly at a rate $d\eta/dt$. Since the nonlinear phase of development of the nonuniformities is slower than the linear regime, and that the extent of the TMZ is bounded by twice the amplitude of the perturbation, an upper bound to the initial growth of the TMZ can be obtained as

$$\frac{\delta}{t} < 2\frac{d\eta}{dt} \quad . \tag{3.21}$$

Later, as the thickness of the TMZ increases, the turbulence intensity decreases. If δ is taken to be proportional to the scale of the energy-containing turbulent motions, the turbulent kinetic energy per unit volume E_{turb} goes as $E_{turb} \propto \delta^2/t^2$. By integrating across the interface, the total turbulent energy per unit area is then $E_{turb\ tot} \propto \delta \times \delta^2/t^2$. In the absence of viscous stress $E_{turb\ tot}$ is constant, so $\delta \propto t^{2/3}$. Barenblatt (1983) has modeled analytically the decay of a plane region of turbulence separating two semi-infinite fluids of the same density and formally obtained the same result. Moreover, when viscous dissipation is taken into account, he obtains that the width of the turbulent layer grows as $\delta \propto t^{\alpha}$, where the exponent $\alpha < 2/3$ depends on two turbulence model constants. Equivalent models for gases of disparate densities have not been proposed.

These simple qualitative arguments are summarized in figure 3.7. However, these do not yield quantitative predictions; for example, the slope of the linear portion of the linear growth curve can not be determined accurately. The time t^* at which transition occurs from the linear (Eq. 3.20) to the power law regime can be crudely estimated for the inviscid case by patching the two solutions using simple arguments involving the conservation of energy at the interface (*cf.* Appendix A). Then the transition time goes as

$$t^* \propto E_{turb\ tot}{}^{-1/2} \propto E_k{}^{-1/2} \propto [u]^{-1} \quad , \tag{3.22}$$

since the total energy initially deposited at the interface is proportional to the square of the velocity jump. Thus it can be seen that the linear portion of the curve is shortened as the incident shock Mach number is increased. It is obvious from the figure that viscous dissipation reduces the transition time, *i.e.*, $t^*_{vis} < t^*$.

So far the time evolution of the TMZ has been treated only by detailed numerical computation using turbulence models, *e.g.*, by Andronov *et al.* (1982) and Leith (1986). Due to the lack of experimental data for these flows, the models are usually tuned to results from constant-gravity experiments with liquids (Read 1984) and to shear-driven turbulence experiments.

Mikaelian (1985b) adapted the constant-acceleration experimental results of Read in a manner similar to the way in which Richtmyer translated Taylor's theoretical results to the impulsive case (*cf.* Section 3.2.1.2). For the shock-induced growth of an initially flat interface between two gases of different densities, he obtained the relation

$$\delta = 0.28\,[u]\,A'\,t \quad . \tag{3.23}$$

Thus, for this case, the function f of Eq. (3.20) becomes

$$f = 0.28\,A'. \tag{3.24}$$

For strong incident shocks, these processes may inherently be compressible, and a significant amount of wave energy could be radiated from the interface. To quantify the magnitude of this effect on the results reported in the next chapters, a relative Mach number M_{rel} can be defined from the maximum possible shear velocity that can be induced at the interface by impulsive acceleration (*cf.* Appendix B). It is found that M_{rel} varies from M_{rel} = 0.24 for the air/CO_2 interface accelerated by a M_s = 1.12 incident shock, to M_{rel}= 2.24 for air/SF_6, M_s = 1.66. Since these are values corresponding to an upper limit to the shear velocities actually present within the interface, it is not possible to use an established Mach number criterion, such as that of Papamoschou & Roshko (1988) obtained in the study of compressible shear layers, for the determination of the onset of influence of compressibility in the present experiments. For now, perhaps the only method to determine if the effects of compressibility are important is to perform a full 2-D numerical calculation and evaluate how much energy resides in the acoustic modes. If a certain fraction of the total kinetic energy deposited by the shock at the interface is exceeded, then the process could be ruled compressible.

The effect of multiple wave interaction with the turbulent interface is an even more difficult problem. It is important to note that, even in the absence of the baroclinic instability at the interface, the passage of a shock wave through a turbulent region can lead to dramatically increased mixing simply by rapid distortion (Hunt 1978, Wu *et al.* 1985) and shock scattering (Hesselink & Sturtevant 1988). The interaction of a shock with a region of highly nonisotropic turbulence is impossible to treat analytically since detailed information about the initial

turbulent state is required. The tendency to return to isotropy may result in a smaller net enhancement of the turbulence. Clearly, the combination of shock-intensification of pre-existing turbulence and turbulence generation by baroclinic instability can at present only be treated experimentally. The experiments reported in Chapter 5 attempt to address some of these issues.

Chapter 4

SINGLE-SCALE PERTURBATIONS

Experiments to study the growth of single scale perturbations on a continuous interface under impulsive acceleration are presented in this section. The two gases are initially separated by the sliding plate. Consequently, with the present orientation of the shock tube, only the light-heavy configuration is studied. Although the initial amplitude of the perturbation can not be determined accurately, the results can be compared to the linear theory, *i.e.*, Eq. (3.18), if experiments are performed with different wave reverberation periods. The agreement between the calculated and observed growth rates is satisfactory.

4.1. Experimental Setup.

Perturbations on the interface can be introduced by taking advantage of the fact that, because of the no-slip condition on the surface of the plate, the plate drags along a certain amount of fluid as it retracts. This fluid then accumulates at the side wall and, just as the plate is fully retracted, propagates out along the interface as a dispersive gravity wave, leaving behind a quasi-sinusoidal perturbation on a thick diffusive interface. Figure 4.1a shows a schlieren picture of the interface between air and SF_6 just after the plate is retracted. The interface is the dark region near the top of the photograph. The accumulation of fluid pumped by the plate can be seen on the left portion of the interface. Figure 4.1b shows a schlieren picture of the same interface taken 0.9 s after full plate retraction, after the wave has propagated to the other side of the test section. The quasi-sinusoidal nature of the perturbation on the interface can also be seen. Figure 4.1c sketches the features of the perturbations. However, the amplitude and wavelength of the perturbation can not be determined accurately from the photograph. From pictures of the evolution of the interface after the start of the shock-excited instability, it will be seen that there are about four waves present on the interface. The experiments are performed in a manner such that the incident shock wave interacts with the interface perturbation described above. The effect of the reverberations of the incident wave on the development at the interface is also studied.

Figure 4.2 shows a generic x–t diagram for the interaction of a moderately weak shock wave with a light-heavy interface. At t = 0, the shock is incident at the interface and

impulsively accelerates the gases towards the end wall. The shock transmitted in the heavy fluid **2** then reflects from the end boundary and interacts with the moving interface at $t=t_1$, causing it to reverse its motion. At the same time expansion waves are reflected back into fluid **2** and a shock is transmitted into the light gas. Waves trapped in gas **2** then reverberate between the interface and the end wall and gradually bring the interface to rest.

In the experiments reported in this study, the time between reverberations can be modified by changing the initial location of the interface with respect to the end wall of the shock tube. Two configurations are used:

The 'close end wall' experiments (*cf.* Section 2.2.3) are performed with the interface initially in the field of view of the windows, and the end wall of the shock tube is moved 10 cm downstream of the interface. This setup is used to observe the evolution of the interface at early times after the interaction with the incident shock and also to study the effects of multiple impulsive accelerations caused by reverberations of the primary wave between the interface and the end wall of the shock tube.

In the other configuration, the 'long time' experiments, the interface is initially located in the interface section (*cf.* Section 2.2.2), either 32 cm or 65 cm upstream of the flow visualization windows. The end of the shock tube is adjusted, using the contoured plugs described in Section 2.1.2, so that the first reflection interacts with the interface just as the latter is about to leave the window. Thus, a 'snapshot' view of the interface a long time after it interacts with the incident shock, as well as of the effects of the first reshock, is obtained. Table 4.1 lists the relevant tube dimensions for various gas pairs and incident shock strengths. Although only R-22 and SF_6 are used as test gases for the experiments reported here, the other gas combinations will be referred to in the next chapter. Also included in the table are the time at which the interface first appears in the field of view of the windows after the start of the interaction and the time at which the interaction with the first reshock takes place.

Table 4.1. Experimental Conditions - Long Time Experiments

Test Gas	A_0	M_s	Interface-Window Distance (cm)	Interface-End Wall Distance (cm)	Appearance Time (ms)	Reshock Time (ms)
He	-0.76	1.32	32	109	1.45	1.71
		1.48	32	84	0.94	1.11
		1.66	32	70	0.72	0.83
		1.66	65	109	1.47	1.54
Air	0	1.32	32	70	1.97	2.45
		1.48	32	56	1.38	1.64
		1.66	32	51	1.05	1.26
R-22	0.50	1.12	32	102	5.94	8.19
		1.32	32	64	2.60	3.65
		1.48	32	53	1.78	2.43
		1.66	32	50	1.38	1.90
SF_6	0.67	1.12	32	84	6.87	8.71
		1.32	32	56	3.07	4.12
		1.48	32	49	2.11	2.81
		1.66	65	84	3.25	3.86

4.2. Results.

4.2.1. *Growth After Incident Shock.* Figure 4.3 shows pictures obtained from a 35000 fps motion picture of a 'close end wall' experiment for the air/SF_6 interface accelerated by a M_s = 1.32 shock wave. The first picture (the same as figure 4.1b) is taken before the arrival of the shock and shows the nature of the initial perturbation on the interface. The second one, taken a time t = 0.7 ms after the arrival of the incident wave, shows the interface shortly before interacting with the first reshock, seen below the interface. The interaction with the incident shock has compressed the interface, making the perturbation more visible, but not much growth is detected. The pair of thin lines near the top mark the location of the sliding plate.

Figure 4.4 shows pictures obtained from a 35000 fps motion picture of the same experiment, performed in the 'long time' configuration. Figure 4.4a and b show the interface at t = 3.6 ms and t = 4.0 ms, and it is seen that the perturbation has grown only slightly from the beginning of the interaction (*i.e.*, figures 4.3a and b). The pair of oblique waves seen below the interface originate from cylindrical waves that were generated by the arrival of the shock at the interface and at the junction between the interface section and the test section. Although these waves are weak, they can be seen clearly because of the high index of refraction of SF_6. The shadow of the SF_6-rich boundary layer above the interface can be seen on the window as a longitudinally streaky structure, typical of turbulent boundary layers (Kline 1967). The growth rate of the perturbation is small because its initial amplitude is small and the interface is thick.

4.2.2. *Growth After Reflected Shock.* More easily measurable growth rates are observed after the interface interacts with the reverberations of the primary wave.

Figure 4.5 shows pictures, obtained from the same experimental run as in figure 4.4, of the interface after interacting with the first reflected shock. Figure 4.5a shows the interface shortly after the arrival of the reflected shock, seen above the interface. The reshock is curved upwards because the speed of sound in the SF_6-rich boundary layer above the interface is smaller than in the air in the bulk of the fluid above the interface. The interface has been compressed by the reshock and the quasi-periodic nature of the perturbation can easily be distinguished at this point. After that the interface amplitude increases steadily, as seen in the subsequent frames. In figure 4.5b, one can also notice the presence on the side walls of a bulge on the interface, called a 'loop' by Andronov *et al.* (1976). It is caused by the interaction of the reflected shock with the distorted interface within the boundary layer adjacent to the shock tube wall and is a form of shock wave-boundary layer interaction. An intensified Richtmyer-Meshkov instability inside the boundary layer leads to the formation of a two-dimensional wall vortex, clearly seen in figure 4.5d and also appearing as the lighter grey region on the window below the interface in figures 4.5b, c and d. These wall phenomena will be discussed in more detail in Chapter 6. The influence of the wall vortical structure gradually becomes important and leads to the overall deformation of the interface. At this stage the development of the perturbation on the interface is probably dominated in part by the wall vortex. A nonuniform acoustic field below the interface can also be noticed in the last three pictures. These weak waves, seen reverberating between the side walls, originate from the scattering of the incident and reflected shocks at the

distorted interface and boundary layer.

Figure 4.6 is a plot of the evolution of the amplitude of the perturbation on the interface for the same experiment. The arrival of the reshock is indicated on the plot as the vertical line labeled 1, C (for compression wave). As observed in the pictures, the growth before the reshock is very small. However, after the reshock, a phase reversal of the perturbation is detected from the pictures at around t = 4.2 ms, as indicated on the figure with the vertical arrow; the amplitude of the perturbation increases rapidly thereafter at a rate of 6.56 m/s. At about t = 5.0 ms the growth is observed to stop. This slowdown can be caused by the evolution of the perturbation into the slower nonlinear regime or by the increased influence of the wall vortices.

Table 4.2 lists the measured growth rate after the reflected shock $(d\eta/dt)_1$, as obtained from the straight-line least-squares fit of the data, for both interface combinations and various incident shock strengths in the long time configuration.

Table 4.2. Single-Scale Growth - First Reshock - Long Time Configuration

Test Gas	A_0	M_s	$\left(\frac{d\eta}{dt}\right)_1$ (m/s)	Run
R-22	0.50	1.12	5.50	1122C
		1.32	7.05	1123E
		1.48	12.50	1129B
SF_6	0.67	1.12	3.64	1123C
		1.32	6.56	1129A
		1.48	7.50	1202B

4.2.3. *Multiple Wave Reverberations.* The evolution of interface perturbations under repeated impulsive accelerations is examined with experiments in the 'close end wall' configuration.

Figure 4.7 shows pictures from the same experimental run as in figure 4.3. In figure 4.7a (t = 1.0 ms), the interface is shown right after the interaction with the first reshock (shown in figure 4.3b). The interface has been compressed by this wave, and the expansion waves reflected into SF_6 can be noticed as the dark wavy region that mimics the shape of the interface (figure 4.7 a). Subsequently the waves reverberating between the end wall and the interface die down and bring the interface to rest. The fine graining of the trapped wave pattern can be observed from figure 4.7b to figure 4.7d. The increase in amplitude of the perturbation on the interface can also be distinguished. The nonlinear development of the perturbation is observed in figure 4.7d where round spikes of SF_6 are seen penetrating into air. The wall vortical structures are also apparent in these pictures.

Figure 4.8 shows a plot of the time evolution of the measured amplitude of the perturbations for that experiment. The arrival of the each reverberation is indicated by the vertical lines, where C and E denote compression and expansion waves, respectively. The initial growth is small, and the first reshock causes a phase reversal of the perturbation at t = 0.8 ms, as indicated on the figure by the arrow. After the interaction with the expansion waves, the amplitude increases rapidly at 5.45 m/s. At around t = 1.8 ms the growth slows down, possibly because of the interaction with the second reshock (wave 3), the transition into the nonlinear regime or the influence of the wall vortices.

Table 4.3 lists the value of the growth rate after the expansion wave 2, $(d\eta/dt)_2$, as obtained from the straight-line fit of the observed data for all gas combinations and incident shock strengths in the 'close end wall' configuration.

4.3. Growth Rates -- Theory vs Experiments.

Because the initial amplitude of the single-scale perturbation produced on the continuous interfaces can not be determined accurately, the direct verification of the proposed theory (Eq. 3.18) is unfortunately not possible. However, because of the varied set of experiments performed with each gas combination, an indirect method to validate the formula is used as follows:

The initial amplitude is derived, assuming that the theory is valid, from the growth rates after the first reshock in the long time configuration, since those are measured with the best precision. The visual thicknesses before and after the arrival of the waves (verified against

Table 4.3. Single-Scale Growth - Second Reverberation - Close End Wall Configuration

Test Gas	A_0	M_s	$\left[\frac{d\eta}{dt}\right]_2$ (m/s)	Run
R-22	0.50	1.12	0.72	0318C
		1.32	2.13	0317A
		1.48	2.95	0325A
		1.66	3.35	1202D
SF_6	0.67	1.12	1.14	0316B
		1.32	5.45	0319A
		1.48	11.68	0324A
		1.66	8.87	0406A

concentration probe measurements, *cf.* Appendix C) are used to compute the growth reduction factor. Table 4.4 lists the initial amplitude obtained in that manner.

From those results, the initial amplitude of the single-scale perturbation on the air/SF_6 interface is found to be 0.052 ± 0.006 mm. For the air/R-22 interface, η_0 = 0.17 ± 0.04 mm. The relatively small scatter in the data can be considered as a first check of the formula. Also, the theory correctly predicts the time of phase reversal, which is independent of the initial amplitude of the perturbation. It is not clear why the air/R-22 interface has a larger initial perturbation than the air/SF_6 interface, since both test gases have nearly the same kinematic viscosity. In fact, when comparing the initial amplitude of the perturbation on the air/R-22 interface (shown in figure 4.9) with that on the air/SF_6 interface (figure 4.1b), it does appear that the air/R-22 interface has a larger amplitude. One should note that in this configuration the theory (Eq. 3.18) predicts growth rates about eight times slower than those calculated from the relation for the discontinuous interface.

Next, these values are compared to an average initial amplitude η_0 obtained from the growth rate results in the 'close end wall' configuration. Table 4.5 lists the initial amplitudes calculated

Table 4.4. Single-Scale Growth - Initial Amplitude - Long Time Configuration

Test Gas	A_0	M_s	$\left(\frac{d\eta}{dt}\right)_1$ (m/s)	η_0 (mm) *calculated*	Run
R-22	0.50	1.12	5.50	0.21	1122C
		1.32	7.05	0.13	1123E
		1.48	12.50	0.16	1129B
SF_6	0.67	1.12	3.64	0.057	1123C
		1.32	6.56	0.046	1129A
		1.48	7.50	0.052	1202B

from the growth rate after the second reverberation $(d\eta/dt)_2$. In this case, since the time duration of the interaction of the expansion waves with the interface is small, the impulsive formula can be used instead of integrating the constant gravity relation (Eq. 3.13) for the variable acceleration produced by the waves. For SF_6, the initial amplitude is found to be $\eta_0 = 0.076 \pm 0.016$ mm, and for R-22 $\eta_0 = 0.17 \pm 0.06$ mm. The agreement with the values obtained from the experiments in the 'long time configuration' is reasonable. The seemingly large discrepancy between the two results (as much as 46%) could be attributed to a relatively small error (as little as 11%) in the determination of the factor ψ for each wave, or to the fact that the linear theory has been used even though the amplitude of the perturbation no longer satisfies the criterion $\eta \ll 1/k$ at the later times. The magnitude of this error is not so large, considering that in this 'close end wall' configuration this method predicts growth rates about twenty times lower than the Richtmyer formula (Eq. 3.7). In addition, the discontinuous interface theory fails to predict correctly the time of observed phase reversal of the perturbation.

Another way to look at the results is to use the calculated values of initial amplitude, obtained from 'long time configuration' data, in Eq. (3.18) to calculate the evolution of the perturbation in the 'close end wall' configuration. Table 4.5 shows a comparison between the measured growth rates after the expansion wave and those obtained from the initial amplitude

Table 4.5. Single-Scale Growth - Comparison with Theory - Close End Wall Configuration

Test Gas	A_0	M_s	$\left[\frac{d\eta}{dt}\right]_2$ (m/s)		η_0 (mm)	Run
			measured	*calculated*	*calculated*	
R-22	0.50	1.12	0.72	0.48	0.26	0318C
		1.32	2.13	2.06	0.18	0317A
		1.48	2.95	3.80	0.13	0325A
		1.66	3.35	4.25	0.13	1202D
SF_6	0.67	1.12	1.14	1.10	0.054	0316B
		1.32	5.45	3.01	0.094	0319A
		1.48	11.68	7.69	0.079	0324A
		1.66	8.87	5.91	0.078	0406A

as discussed. The maximum discrepancy between the two sets of results is of the same order as in the comparison between the calculated initial amplitudes. The calculated time of phase reversal of the perturbation also agrees well with the observations in this case.

To show that the perturbation is two-dimensional, experiments have been performed with the interface section rotated 90° with respect to the test section, in which case no single-scale perturbation could be detected.

4.4. Summary.

The experiments reported in this chapter have confirmed that a significant reduction in the growth rate of single-scale perturbations can be achieved by decreasing the density gradient initially present at the interface. For the interfaces under consideration, where $\delta/\lambda \sim 0.8$, the arrival of each wave induces a perturbation growth rate about three times smaller than predicted by the linear theory for the discontinuous interface. The growth rate measurements were compared to a new model that accounts for the slower growth, and relatively good agreement has been achieved between the analytical and experimental results. The seemingly large discrepancies observed when comparing the measured and calculated data are small relative to

the large reduction in growth rates predicted by the new model. According to the new theory, the shock-excited growth of an interface after one impulsive acceleration can be reduced tenfold if the discontinuous interface is replaced by a continuous one for which $\delta/\lambda \sim 3$. In the limit $\delta/\lambda \rightarrow \infty$, the growth rate becomes independent of the wavelength of the perturbation, and the dominant length scale becomes the thickness of the interface.

Chapter 5

PLANE INTERFACES

This chapter reports the results of measurements of the 'visual thickness', obtained from flow visualization experiments by the schlieren method, of initially plane interfaces between two gases under impulsive accelerations. It is found that when such interfaces are processed by just one incident shock wave of strength of order M_s = 1.5, they grow slowly and require observation over extended times. Thus, experiments are performed with the interface initially at two different positions with respect to the flow visualization windows to examine for a long time interval the time evolution of the turbulent mixing zone (TMZ) developing between the two gases. The observed growth rate of thin interfaces formed by plastic membranes have been found to be substantially smaller than that reported by previous investigators. Also, thick, diffusively-smoothed interfaces initially grow much more slowly than the discontinuous ones do. Experiments performed with the interface repeatedly processed by reflections of the primary wave reverberating between the end wall of the shock tube and the interface have exhibited the same characteristics. In experiments investigating the interaction of shock waves with plane, smooth interfaces, where naturally-occurring growth rates are small, care must be taken to distinguish effects introduced by the experimental apparatus, including acoustic noise and shock wave-boundary layer interaction, from those of the primary mechanisms under study. In these experiments, it is found that vortical wall jets formed by shock wave-boundary layer interaction at the interface grow much more rapidly than the shock-processed interfaces in the bulk of the fluid. These wall structures can reduce the apparent growth of interfaces by vorticity-induced strain.

5.1. Experimental Setup.

In the experiments reported in this chapter a nominally flat interface is initially located near the end wall of the tube and the tube is set precisely vertical. Thus, the development of mixing of two gases induced by an incident shock parallel to the interface, and its reverberations, is studied. Both initially continuous and discontinuous interfaces are investigated. The time period between the reverberations can be modified by changing the initial location of the interface with respect to the end wall of the shock tube.

To investigate the problem of the evolution of the interface after the interaction with the incident shock, the experiments are performed with the 'long time' and 'close end wall' configurations (*cf.* figure 2.8 and Table 4.1 for the relevant shock tube dimensions).

The 'long time' configuration allows an accurate determination of the average growth rate of the TMZ from the start of the interaction since its thickness is fairly large and easily measurable while it is in the field of view of the windows. Experiments in the 'close end wall' configuration are performed to obtain data on the initial growth of the interface just after the interaction with the incident shock. In addition, these experiments are used to investigate the response of the interface after multiple impulsive accelerations.

With the incident shock growth rates measured in both 'close end wall' and 'long time' configurations, the growth profile of the TMZ can be obtained. The effect on the reshock growth of the time delay before the first reshock of the interface is also studied. Finally, as the interface is slowed to a stop, the 'close end wall' experiments allow the measurement of growth rates at late times.

For experiments with a discontinuous interface, a membrane is used to form the interface and for experiments with a continuous interface the sliding plate initially separates the gases. By increasing the delay between plate retraction and firing of the shock tube, the gases are allowed to diffuse into each other, leading to a thicker continuous interface. Thus by adjusting this time delay (usually between 0 and 6 seconds) the initial conditions at the interface when it is accelerated by the shock can be controlled. Typically, the initial thickness of the continuous interfaces varies from 15 to 60 mm. To ensure that the visual thickness measurements from the schlieren photographic records are representative of the actual thickness of the interface, these were compared to concentration probe measurements (*cf.* Appendix C).

5.2. Wave Diagrams.

Selected experimental wave diagrams for the interaction of a shock wave with air-air, light-heavy and heavy-light interfaces, initially located near the end wall of the shock tube, are presented in this section. They are compared to the simple gasdynamics theory (*cf.* Section 6.3.1).

5.2.1. *Long Time Configuration.*

5.2.1.1 Air-Air Discontinuous Interface. Figure 5.1 shows the wave diagram for an air/air interface accelerated by a M_s = 1.32 shock wave. The end wall is located 70 cm downstream of the initial position of the interface. The data for this and subsequent $x-t$ diagrams were obtained from high-speed motion picture and pressure transducer records. To obtain the origin of this and other 'long time' wave diagrams, the observed time of arrival of the reflected shock at the interface is matched with the calculated value. A weak wave which might have been reflected from the membrane was not detected. At t = 1.53 ms, the wave transmitted through the interface reflects from the end wall as a M = 1.29 shock. At t = 2.47 ms, this reflected shock interacts with the membrane, causing it to slow down almost to a stop. The reflected shock traverses the membrane and another weak wave is reflected back towards the end wall. By this point 1-D gasdynamics theory would predict that the reflected wave would bring the gases to rest. However, because the reflected shock accelerates the slowly moving gas in the boundary layer upwards, and, since on average the flow must be at rest, the air in the middle of the test section has to move downwards. Indeed the membrane is observed to proceed slowly down the tube, at a speed of 0.7 m/s.

5.2.1.2 Light-Heavy Discontinuous Interface. Figure 5.2 shows the wave diagram for an air/SF_6 interface accelerated by a M_s = 1.32 shock wave. At t = 0, the shock is incident at the interface, transmitting a M = 1.48 shock into SF_6 and reflecting a M = 1.09 shock in air. The transmitted shock reflects from the end wall at t = 2.79 ms as a M = 1.46 shock and interacts with the interface at t = 4.12 ms. The interface then reverses its motion and expansion waves are reflected into SF_6. The agreement between the observed trajectories of the waves and the interface with familiar results from 1-D gasdynamics theory is good. This suggests that the energy lost to the rupture of the membrane is negligible compared to that put in the motion of the gas. It would also seem to suggest that the presence of a density gradient at the interface reduces the adverse effects of the membrane on wave refraction, since better agreement is achieved between observed and calculated trajectories for the $x-t$ diagram of air/SF_6 than for the air/air case.

5.2.1.3 Light-Heavy Continuous Interface. Wave diagrams of experiments investigating the growth of a smooth transition between two gases are essentially the same as the one shown in figure 5.2. There is also good agreement with the 1-D gasdynamics theory for the trajectory of the interface and waves.

5.2.1.4 Heavy-Light Discontinuous Interface. Figure 5.3 shows the wave diagram for an air/He interface, accelerated by a M_s = 1.32 shock wave. The main difference between this $x-t$ diagram and that of figure 5.2 is that all reverberations are shocks, so the interface never reverses its motion but is gradually slowed down by the reshocks. There is good agreement between the observed shock and interface trajectories and those calculated from 1-D gasdynamics, indicating that there was no leakage through the membrane before this run.

5.2.2. *Close End Wall Configuration.*

5.2.2.1 Light-Heavy Discontinuous Interface. Figure 5.4 shows the wave diagram for an air/SF_6 interface accelerated by a M_s = 1.32 shock wave. It can be seen from the diagram that at t = 0 the interface is impulsively accelerated toward the end wall. At t = 0.5 ms, the wave transmitted into SF_6 reflects from the end wall as a M = 1.46 shock. At t = 0.8 ms, this reflected shock interacts with the interface, causing it to reverse its motion. At the same time, an expansion wave is reflected into the SF_6. The effect of this and subsequent waves reverberating between the interface and the end wall is to bring the interface to rest. After about 1.7 ms the interface is stationary, and the effect of the remaining waves is negligible. The observed trajectories of the waves and of the interface agree with results from 1-D gasdynamics theory.

5.2.2.2 Light-Heavy Continuous Interface. The $x-t$ diagram for these experiments is essentially the same as the one shown in figure 5.4., and there is also good agreement with the 1-D gasdynamics theory for the trajectory of the interface and the waves.

5.2.2.3 Heavy-Light Discontinuous Interface. Figure 5.5 shows the wave diagram for an air/He interface, accelerated by a M_s = 1.30 shock wave. The main difference between this $x-t$ diagram and that of figure 5.3 is that the period between reverberations is shorter. For most of the run there is good agreement between theory and observations. However, at late times,

where wall effects distort the interface and the configuration becomes two-dimensional, the agreement is not as satisfactory.

5.3. Air-Air Interfaces.

A first step into the investigation of the development of discontinuous interfaces between gases of different densities is to perform experiments to study the time evolution of a nitrocellulose membrane after its impulsive acceleration by the incident shock and its first reverberation. These are presented in this section.

Figure 5.6 shows pictures obtained from a 35000 fps motion picture of the interaction of an air/air interface with a M_s = 1.32 shock wave, whose wave diagram has been shown in figure 5.1. In figure 5.6a (t = 2.31 ms), the membrane is seen as it traveled to the middle of the window. The membrane is still quite flat with small nonuniformities developing on its surface. The edges of the membrane are curved upwards and do not extend to the side walls due to the presence of the boundary layer, visible in the picture. It is believed that at this time the membrane is still intact in a single piece. The reflected shock can be seen at the bottom of the window. In figure 5.6b (t = 2.56 ms), the reflected shock has just traversed the membrane and is traveling upward. The membrane has been slowed almost to a stop. The bifurcation of the reflected shock at the side walls can clearly be seen and is reminiscent of observations by Mark (1957). These wall effects will be discussed in more detail in Chapter 6. After the reshock, the membrane stays relatively flat and the gap at the side walls increases in size, perhaps due to erosion by the thickening boundary layer. In figure 5.6c (t = 4.73 ms), the membrane has moved slightly toward the end of the tube, and some thickening of the interface region is observed probably due to the development of three dimensional features. The membrane is still curved upwards and nonuniformities are more apparent.

Figure 5.7 shows a plot of the evolution of the thickness of the interface region formed by the distorted membrane in this experiment. The step-like nature of the data is due to the limited resolution of the measurements at these small thicknesses. The growth rate observed after the incident shock is negligible for the time interval the interface is within the observation window. Assuming that the initial thickness is zero, the average growth rate from t = 0 is calculated to be 0.9 ± 0.1 m/s. After the reshock the apparent thickness increases at a rate of 0.5 ± 0.1 m/s.

Note that throughout, the rms deviation of straight-line least-squares fit of the data, indicated by straight solid lines in figs. 5.7, 5.10 and subsequent plots for the time evolution of the thickness of the TMZ, is used to designate the bounds of the growth rate results. In these and subsequent plots, no attempt is made to distinguish departure from linear growth. Thus it can be seen that membrane perturbations still evolve after rupture, presumably due to a Richtmyer-Meshkov instability of the membrane material.

Figures 5.8a and b show pictures of the air/air interface for incident shock Mach numbers 1.48 and 1.66, respectively (*cf.* Table 4.1 for the position of the end wall). By comparing figures 5.6 and 5.8, it can be seen that, as the Mach number is increased, the interaction with the incident wave causes more membrane deterioration. The wrinkled shape of the membrane after rupture is demonstrated by the three-dimensional structure of the acoustic waves reflected by the membrane after the arrival of the reshock, as seen in figure 5.8b at t = 1.28 ms. After corresponding late times, the membrane is also more deformed for strong incident waves.

It has been seen that a nitrocellulose membrane does not shatter in pieces after interaction with the incident shock wave, but translate down the shock tube at a velocity close to that predicted if the membrane were absent. This is because the membrane is initially very flat, so that there are few perturbations on the interface, and there is no density gradient across the interface, so that the Richtmyer-Meshkov instability is suppressed. However, because of the obstruction they create in the flow, there is a departure to the behavior predicted by the simple gasdynamics theory after interaction with the first reshock.

5.4. TMZ Growth Measurements -- Discontinuous Interfaces.

The time evolution of initially plane interfaces between gases of different densities under impulsive acceleration is presented in this section. The perturbations on the discontinuous interface are introduced by the rupture of the supporting nitrocellulose membrane. It is found that, in this case, because of the large density gradient present at the interface, the membrane shatters in pieces that are subsequently entrained in the flow, as opposed to the air-air interfaces where the membrane stays in one piece.

5.4.1. *Growth After Incident Shock.* To examine the time evolution of the TMZ at discontinuous interfaces after their interaction with the first incident shock, experiments were performed in both the 'long time' and 'close end wall' configurations. Experiments in the 'close end wall' configuration, where the interface is initially just above the field of view of the flow visualization windows, allow the observation of the interface a short time after interaction with the incident shock. With the interface initially 32 cm (or 65 cm where noted) upstream of the windows, the experiments in the 'long time' configuration allow the observation of the interface a long time after the arrival of the incident shock; an accurate determination of the average growth rate from $t = 0$ is thus possible.

5.4.1.1 Light-Heavy Interface. Figure 5.9 shows frames taken from 35000 fps motion pictures of the interaction of an air/SF_6 interface with a $M_s = 1.32$ shock wave for both 'long time' and 'close end wall' experiments. The wave diagrams for those two runs were presented in figures 5.2 and 5.4. In figure 5.9a, at $t = 0.34$ ms, the interface is seen shortly after interaction with the incident shock. The interface appears flat, suggesting that any perturbations caused by the breaking of the membrane are small. The shock transmitted into SF_6 can be seen as it propagates toward the end wall at the bottom of the picture. The second picture, taken $t =$ 3.59 ms after the arrival of the incident shock at the interface, shows the latter about halfway in the window. Turbulence is developing at the interface and is more apparent when compared with figure 5.9a. The thick SF_6-rich boundary layer can be seen on the side walls above the interface.

Figure 5.10 is a plot of the evolution of the TMZ δ for both 'close end wall' and 'long time' experiments. The thickness of the interface a short time after the interaction with the incident shock (obtained from the 'close end wall' results) is so small that a fit to the data is not reliable enough to quote the incident shock growth rate for this time interval. However, an upper bound can be established at 3.8 m/s, as shown in the figure. The growth rate measured while the interface is in the field of view of the windows for the 'long time' experiment, *i.e.*, the so-called local growth rate, is only 1.0 ± 0.3 m/s. Finally, the average growth rate from $t = 0$ to the time of reshock is 2.3 ± 0.1 m/s. It should be noted that the thickness of the simple laminar molecular diffusion layer between air and SF_6 would be less than 1 mm at the time of the

reshock, as opposed to an observed TMZ thickness of 9 mm.

5.4.1.2 Heavy-Light Interface. Figure 5.11 shows frames obtained from 60000 fps high-speed schlieren motion pictures of the interaction of an air/helium interface with a M_s = 1.30 shock wave in the 'close end wall' configuration, and with a M_s = 1.32 shock in the 'long time' configuration. The wave diagrams of those two experiments were presented in figures 5.3 and 5.5. In figure 5.11a, taken 0.10 ms after the arrival of the incident shock, not much growth is observed since the beginning of the interaction. The second one, taken 1.49 ms after the arrival of the incident shock, shows the interface still traveling downwards. The fine scale structure in the interface region suggests that turbulence is present. The thick helium-rich boundary layer is clearly seen on the side walls and on the window above the interface. A 'toe' of helium under the air boundary layer is also visible, especially on the left side wall. As is often observed for the air/helium interfaces, fragments of nitrocellulose, probably ejected during rupture of the membrane, are convected ahead of the interface and are more visible in this case near the right wall.

Figure 5.12 is a combined plot of the evolution of the TMZ after the interaction with the incident shock for these experiments. The upper bound to the growth measured in the 'close end wall' configuration is 12.6 m/s and the growth rate measured while the interface is in the field of view of the windows in the 'long time' configuration is 0.4 ± 0.1 m/s. The average growth from t = 0 to the time of first reshock is 3.3 ± 0.2 m/s. Note that a laminar diffusion layer between the two gases would only be about 1 mm thick at the time of the reshock, as opposed to an observed TMZ thickness of 5.5 mm.

5.4.2. *Growth After First Reshock.* The development of the TMZ after the arrival of the first reflection of the primary wave is examined in details with experiments in the 'long time' configuration.

5.4.2.1 Light-Heavy Interface. Figure 5.13 shows frames taken from a 35000 fps motion picture of the same experimental run described in the wave diagram of figure 5.2. (The interface is shown just before the reshock in figure 5.9b). The first picture, at t = 4.39 ms, shows the interface after the passage of the reflected shock. The 'loop' or wall vortex can also

be distinguished on the side walls. A nonuniform acoustic field below the interface can also be noticed. These weak waves, seen reverberating between the side walls, originate from the scattering of the incident and reflected shocks at the distorted interface and boundary layer. This region appears very disturbed only because the high index of refraction of SF_6 makes the waves more visible to the schlieren system. The second picture, at t = 5.19 ms, shows the interface still moving upward after the first reshock. Turbulence, generated and intensified by the interaction of the reflected wave with the already turbulent interface, has caused the thickness of the TMZ to increase. The wall vortex structure is even more visible at the side walls and also appears on the window as the grey region above the image of the interface. It is important to distinguish between the TMZ and the wall vortex when measuring the growth at the interface, as indicated in figures 5.13a and b.

The time evolution of the thickness of the TMZ after the reshock for this experiment is shown in figure 5.10. It is seen that the interface is compressed noticeably by the reshock, and that thereafter the growth rate is 5.6 ± 0.6 m/s.

5.4.2.2 Heavy-Light Interface. Figure 5.14 shows pictures obtained from a 60000 fps high speed schlieren motion picture of the interaction of a M_s = 1.32 shock wave with an air/helium interface. The wave diagram of this run is shown in figure 5.3 and the interface before the reshock is shown in figure 5.11 b. At t = 1.71 ms (figure 5.14a), the interface is shown instants after the interaction with the reflected shock, which is now seen just above the interface. Since the speed of sound in the helium-air boundary layer is much larger than in the air in the bulk of the fluid above the interface, precursor waves form on the side walls as the reshock crosses the interface. The turbulence intensity at the interface seems to have increased and the thickening of the TMZ can be noticed. Some 0.18 ms later (figure 5.14b), the interface still propagates toward the end of the tube. Its thickness has increased and larger scales have appeared on the interface. The extent of the boundary layer region at the interface has also increased and could be affecting the development of the TMZ at this stage.

The time evolution of the TMZ after the reshock for this experiment is shown in figure 5.12. As opposed to the light-heavy interface, no interface compression is caused by the reshock and that the latter induces a growth rate of 9.2 ± 1.4 m/s at the TMZ (in this case not

all data points were used to fit the data).

Figures 5.15a and b compare the evolution of the air/He interface at two higher incident shock strengths. The qualitative features of the TMZ as well as the precursor waves are similar. In figure 5.15a, for air/He M_s = 1.48, the presence of large scale structures in the TMZ is more apparent. This could validate the hypothesis that the entrainment mechanism at the interface involves the merging of small scales into larger ones. Two oblique waves can also be seen in figure 5.15b above the interface. These are Mach waves originating from small disturbances on the side walls of the test section upstream of the windows, because the flow velocity induced in air by the refraction of the incident shock at the interface is supersonic (M = 1.13).

5.4.3. *Growth After Multiple Wave Reverberations.* Experiments to study the entrainment resulting from the multiple impulsive acceleration of a flat discontinuous interface initially separating two gases were performed. The nitrocellulose membrane separating the two gases at the start of the experiment is located 10.5 cm from the end wall of the tube.

5.4.3.1 Light-Heavy Interface. Figure 5.16 shows pictures obtained from a motion picture taken at 35000 fps of the same experiment as described in the wave diagram of figure 5.4. (In figure 5.9a, at t = 0.34 ms, the interface is seen just after interaction with the incident shock). Figure 5.16a is taken at t = 1.03 ms, after the first reshock but before the second reflection, a rarefaction (seen in the picture as the dark band below the interface), interacts with the interface. Clearly, the thickness of the interface has increased. Figure 5.16b shows the interface at t = 2.06 ms. The interface is now stationary. Turbulence, apparent in the picture, has caused a thickening of the TMZ. The wall vortex is even more apparent at the side walls and also appears on the viewing window below the image of the interface.

Figure 5.17 is a plot of the evolution of the thickness δ of the TMZ for this experiment. As has been seen in figure 5.12, an upper bound to the growth induced by the incident shock can be established at 3.8 m/s. After the first reshock the thickness is measured to increase at a rate of 10.2 $\pm$ 1.5 m/s. The second reverberation, an expansion, does not slow the growth. Shortly afterwards the growth seems to be reduced noticeably, possibly because of the interaction with the third reverberation, a shock, or the influence of the wall vortices. The interface thickness

then increases approximately linearly in time at a rate of 2.9 ± 0.2 m/s. After 5 ms the thickness is about 20 mm. It should be noted that the simple laminar diffusion layer between air and SF_6 would be less than 1 mm after the same time interval.

5.4.3.2 Heavy-Light Interface. Figure 5.18 shows photographs obtained from a 60000 fps high-speed schlieren motion picture of the same run as in figure 5.5. The interface is shown just after the arrival of the incident shock in figure 5.11a. After the first reshock, as seen in the first picture at t = 0.23 ms, the interface thickness increases. A so-called reverse wall vortex (*cf.* Section 6.1.2.2) at the side wall and its image on the windows can also be seen. Figure 5.18b, at t = 0.63 ms, shows turbulence developing at the interface, now stationary. However, penetration of the vortical wall jet 25 mm into the helium has caused the deformation of the interface. What appears to be fairly large scale structures of wavelength 10-25 mm can be seen on the interface in figure 5.18b. Figure 5.19 shows the time evolution of the thickness of the TMZ at the interface. The upper bound to the incident shock growth rate is 12.6 m/s and after the first reshock the growth rate is 9.9 ± 2.1 m/s. The late-time growth rate is measured to be 10.7 ± 0.5 m/s. In this case, as opposed to results from the light-heavy experiments, the thickening of the interface does not slow down at late times. At t = 1.5 ms, the thickness of the interface is about 15 mm as compared with δ_{diff} ~ 1 mm for a laminar diffusion layer between the same two gases.

5.4.4. *Summary of Results.* The parameters and measured growth rates for the discontinuous interfaces for both 'long time' and 'close end wall' experiments are given in Tables 5.1 and 5.2.

It should be noted that for some of the 'long time' experiments, the interaction of the reshock with the boundary layer at the interface is so violent that the interface can not be distinguished from the wall vortex, making the measurement of the TMZ growth impossible. That is why some of the entries in Table 5.1 are missing.

5.5. TMZ Growth Measurements -- Continuous Interface.

Since the sliding plate is used to separate the gases at the start of these experiments, only the light-heavy continuous interfaces are investigated. The perturbations on a continuous

Table 5.1. Experimental Parameters - Discontinuous Interface - Long Time

Test Gas	A_0	M_s	$\frac{d\delta}{dt}$ (m/s)			Run
			Wave 0		*Wave 1*	
			avg	local		
He	-0.76	1.32	3.3	0.4	9.2	1213C
		1.48	5.1	0	30.4	1109A
		1.66	11.5	10.3	30.9	1214B
		1.66[1]	5.5	5.2		1208B
Air	0	1.32	0.9	0	0.5	1022C
		1.48	2.4	2.6	1.0	1024C
		1.66	3.6	5.3	4.1	1101B
R-22	0.50	1.12	1.8	0.3	4.5	1210A
		1.32	3.4	0		1214C
		1.48	3.3	3.9		1213D
		1.66	3.2	0		1214A
SF_6	0.67	1.12	2.3	0	4.2	1018A
		1.32	2.3	1.0	5.6	1108C
		1.48	3.4	2.9		1104C
		1.66[1]	2.5	0		1111A

1. Interface-Window Distance = 65 cm.

interface are introduced by the pumping action of the retracting plate. However, since in most cases the large scale perturbations are allowed to be damped out by letting the gases diffuse into each other for up to 6 seconds, the random small-scale perturbations possibly present on the interface are in the form of velocity and density fluctuations.

Because the initial perturbations on the continuous interfaces are small and their thickness is large, their growth rate is expected to be very small, as has been discussed in Chapter 4. It is

Table 5.2. Experimental Parameters - Discontinuous Interface - Close End Wall

Test Gas	A_0	M_s	$\frac{d\delta}{dt}$ (m/s)			Run
			Wave 0[1]	*Wave 1*	*Late time*	
He	-0.61	1.12	18.3	11.7	2.20	0430B
	-0.76	1.30	12.6	9.9	10.7	0521B
	-0.76	1.50	14.1	22.2		0525A
	-0.57	1.68	11.4	19.2	6.8	0608A
Air	0	1.12	3.6	0.5	0.5	0428A
		1.32	5.1	1.8	0.2	0521C
		1.48	5.3	0.8	0	0604A
		1.66	7.1		0.2	0604B
CO_2	0.20	1.12	4.8	2.6	1.5	0429C
		1.32	6.5	0.9	0.8	0521A
		1.48	5.0	2.5	0.5	0525C
		1.66	9.5	6.6	1.8	0607B
R-22	0.50	1.12	5.5	4.7	2.6	0429B
		1.32	4.4	2.9	1.7	0518B
		1.48	7.0	4.9	2.5	0525B
		1.66	6.3		6.5	0607A
SF_6	0.67	1.12	4.5	6.6	3.1	0429A
		1.32	3.8	10.2	2.9	0501A
		1.48	3.3	9.4	3.7	0523B

1. Upper Bound

observed experimentally that the growth induced by the arrival of the incident shock at the interface is negligible and that noticeable growth is measured only a long time after the arrival of the reverberations at the interface.

5.5.1. *Growth After First Reshock.* The response of a continuous interface to the incident and first reflected wave is examined with experiments in the 'long time' configuration. The $x-t$ diagrams for these runs are similar to those obtained with the discontinuous interfaces (*e.g.*, figure 5.2).

Figure 5.20 shows schlieren photographs obtained from a 35000 fps motion picture of an air/SF_6 interface initially accelerated by a M_s = 1.32 shock. Since the initial thickness of the interface can not be monitored before a run in the 'long time' configuration, it is inferred from observations in the 'close end wall' configuration (*cf.* Section 5.5.2) and from concentration probe measurements (*cf.* Appendix C). For this case the initial thickness δ_0 is assumed to be 30 mm. Figure 5.20a shows the interface 3.59 ms after the start of the interaction. Its measured thickness is δ = 20 mm, less than the initial value because of compression by the incident shock and slow growth. The edges of the interface are curved upwards as a result of the influence of the developing boundary layer on the side walls. At t = 4.39 ms (figure 5.20b), the interface is seen shortly after the reshock. Its thickness has been compressed again by the wave, but no turbulent growth is observed. The start of roll-up of a two dimensional vortex structure can be noticed on the side walls, a manifestation of the shock-boundary layer interaction at the interface. Figure 5.20c (t = 5.19 ms) shows the wall vortex now fully developed, and its image on the observing window can clearly be seen below the interface. By this time, the vortices dominate the development of the interface. Stretching of the interface caused by the vortices could inhibit the turbulent spreading of the TMZ.

Figure 5.21 shows a plot of the evolution of the thickness of the interface. Before the first reflection, a local growth rate of 0.2 $\pm$ 0.1 m/s is measured. The average growth rate from t =0 can not be measured accurately, but an upper bound of 0.2 m/s can be established. After the compression caused by the reshock, modest growth of 1.1 $\pm$ 0.3 m/s is observed.

Table 5.3 lists the local incident shock and reshock growth rates for the 'long time' continuous interface experiments. In addition, an upper bound to the average incident shock growth is presented. However, in most cases, the reshock growth rates can not be obtained due to the violence of the shock wave-boundary layer interaction at the interface.

Table 5.3. Experimental Parameters - Continuous Interface - Long Time

Test Gas	A_0	M_s	δ'_0 (mm)	$\frac{d\delta}{dt}$ (m/s)			Run
				Wave 0		*Wave 1*	
				avg[1]	local		
R-22	0.50	1.12	13	0.2	1.1		1122B
			29	0	0	0.2	1122A
		1.32	12	0.3	3.0		1123D
			26	0	1.0		1128A
		1.48	9	0.8	0.4		1129C
			9	1.2	0.2		1205A
			21	0	0.6		1202A
		1.66	10	0.8	4.2		1202C
			15	1.0	3.5		1202B
SF_6	0.67	1.12	15	0.2	0.1	4.8	1123A
			29	0	0		1123B
		1.32	11	0.2	0.5		1128B
			20	0.2	0.2	1.1	1128C
		1.48	9	1.8	2.3		1203A
			19	1.4	0		1203B
		1.66[2]	10	0.9	2.2		1206A
			17	0	7.2		1205B

1. Upper Bound
2. Interface-Window Distance = 65 cm.

5.5.2. *Growth After Multiple Wave Reverberations.* Experiments to study the growth of a smooth transition between two gases under multiple wave accelerations were performed. At the start of the experiment, the interface is in the field of view of the flow visualization windows, 10.0 cm from the end of the tube. The $x-t$ diagrams for these experiments are similar to those for the discontinuous interfaces (*e.g.*, figure 5.4).

Figure 5.22 shows a spark schlieren photograph of an interface between air and SF_6 1.91 ms after the arrival of a M_s = 1.32 shock wave and interaction with several reverberations. The interface is compressed to a thickness of 13 mm by the incident shock and has not increased in thickness since the refraction of the incident shock at the interface. In fact, the interface does not look turbulent at all. However, the effect of the shock-boundary layer interaction can clearly be seen on the side walls of the test section and also on the window as the light grey region below the interface.

Figure 5.23 shows the evolution of the thickness of the interface under multiple impulsive accelerations, measured from a high-speed motion picture of the same experiment. At relatively early times, the interface is successively compressed and expanded by the reverberating waves. At later times the interface is at rest and its thickness increases approximately linearly with time at a rate of 2.4 ± 0.1 m/s. From t = 2 ms to t = 8 ms, the interface thickness has increased by about 15 mm. Under the sole action of laminar diffusion, the thick air/SF_6 interface would have grown by less than 0.05 mm during the same time interval. In all of the experiments with continuous interfaces, growth only becomes apparent after the interface has been decelerated to zero velocity by interaction with several re-reflected waves. It is speculated that the interface is initially so smooth that growth does not occur until small-scale random perturbations are deposited on it by the random acoustic field visible in figure 5.22 below the interface. This acoustic field is presumably generated by the experimental arrangement, for example, by the scattering of the primary shock waves from the distortions on the interface near the walls, induced by the shock wave-boundary layer interaction.

The parameters and late time growth rates for all experiments with continuous interfaces are given in Table 5.4. Only the late time growth rates are presented since the growth rates after the incident and reflected shocks are measured to be negligible, and the uncertainty involved in the determination of any upper bound is very large.

A comparison between continuous and discontinuous interfaces in the 'close end wall' configuration shows that, although the initial growth of the thin interfaces is much more rapid, their late-time growth after many reverberations is comparable, perhaps fortuitously, to that of the thicker interfaces.

Table 5.4. Experimental Parameters - Continuous Interface - Close End Wall

Test Gas	A_0	M_s	δ'_0 (mm)	$\frac{d\delta}{dt}$ (m/s) *Late time*	Run
CO_2	0.20	1.15	13	0.2	1013C
			22	0.2	1013D
		1.32	13	0.7	1006B
			16	0.6	0319B
			19	0.5	1010A
			21	0.3	1007A
		1.48	10	0.5	0326C
R-22	0.50	1.12	13	1.0	0318A
			29	0.1	0318B
		1.32	11	2.8	0317B
			27	1.1	0317C
		1.48	9	3.1	0325B
			21	1.0	0326A
		1.66	10	3.3	0407B
			21	1.6	0407C
SF_6	0.67	1.13	14	1.6	1013B
			29	1.5	1013A
			34	0.4	1010C
		1.32	11	2.4	1002A
			16	2.1	0919A
			31	1.3	1006A
			31	1.0	0927A
		1.48	9	4.4	0324B
			20	1.2	0324C
		1.66	17	3.4	0406C

Note that at late times, as in figs. 5.13b, 5.20c and 5.22, the vortical structures at the walls are sufficiently large that the strain they induce on the interface near the center of the shock tube can make the interface thinner than it would otherwise be. This effect is discussed in more

detail in Section 6.2.

5.6. Discussion.

5.6.1. *Profile for Incident TMZ Growth.* In the 'long time' experiments with the discontinuous interface it has been noticed that the growth rate measured while the TMZ is in the field of view of the observing window is almost always smaller than the average growth from $t = 0$. Moreover, the upper bound to the incident shock growth in the 'close end wall' configuration is usually larger than the average growth in the 'long time' configuration. These observations indicate that the thickening of the interface slows down as time increases. This can be expected since, as discussed in Chapter 3, the nonlinear growth of a perturbation is always slower than its linear phase of development; furthermore, as turbulent mixing develops, the turbulence intensity decreases in time due to both the thickening of the interface, which spreads the energy over a larger volume, and viscous dissipation. In fact, using simple dimensional arguments, it has been found (*cf.* Section 3.3) that the thickening of the interface follows a power law, *i.e.*, $\delta \propto t^{\alpha}$, where $\alpha \leq 2/3$.

Thus, with the experimental results in both 'long time' and 'close end wall' configurations, it would seem to be possible to infer the power law governing the time evolution of the TMZ after intercation with the incident shock. Figures 5.24a and b show various power law fits to the incident shock data from the TMZ plots of figures 5.10 and 5.12 for the discontinuous interfaces between air and SF_6 and air and helium respectively, with $M_s = 1.32$. It is seen that it is difficult to determine the exponent α with any accuracy because of the uncertainty in the data and the relative proximity of the various curves. The exponent can also be obtained by straight-line least square fit of the incident shock data from both 'long time' and 'close end wall' experiments, plotted on log-log scale. In this case, the rms error of the fit is compounded by the large relative error on the data points at the early times, and it is found that the exponent can achieve pretty much any value between 0 and 1, although the arguments of Section 3.3 require that $\alpha \leq 2/3$.

5.6.2. *Correlation of Growth Rate Results.* The results for the average growth rate after the incident shock in the 'long time' configuration can be correlated by plotting the growth rate $(d\delta/dt)_{0\,avg}$ normalized by the velocity jump caused by the wave, $[u]_0$, as a function of Atwood ratio A'_0. The results are presented in figure 5.25 for four incident shock Mach numbers and

four gas combinations. The empirical correlation for similar experiments obtained by Zaitsev *et al.* (1985) is also included in the plot along with the Mikaelian-Read formula (Eq. 3.23). The results of the present study clearly show smaller growth rates than those reported by Zaitsev *et al.*, although, with the longer interface-end wall distance used in those experiments, their local growth rates should have been lower than those reported here. One can also see that the direct application of constant gravity Rayleigh-Taylor mixing results to the impulsive case is not adequate at all.

The results for the growth rate after the first reshock in the 'close end wall' configuration can be correlated by plotting the reshock growth rate $(d\delta/dt)_1$ normalized by the velocity jump caused by the wave, $[u]_1$, as a function of reshocked Atwood ratio A'_1. These results are presented in figure 5.26 for four incident shock Mach numbers and five gas combinations. The empirical correlation for a similar experiment obtained by Zaitsev *et al.* (1985) is also included in the plot. In addition, the Mikaelian-Read formula (Eq. 3.23) is shown in the figure, with the added assumption that the incident shock does not induce any growth but only produces perturbations on the interface that are subsequently amplified by the first reshock. The present study again clearly shows smaller growth rates than those reported by Zaitsev *et al.* (1985).

Possibilities for the disagreement between the present results and those of Zaitsev *et al.* (figures 5.25 and 5.26) include differences between the schlieren systems used in the two experiments, possible differences of the membrane thickness and composition, or some other, unknown, features of the experimental setup.

The results for the discontinuous interface shown in figure 5.26 for the reshock growth, and less markedly in figure 5.25 for the growth of the TMZ after the incident shock, exhibit a dependence on the strength of the shock not accounted for by the normalization: Relatively faster growth is observed for the weaker waves. This could be due to the higher compression produced by the stronger waves, which could have an inhibiting effect on the generation of turbulent energy at the interface. Moreover, since the initial perturbations at the interface are produced by the breaking of the membrane by the incident shock, the difference in strength of the waves could produce different perturbations. From Eq. (3.9), it can be seen that the total kinetic energy E_k of the fluctuating motions caused by the baroclinic instability at the interface is strongly dependent on the properties of the initial perturbations. In fact,

$$E_k \propto <\eta^2> \bar{k} \quad , \tag{5.1}$$

where $<\eta^2>$ is the spatial variance of the amplitude of the initial perturbation and $\bar{k}$ its average wavenumber. The variation in initial conditions could then be responsible for the decrease in growth rates. Because the energy available for the fluid motions is deposited at the interface only at the time of impulsive acceleration, the role played by the initial conditions on the subsequent entrainment between the two gases could be more important for the shocked case than for the constant-gravity case, where energy is continuously supplied to the flow. It is thus doubtful that the instability induced by the shocks at the plane interface achieves a regime of self-similar mixing that is independent of initial conditions.

One can also note that the growth rate after incident shock is higher for $A'_0 > 0$, *i.e.*, for the light-heavy configuration, than for $A'_0 < 0$. For the incident shock, $A'_0 > 0$ is the 'unstable' case, and the perturbations immediately begin to increase amplitude upon acceleration, while for $A'_0 < 0$ the perturbations on the interface must first reverse phase before they grow. The opposite phenomenon is observed for the growth after the first reflected shock; it is noted that the reshock growth rate is higher for $A'_1 < 0$, than for $A'_1 > 0$. For the reflected shock, $A'_1 < 0$ is now the 'unstable' case and the perturbations immediately begin to increase amplitude upon reshock, while for $A'_1 > 0$ the perturbations on the interface must first reverse phase before they grow. This is further evidenced by the fact that, for the 'light-heavy' configuration, the TMZ seems compressed noticeably by the reshock (*cf.* figure 5.10), while for the 'heavy-light' configuration very little compression is observed, as seen in figure 5.12. In addition, the fact that the incident shock accelerates interfaces with negative Atwood ratio to higher velocities than those with positive Atwood ratio might cause a more energetic pre-reshock state. If one or more of these effects are the cause of the above observations, it would again indicate that the reshock growth rate is sensitive to the initial pre-growth state of the interface.

On the other hand, a comparison of reshock growth rates for the discontinuous interface in both the 'long time' and 'close end wall' configuration does not uncover any particular trend. For the light-heavy interfaces, the reshock growth rates are larger for the 'close end wall' experiments. The opposite is observed for the air/He interfaces, where faster growth is measured for the 'long time' experiments. The interaction of the reshock with the interface increases the turbulent energy by two main mechanisms: One mechanism is the production of

turbulent energy by baroclinic vorticity generation, as the shock interacts with the local density gradients present within the interface. If the turbulence at the interface is allowed to develop for a long time before the arrival of the reshock, then one would expect the density gradients to be reduced. Thus more turbulent energy would be created if the interface interacts with the reshock just as it is enters the nonlinear growth regime, when the amplitude of the perturbation is large and mixing has not started yet. The other mechanism involves the intensification of pre-existing turbulence at the interface by shock induced rapid distortion. In this case, it is generally agreed that the ratio of turbulent kinetic energy after the passage of the wave to that before is a function of shock compression. Since the turbulence intensity decreases as the TMZ thickness increases, more intensification would be achieved with a thin, thus more energetic, interface. These arguments seem to point out that reshock growth rates would be larger if the time delay before the reshock is smaller, as it has been observed with for the light-heavy interfaces. It is not known why the opposite is observed for the air/He interfaces.

Figures 5.27 and 5.28 are attempts to correlate the growth rates of discontinuous interfaces in view of the above discussion. The growth rates after the incident shock are now normalized by the compression η'_0/η_0 (calculated from the 1-D gasdynamics theory), as well as the velocity jump $[u]_0$ caused by the incident shock at the interface. The reshock growth rates are normalized by the sum of the absolute values of the velocity jumps induced by the incident shock and the first reflection. The results are further adjusted by dividing them by the total compression η'_1/η_0 produced by those first two waves. With these correlations, the results for positive and negative Atwood ratios seem to collapse reasonably well for both growth rate measurements.

In agreement with the results presented in Chapter 4, perturbations on a thick interface grow much more slowly than on a discontinuous interface. Furthermore, the nonuniformities contained in the diffusively-smoothed interfaces of the present experiments are probably small. Thus it is not surprising that each reverberation induces so little growth in the experiments with continuous interfaces and that growth is observed only after a long time delay.

The presence of the additional parameter δ'_0 makes the correlation of the late-time growth results for thick interfaces in the 'close end wall' configuration less straightforward. For present purposes, the growth rate is normalized by multiplying it by the thickness of the interface after

compression by the incident shock, and by dividing it by the sum of the absolute value of the velocity jumps induced by each reverberation. Using the sum of all velocity jumps introduces a slightly different Mach number dependence than does the use of only one velocity jump, as was done in figures 5.25 and 5.26. Note that this correlation is not dimensionless. Figure 5.29 shows the late-time growth rates for four different shock strengths and three different gas combinations. A straight-line fit to the data in figure 5.29 yields

$$\left[\frac{d\delta}{dt}\right]_{lt} = (0.17 \pm 0.03 \text{ mm}) \frac{A_0}{\delta'_0} \sum_{i=0}^{N-1} |[u]_i| \ , \tag{5.2}$$

where $(d\delta/dt)_{lt}$ is the late-time growth rate, $[u]_i$ the velocity jump induced by the ith wave, A_0 the initial Atwood ratio and δ'_0 the thickness (in mm) of the interface after the incident shock. The value of N used to form the normalization is usually 4.

5.7. Summary.

The experiments reported in this chapter have elucidated the physical processes taking place when one, two or many shock waves interact with a plane interface separating two gases of different densities.

For the discontinuous interface formed by a thin plastic membrane, the perturbations on the interface are introduced by the rupture of the membrane and it is found that they evolve rapidly into the nonlinear turbulent mixing regime. Comparatively more growth is observed for the light-heavy than for the heavy-light interfaces since the latter have to undergo a phase reversal before they grow. Experiments performed in two different configurations have allowed the observation of the incident shock growth for a long time period, but the large uncertainty in the data at the early times prevents the accurate determination of the power law describing the time evolution of the interface. Results for the reshock growth rates of these interfaces show that a noticeable increase of the turbulence intensity can be caused by the interaction of a shock wave with an already turbulent interface. It is seen that comparatively lower growth rates are induced by the stronger waves because they produce a larger compression of the perturbations. For some experiments, the entrainment process at the interface has been shown to be dominated by the evolution of large scale structures. Both incident shock and reshock growth rate results are nearly an order of magnitude smaller than those observed by other investigators for similar experiments.

Experiments with continuous interfaces have demonstrated that a dramatic reduction in the growth of a possible turbulent mixing zone can be achieved by reducing the density gradient at the interface. These interfaces exhibit growth only at late times, after the development of perturbations introduced by the reverberation of waves between the end wall, the side walls and the distorted interface under the influence of boundary layers. The vortical structures created by the shock wave-boundary layer interaction on the edges of the interface induce strain, that would effectively reduce the turbulent spreading of the interface.

Chapter 6

WAVE PHENOMENA AND WALL EFFECTS

The experimental study of the interaction of shock waves with an interface between gases of different densities has demonstrated that secondary effects, introduced by the apparatus, can impair the development and observation of the primary phenomenon under study. These effects can be classified in two groups: two- and three-dimensional wave phenomena and viscous boundary layer interactions. It is found that 2-D and 3-D wavefronts are generated by disturbances on the side walls of the shock tube. After these waves reverberate between the side walls, the end wall and the interface, they are responsible for the introduction of small perturbations on the smooth, thick interfaces. The propagation of the reshocks over the wall boundary layers lead to wave bifurcation, and their interaction with the distorted interface within the boundary layer causes the formation of a wall vortex, which can deform the interface by vorticity-induced strain.

6.1. Boundary Layers and Wall Vortices.

In the experiments reported here, a viscous boundary layer develops in the fluid behind the shock, deforming the interface near the walls. The interaction of the reshocks with this perturbation leads to the formation of wall vortices which distort the interface in the bulk of the fluid by vorticity-induced strain. Furthermore, as the reshock propagates into the slow-moving boundary layer fluid, shock bifurcation can occur, enhancing the mutual penetration of the two fluids across the interface.

6.1.1. *Boundary Layer Behind a Shock Wave.* The development of a laminar boundary layer behind a shock wave has been treated by many authors (*e.g.*, Mirels 1955). In the present study, since the pressure (Reynolds number) is high and the walls of the shock tube are rough, the boundary layers are likely to be turbulent and the analysis of Mirels (1964,1983) is used.

Mirels' analysis assumes that the compressible turbulent boundary layer obeys a 1/7 velocity profile, and the gas specific heat ratio γ and Prandtl number Pr are constant throughout the layer, a reasonable approximation for the relatively weak shock waves considered in this study. Since the static temperature T is allowed to vary through the boundary layer, the dynamic

viscosity μ of the gas is assumed to follow a $T^{1/2}$ temperature dependence, although the calculated boundary layer thickness is not very sensitive to the prescribed power law dependence for the shock strengths under consideration. Of primary interest is the determination of the boundary layer thickness ε in the test gas at the interface, after it has traveled a distance L following the arrival of the incident shock. The expression for ε is

$$\varepsilon(L) = 0.05745\,(0.125 + S\,(W-1))^{-4/5} \left[\frac{T_f}{T_0}\right]^{4/5} \left[\frac{T_m}{T_0}\right]^{-1/2} \left[\frac{\nu_0}{[u]}\right]^{1/5} L^{4/5} \,, \qquad (6.1)$$

where

$$W = \left[1 - \frac{2}{\gamma+1}\left[\frac{M_s^2-1}{M_s^2}\right]\right]^{-1/2} \qquad (6.2a)$$

is the velocity parameter, and the temperature ratios of interest are obtained from

$$\frac{T_m}{T_0} = 0.5\left[1+\frac{T_f}{T_0}\right] + 0.22\left[\frac{T_f}{T_0}\right]\left[\frac{T_r}{T_0} - 1\right] \qquad (6.2b)$$

$$\frac{T_r}{T_0} = 1 + \frac{Pr^{1/3}\,(W-1)^2}{\frac{\gamma+1}{\gamma-1}W - 1} \,, \qquad (6.2c)$$

and T_0 and T_f are the static temperatures in the bulk of the fluid ahead and behind the shock respectively, T_m is the mean temperature in the boundary layer and T_r is the so-called recovery temperature. The interface velocity is $[u]$, and ν_0 is the kinematic viscosity in the gas ahead of the shock. The parameter S and the numerical constant 0.125 in Eq. (6.2) are obtained from a straight line fit to a numerical integration; the values of the parameter $S = S(\gamma, Pr)$ are listed in Table 6.1 for the gases under consideration. The constant 0.05745 is derived from an empirical relation for turbulent boundary layers.

The thickness of the boundary layer in the test gas, when the interface has traveled to the middle of the observing windows (L = 38 cm) after the interaction with the incident shock, is

Table 6.1. Turbulent Boundary Layer Parameter S

Gas	Air	CO_2	R-22	SF_6	He
S	0.039	0.036	0.033	0.031	0.045

given in Table 6.2 for the experiments in the 'long time configuration'. There is good agreement between the calculated and observed thickness of the boundary layer at the interface.

6.1.2. *Interaction of Reflected Waves with Interfaces and Boundary Layers.* When a shock propagates into a fluid already under the influence of a boundary layer, the wave has to adjust to the nonuniform velocity field near the wall of the shock tube. Because the slower-moving boundary layer fluid has a lower stagnation pressure than the freestream flow, it can accumulate at the foot of the shock (as the so-called Mark bubble) and lead to wave bifurcation. A similar phenomenon can occur if the shock wave propagates over a boundary layer of a different composition than that of the fluid outside the boundary layer, as can happen in the present experiments when the reflected shock crosses the interface. In this situation, the accumulation of boundary layer fluid at the base of the shock is often referred to as the Hess bubble. Finally, the Richtmyer-Meshkov instability excited by the interaction of the reflected shock with the distorted interface within the boundary layer leads to the formation of so-called wall vortices.

6.1.2.1 Shock Propagation in a Boundary Layer. The basic processes occurring when a shock wave propagates into a fluid already under the influence of a boundary layer are presented in this section.

Mark (1957) has studied the shock-boundary layer interaction for a shock wave reflecting from the end wall of a shock tube (figure 6.1a). Figure 6.1b shows a schematic for the interaction; the analysis is performed more easily in shock-fixed coordinates (figure 6.1c).

Table 6.2. Boundary Layer Thickness at the Interface -- Long Time Configuration

Test Gas	A_0	M_s	ε (mm) @ L = 38 cm		Bifurcation of Reshock:	
			calculated	measured	in Test Gas	in Air
He	-0.76	1.32	7.8	7	no	yes
		1.48	7.2	6	no	yes
		1.66	6.8	6	no	yes
		1.66[1]	11.3	9	no	yes
Air	0	1.32	5.5	5	yes	yes
		1.48	5.0	5	yes	yes
		1.66	4.8	5	yes	yes
R-22	0.50	1.12	5.0	5	no	no
		1.32	4.2	5	yes	no
		1.48	3.8	3	yes	no
		1.66	3.5	3	yes	no
SF_6	0.67	1.12	4.8	4	no	no
		1.32	3.9	4	yes	no
		1.48	3.5	4	yes	no
		1.66[1]	5.3	4	yes	no

1. L = 71 cm

Mach numbers characterizing the outer flow (M_3) and the boundary layer flow closest to the wall (M_{BL}) can be defined; if $M_{BL} > 1$, a shock forms in the boundary layer. Mark proposed that when the stagnation pressure in the boundary layer fluid $p_{BL\,ST}$ exceeds the static pressure behind the reflected shock p_5 then the boundary layer fluid passes continuously under the foot of the reflected shock and into the region behind it. However, for certain values of the incident shock Mach number M_1, it is possible that $p_{BL\,ST} < p_5$. For this case, a simple steady through flow of the boundary layer fluid cannot be expected. Rather, Mark proposed that this fluid gathers up as a bubble in a region adjacent to the foot of the shock. Assuming that the ratio of specific heats stays constant throughout the boundary layer, Mark found that the bubble appears

if the Mach number of the wave incident onto the end wall is within the interval $1.32 < M_1 < 6.45$ for diatomic gases ($\gamma = 7/5$). For monatomic gases ($\gamma = 5/3$), this interval is within $1.57 < M_1 < 2.80$, although in this range the difference between p_5 and $p_{BL\,ST}$ is small enough to prevent the experimental observation of bifurcation for monatomic gases. Also, since the value of γ in diatomic gases decreases as a result of the temperature rise across a shock, the interval of bifurcation is effectively increased. Polyatomic gases, with their low specific heat ratios, have an even larger interval of bifurcation. Figure 5.8a shows an example of the bifurcation of the reflected shock in air.

In addition, the disturbance produced by the Mark bubble causes at least one oblique shock to form at the base of the reflected wave. The turning angle of the first oblique wave can be calculated by assuming that the pressure p_6 behind it is equal to the stagnation pressure in the bubble $p_{BL\,ST}$. If the flow behind this wave is supersonic (*i.e.*, $M_6 > 1$), another oblique shock forms to bring the static pressure back to p_5. If $M_6 < 1$, the necessary increase in pressure is accomplished by a streamtube area change. Because it is processed by one or two oblique shocks as compared to a normal shock for the flow in the bulk of the fluid, the velocity of the jet of fluid over the bubble is larger than that of the main flow behind the reflected shock, with a dividing streamline (*i.e.*, a shear layer) separating the two streams (figure 6.2). Ignoring the initial thickness of the boundary layer, it is then supposed that the extent of the bifurcation region evolves conically in space-time.

In the present experiments, the same bifurcation phenomenon can occur when the reshock crosses the interface between the two gases of different properties since the boundary layer fluid has a different composition than that of the main flow. In this case, Hess (1957) proposed that the jet of fluid over the bubble can penetrate into the other fluid across the interface and also possibly back under the boundary fluid layer (figure 6.3). This mechanism has been used to explain the contamination of hot test fluid by cold driver gas in shock tunnels (Davies & Wilson 1969, Stalker & Crane 1978). The bifurcation wave pattern over the bubble is determined from the same pressure matching arguments described above, where the first oblique shock over the bubble can be viewed as a precursor wave. The precursor shock problem has received a considerable amount of attention in experiments (Griffith 1956), theory (Hess 1957) and numerical computations (Glowacki *et al.* 1986). The precursor shock problem has also been studied analytically and experimentally in the context of shock reflection at an inclined interface

between two different fluids (*e.g.*, Jahn 1956, Abd-El-Fattah *et al.* 1976).

Table 6.2 also lists the predicted occurrence of bifurcation of the reshock in the test gas to form a Mark bubble, and also the occurrence of formation of a Hess bubble in air after the reshock crosses the interface. Figure 6.4 shows a construction, performed using the approach described above, for the bifurcation of the reshock as it crosses the air/He interface for an experiment in the 'long time' configuration (M_s = 1.66). The actual shape of the bubble can not be determined exactly with the simple arguments presented above; full numerical simulations (*e.g.*, Glowacki *et al.* 1986) have been used to solve this type of problem in more detail. It is seen that there is good agreement between the theory and the results of figure 5.15b for the wave pattern at the base of the shock. For all the cases where bifurcation occurs in air above the interface, the calculated velocity of the jet over the bubble is not much faster than that of the flow behind the reshock, so that contamination of the interface is not expected, nor observed.

As seen in Table 6.2, bifurcation of the reshock in air above the interface is not predicted for experiments with the light-heavy interfaces. Thus the Mark-Hess bubble jet phenomenon can not explain the formation of wall structures at the interface and the contamination of test gas by air for those experiments.

6.1.2.2 Wall Vortices. Wall vortices are created by the Richtmyer-Meshkov instability induced by the interaction of the reshock with the distorted interface within the boundary layer, or by interacting with the interface perturbed by the presence of a bulge in the supporting plastic membrane.

For both continuous and discontinuous interfaces, the velocity deficit at the wall is seen as causing the perturbation on the interface, with the crest near the wall and the trough as the flat part of the interface in the bulk of the fluid (figure 6.5). For the light-heavy interface, the interaction of the reshock with the interface is Rayleigh-Taylor 'stable' and a phase reversal of the perturbation is expected. If the region near the wall is modeled as a straight oblique interface, valuable insight can be obtained from the results of Haas for inclined interfaces (*cf.* figure 9a of Sturtevant 1988). Figure 6.6a shows the initial conditions. The discontinuous interface separates air from He, and the incident shock (M_s = 1.20) comes from below. This corresponds to the interaction of the reshock with an initially light-heavy interface for the

experiments of interest here. Figure 6.6b shows the interface 0.77 ms after the start of the interaction. The interface reverses phase, leading to the formation of a bubble of helium (the light gas) directed into air, and a spike of air (the heavy gas) rolls up as it penetrates into helium. These observations can be applied to the interaction of the reshock with the interface distorted by the boundary layer, where the phase reversal of the trough evolves as a spike of heavy fluid that eventually forms a vortex pair as seen experimentally in figures 5.20 and 5.22. In this case, the result of Haas presented in figure 6.6 applies to the right-hand part of the interface in the schematic of figure 6.7. Because a major portion of the interface is not perturbed by the boundary layers and thus remains flat, it is not affected much by the Richtmyer-Meshkov instability. Because of this, the spike grows faster than any other part of the interface, and the shape of the interface evolves as sketched in figure 6.7c, with an upward curvature of the middle of the interface. For the case of heavy-light interfaces, the interaction of the reshock with the interface is 'unstable'. Then, the perturbation within the boundary layer immediately increases in amplitude and no wall vortex is formed, as has been confirmed in the experiments (*cf.* figures 5.14 and 5.15), although, for these cases, a large disturbance is left on the side walls above the interface after the passage of the reshock.

In the case of interfaces initially formed by thin plastic membranes, it is possible to reverse the formation of the wall vortex by modifying the perturbation on the side walls at the interface. For example, for a light-heavy discontinuous interface that is initially bulged slightly upwards (by a small pressure difference across the membrane), the interaction with the incident shock is 'unstable', and the upward bulge increases in amplitude. At the same time as the interface propagates down the shock tube, it is pulled back on the sides by the action of the boundary layer. The resulting perturbation on the interface caused by both the bulge and the boundary layer is sketched in figure 6.8a. Upon the arrival of the reshock the interface reverses phase, leading to the formation of wall vortices (figure 6.8b) which roll up in the opposite direction of the vortices of figure 6.7, since the oblique part of the bulge perturbation has a different orientation than that of the wall perturbation described in figure 6.7. For this case, the bulge perturbation dominates the boundary layer perturbation of the interface. Thus, using the same arguments, it is seen that a very small initial downward bulge on the interface can explain the appearance of wall structures even for heavy-light interfaces, as observed in figure 5.18.

To quantify the effects of the wall vortices, their penetration into the test gas has been measured for the experiments with the light-heavy continuous interfaces in the 'long time' configuration. Figure 6.9 shows the wall vortex penetration speed u_p after the interaction of the interface with the first reshock, measured in a reference frame moving with the interface, normalized by the reshock velocity jump $[u]_1$ and plotted against the Atwood ratio A'_1. The multiple points for a given interface at a fixed shock strength are for different interface thicknesses. The relevant parameters are given in Table 5.3, since those measurements were obtained from the same experimental runs. A straight-line least-squares fit of the data (constrained to pass through the origin since the Richtmyer-Meshkov instability would be absent there) is also shown on the figure as

$$\frac{u_p}{[u]_1} = (0.26 \pm 0.08) A'_1 \ . \tag{6.3}$$

Although in this case the evolution of the perturbation is highly nonlinear, if this relation is compared directly with Richtmyer's formula (Eq. 3.7), with λ = 114 mm as the width of the shock tube since the perturbation is mainly two-dimensional, it is found that $\eta'_1 \simeq 5$ mm which, perhaps fortuitously, is about the thickness $\varepsilon(L)$ of the boundary layer at the interface at the time of the reshock. If the value of penetration velocity, measured in the laboratory frame of reference, is directed toward the test gas, the wall vortex can ultimately contaminate the entire test gas slug by making its way to the end wall of the shock tube. The mechanism of wall vortex formation could thus explain the results of Stalker & Crane (1978) who, for some cases, observed test gas contamination even though usually successful bifurcation arguments had precluded its appearance.

6.2. Influence of Wall Vortices on TMZ Growth Measurements.

The mechanism of wall vortex production has been presented in the previous Section. For shocks of modest strength ($M_s \simeq 1.5$) and interfaces between gases initially at one atmosphere with Atwood ratios of order one, the wall vortex has been seen to extend up to about 2 cm into the bulk of the fluid. At reduced pressure, the scale of the wall effect is expected to be larger, because the boundary layers are thicker. Indeed, the extent of the wall effect should scale approximately as $p_0^{-1/2}$ for a laminar boundary layer and as $p_0^{-1/5}$ for a turbulent one, where p_0 is the initial shock tube pressure. Thus, for experiments at 0.01 atm, the wall vortex will be

10× or 2.5× bigger, if the boundary layer is laminar or turbulent, respectively. Moreover, when a nitrocellulose film is used to initially separate the gases, the influence of the membrane on shock refraction at the interface increases as the initial shock tube pressure is reduced, as discussed in Section 6.3.1. It has been seen that the shock formation length d_{shock} downstream of the membrane becomes very long at low pressures. In experiments with discontinuous interfaces, Houas *et al.* (1988) have demonstrated the effect of initial pressure on both the domination of the development of the instability by the boundary layer and on the influence of the membrane on wave refraction at the interface.

It is important that in shock tube experiments flow visualization methods be used to distinguish between the wall vortex and the interface in the bulk fluid. For example, the streak schlieren method does not seem to be appropriate for TMZ growth studies. The mechanism for the generation of the wall vortex at an interface, namely, the Richtmyer-Meshkov instability, is different than that which causes reflected shock waves in molecular gases to bifurcate on the side walls of shock tubes. Thus, use of monatomic gases does not alleviate the wall jet effect, though the occurrence of bifurcation may aggravate it. In studies of the Richtmyer-Meshkov instability and in reflected-shock shock tubes and tunnels, it is necessary that the test sections be designed large enough that the wall vortices and bifurcation bubbles do not occupy the entire flow or that the long-range effects of vortex induction do not seriously compromise the accuracy of measurements.

Figure 6.10a shows the growth rate after one reshock of both the TMZ and the wall vortex for the air/helium interface with a M_s = 1.30 incident shock wave. In figure 6.10b data obtained from figure 3 of Andronov *et al.* (1976) are shown on the same scale for comparison. In both experiments the interface was initially 16.9 cm from the end of the test section. In the Andronov *et al.* experiment, the interface was formed by a 0.3 - 0.5 μm "organic film" (perhaps the same kind of membrane used in the present study) and the test section was rectangular with dimensions 4 cm × 12 cm. The reshock growth rate is determined to be about 70 m/s. In figure 6.10a the reshock growth rate of the TMZ is 7.5 ± 1.2 m/s (in this case not all the points shown were used to fit the data), and that of the wall jet is 49 ± 5 m/s. It can be seen that there is better agreement for the wall vortex results of the present experiments and the TMZ growth measurements of Andronov *et al.* It is not known whether the small width (4 cm) of the test section used by Andronov *et al.* is responsible for the marked disagreement between the TMZ

growth rates reported in the two studies. Other possibilities for the disagreement between the present results and those of Andronov *et al.* include differences between the schlieren systems used in the two experiments, possible differences of the membrane thickness and composition, or some other, unknown, features of the experimental setup.

As mentioned in the previous chapters, the strain induced on the interface by the wall vortex structures can lead to reduced reshock and late-time growth rates. For example, for the continuous interface between air and SF_6 accelerated by a $M_s = 1.32$ shock in the 'long time' configuration, the strain rate on the interface at the center of the test section can be evaluated (*cf.* Appendix D) to be about 60 s^{-1}, which produces a thinning rate of the interface of the order of 0.6 m/s. The measured reshock growth rate for this case is 1.1 m/s. The nonlinear coupling between the growth due to turbulent entrainment and the stretching caused by vortex induction prevents a straightforward correction of the results. However, it is safe to say that, in the case where very little growth is observed such as in the continuous interface experiments, the strain at the interface plays a major role. For the discontinuous interface 'long time' experiments, the vorticity-induced thinning rate of the interface is about 10% of the reshock growth rate, while for the 'close end wall' configuration, it is about 10% of the late time growth rate. For the continuous interface, the thinning rate is about 50% of the reshock and late-time growth rates.

6.3. Wave Phenomena.

6.3.1. *Validity of Simple One-Dimensional Gasdynamics.* In this work the motion of the interface and waves after their interaction is calculated using simple 1-D gasdynamics theory. It is assumed that the specific heat ratio of the gases remains constant, that the reflected and transmitted waves are centered at the interface, and that the latter is impulsively accelerated to its final velocity. Thus, the presence of the membrane for the discontinuous interface and that of the finite density gradient for the continuous interface are ignored, along with relaxation effects, in the calculations of front velocities for comparison with experimental observations.

6.3.1.1 Molecular Vibrational Relaxation Effects. The propagation of a shock wave into a polyatomic gas initially at room temperature can provoke the excitation of vibrational energy modes, which can lead to a change in some of the properties of the gas, including heat capacities and specific heat ratio. Thus errors are made by using the specific heat ratio at room temperature in the calculation of the wave refraction phenomenon at the interface. For the test

gases under consideration, only CO_2, R-22 and SF_6 exhibit such a change in properties at the temperatures attained in the experiments reported here. For the strongest incident shock (M_s = 1.66) the specific heat of CO_2 decreases from $\gamma = 1.29$ to 1.23. Using $\gamma = 1.29$ throughout the calculation causes an error of only 2% in the interface velocity, but overestimates the speed of the waves in CO_2 by as much as 8%. At the same extreme experimental conditions, the specific heat ratio of R-22 decreases from $\gamma = 1.17$ to $\gamma = 1.13$, and that of SF_6 from $\gamma = 1.09$ to $\gamma = 1.08$. Errors of the same magnitude as for CO_2 are made if the room temperature values are used. Since the important dynamical parameter for the Richtmyer-Meshkov instability is the velocity of the interface, it is sufficient to use the room temperature value for the specific heat ratio.

The excitation of vibrational energy levels is achieved through molecular energy exchange, and thus depends on the collision rate between the molecules of the gas. If equilibrium takes a finite time to be reached, a vibrational relaxation zone appears behind the shock. Lighthill (1956) has calculated that for shock propagation in CO_2 vibrational relaxation effects cause the full dispersion of the wave if its Mach number is below $M < 1.04$. If $M > 1.04$ a shock forms, but it is followed by a relaxation zone whose extent decreases as the strength of the wave is increased. These findings have been verified experimentally by Griffith & Kenny (1957). For the present experiments, since the weakest incident wave produces a transmitted shock of strength $M = 1.14$ in CO_2, it is assumed that relaxation effects are negligible. Unfortunately, such theoretical or experimental background is not available for R-22 and SF_6. However, since R-22 and SF_6 have a large number of vibrational modes (9 and 15 respectively), it is likely that the rotational-vibrational coupling is very efficient and rapid. Even if vibrational modes are excited by the propagation of a shock wave, the process is fast and the possible relaxation zone would be small for moderate wave strength at atmospheric pressure. Operating at low pressures would slow down the relaxation process, and strong waves would cause dissociation. Following these arguments, vibrational relaxation effects in R-22 and SF_6 are also neglected for the present experiments.

6.3.1.2 Effect of the Membrane at the Discontinuous Interface. The effect of the membrane on the refraction of the incident wave at a discontinuous interface can be estimated by considering the influence of the membrane's inertia. The interaction can be analyzed by modeling the membrane as a piston, assuming that it does not break and that its acoustic

impedance is large compared to the gases so that the wave does not immediately transmit through. The arrival of the incident shock at the interface then induces a constant acceleration $a = \Delta p\, A/m$ of the membrane of mass m, applied until the interface attains its final velocity $[u]_0$. The pressure difference across the membrane is Δp, and the cross-sectional area of the shock tube is A. The subsequent motion of the membrane causes the formation of compression waves in the test gas downstream of the interface, and after a certain distance d_{shock}, these waves coalesce into a shock wave. Since the motion of the piston is assumed to be parabolic in time, a simple expression for the shock formation distance d_{shock} can thus be obtained as follows (*cf.* Thompson 1984):

$$d_{shock} = \frac{2 m c_2^2}{(\gamma_2 + 1) \Delta p\, A} , \tag{6.4}$$

where c_2 and γ_2 are the speed of sound and the specific heat ratio in the test gas, respectively. The pressure difference across the piston Δp can be estimated from the pressure behind the reflection of the incident shock from a rigid end wall, since the acoustic impedance of the membrane is assumed to be very large. Such a pressure estimate gives a lower limit to d_{shock} since the pressure difference across the membrane decreases as its forward motion generates expansion waves back into air. Table 6.3 lists the shock formation distance for five interfaces, calculated for an incident shock Mach number M_s = 1.32.

Table 6.3. Shock Formation Distance --- M_s = 1.32

Interface	Air/air	Air/CO_2	Air/R-22	Air/SF_6	Air/He
d_{shock} (mm)	0.25	0.16	0.07	0.04	2.0

It can be seen that, for a given incident shock, the shock formation length increases as the molecular weight of the test gas is decreased. It is expected that the 1-D gasdynamics theory is valid when the waves emerging from the interface are at least a distance d_{shock} away from the

interface. Also, since $\Delta p \sim p_0 M_s^2$ where p_0 is the initial pressure in the test section, the shock formation length decreases as the strength of the incident wave is increased. On the other hand, reducing the initial pressure causes d_{shock} to increase. Therefore, the use of a light test gas at low initial pressure can lead to an unacceptably long shock formation length (*e.g.*, for Air/He with M_s = 1.32 at p_0 = 0.01 atm, d_{shock} = 0.2 m). For such a case, the influence of the membrane on wave refraction at the interface certainly can not be considered negligible.

6.3.1.3 Effect of the Finite Density Gradient at the Continuous Interface. For the continuous interface, the 1-D gasdynamics theory is valid at large distances from the interface, since, under these conditions, the thickness of the interface is negligible compared to the distance traveled by the waves. A better description of the waves when they are still near the interface can be achieved by using the theory of Chisnell (1955) for 1-D wave propagation in nonuniform media. This approach assumes that the interface can be split into a series of infinitesimal interfaces between gases of constant properties (figure 6.11). The arrival of a wave at an infinitesimal interface produces a reflected wave and a transmitted wave. The transmitted wave then interacts with the next interface, but it is assumed that the interaction of the reflected wave with the previous interface is negligible, *i.e.*, double reflection is not considered. A simple differential equation can then be written down for the strength of the reflected and transmitted waves as a function of varying material properties. If the two gases across the interface have the same ratio of specific heats, the equation can be integrated directly, otherwise the resulting wave pattern can be obtained by a numerical solution of the differential equation.

The wave phenomena resulting from the interaction of a shock wave with a thick light-heavy diffusive interface between two gases has been studied experimentally by Weber (1983) for incident shock Mach numbers between 1 and 2. The results have been compared to the 1-D gasdynamics and Chisnell theories and to a full numerical solution of the 1-D equations of compressible motion. Weber obtained the best agreement with the experimental results using the numerical simulation for the diffusive interface, although good agreement was observed with the simple gasdynamics theory when the waves had traveled about four layer thicknesses away from the interface. At such distances it was found that the theory of Chisnell overpredicted the strength of the transmitted and reflected shocks, although this method achieved better agreement with the experiments when the waves were closer to the interface, in the expected range of validity of that theory.

Although it is found that the interface acceleration is not exactly impulsive in the present experiments because of the presence of the membrane at the discontinuous interface or the finite density gradient at the continuous interface, the time taken to accelerate the interface to its final velocity is nevertheless short enough for the impulsive theory to be used.

6.3.2. *Two- and Three-Dimensional Wave Patterns.* The propagation of the interface and waves in the shock tube and test section is not perfectly one-dimensional owing to nonuniformities on the side walls of the tube, small disturbances in the test section and the presence of viscous boundary layers.

The refraction of the incident shock at the interface illustrates some of these influences. Figure 6.12 shows spark schlieren photographs of the air/SF_6 interface, initially located in the field of view of the windows. The interface is accelerated by a M_s = 1.32 shock wave just after retraction of the sliding plate, as evidenced by the presence on the left part of the interface of the ball of fluid pumped by the plate (figure 6.12a). The photograph shows the interface just after the arrival of the incident shock. Because of the presence of small disturbances on the side walls of the tube, such as joints for the plate guide plug and grease left from the edges of the sliding plate, the reflected and transmitted shocks emerging from the interface are accompanied by cylindrical acoustic waves that originate from the wall at the interface. Another front also appears on the left side because of the perturbation introduced by the slot into which the plate is retracted. Since the speed of sound is higher in air than in SF_6, the fronts propagate faster above the interface. This leads to the generation of precursor waves below the interface (figure 6.12b). Furthermore, the cylindrical wave in SF_6 propagates faster downstream than the transmitted shock, and the two interact leading to the reflection of the acoustic wave. Since the angle between the cylindrical wavefront and the shock remains constant in time as they propagate downstream, the weak reflected wave is straight and at the same angle. In this case the parameters are such that this reflection comes back to the interface where it meets the wall. Figure 6.13 is a construction for the shocks, the acoustic waves and their reflections, with the velocities calculated with the simple 1-D gasdynamics theory, for the interface of figure 6.12b at the same time interval after the interaction with the incident shock. There is good agreement between the two figures.

When the transmitted shock reflects from the end of the shock tube, cylindrical acoustic waves are also generated from the corners at the end of the tube because of the disturbance caused by the displacement thickness of the boundary layer into which it propagates. For experiments in the 'close end wall' configuration, the reverberation between the end wall and the interface of this wave pattern and the one discussed above lead to the randomization of the acoustic wave field, as shown in figure 4.6. The interaction of all these waves with the interface is the suggested mechanism for introducing perturbations on the smooth continuous interfaces, the growth of which has been measured in this work and presented in Chapter 5.

When the interface velocity is supersonic with respect to one of the gases adjacent to the interface, small disturbances on the walls of the test section cause the appearance of Mach waves, as seen in figure 5.15b. In this case the Mach number of the air flow is $M = 1.10$, corresponding to a Mach angle of 65°, which agrees with the observed value.

The result of the interaction of the reshock with the boundary layer above the interface is an other example of the two-dimensionality of the wave pattern. Because the boundary layer above the interface is composed mainly of test gas, its local speed of sound differs from that of the air in the bulk of the fluid. After the reshock crosses the interface, the wave transmitted into air has a different velocity than that propagating into the boundary layer. For the light-heavy interface the transmitted shock is bowed upwards, as seen in figure 4.5, because the speed of the wave in the boundary layer is lower. For the case of a heavy-light interface, the transmitted shock is preceded by a precursor shock, as seen in figures 5.14 and 5.15, and as discussed in Section 6.1.2.1.

Chapter 7

CONCLUSIONS

The interaction of shock waves with a contact surface between gases of different densities has been studied experimentally and theoretically. The investigation was motivated by a desire to obtain a more detailed physical understanding of the effects of interface density contrast and initial thickness, and incident wave strength on the Richtmyer-Meshkov instability. The experiments were performed in a new facility built specially for the study of shock-excited interfacial instabilities. The interface was formed by a thin (0.5 μm) plastic membrane or by retracting a metal plate initially separating the two fluids, and was located near the end of the shock tube, to study the effects on the instability of the incident shock and of its reverberations between the end wall and the interface. Air was used on one side of the interface and either helium, carbon dioxide, refrigerant-22 or sulphur hexafluoride was used on the other side as the test gas. Schlieren photography and high-speed cinematography, along with fast response pressure measurements, were used to study the time evolution of the shock-initiated instability. The most important results of the present work are (i) that the reduction in growth rate of a single-scale perturbation, caused by a decrease of the density gradient at the interface, has been observed experimentally and verified theoretically; (ii) that the growth of the turbulent mixing zone developing on discontinuous interfaces initially supported by thin plastic membranes is nearly an order of magnitude less than those reported by other investigators; (iii) that the growth of the turbulent mixing zone developing on thick, diffusive interfaces is much smaller than that observed on thinner interfaces; and (iv) that the appearance of wall vortices, formed by the interaction of reflected shocks with the distorted interface within the viscous boundary layer at the side walls, impairs the observation and the development of the primary phenomena of interest in the bulk of the fluid.

The linear theory for the Richtmyer-Meshkov instability has been modified to include the effects of a finite density gradient at the interface. The growth rate of perturbations on such an interface is slowed down as compared to those on a thinner one, and the reduction in growth rate can be calculated as a function of interface thickness, perturbation wavelength and interface density ratio by numerically solving the linear stability eigenvalue equations of motion for a

variable density profile. In the experiments, the perturbation on the thick interfaces was introduced by taking advantage of the pumping action of the retracting plate initially separating the two fluids. It has been observed that the growth rates of perturbations of wavelength $\lambda \approx 25$ mm on interfaces of thickness $\delta \approx 10$ mm after the incident shock are about three times smaller than those predicted by the linear theory for discontinuous interfaces, and are eight and twenty times slower after the first and second reverberation, respectively. Reasonable agreement has been obtained between the modified linear theory and the experimental results.

Experiments were performed to measure the visual thickness of the mixing zone induced by shock waves incident on continuous and discontinuous interfaces between gases of different densities. To observe the growth caused by the incident shock over a long time, and to examine the effects of the period of reverberations on the development of the instability, experiments were performed with various interface-window and interface-end wall distances. For thin interfaces initially supported by thin plastic membranes, the arrival of the incident shock breaks the membrane and introduces perturbations on the interface. These evolve rapidly into a turbulent mixing zone which is made more vigorous upon interaction with the reflected waves by the mechanisms of baroclinic vorticity generation and turbulence rapid distortion. As expected from simple physical considerations involving conservation of energy at the interface, it is found that the growth of the turbulent mixing zone caused by the incident shock slows down as time increases, although the accurate determination of the governing power law can not be accomplished due to the large relative error in the data measured a short time after the interaction with the incident shock. Also, the growth rates after the incident shock measured in the present study are nearly an order of magnitude less than those reported by previous authors for similar experiments. Results for the interaction of the first reflected shock with the already turbulent interface have demonstrated that the growth induced by the first reflected shock is sensitive to the initial pre-growth state of the interface. For the initially light-heavy interface, it was found that the growth rates after the first reshock are larger when the period of reverberations is decreased, and that the opposite is observed for the initially heavy-light interfaces. For both incident and reflected shock growth rates, the stronger waves induce comparatively less growth, and it is speculated that this is because the higher compression produced by the stronger waves actually reduces the amplitude of the perturbations on the

interface. Using this idea, the growth rates after the incident shock are successfully correlated by a normalization involving the interface velocity and the incident shock compression. Similarly, the growth rates after the reshock are correlated using the sum of the absolute values of the velocity jumps induced by the incident shock and the first reshock, and the total compression produced by those two waves. It appears that the late time growth of the turbulent mixing zone is accomplished by the merging of large scales at the interface, but since the total kinetic energy available for the turbulent motions at the impulsively accelerated interface is dependent on the wavelength of the initial perturbation and remains constant in time after the arrival of the shock, as opposed to the case of constant gravity Rayleigh-Taylor turbulent mixing for which it increases in time and does not depend on the wavelength of the perturbation, it is not certain whether the development of mixing at the interface achieves an asymptotic stage of self-similar turbulence independent of initial conditions. Since the thick interfaces formed by the retracting sliding plate are smoothed by molecular diffusion, the combination of low density gradient and small perturbations is such that they exhibit growth only after being perturbed by noise induced by wave reverberation between the interface, the side walls and the end boundary of the shock tube.

The development of viscous boundary layers on the side walls of the shock tube in the fluid in motion behind the incident shock wave can cause the bifurcation of the reflected waves and thereafter the formation of wall bubbles and interface-contaminating jets. The appearance of bifurcation wave patterns has been observed and has successively been compared with the well-known theoretical model. The generation of vortical structures by shock wave-boundary layer interaction at the interface has been demonstrated. Even if wave bifurcation arguments preclude the appearance of interface penetration jets, significant contamination can be caused by the wall vortex mechanism. The need for experimental methods to distinguish the effects of these wall vortices from the primary phenomena under study has also been pointed out. For example, it has been shown that better agreement is achieved between the wall vortex growth results of the present study and the turbulent mixing zone data published by other investigators. Moreover, the strain induced by the vorticity in these wall structures tends to thin the interface; the magnitude of this effect in most of the present experiments is estimated to be of order 10% for discontinuous interfaces and 50% for continuous interfaces.

The present observations present a clear view of the principal physical processes taking place when shock waves interact with a contact surface between gases of different densities. The accurate characterization of the mixing at the interface requires the identification of extraneous phenomena introduced by the experimental apparatus. This could be achieved more easily by using different flow visualization and measurement techniques. Finally, the direct utilization of these results in technological applications of the shock-excited instability needs a further enlargement of the data base available for these flows.

Appendix A

TRANSITION TIME OF TURBULENT MIXING ZONE

As discussed in Chapter 3, the development of a turbulent mixing zone at a shock-excited interface between two fluids of different densities is initially linear in time and ultimately obeys a power-law. Thus for the early times, the time evolution of the TMZ thickness δ follows (*cf.* Eq. 3.20):

$$\delta = [u]\, t\, f(A') \quad . \tag{A.1}$$

The kinetic energy E_k of the fluctuating motions initiated by the shock has been shown (Eq. 3.9) to be proportional to the square of the velocity jump $[u]$. It is assumed that a fraction F of the energy deposited by the shock goes into the turbulent motions, where F has been estimated to be about $0.1A'^2$ by Mikaelian (1985c). Thus from Eq. (A.1) it follows, for the initial stages of the development of the TMZ, that

$$\delta \propto E_k^{1/2}\, t \quad . \tag{A.2}$$

At the later stages, for the case where viscous energy dissipation is negligible, it has been shown that the power law is

$$\delta \propto E_{turb\ tot}^{1/3}\, t^{2/3} \quad . \tag{A.3}$$

Since $E_{turb\ tot} = F\, E_k$, it then follows that

$$\delta \propto E_k^{1/3}\, t^{2/3} \quad . \tag{A.4}$$

These arguments have been summarized in figure 3.7.

The time t^* at which the TMZ goes from linear to power law behavior can be estimated by patching the two solutions at a thickness δ^*, *i.e.*,

$$\delta^* \propto E_k^{1/2} t^* \propto E_k^{1/3} t^{*2/3} \quad . \tag{A.5}$$

It is easily seen that $t^* \propto E_k^{-1/2}$.

Appendix B

COMPRESSIBILITY EFFECTS -- CONVECTIVE MACH NUMBER

The onset of compressibility effects on the development of the shock-excited instability at an interface between two gases of different densities can be evaluated from the shear velocities possibly present within the interface.

These can be estimated by modeling the perturbation on any interface as a 2-D square wave, as shown in figure B.1. It is further assumed that the wave refraction phenomena is purely one-dimensional to isolate the effects of the incident and transmitted shocks. For the light-heavy interface, the transmitted shock is slower than the incident wave and the maximum possible velocity jump present at the interface involves the test fluid at rest and the air in motion behind the incident wave (figure B.1a). The maximum Mach number is obtained by normalizing this velocity difference by the speed of sound of the unshocked test gas. For the heavy-light interface, the transmitted shock speeds ahead of the incident wave, and the maximum velocity jump involves the air at rest and the test fluid in motion behind the wave (figure B.1b). A maximum Mach number value is obtained by using the speed of sound of the air ahead of the incident shock. A list of maximum relative Mach number M_{rel} is presented in Table B.1 for the experimental conditions under consideration.

However, because in reality the perturbation is more complex than that used in this simple model, the wave refraction phenomena at the interface is going to be at least two-dimensional, and the shear velocities are going to be smaller than those computed above. Furthermore, this picture of the interaction only applies before the incident shock reflects from the troughs to bring the air above the interface to the interface velocity $U_2 = [u]$. If the exact shear velocities within the interface were known, these could be compared with established criteria for the onset of compressibility, such as that of Papamoschou and Roshko (1988). This particular criterion, obtained in studies of turbulent mixing layers, expressed the compressibility limit as a function of a so-called convective Mach number based on the shear velocities in a reference frame moving at the phase speed of the most unstable mode of the idealized vortex sheet at the same conditions.

Table B.1. Maximum Relative Mach Number M_{rel}

Test Gas	A_0	M_s	Δu_{max} (m/s)	M_{rel}
He	-0.76	1.12	92.6	0.27
		1.32	226.8	0.66
		1.48	330.0	0.95
		1.66	428.2	1.24
CO_2	0.20	1.12	65.5	0.24
		1.32	162.1	0.60
		1.48	231.9	0.86
		1.66	304.9	1.13
R-22	0.50	1.12	65.5	0.36
		1.32	162.1	0.90
		1.48	231.9	1.29
		1.66	304.9	1.69
SF_6	0.67	1.12	65.5	0.48
		1.32	162.1	1.19
		1.48	231.9	1.71
		1.66	304.9	2.24

It is thus seen that the maximum relative Mach number serves as an upper limit to the possible convective Mach numbers present at the shock-excited interface, and that the establishment of an absolute criterion for this case is unfortunately not possible at this point. The computed values for M_{rel} are so far useful only to compare a case with respect to another one. Perhaps a better way to determine if the effects of compressibility are important would be to look for the formation of shock and expansion waves resulting from the development of the instability at the interface, and to quantify the fraction of the energy initially deposited by the shock that goes into acoustic modes. This is better accomplished with numerical simulations.

Appendix C

CONCENTRATION PROBE MEASUREMENTS

To obtain the structure of the continuous interface formed by the retraction of the sliding plate at the start of an experiment and to ensure that the visual thickness measured with the schlieren flow visualization system is representative of the actual thickness of the interface, a survey of the density profile of the interface was performed using a concentration probe.

C.1. Measurement Technique.

The measurements were performed with a Brown-Rebollo (1972) sampling probe, which was developed at Caltech for studies of mixing in steady inhomogeneous shear layers. A schematic of the probe is presented in figure C.1. Its principle of operation is simple; it is attached to a vacuum pump, and the platinum wire is maintained at a fixed temperature using a feedback bridge. The probe is pointed into a stream and samples gas from the stagnation region just upstream of the tip. If the flow velocity of the sampled stream is much less than the stagnation speed of sound, the gas properties have the same value if evaluated at static conditions as they do at stagnation conditions, and thus the probe is velocity insensitive. The voltage necessary to keep the wire at the preset temperature then varies only as a function of sampled gas properties.

The sampling probe assembly is shown in figure C.2. The probe used in the measurements reported here was originally fabricated by Chiun Wang for experimental studies of curved inhomogeneous shear layers (Wang 1984), and was later bent for incorporation in the present setup. The sensitive end of the probe is scanned through the interface by rotation about the axis of the gear on the right. A gear-driven Helipot (left) records the position of the probe. The probe is used with a Caltech Matilda^{TM} constant temperature hot-wire feedback bridge, set at a bridge resistance of R = 19.3 Ω and an offset of 6.1 on the potentiometer, with the output processed by a low-pass filter set at 20 Hz. The probe was calibrated against known gas mixtures at atmospheric pressure, and the results are shown in figure C.3. It is seen that the probe is more sensitive for SF_6 and R-22 than for CO_2 and that the full-scale sensitivity of the probe is not very large, only 0.15 V for SF_6. Moreover, the sensitivity is not very good for low test gas concentrations since a small change in probe output voltage yields a large variation in

interface composition. The curves are obtained from fourth-order polynomial least square fits to the data points.

C.2. Interface Measurements.

The experimental arrangement to probe the continuous interface is shown in figure C.4. The sampling probe assembly is installed at a rectangular slot upstream of the viewing windows where the interface is located. The probe is rotated manually, and the position and composition signals are recorded by the data acquisition system. These data are then reduced to concentration profiles using the calibration curves of the probe and the position calibration for the Helipot. Because of the physical limitations imposed by the width of the test section and the distance from the probe assembly to the interface, sampling is only possible down to a distance 9 mm below the interface.

Figure C.5 shows interface composition data plotted versus probe position for two different times after plate retraction to form an air/SF_6 interface. Each set of points represents the results from one scan. The error bars and the scatter indicate the resolution limit of the least significant bit of the Computerscope data acquisition recorder. The solid lines are obtained by fitting a straight line to the portion of data over which the lines are shown solid. It can be seen that significant thickening of the interface by molecular diffusion is observed in 10 seconds.

Figure C.6 is a summary of the air/SF_6 data for various time delays. The curves drawn are cubic least-square fits to the data points. Similar plots for air/R-22 and air/CO_2 interfaces are shown in figures C.7 and C.8. Table C.1 lists the measured maximum-slope thickness δ_{ms} of these interfaces as a function of time after plate retraction.

A log-log plot of interface thickness versus time is presented in figure C.9. The solid line has a slope of 1/2 and is added for comparison of the data with a pure diffusive process. It is seen that the air/SF_6 and air/CO_2 interfaces follow the line reasonably well. It is not known why the thickening of the air/R-22 interface is much slower. For a given time after plate retraction, the air/CO_2 interface is thicker than the air/R-22 and air/SF_6 interfaces, which can be explained by its larger molecular diffusion coefficient D. In fact, D = 0.204 cm^2/s for air/CO_2 mixtures, as compared to D = 0.104 cm^2/s and D = 0.097 cm^2/s for air/R-22 and air/SF_6,

Table C.1. Maximum-Slope Thickness of Continuous Interfaces from Probe Measurements

Test Gas	A_0	Time (s)	δ_{ms} (mm)
CO_2	0.20	1.6	21
		4.0	29
		6.0	40
R-22	0.50	0.4	20
		4.0	24
		8.0	26
SF_6	0.67	0.4	14
		2.0	22
		3.5	23
		4.9	24
		6.2	26
		7.7	35
		10.2	48

respectively.

The maximum slope thicknesses obtained from concentration probe measurements can be compared to the visual thicknesses δ_{visual} measured from schlieren photographic records (Table C.2). It is seen that the values obtained from the visual records are in general agreement with the probe results. A perfect match between the two sets of data cannot be expected since the schlieren flow visualization system is sensitive to a only a certain range of density gradients present within the interface and that the actual region of maximum slope is always smaller than the maximum slope thickness. With the present schlieren system sensitivity, adjusted so that the interface can easily be distinguished from the image of the shock wave-boundary layer interaction taking place on the observing window, the visual thickness of air/SF_6 interfaces is larger than the maximum slope thickness, and the opposite is observed for the air/R-22 and

Table C.2. Visual Thickness of Continuous Interfaces

Test Gas	A_0	Time (s)	δ_{visual} (mm)
CO_2	0.20	0	16
		3	19
		4	21
R-22	0.50	0	16
		4	27
		6	29
SF_6	0.67	0	16
		4	25
		5	27
		6	30

air/CO_2 interfaces.

Furthermore, as the interface is processed by shock waves in the experiments, the density gradients are increased, and the visual thickness should match more closely the maximum slope thickness. Such problems are not present in the discontinuous interface experiments since the gradients are already large and the turbulent mixing zone is characterized by structures that are readily picked up by the flow visualization system.

Appendix D

INTERFACE STRAIN INDUCED BY WALL VORTICES

The strain induced by the wall vortices created by the interaction of the reflected shocks with the distorted interface within the boundary layer can be evaluated from basic incompressible vorticity-dynamics formulas (*cf. e.g.*, Rosenhead 1931). In general, for a infinite system that is periodic in the y-direction and consisting of "K" point vortices of circulation Γ_i each (figure D.1), the velocities induced at any point are

$$u(x,y) = \frac{1}{2\mathbf{D}} \sum_{i=1}^{K} \Gamma_i \frac{-\sin\left[\frac{2\pi}{\mathbf{D}}(y-y_i)\right]}{\left[\cosh\left[\frac{2\pi}{\mathbf{D}}(x-x_i)\right] - \cos\left[\frac{2\pi}{\mathbf{D}}(y-y_i)\right]\right]} \qquad \text{(D.1a)}$$

$$v(x,y) = \frac{1}{2\mathbf{D}} \sum_{i=1}^{K} \Gamma_i \frac{\sinh\left[\frac{2\pi}{\mathbf{D}}(x-x_i)\right]}{\left[\cosh\left[\frac{2\pi}{\mathbf{D}}(x-x_i)\right] - \cos\left[\frac{2\pi}{\mathbf{D}}(y-y_i)\right]\right]} \qquad \text{(D.1b)}$$

The configuration under consideration for the study of the effects of the wall vortices is shown in figure D.2. Two counterrotating point vortices of circulation strength Γ are located a distance d form the side walls. The width of the test section is **D** = 114 mm. The coordinate system is such that the x-axis is in the direction of the shock tube. For this specific case, K = 2, and the velocity field at any point within the test section is readily obtained by using Eqs. (D.1a) and (D.1b).

Of primary importance is the calculation of the strain rate $\dot{s}$, defined as $\dot{s} \equiv \partial u/\partial x$ or $\dot{s} \equiv -\partial v/\partial y$ since the flow is assumed incompressible. At the center of the test section (y = **D**/2) the strain rate is then

$$\dot{s} = -\frac{2\pi\Gamma}{D^2} \frac{\sinh\left[\frac{2\pi x}{D}\right] \sin\left[\pi - 2\pi\frac{d}{D}\right]}{\left[\cosh\left[\frac{2\pi x}{D}\right] - \cos\left[\pi - 2\pi\frac{d}{D}\right]\right]^2} \quad , \tag{D.2}$$

and can then be calculated at any height x given the value of d and Γ.

For example, for the continuous air/SF_6 interface with M_s = 1.32 in the long time configuration (*cf.* figure 5.20), the location of the vortices is at d = 10 mm, and the middle of the interface is at x = -20 mm with respect to the wall vortices. The circulation Γ can be estimated by evaluating the tangential velocity u_t of the roll-up of the vortex from $\Gamma = 2\pi u_t r$, where r is the radius of the vortex (figure D.3). For this particular case, $u_t \approx 10$ m/s and $r \approx 10$ mm, then $\Gamma \approx 0.6$ m^2/s, and the strain rate is calculated to be $\dot{s} \approx 30$ s^{-1}. Because the test section is actually three-dimensional, wall vortices develop on all four side walls. Thus, there is another pair of similar vortices in the $x-z$ plane, and the contribution to the strain rate induced at the interface by this pair has the same magnitude as that of the other pair. Neglecting 3-D effects the total strain rate is then simply the sum of both and $\dot{s}_{tot} \approx 60$ s^{-1}.

The rate of change of the thickness of the interface caused by the vorticity-induced strain can then be estimated as

$$\left[\frac{d\delta}{dt}\right]_{vortex} = -\delta \dot{s}_{tot} \quad , \tag{D.3}$$

where the negative value is used because this particular flow field causes a thinning of the interface. For the particular case under consideration, since the thickness of the interface $\delta \approx 10$ mm, then $(d\delta/dt)_{vortex} \approx$ -0.6 m/s.

REFERENCES

Abd-El-Fattah, A.M., Henderson, L.F. & Lozzi, A. 1976 Precursor Shock Waves at a Slow-Fast Gas Interface, *J. Fluid Mech.* **76**, 157.

Afanas'ev, Yu.F., Basov, N.G., Gamalii, E.G., Krokhin, O.N. & Rozanov, V.B. 1976 Symmetry and Stability of Laser-Driven Compression Thermonuclear Targets, *JETP Lett.* **23**, 566.

Andronov, V.A., Bakhrakh, S.M., Meshkov, E.E., Mokhov, V.N., Nikiforov, V.V, Pevnitskii, A.V. & Tolshmyakov, A.I. 1976 Turbulent Mixing at Contact Surface Accelerated by Shock Waves, *Sov. Phys. JETP* **44**, 424.

Andronov, V.A., Bakhrakh, S.M., Meshkov, E.E., Nikiforov, V.V, Pevnitskii, A.V. & Tolshmyakov, A.I. 1982 An Experimental Investigation and Numerical Modeling of Turbulent Mixing in One-Dimensional Flows, *Sov. Phys. Dokl.* **27**, 393.

Baker, W.S. & Mossman, A. (editors) 1971 *Matheson Gas Data Book*, East Rutherford, N.J.

Baker, G.R., Meiron, D.I. & Orszag, S. 1980 Vortex Simulations of the Rayleigh-Taylor Instability, *Phys. Fluids* **23**, 1485.

Barenblatt, G.I. 1983 Self-Similar Turbulence Propagation from an Instantaneous Plane Source, In: *Non-Linear Dynamics and Turbulence*, edited by G.I. Barenblatt, G. Ioos and D.D. Joseph, Pitman, Boston, 48.

Bellman, R. & Pennington, R.H. 1956 Effects of Surface Tension and Viscosity on Taylor Instability, *Quart. Appl. Math.* **13**, 151.

Benjamin, R.F., Trease, H.E. & Shaner, J.W. 1984 Coherent Density Gradients in Water Compressed by a Modulated Shock Wave, *Phys. Fluids* **27**, 2390.

Benjamin, R.F. & Fritz, J.N. 1987 Shock Loading a Rippled Interface Between Liquids of Different Densities, *Phys. Fluids* **30**, 331.

Brown, G.L. & Rebollo, M.R. 1972 A Small, Fast-Response Probe to Measure Composition of a Binary Gas Mixture, *AIAA J.* **10**, 649.

Chandrasekhar, S. 1961 *Hydrodynamic and Hydromagnetic Stability*, Oxford University Press, Oxford, 433.

Chisnell, R.F. 1955 The Normal Motion of a Shock Wave Through a Non-Uniform Medium, *Proc. Roy. Soc. A* **232**, 350.

Cole, R.H. 1948 *Underwater Explosions*, Princeton University Press, Princeton, 348.

Davies, L. & Wilson, J.L. 1969 Influence of Reflected Shock and Boundary-Layer Interaction on Shock-Tube Flows, *Phys. Fluids* **12**, Suppl. I, 37.

Detleff, G., Thompson, P.A., Meier, G.E.A. & Speckmann, H.-D. 1979 An Experimental Study of Liquefaction Shock Waves, *J. Fluid Mech.* **95**, 279.

Duff, R.E., Harlow, F.H. & Hirt, C.W. 1962 Effects of Diffusion on Interface Instability Between Gases, *Phys. Fluids* **5**, 417.

Emery, M.H., Gardner, J.H. & Boris, J.P. 1982 Rayleigh-Taylor and Kelvin-Helmoltz Instability in Targets Accelerated by Laser Ablation, *Phys. Rev. Lett.* **48**, 677.

Frost, D.L. 1988 Dynamics of Explosive Boiling of a Droplet, *Phys. Fluids* **31**, 2554.

Glowacki, W.J, Kuhl, A.L., Glaz, H.M. & Ferguson, R.E. 1986 Shock Wave Interaction with High Sound Speed Layer, in:
Shock Waves and Shock Tubes, edited by D. Bershader and R. Hanson, Stanford University Press, 188.

Gray, D.E. (editor) 1972 *American Institute of Physics Handbook*, 3rd Edition, McGraw-Hill, New York.

Griffith, W.C. 1956 Interaction of a Shock Wave with a Thermal Boundary Layer, *J. Aero. Sciences* **23**, 16.

Griffith, W.C. & Kenny, A. 1957 On Fully Dispersed Shock Waves in Carbon Dioxide, *J. Fluid Mech.* **3**, 286.

Grun, J., Emery, M.H., Kacenjar, S., Opal, C.B., McLean, E.A., Obenschain, S.P., Ripin, B.H. & Schmitt, A. 1984 Observation of the Rayleigh-Taylor Instability in Ablatively Accelerated Foils, *Phys. Rev. Lett.* **53**, 1352.

Hess, R.V. 1957 Interaction of Moving Shocks and Hot Layers, NACA TN-4002.

Hesselink, L. & Sturtevant, B. 1988 Propagation of Weak Shock Waves Through a Random Media, *J. Fluid Mech.* **196**, 513.

Hirschfelder, J.O., Curtiss, C.F. & Bird, R.B. 1954 *Molecular Theory of Gases and Liquids*, John Wiley & Sons, New York, 539.

Houas, L., Farhat, A. & Brun, R. 1988 Shock Induced Rayleigh-Taylor Instability in the Presence of a Boundary Layer, *Phys. Fluids* **31**, 807.

Hunt, J.C.R. 1978 A Review of the Theory of Rapidly Distorted Turbulent Flows and its Applications, *Fluid Dynamics Transactions* **9**, 121.

Jacobs, J.W. & Catton, I. 1988 Three-Dimensional Rayleigh-Taylor Instability. Part 2, *J. Fluid Mech.* **187**, 353.

Jahn, R.G. 1956 The Reflection of Shock Waves at a Gaseous Interface, *J. Fluid Mech.* **1**, 457.

Kiang, R.L. 1969 Nonlinear Theory of Inviscid Taylor Instability Near the Cutoff Wavenumber, *Phys. Fluids* **12**, 1333.

Kline, S.J. 1967 Observed Structure Features in Turbulent and Transitional Boundary Layers, In: *Fluid Mechanics of Internal Flow*, Elsevier, New York, 27.

Kreith, F. & Black, W.Z. 1980 *Basic Heat Transfer*, Harper & Row, New York.

Landau, L.D. & Lifshitz, E.M. 1959 *Fluid Mechanics*, Pergamon Press, New York, 479.

Leith, C.E. 1985 Acceleration-Induced Turbulent Mixing: Model One, Unpublished Report, Lawrence Livermore National Laboratory.

Leith, C.E. 1986 Development of a Two-Equation Turbulent Mix Model, Report UCRL-96036, Lawrence Livermore National Laboratory.

LeLevier, R., Lasher, G.J. & Bjorklund, F. 1955 Effect of a Density Gradient on Taylor Instability, Report UCRL-4459, University of California Radiation Laboratory.

Lewis, D.J. 1950 The Instability of Liquid Surfaces when Accelerated in a Direction Perpendicular to their Planes. II, *Proc. Roy. Soc. A* **202**, 81.

Liepmann, H.W. & Roshko, A. 1957 *Elements of Gasdynamics*, John Wiley & Sons, New York.

Lighthill, M.J. 1956 Viscosity Effects in Sound Waves of Finite Amplitude, In: *Surveys in Mechanics*, edited by G.K. Batchelor and R.M. Davies, Cambridge University Press, Cambridge, 250.

Lindl, J.D. & Mead, W.C. 1975 Two-Dimensional Simulation of Fluid Instability in Laser-Fusion Pellets, *Phys. Rev. Lett.* **34**, 1273.

Lim, D. & Babcock, C.D. 1984 Stress Analysis of the Vertical Shock Tube, Private Communication.

Lord Rayleigh 1900 Investigation of the Character of the Equilibrium of an Incompressible Heavy Fluid of Variable Density, In: *Scientific Papers*, Vol. 2, Dover, New York, 200.

Marble, F.E., Hendricks, G.J. & Zukoski, E.E. 1987 Progress Toward Shock Enhancement of Supersonic Combustion Processes, *AIAA Paper* 87-1880.

Mark, H. 1957 The Interaction of a Reflected Shock Wave with the Boundary Layer in a Shock Tube, *J. Aero. Sciences* **24**, 304.

Markstein, G.H. 1957a A Shock Tube Study of Flame Front-Pressure Wave Interaction, In: *Sixth Symposium (International) on Combustion*, Reinhold, New York, 387.

Markstein, G.H. 1957b Flow Disturbances Induced Near a Slightly Wavy Contact Surface, or Flame Front, Traversed by a Shock Wave, *J. Aero. Sciences* **24**, 238.

Marshall, N. (editor) 1976 *Gas Encyclopedia*, Elsevier, New York.

Menikoff, R. & Zemach, C. 1983 Rayleigh-Taylor Instability and the Use of Conformal Maps for Ideal Fluid Flow, *J. Comp. Physics* **51**, 28.

Meshkov, E.E. 1969 Instability of the Interface of Two Gases Accelerated by a Shock Wave, *Sov. Fluid Dynamics* **4**, 101.

Meyer, K.A. & Blewett, P.J. 1972 Numerical Investigation of the Stability of a Shock Accelerated Interface Between Two Fluids, *Phys. Fluids* **15**, 753.

Mikaelian, K.O. 1982a Normal Modes and Symmetries of the Rayleigh-Taylor Instability in Stratified Fluids, *Phys. Rev. Lett.* **48**, 1365.

Mikaelian, K.O. 1982b Rayleigh-Taylor Instabilities in Stratified Fluids, *Phys. Rev. A* **26**, 2140.

Mikaelian, K.O. 1983 Time Evolution of Density Perturbations in Accelerating Stratified Fluids, *Phys. Rev. A.* **28**, 1637.

Mikaelian, K.O. 1985a Richtmyer-Meshkov Instabilities in Stratified Fluids, *Phys. Rev. A* **31**, 410.

Mikaelian, K.O. 1985b Turbulent Mixing Generated by Rayleigh-Taylor and Richtmyer-Meshkov Instabilities, Report UCRL-93499, Lawrence Livermore National Laboratory.

Mikaelian, K.O. 1985c Turbulent Energy at Accelerated and Shocked Interfaces, Unpublished Report, Lawrence Livermore National Laboratory.

Mikaelian, K.O. 1988 Simulation of the Richtmyer-Meshkov Instability and Turbulent Mixing in Shock-Tube Experiments, Unpublished Report, Lawrence Livermore National Laboratory.

Mirels, H. 1955 Laminar Boundary Layer behind Shock Advancing into Stationary Fluid, NACA TN-3401.

Mirels, H. 1964 Shock Tube Test Time Limitation Due to Turbulent-Wall Boundary Layer, *AIAA. J.* **2**, 84.

Mirels, H. 1983 Turbulent Boundary Layer Behind Constant Velocity Shock Including Wall Blowing Effects, *AIAA. J.* **22**, 1042.

Papamoschou, D. & Roshko, A. 1988 The Compressible Turbulent Shear Layer: An Experimental Study, *J. Fluid Mech.* **197**, 453.

Plesset, M.S. 1954 On the Stability of Fluid Flows with Spherical Symmetry, *J. Appl. Physics* **25**, 96.

Read, K.I. 1984 Experimental Investigation of Turbulent Mixing by Rayleigh-Taylor Instability, *Physica D* **12**, 45.

Richtmyer, R.D. 1960 Taylor Instability in Shock Acceleration of Compressible Fluids, *Comm. Pure Appl. Math.* **8**, 297.

Rosenhead, L. 1931 The Formation of Vortices from a Surface of Discontinuity, *Proc. Roy. Soc. A* **134**, 170.

Roshko, A. & Baganoff, D. 1961 A Novel Device for Bursting Shock-Tube Diaphragms, *Phys. Fluids* **4**, 1445.

Saffman, P.G. & Meiron, D. 1989 Kinetic Energy Generated by the Incompressible Richtmyer-Meshkov Instability in a Continuously Stratified Fluid, Private Communication.

Sharp, D.H. 1984 An Overview of Rayleigh-Taylor Instability, *Physica D* **12**, 3.

Smarr, L., Wilson, J.R., Barton, R.T. & Bowers, R.L. 1981 Rayleigh-Taylor Overturn in Supernova Core Collapse, *Ap. J.* **246**, 515.

Smith, J.A., Coles, D., Roshko, A. & Prasad, A.J. 1967 A Description of the GALCIT 6" Shock Tube, GALCIT Report FM-67-1.

Stalker, R.J. & Crane, K.C.A. 1978 Driver Gas Contamination in a High-Enthalpy Reflected Shock Tunnel, *AIAA J.* **16**, 277.

Stull, D.R. & Prophet, H. (project directors) 1971 *JANAF Thermochemical Tables*, 2nd Edition, National Bureau of Standards, Washington.

Sturtevant, B. 1988 Rayleigh-Taylor Instability in Compressible Fluids, In: *Shock Tubes and Waves*, edited by H. Grönig, VCH, Wendheim, Federal Republic of Germany, 89.

Taylor, G.I. 1950 The Instability of Liquid Surfaces when Accelerated in a Direction Perpendicular to their Planes. **I**, *Proc. Roy. Soc. A* **201**, 192.

Thompson, P,A. 1984 *Compressible-Fluid Dynamics*, Maple Press Company, 401.

Thompson, P.A., Kim, Y.-G., Yoon, C.J. & Chan Y. 1988 Nonequilibrium, Near-Critical States in Shock Tube Experiments, In: *Shock Tubes and Waves*, edited by H. Grönig, VCH, Wendheim, Federal Republic of Germany, 343.

Weber, G. 1983 Instationäre Stosswellen in Inhomogenen Gasen, Ph.D. Thesis, RWTH-Aachen.

Youngs, D.L. 1984 Numerical Simulation of Turbulent Mixing by Rayleigh-Taylor Instability, *Physica D* **12**, 32.

Wang, C. 1984 The Effect of Curvature on Turbulent Mixing Layers, Ph.D. Thesis, California Institute of Technology.

Wu, C.-T., Ferziger, J.H. & Chapman, D.R. 1985 Simulation and Modeling of Homogeneous Compressed Turbulence, NASA-CR-176939.

Zaitsev, S.G., Lazareva, E.V., Chernukha, V.V. & Belyaev, V.M. 1985 Intensification of Mixing at the Interface Between Media of Different Densities upon the Passage of a Shock Wave Through It. *Sov. Phys. Dokl.* **30**, 579.

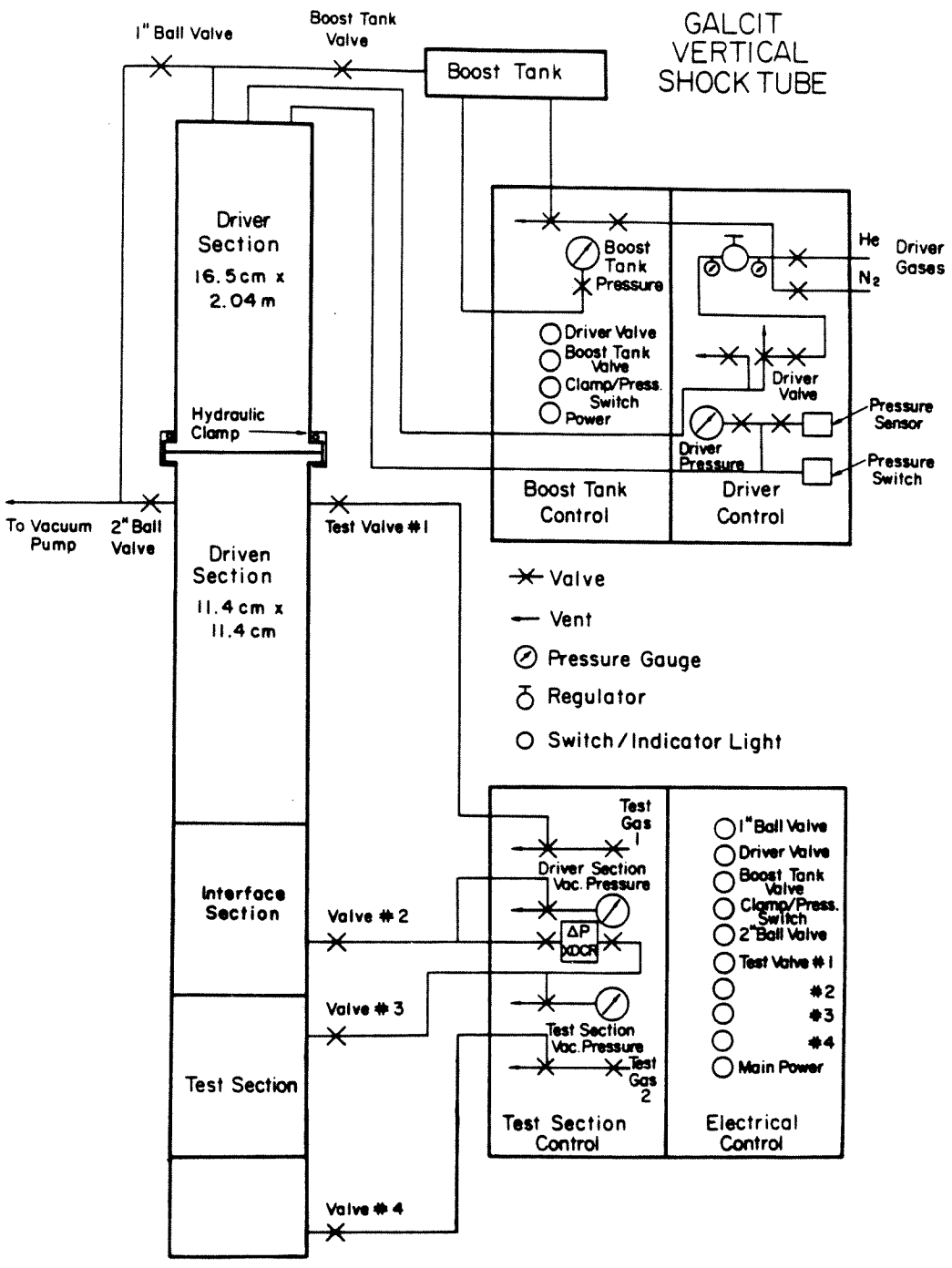

Figure 2.1 GALCIT vertical shock tube -- schematic.

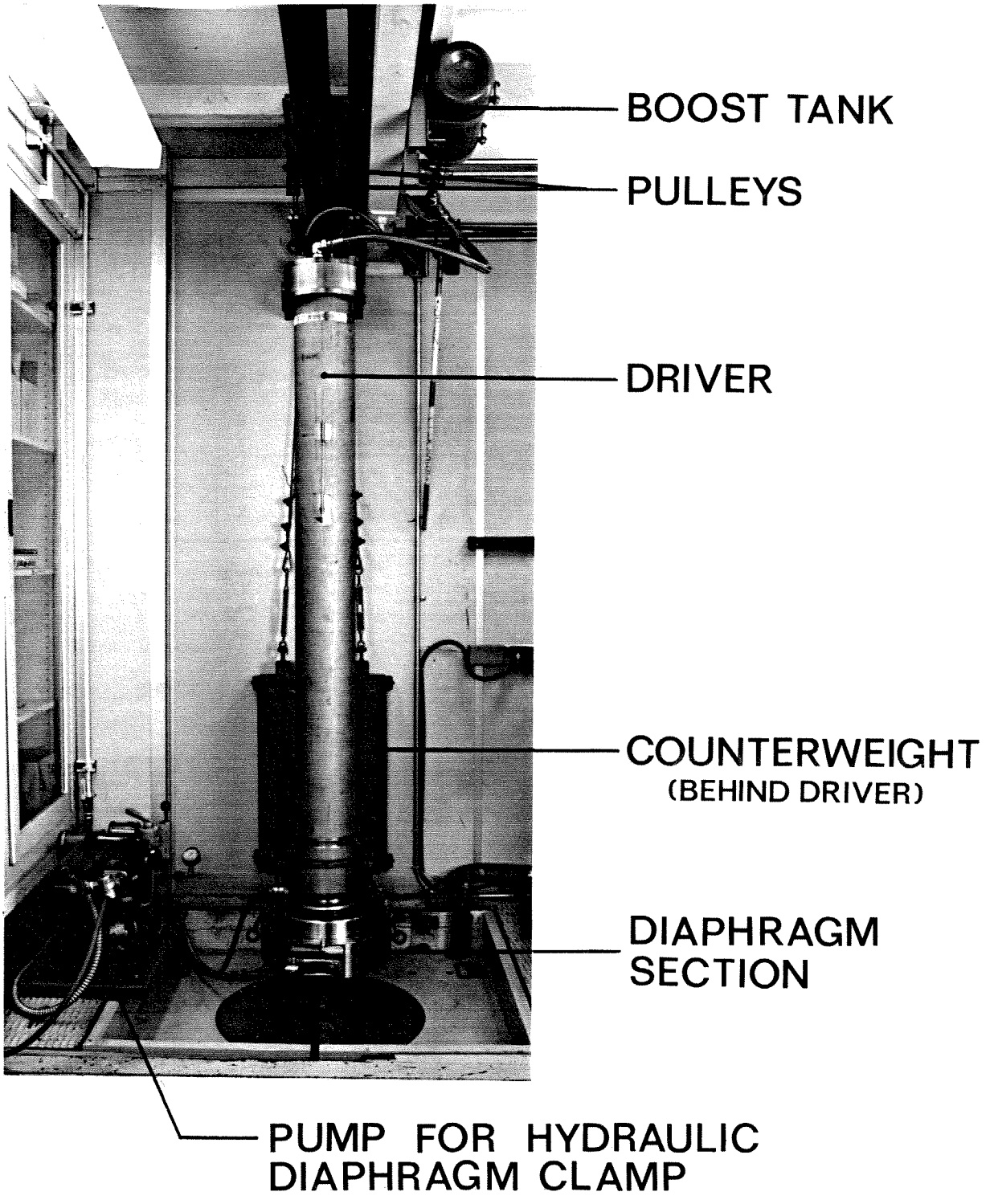

Figure 2.2 Driver section.

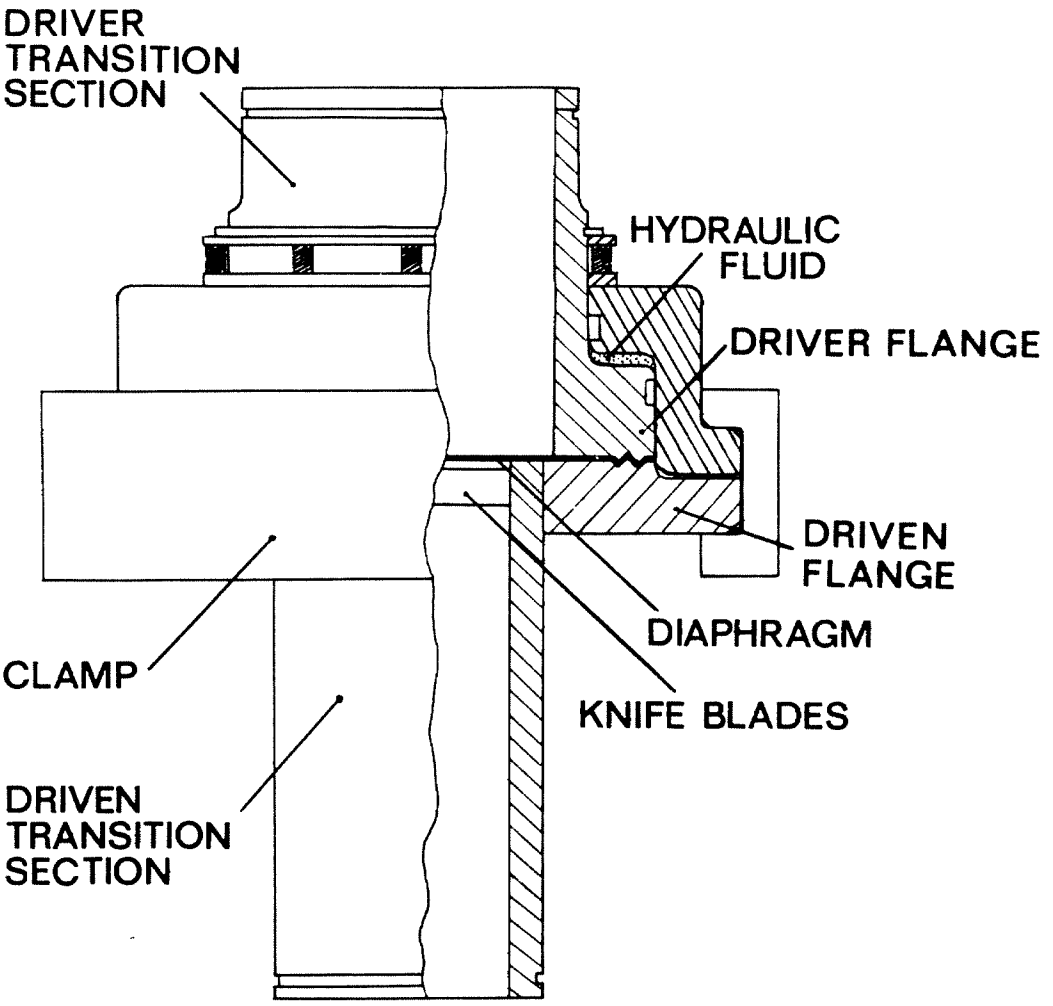

Figure 2.3 Diaphragm section.

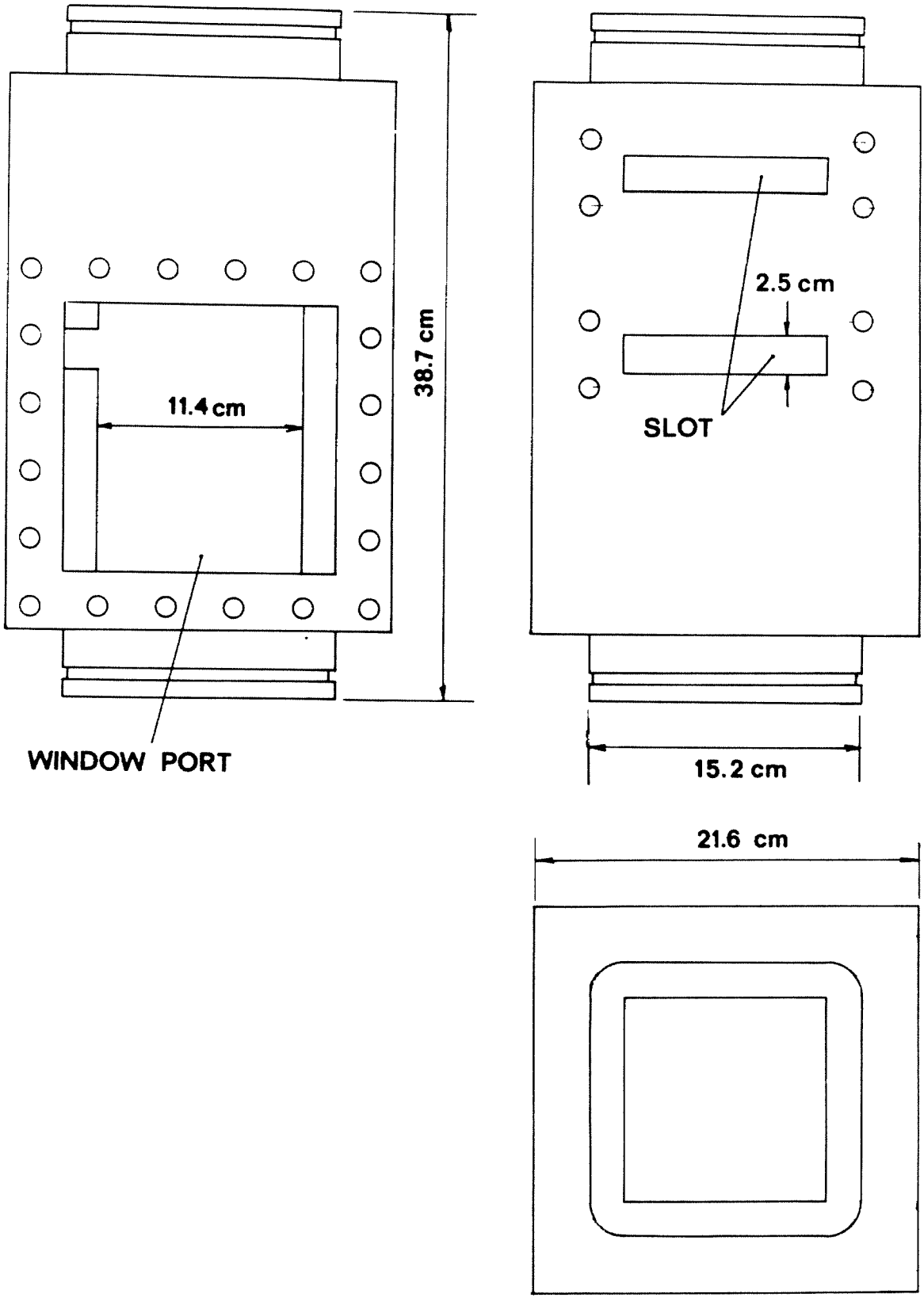

Figure 2.4 Test section.

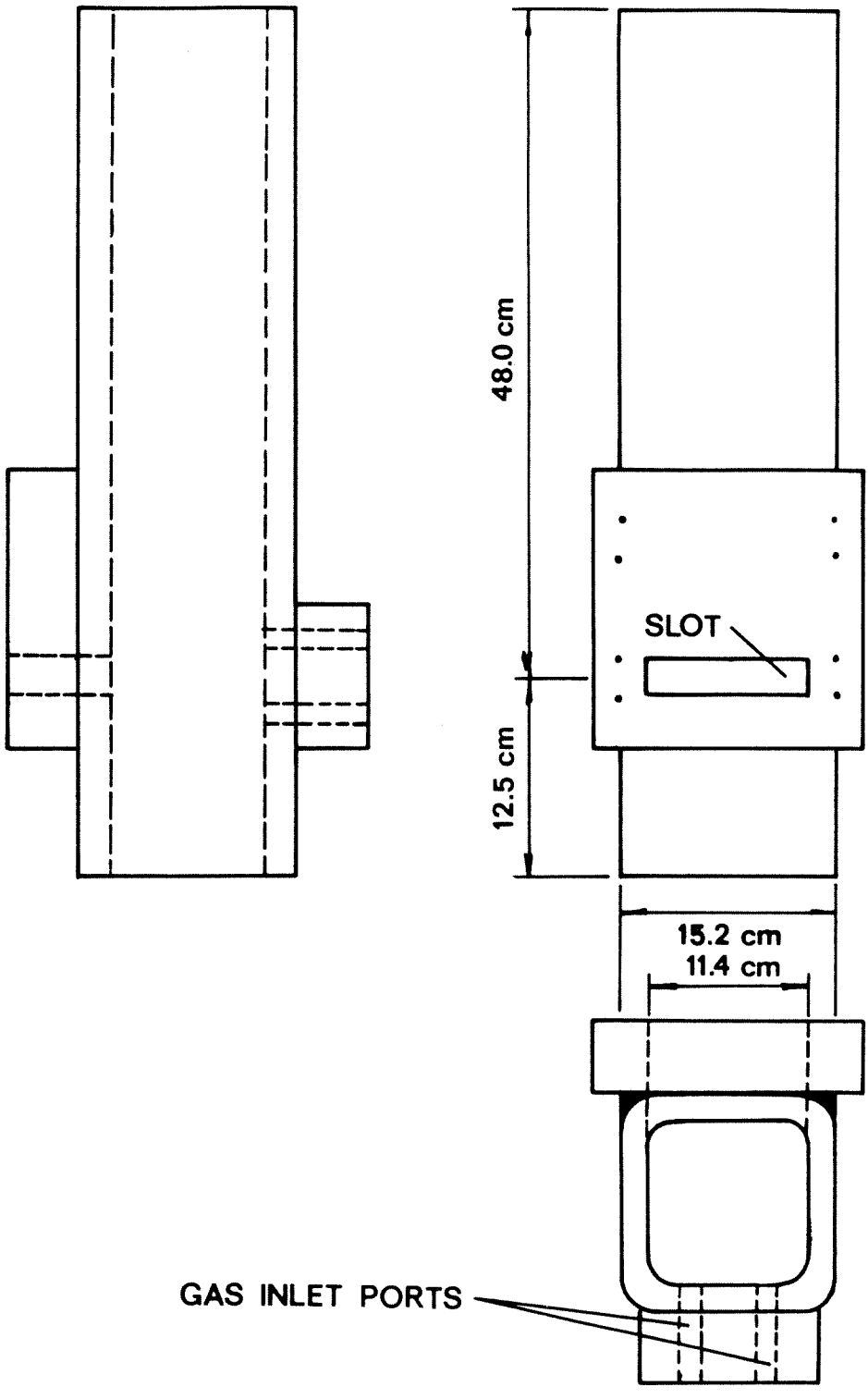

Figure 2.5 Interface section.

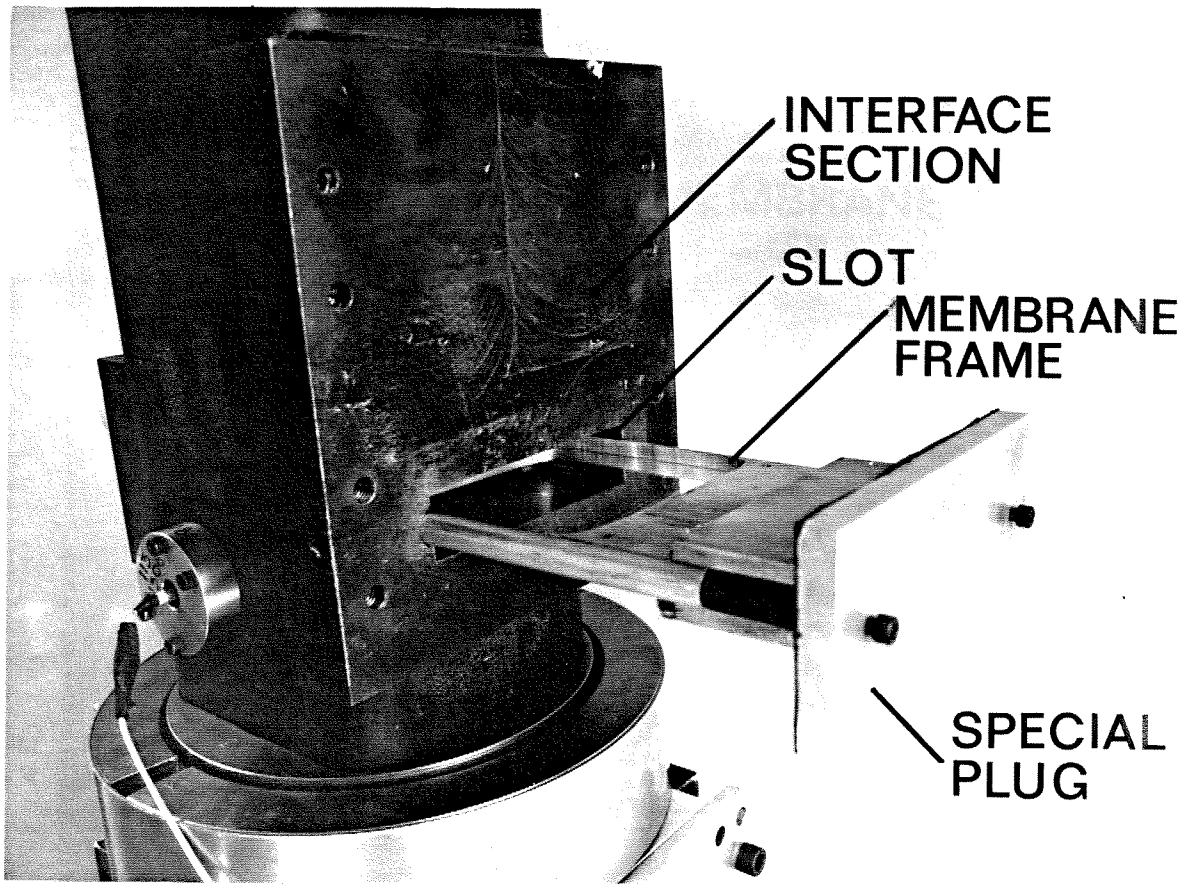

Figure 2.6 Installation of a membrane in interface section.

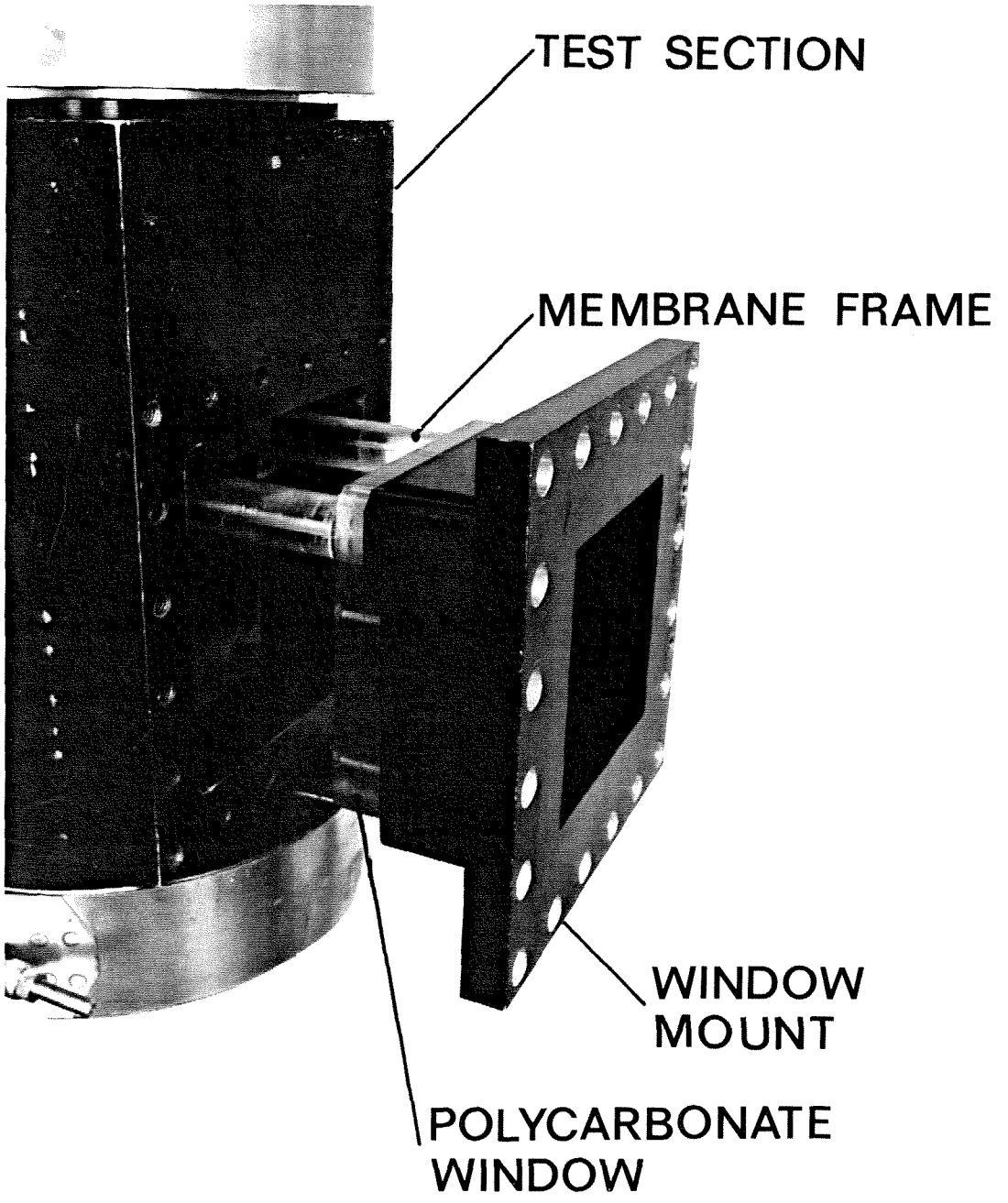

Figure 2.7 Installation of a membrane in test section.

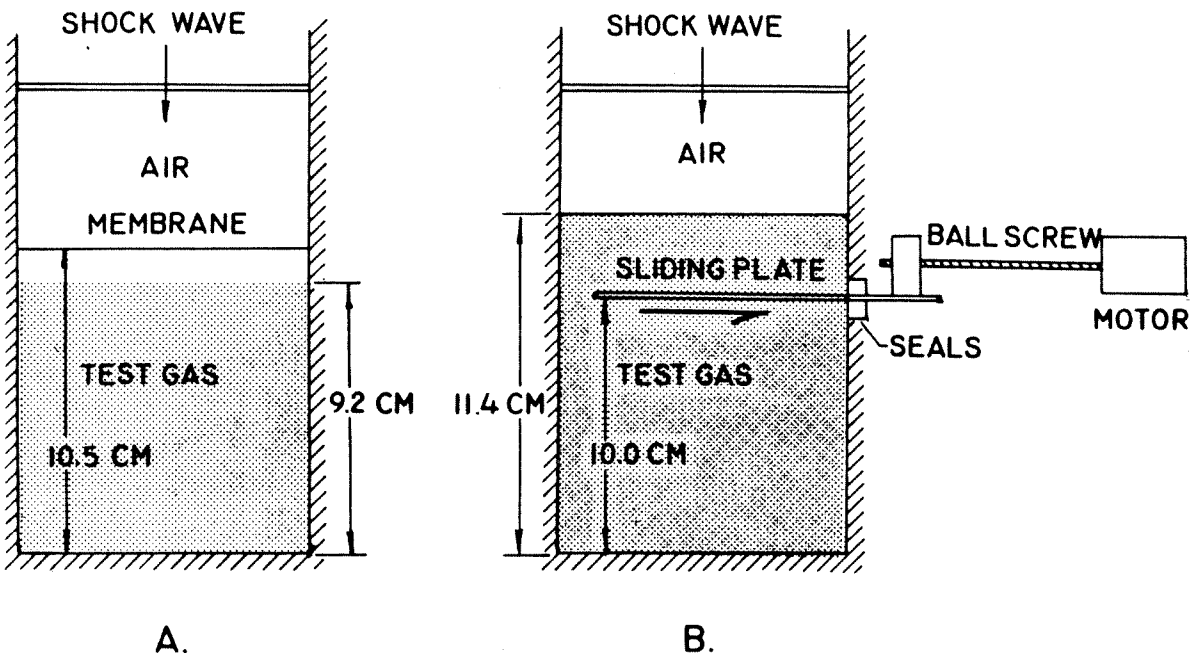

Figure 2.8 Location of interface for close end wall experiments.
The shaded area indicates the field of view of the flow visualization system.

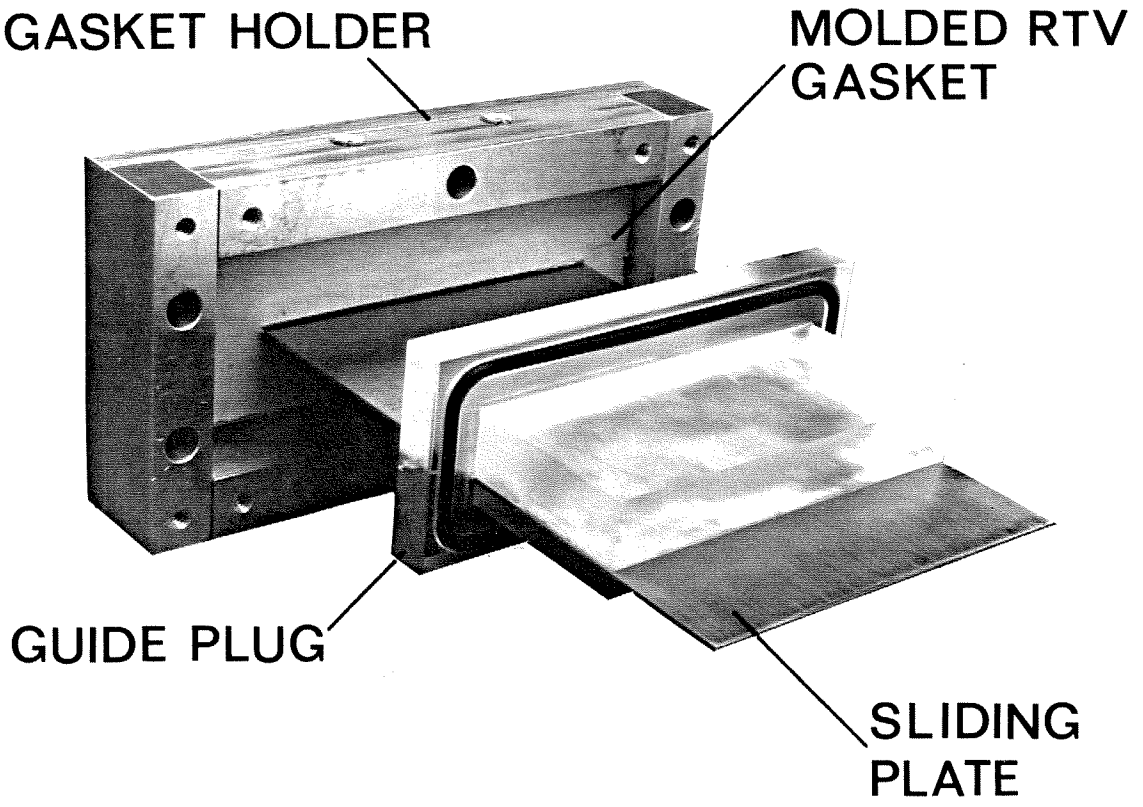

Figure 2.9 Plate seals sub-assembly.

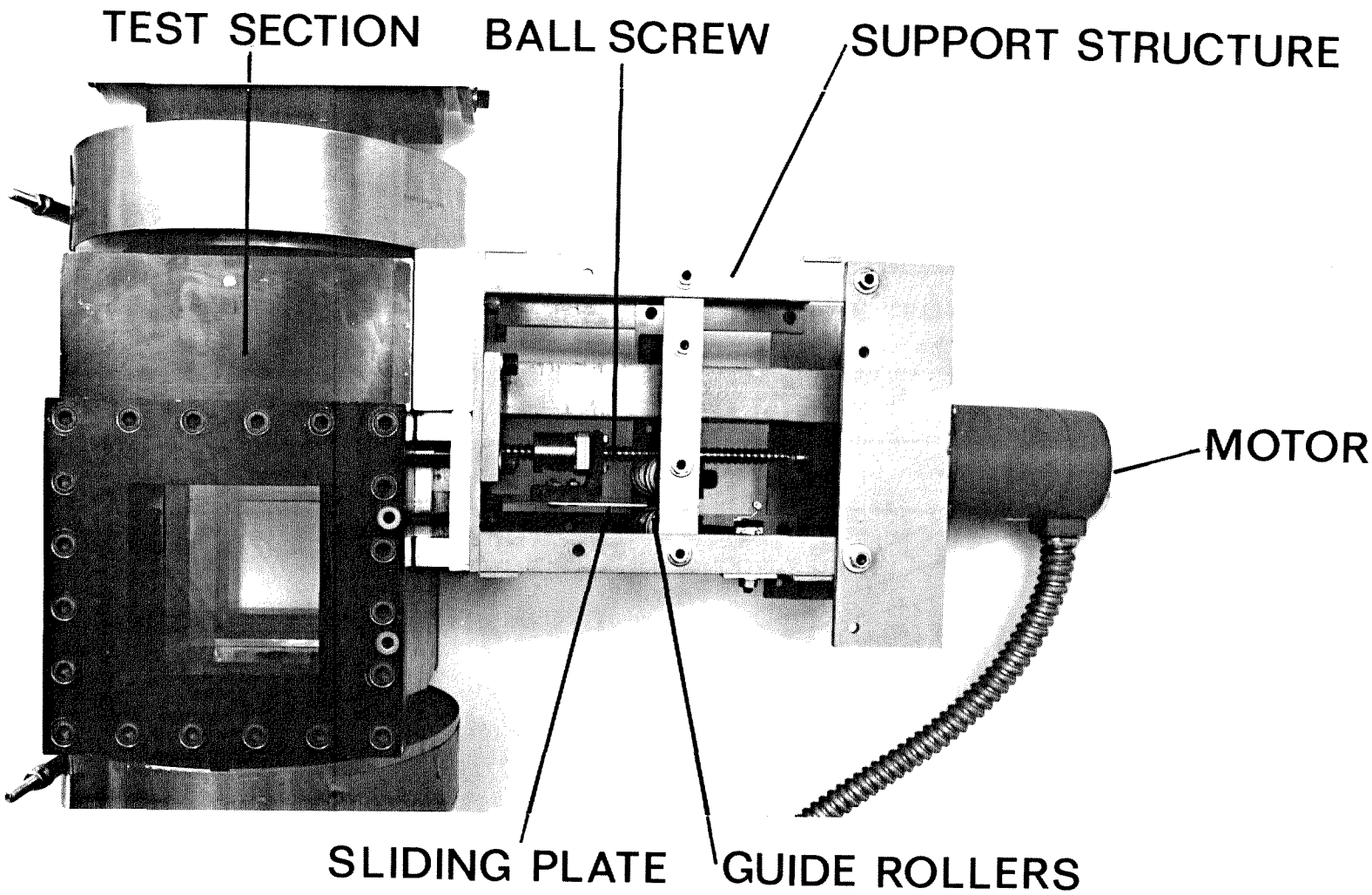

Figure 2.10 Sliding plate mechanism.

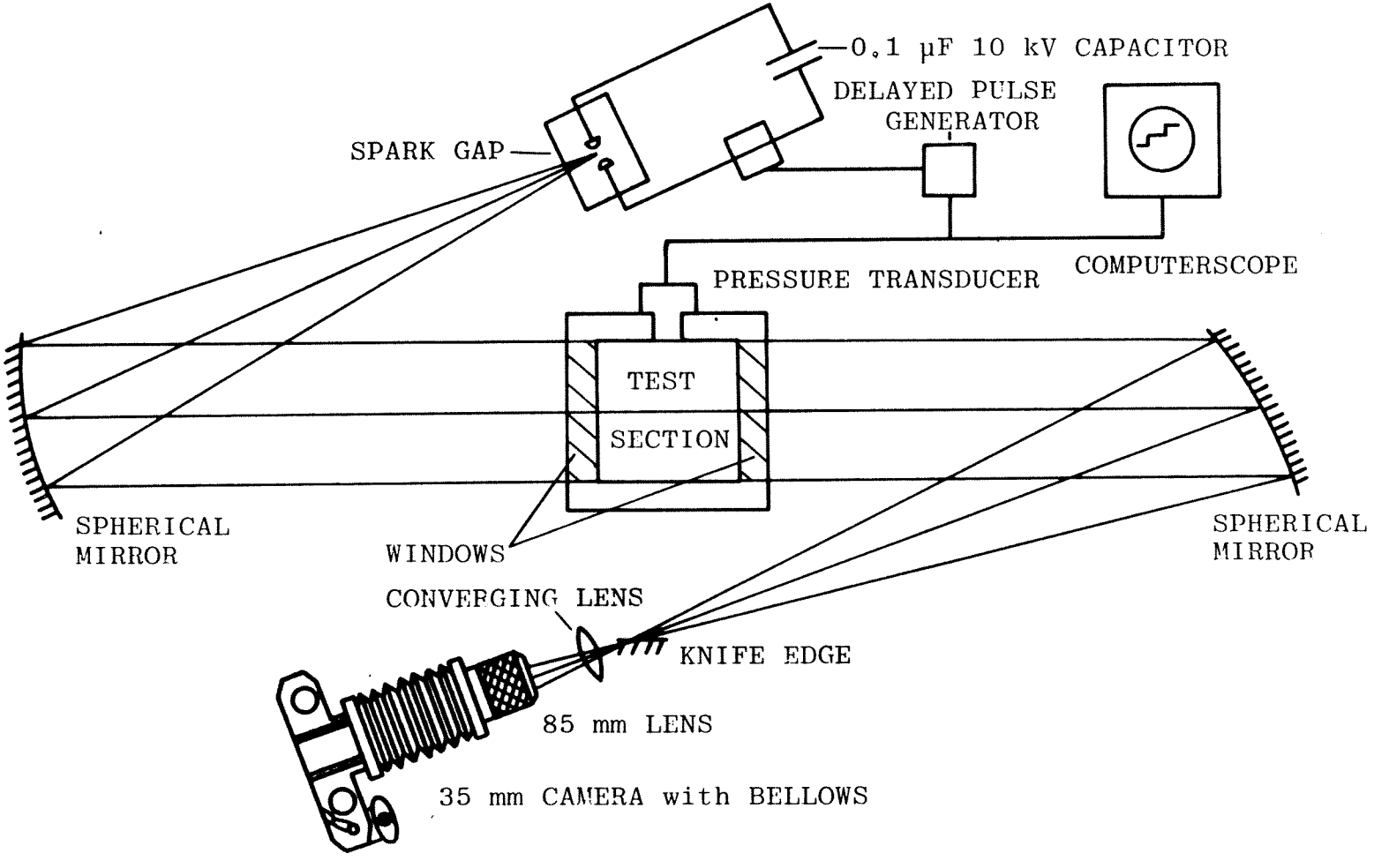

Figure 2.11 Spark schlieren setup.

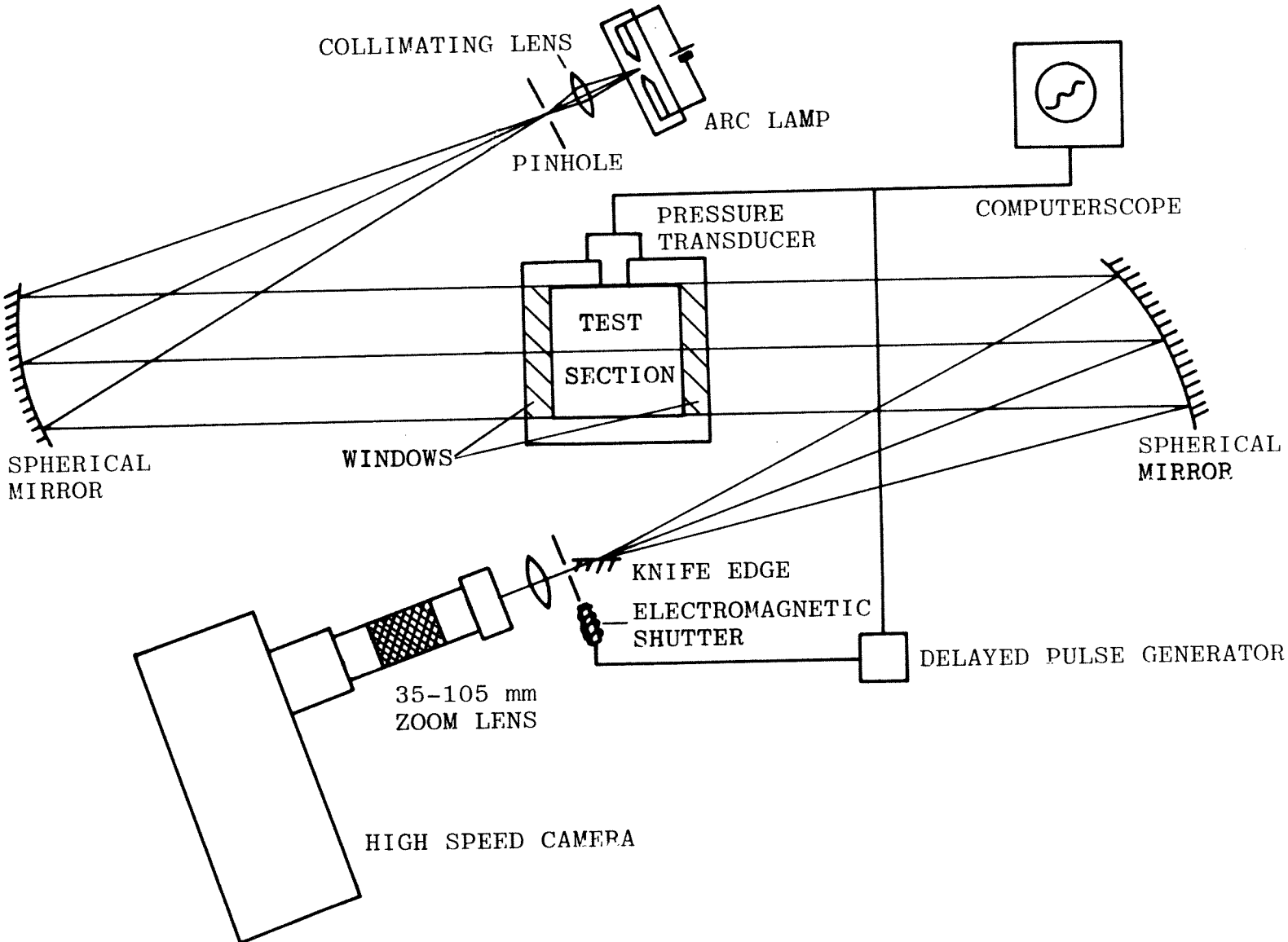

Figure 2.12 High-speed schlieren cinematography setup.

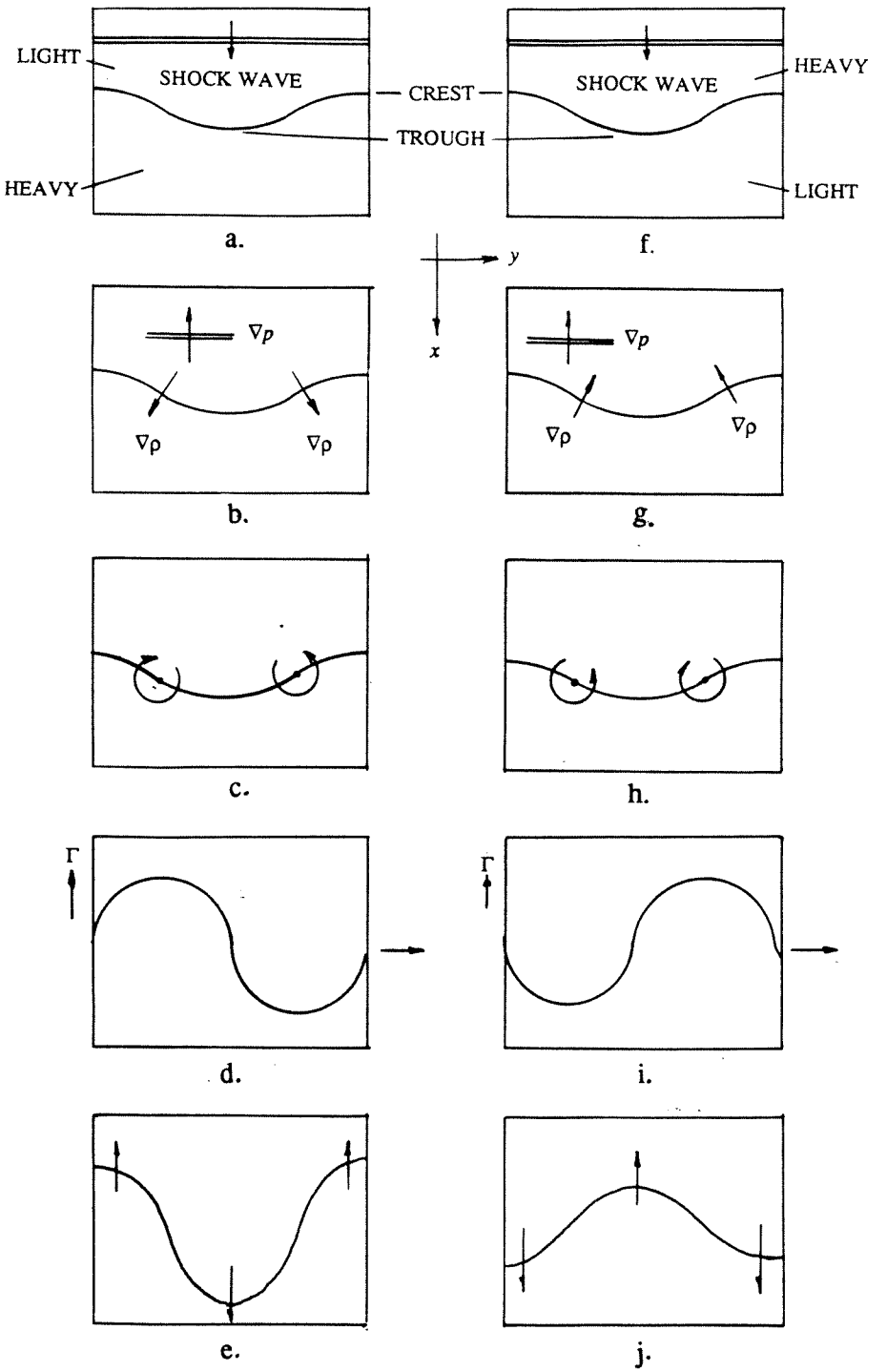

Figure 3.1 Mechanism for the shock-excited instability at an interface between gases of different densities.

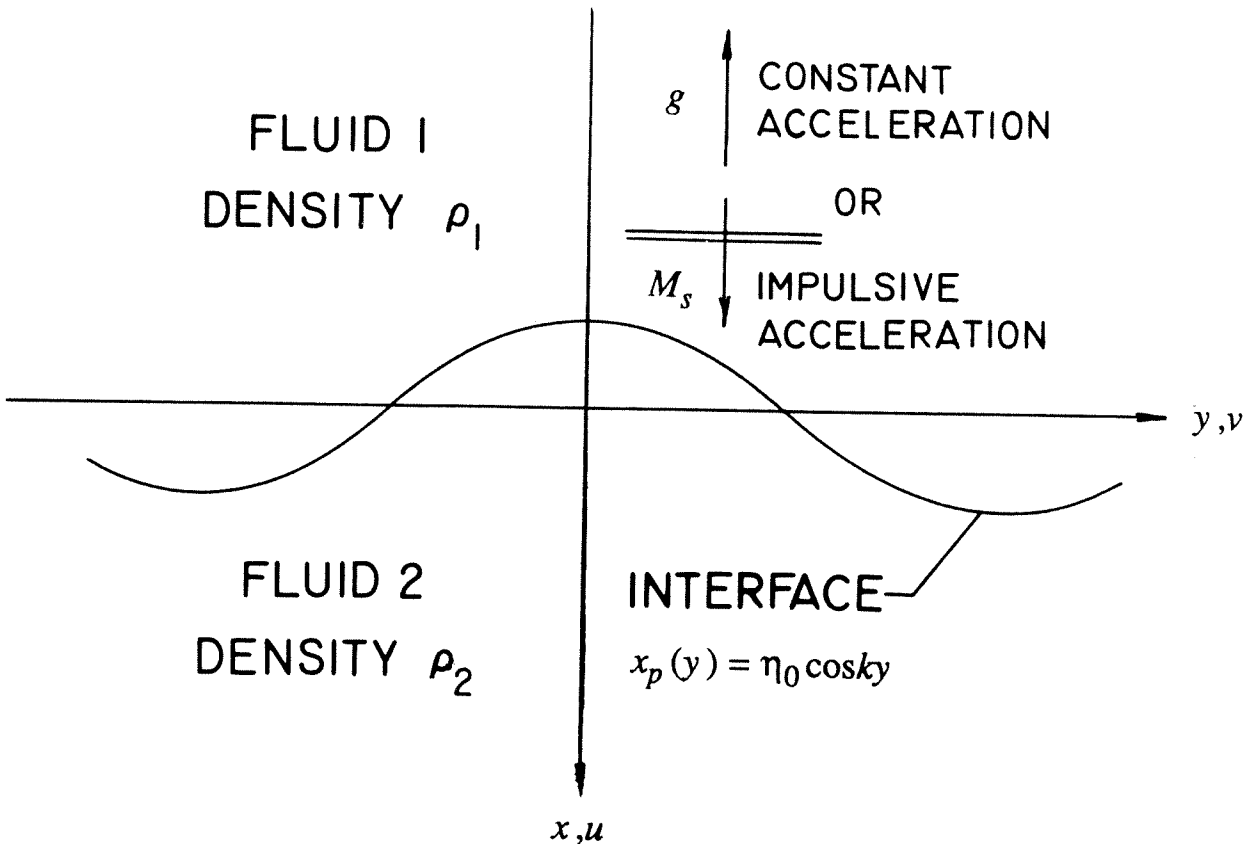

Figure 3.2 Initial configuration for Rayleigh-Taylor and Richtmyer-Meshkov instabilities.

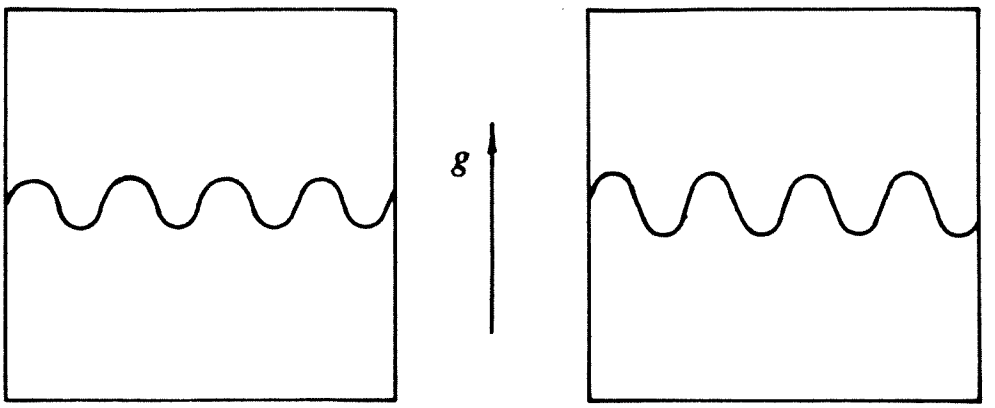

a. Initial configuration.

b. Linear growth.

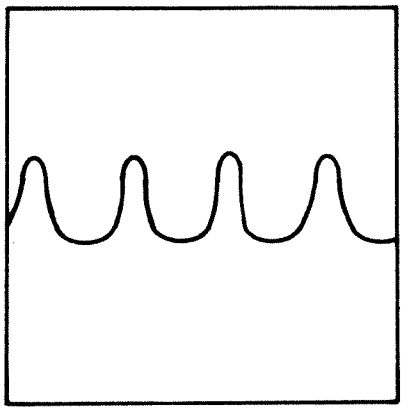

c. Asymmetric development

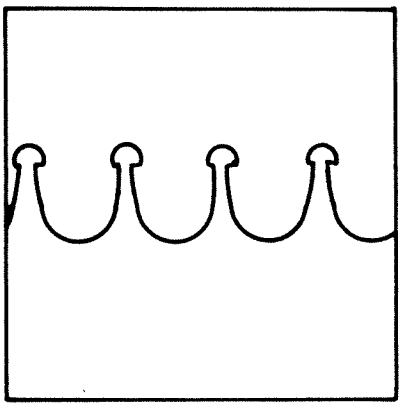

d. Appearance of secondary instabilities.

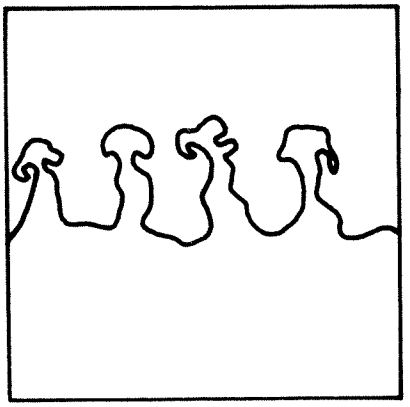

e. Appearance of turbulence.

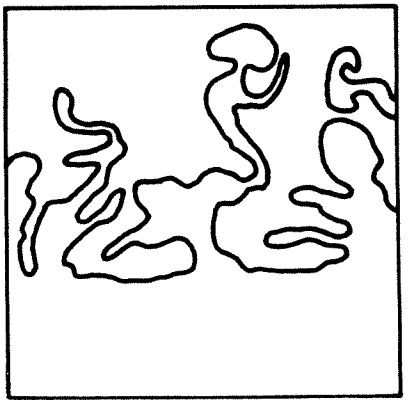

f. Fully developed turbulent mixing layer.

Figure 3.3 Evolution of single-scale perturbations
for Rayleigh-Taylor instability.

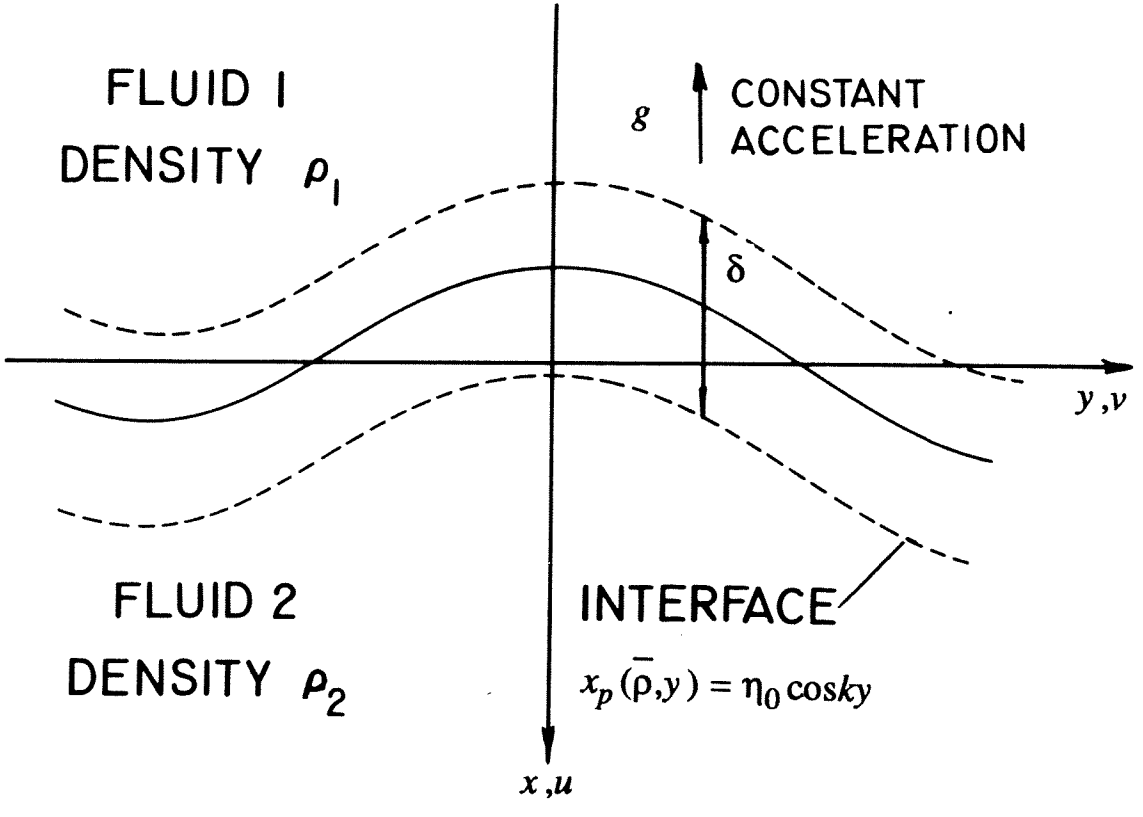

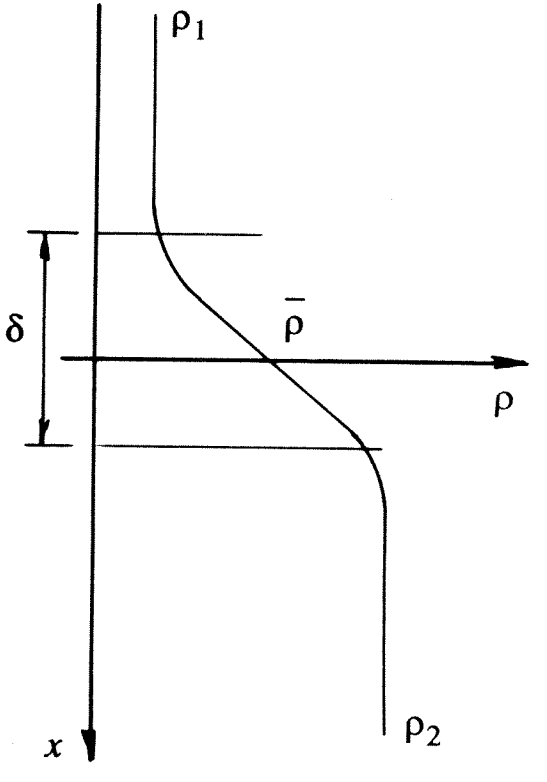

Figure 3.4 Initial configuration for continuous interface.

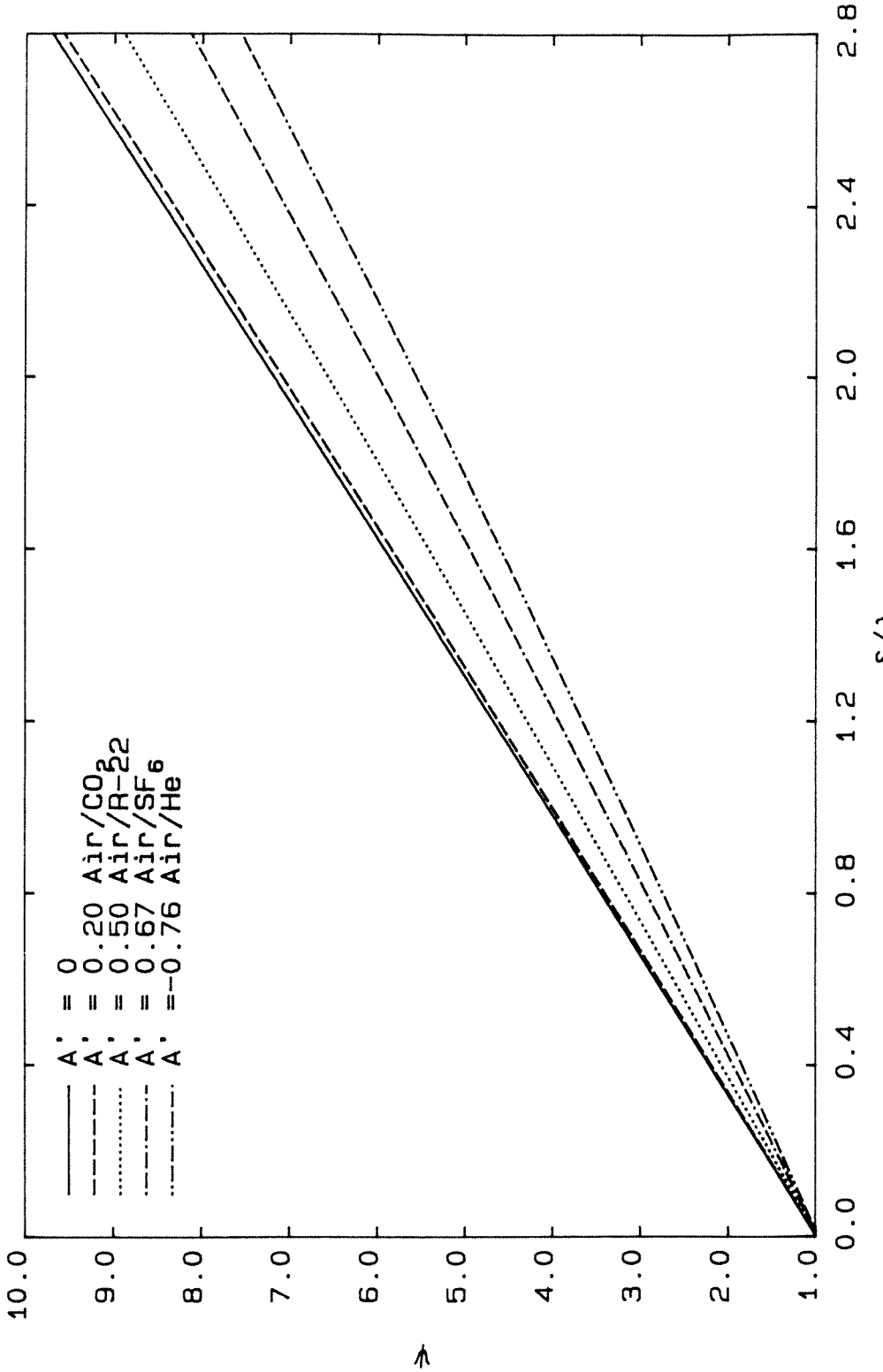

Figure 3.5 Growth reduction factor.

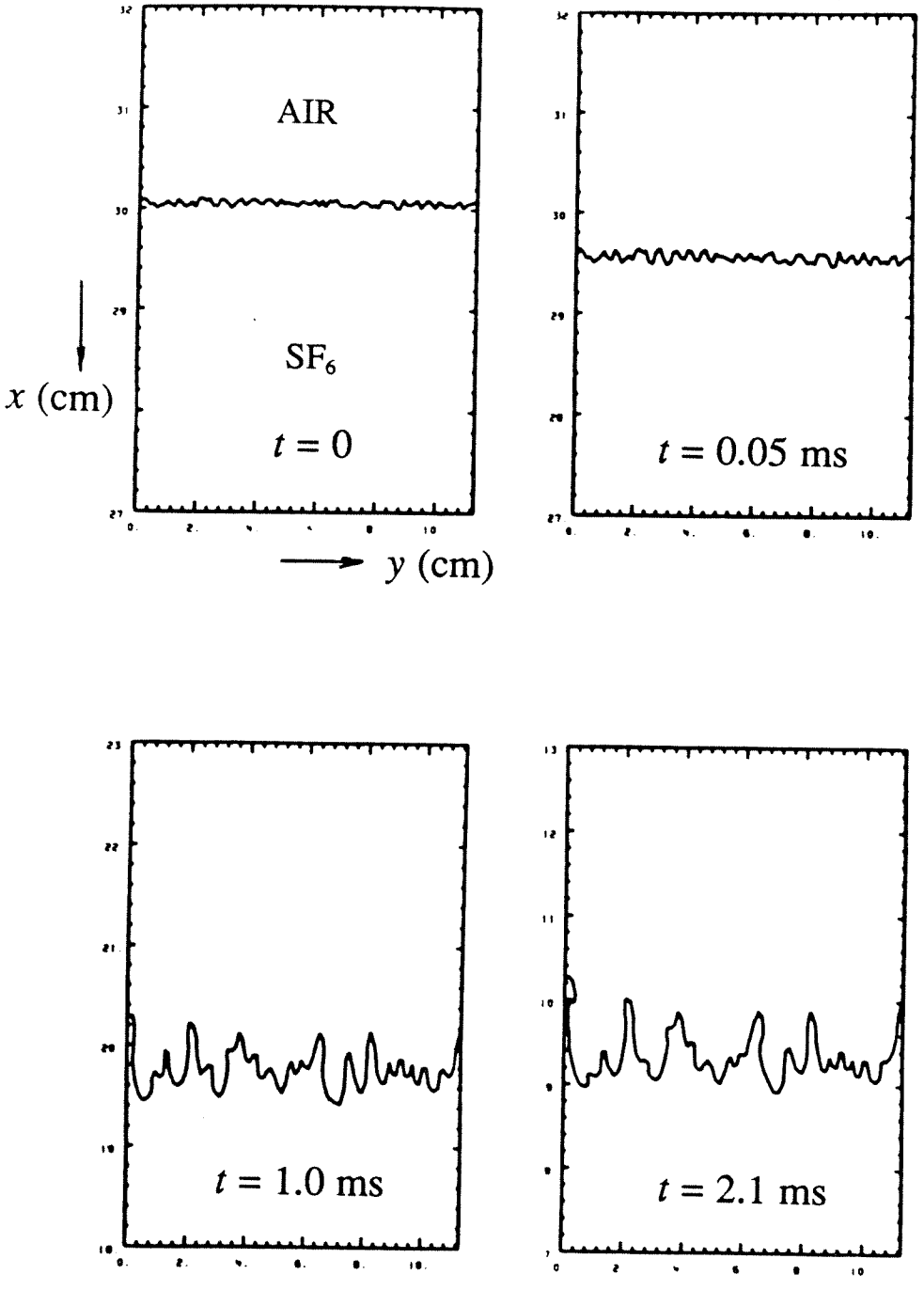

Figure 3.6 Emergence of large scales from random small-scale perturbations (from Mikaelian 1988).

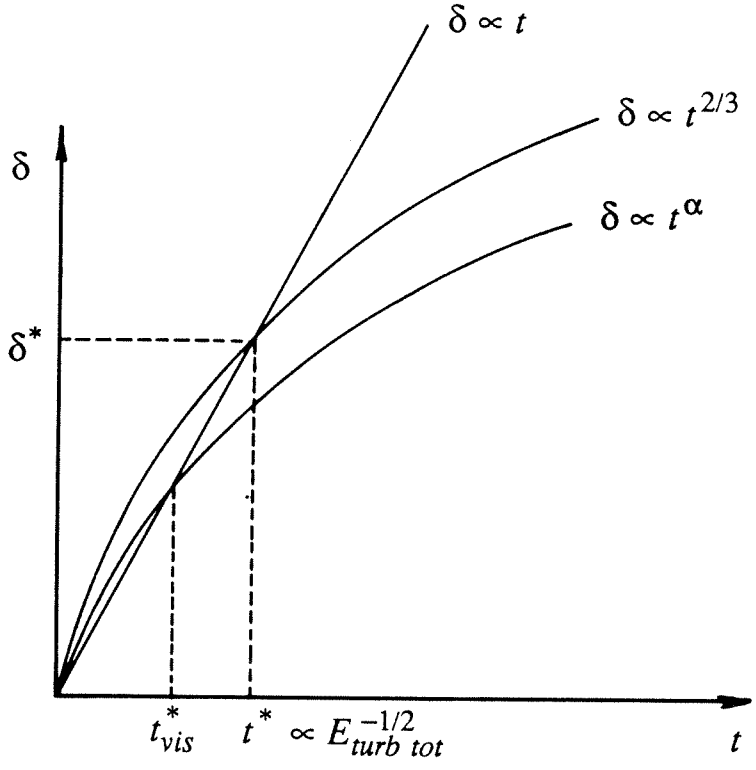

Figure 3.7 Time evolution of the turbulent mixing zone.

a. Interface just after plate retraction.

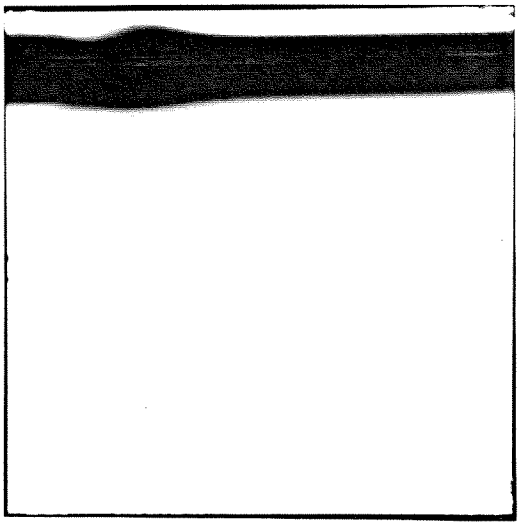

b. Quasi-sinusoidal perturbation on continuous air/SF_6 interface.

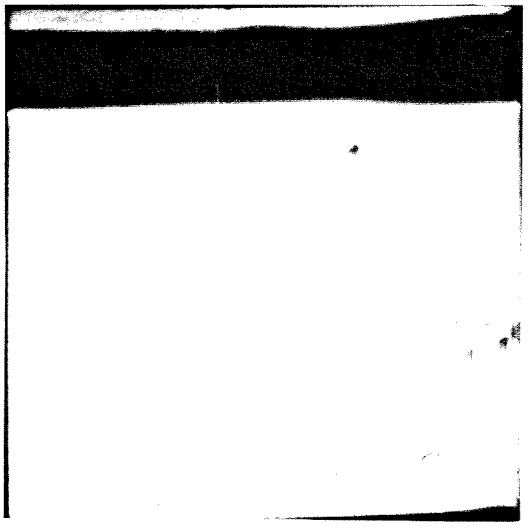

c. Sketch of perturbation.

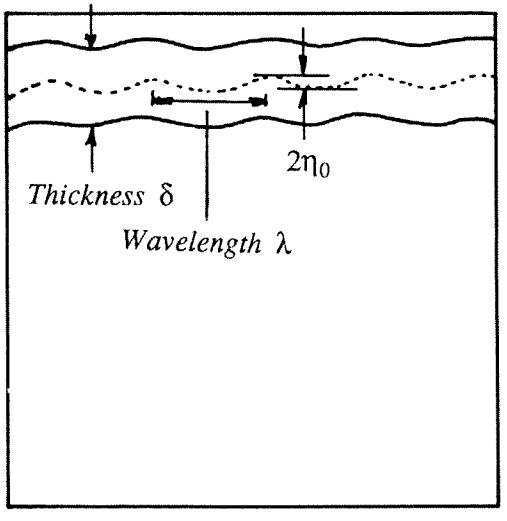

Figure 4.1 Initial conditions at perturbed continuous interface.

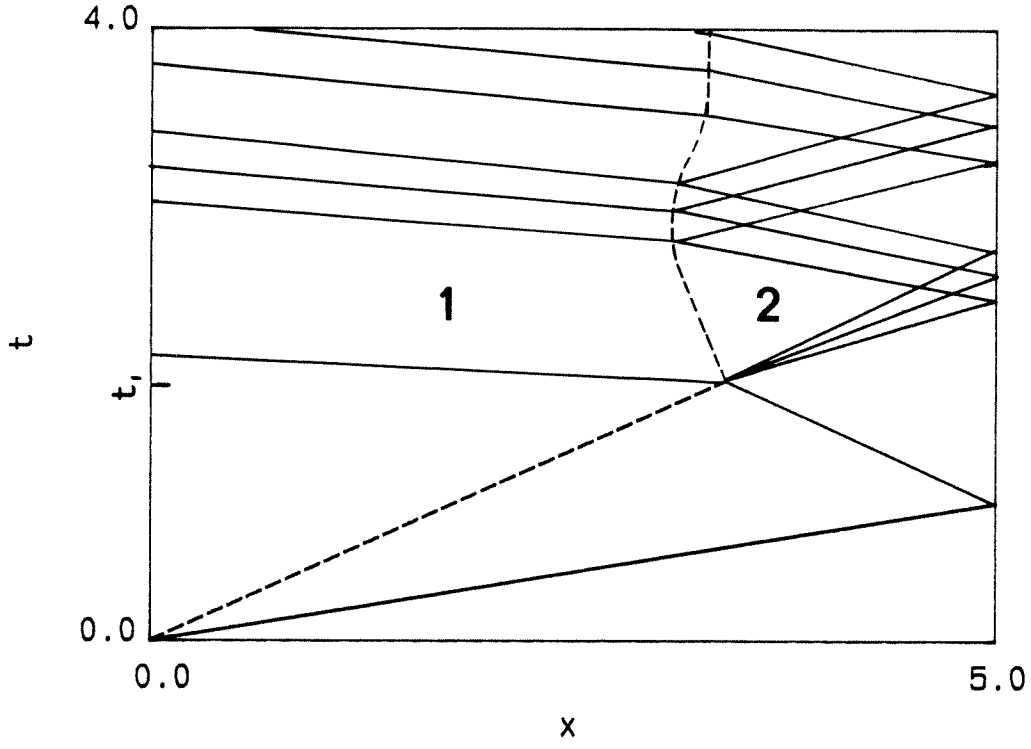

Figure 4.2 Generic $x-t$ diagram for light-heavy interface.
The interface trajectory is indicated by:---.
The wave trajectories are indicated by:— .

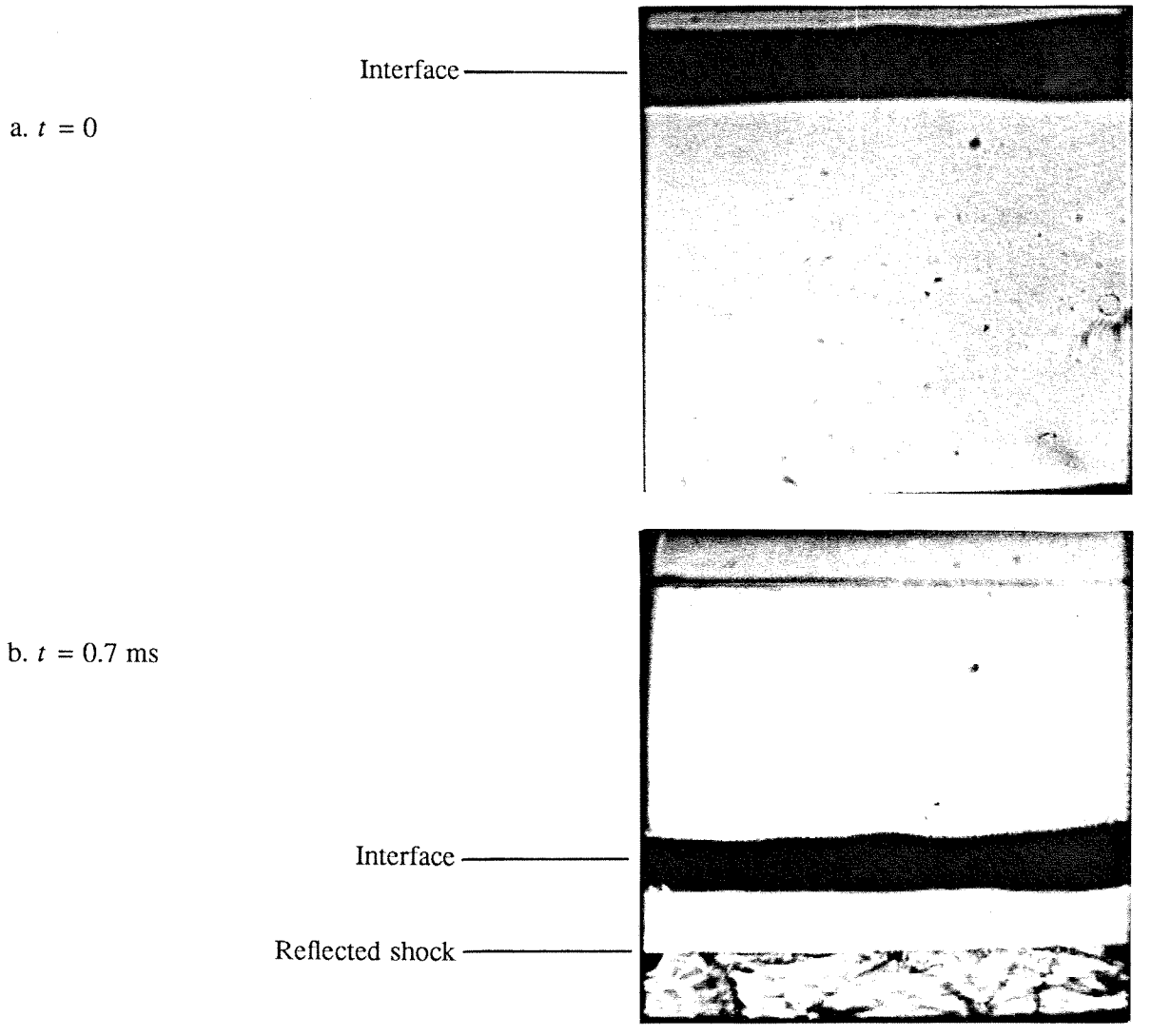

Figure 4.3 Single-scale Richtmyer-Meshkov instability at a continuous interface.
Air/SF_6 M_s = 1.32, close end wall configuration.

a. t = 3.3 ms

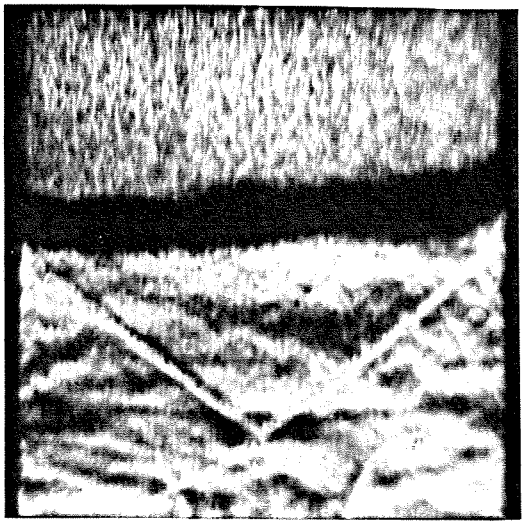

b. t = 4.0 ms

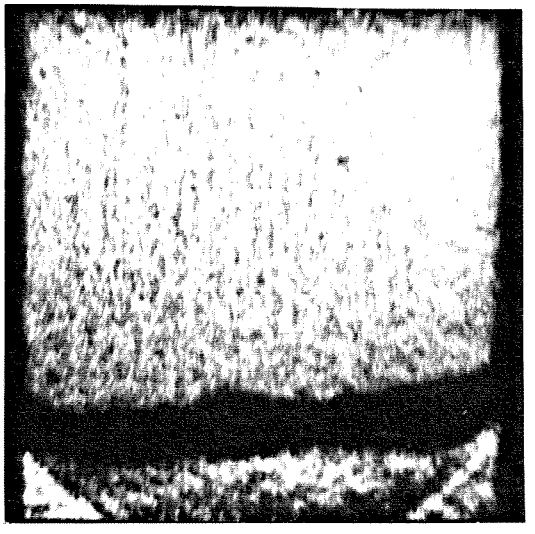

Figure 4.4 Single-scale Richtmyer-Meshkov instability at a continuous interface. Air/SF_6 M_s = 1.32, long time configuration.

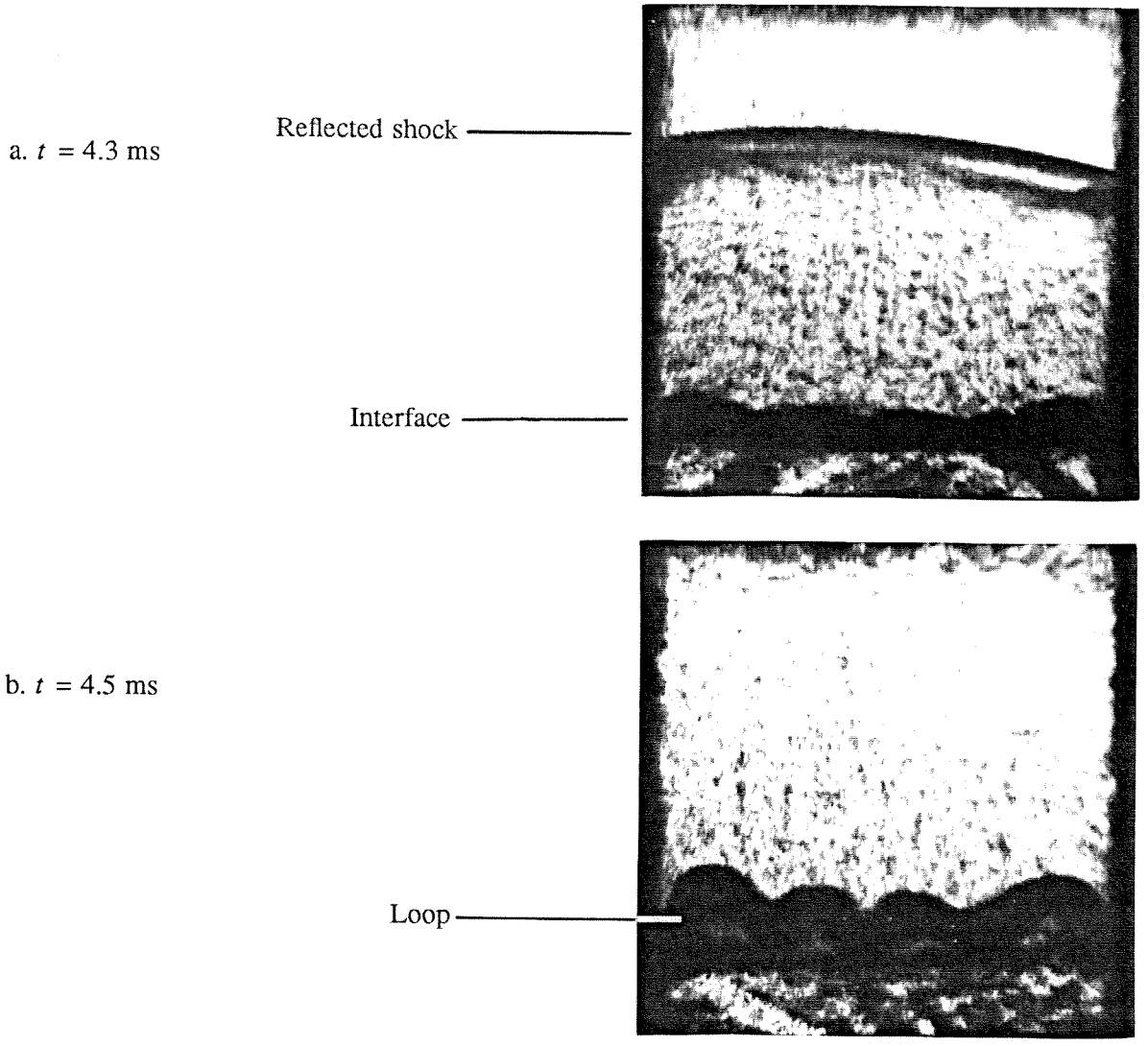

Figure 4.5 Single-scale Richtmyer-Meshkov instability at a continuous interface. Air/SF_6 M_s = 1.32, long time configuration.

c. t = 4.8 ms

d. t = 5.2 ms

Figure 4.5 (continued).

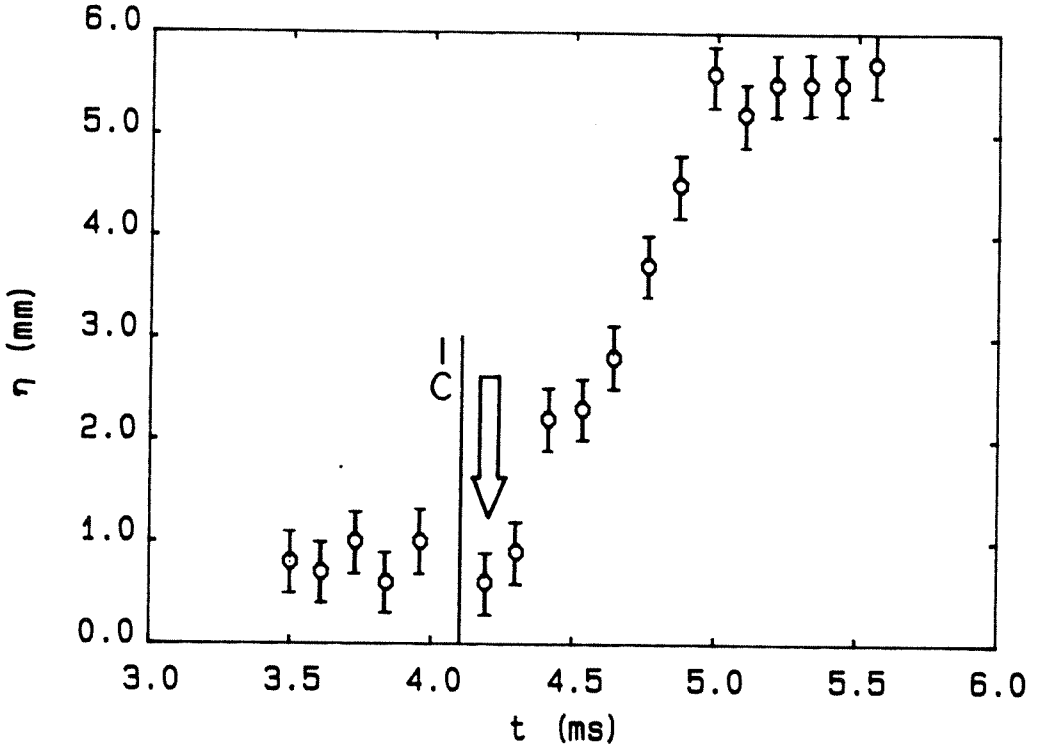

Figure 4.6 Time evolution of a single-scale perturbation on a continuous interface. Air/SF_6 M_s = 1.32, long time configuration.

a. t = 1.0 ms

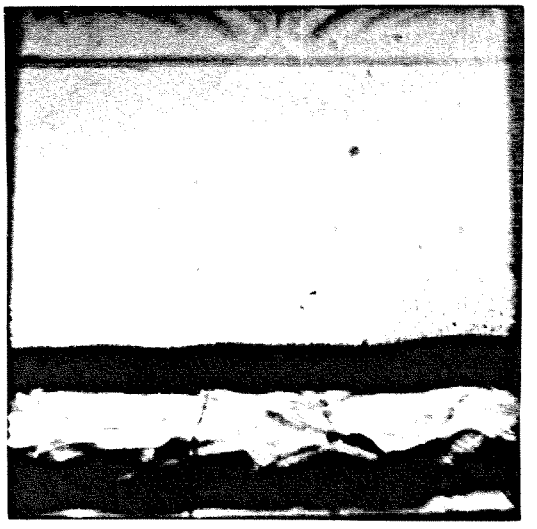

b. t = 1.3 ms

Figure 4.7 Single-scale Richtmyer-Meshkov instability at a continuous interface. Air/SF_6 M_s = 1.32, close end wall configuration.

c. t = 1.5 ms

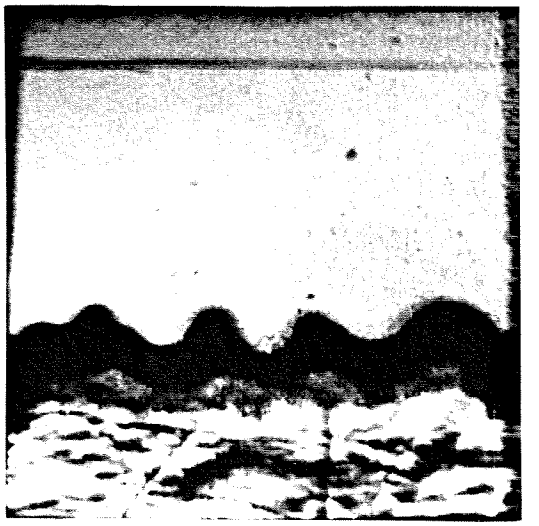

d. t = 1.7 ms

Figure 4.7 (continued).

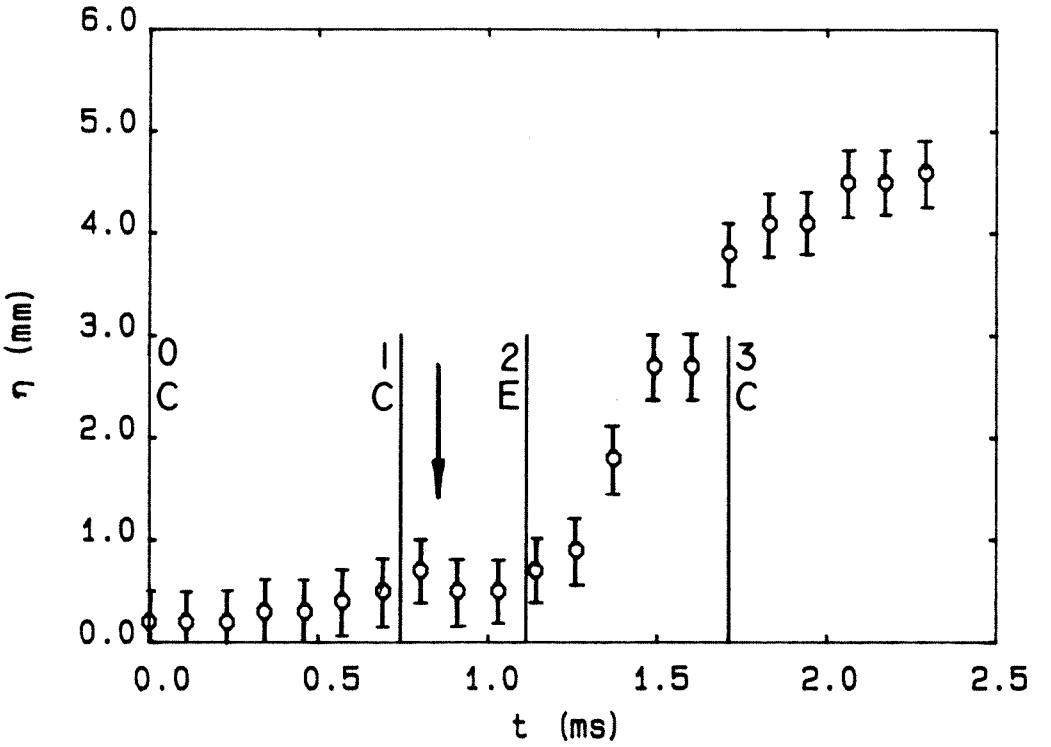

Figure 4.8 Time evolution of a single-scale perturbation on a continuous interface. Air/SF_6 M_s = 1.32, close end wall configuration.

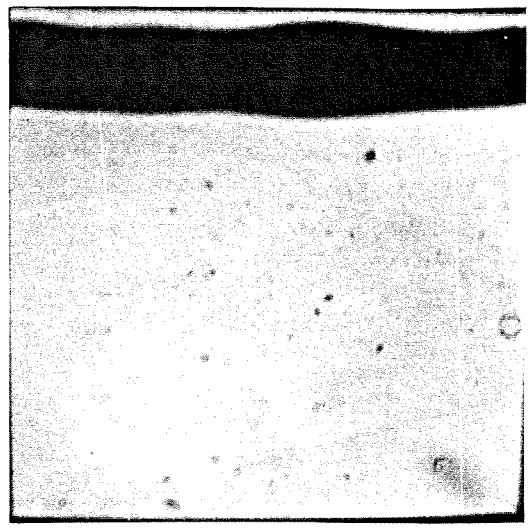

Figure 4.9 Initial single-scale perturbation on an air/R-22 interface.

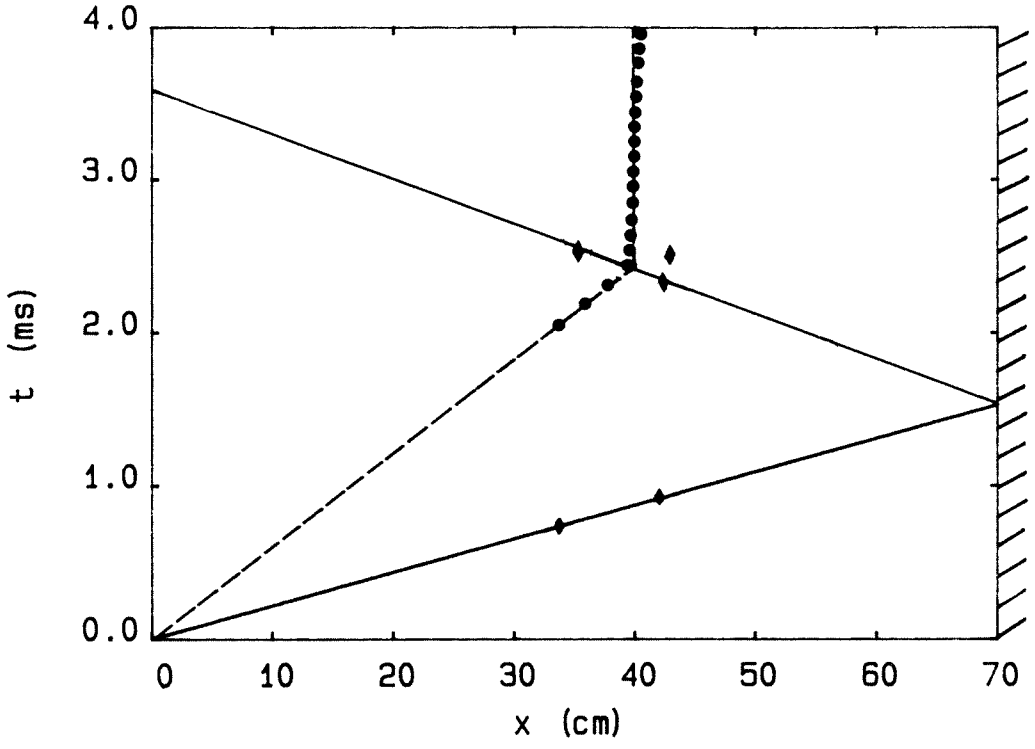

Figure 5.1 Wave diagram for the interaction of a M_s = 1.32 shock wave with a nitrocellulose membrane, long time configuration. The interface trajectory is indicated by: ---- theory, ● experiment. The wave trajectories are indicated by: —— theory, ◆ experiment.

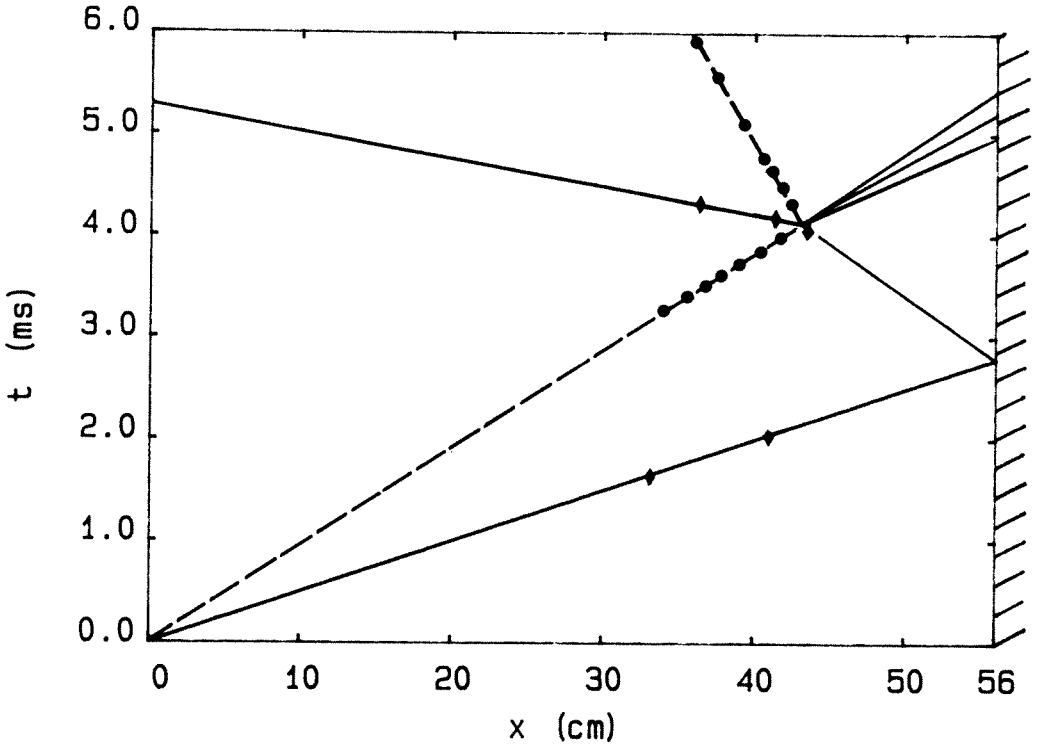

Figure 5.2 Wave diagram for the interaction of a M_s = 1.32 shock wave with a plane discontinuous interface between air and SF_6, long time configuration.
The interface trajectory is indicated by:--- theory, ● experiment.
The wave trajectories are indicated by: —— theory, ◆ experiment.

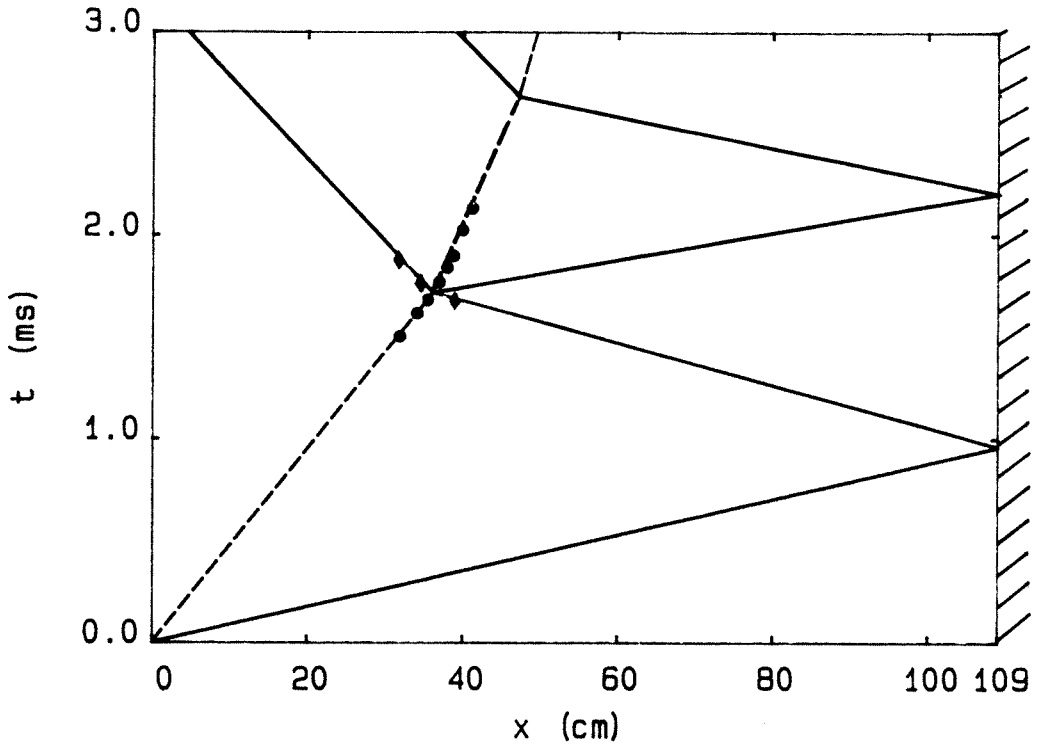

Figure 5.3 Wave diagram for the interaction of a M_s = 1.32 shock wave with a plane discontinuous interface between air and helium, long time configuration.
The interface trajectory is indicated by:--- theory, ● experiment.
The wave trajectories are indicated by:—— theory, ◆ experiment.

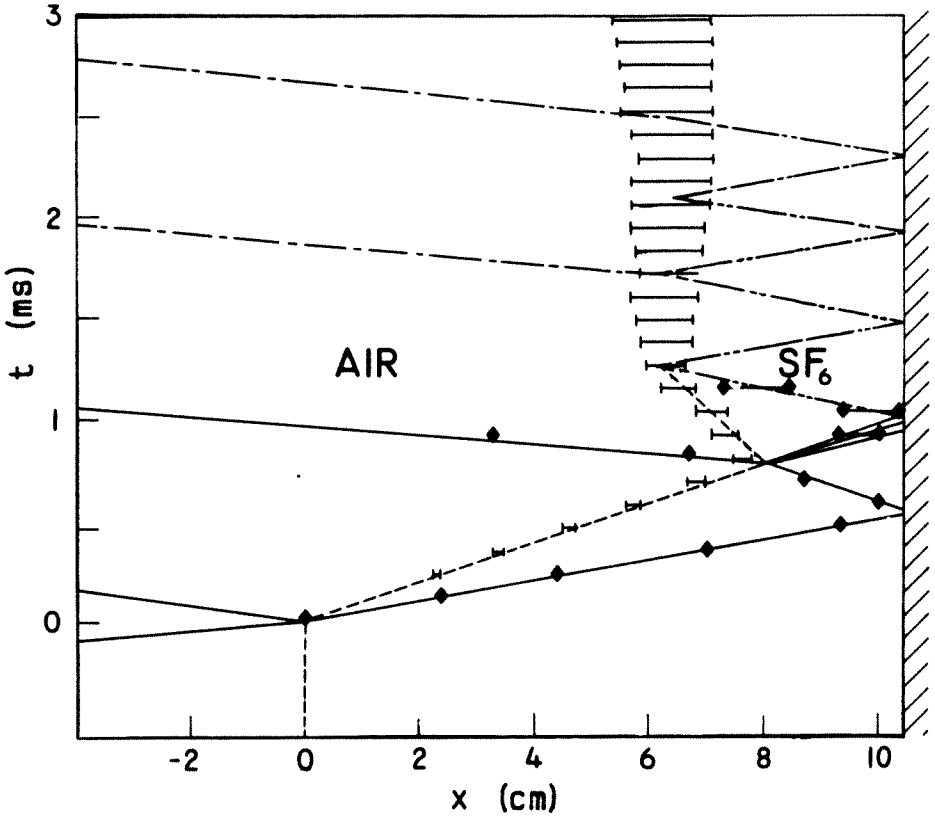

Figure 5.4 Wave diagram for the interaction of a M_s = 1.32 shock wave with a plane discontinuous interface between air and SF_6, close end wall configuration.
The interface trajectory is indicated by: — — theory, ⟷ experiment.
The wave trajectories are indicated by: —— theory, —·— ◆ experiment, — — deduced.

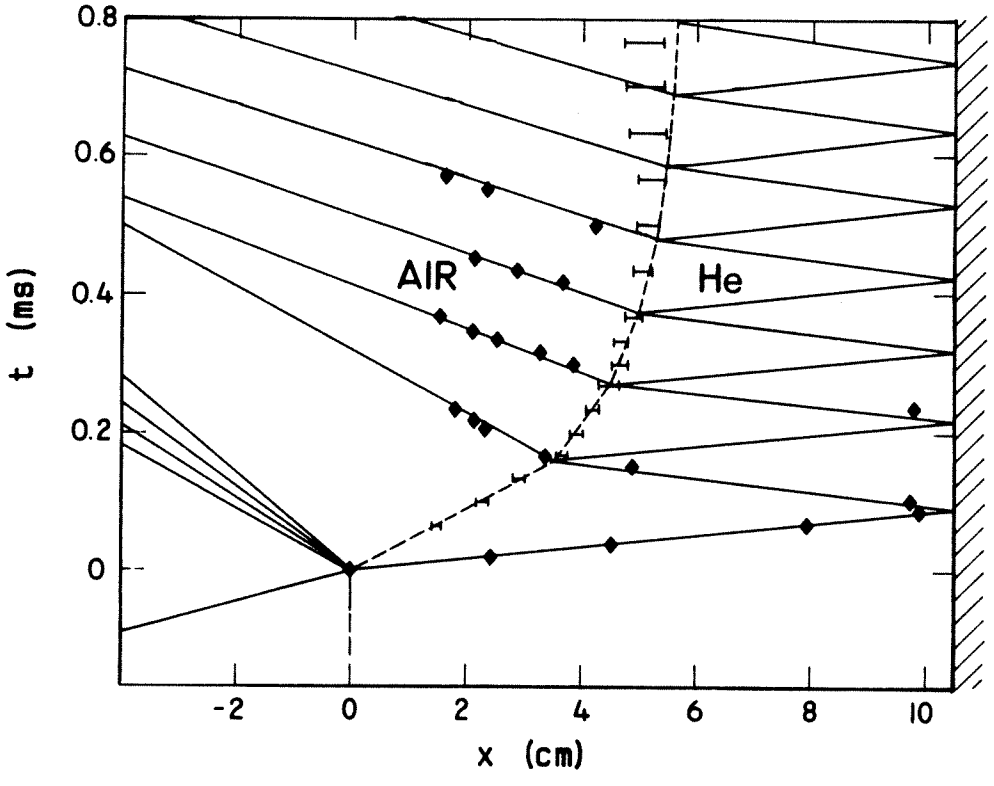

Figure **5.5** Wave diagram for the interaction of a M_s = 1.30 shock wave with a plane discontinuous interface between air and helium, close end wall configuration.
The interface trajectory is indicated by: - - - theory, ⟷ experiment.
The wave trajectories are indicated by: — theory, ◆ experiment.

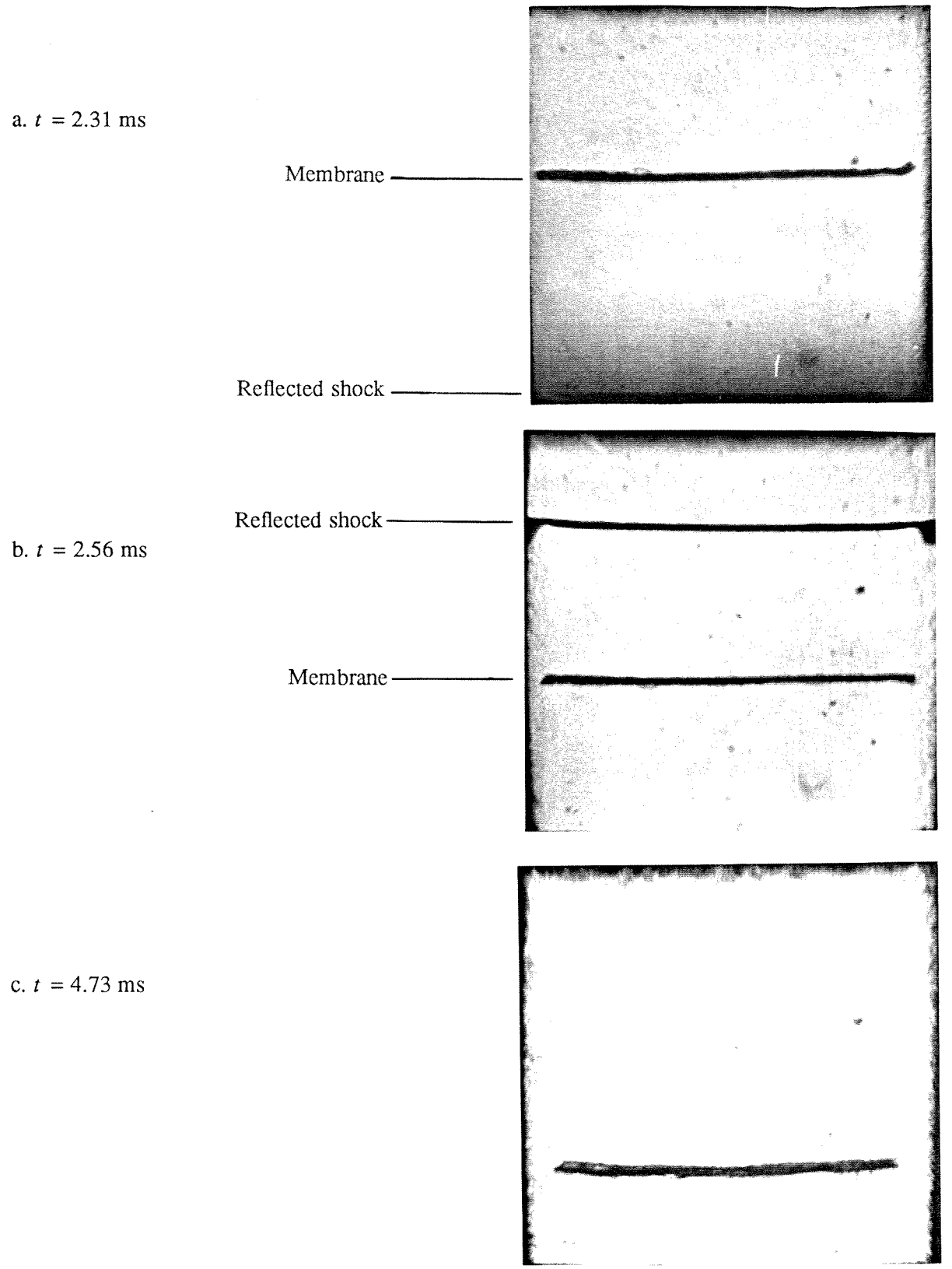

Figure 5.6 Interaction of a nitrocellulose membrane with a M_s = 1.32 shock wave, long time configuration.

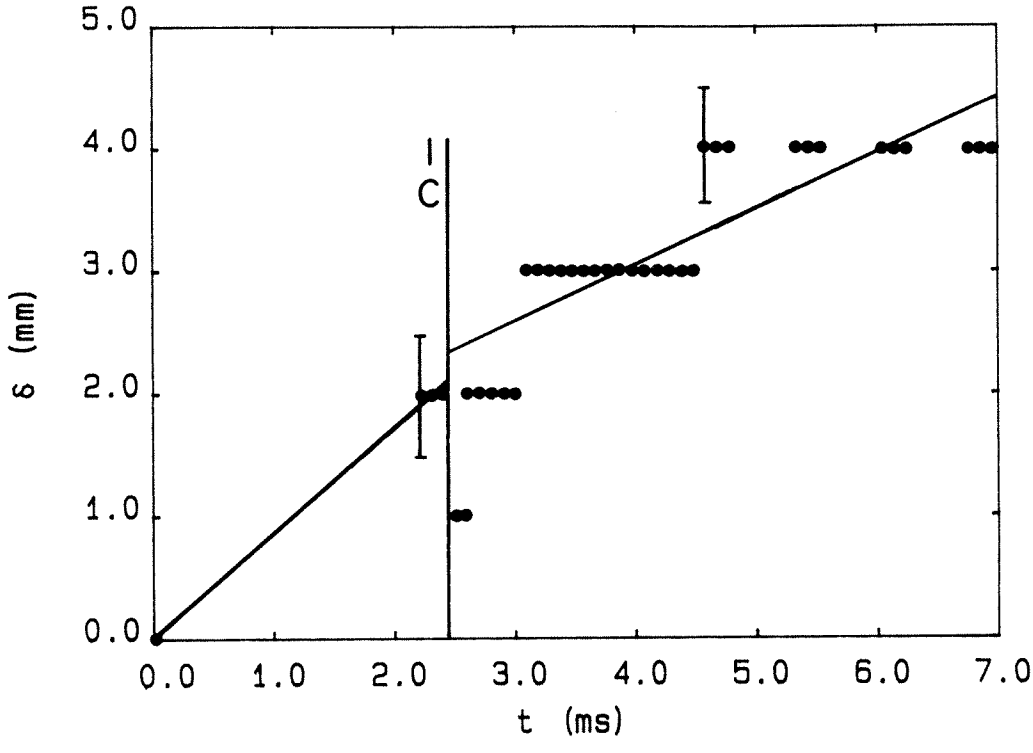

Figure **5.7** Time evolution of the thickness of the interface region formed by the distorted membrane. M_s = 1.32, long time configuration.

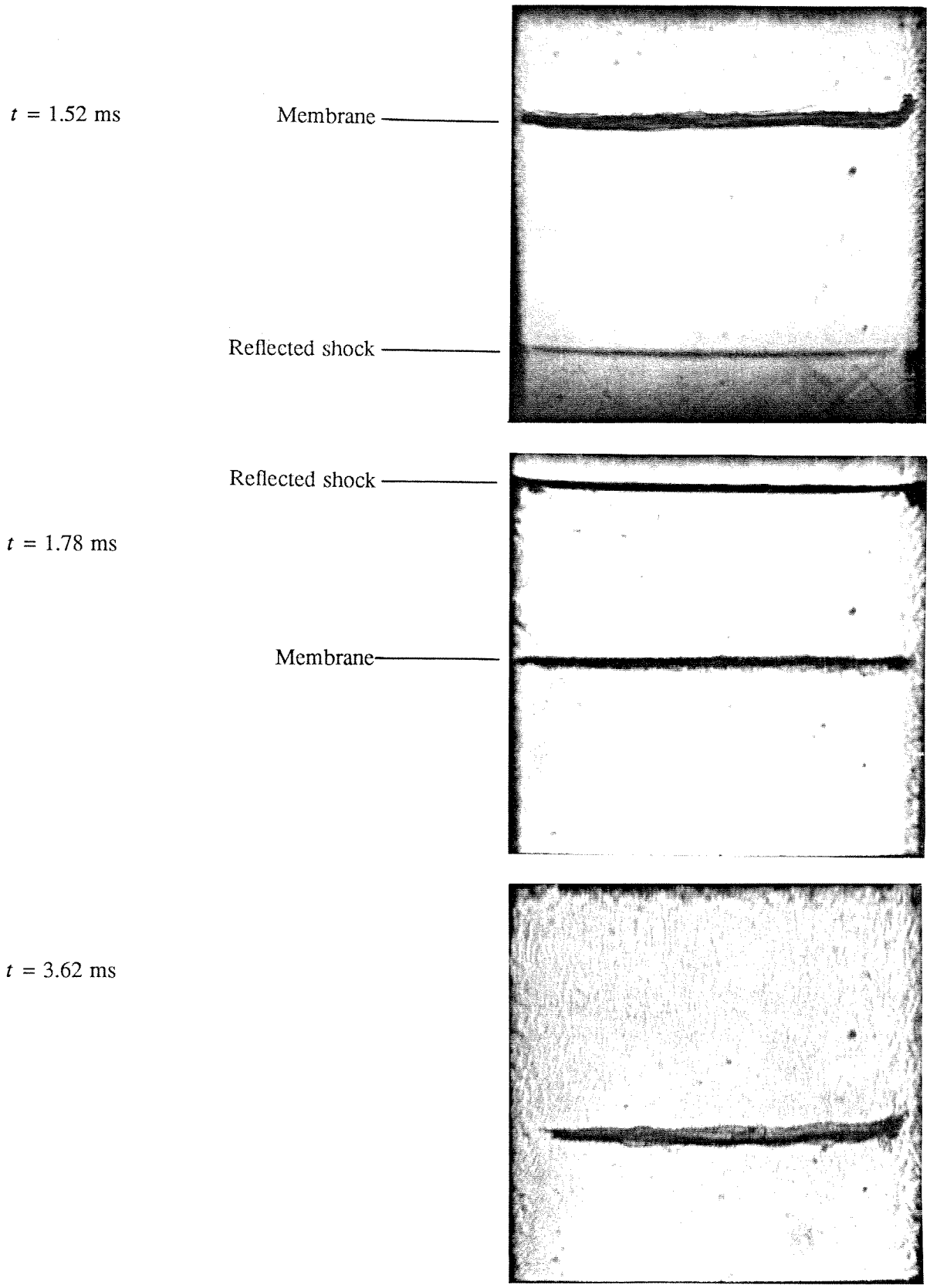

Figure **5.8**a Interaction of a nitrocellulose membrane with a M_s = 1.48 shock wave, long time configuration.

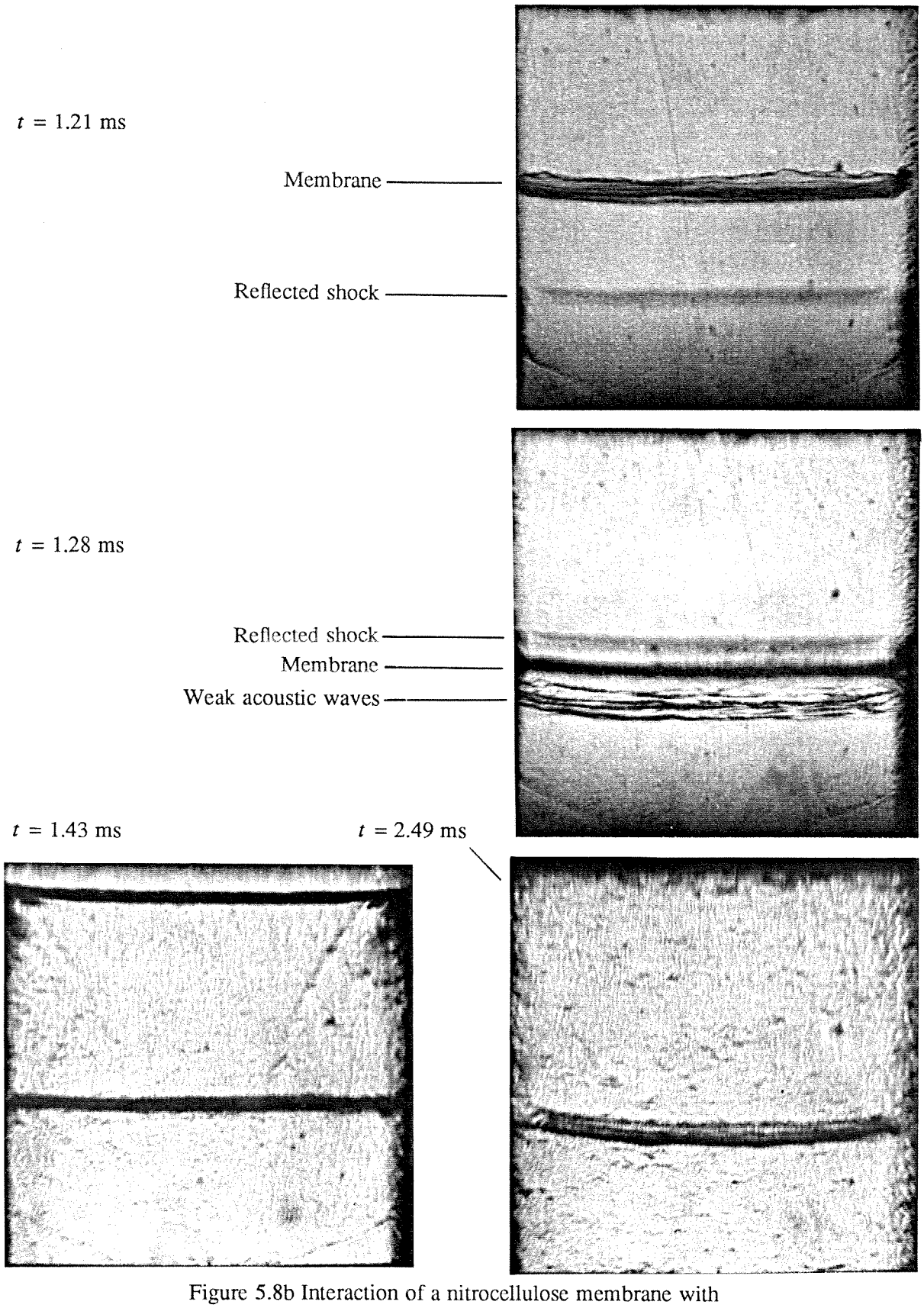

Figure 5.8b Interaction of a nitrocellulose membrane with a M_s = 1.66 shock wave, long time configuration.

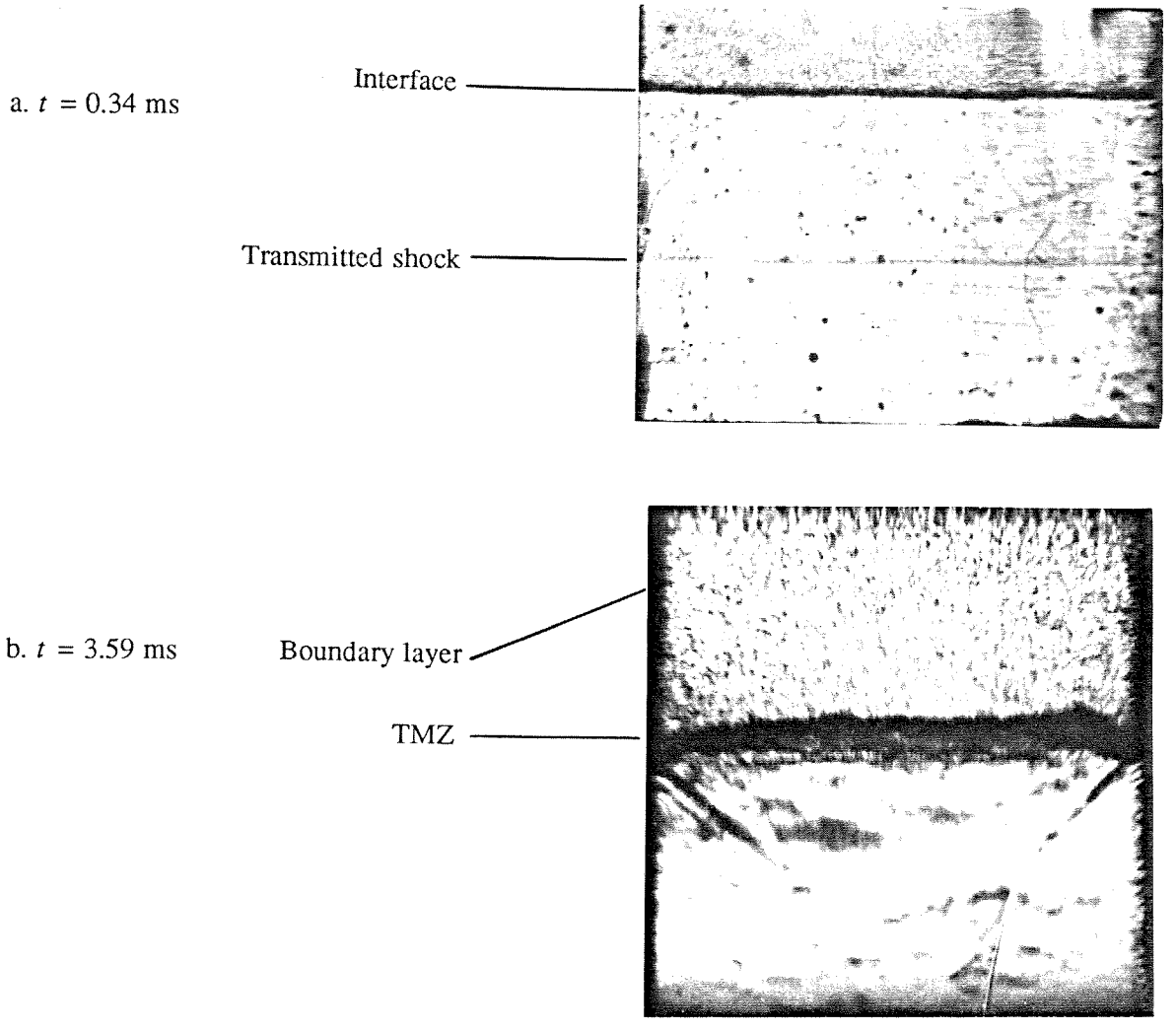

Figure 5.9 Richtmyer-Meshkov instability of a plane discontinuous interface between air and SF_6. M_s = 1.32, close end wall and long time configurations.

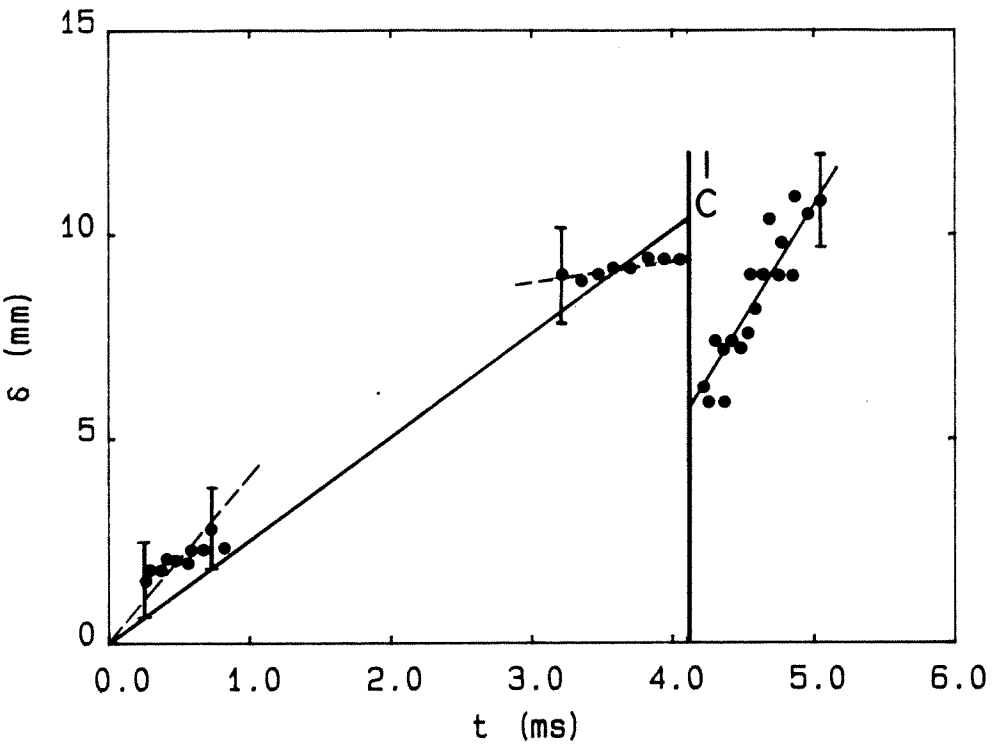

Figure 5.10 Time evolution of the thickness of the TMZ for the plane discontinuous interface between air and SF_6. M_s = 1.32, close end wall and long time configurations. ——: average incident shock growth, reshock growth. – – –: upper bound to early time growth, local incident shock growth.

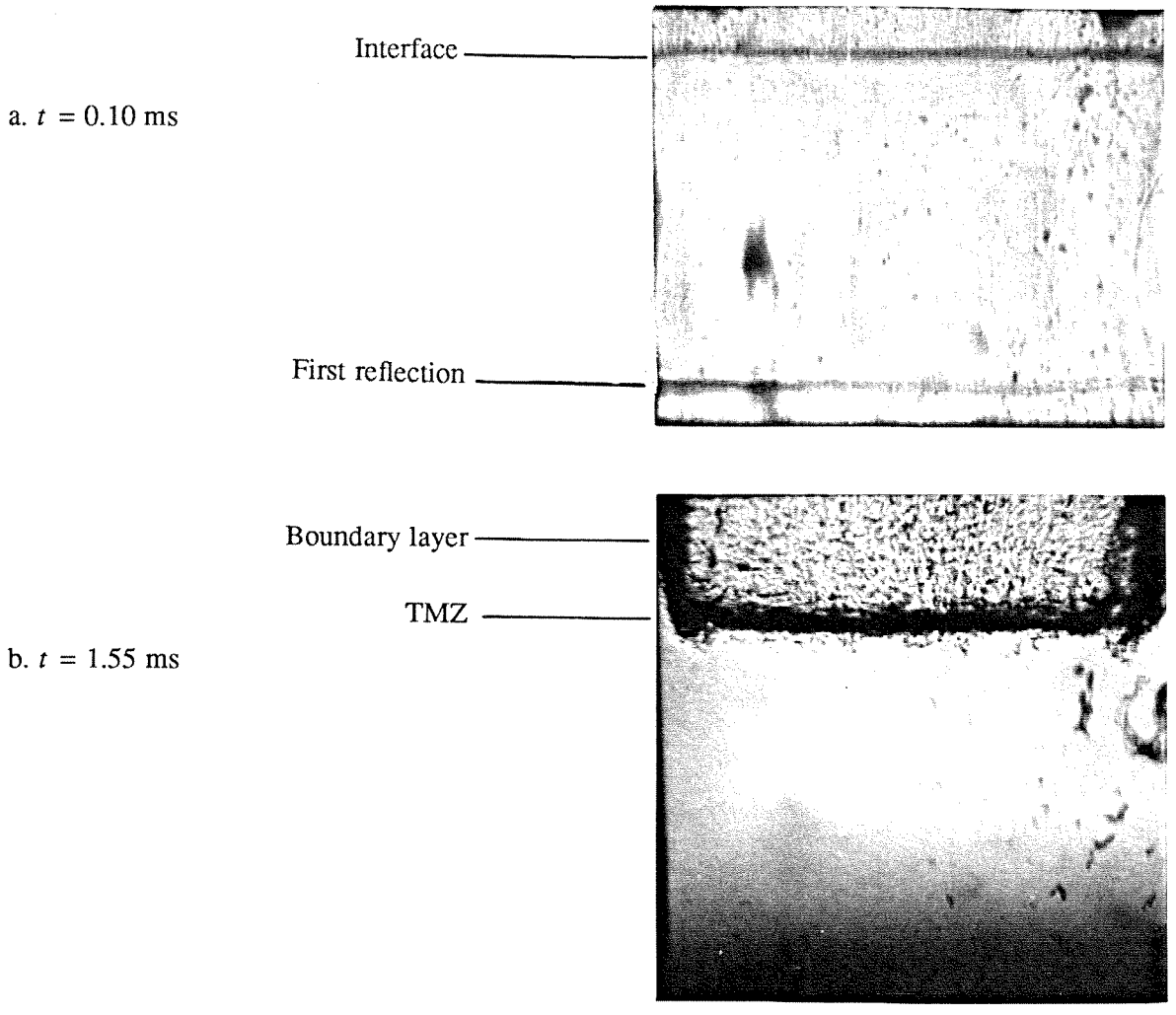

Figure 5.11 Richtmyer-Meshkov instability of a plane discontinuous interface between air and helium. M_s = 1.30, 1.32, close end wall and long time configurations.

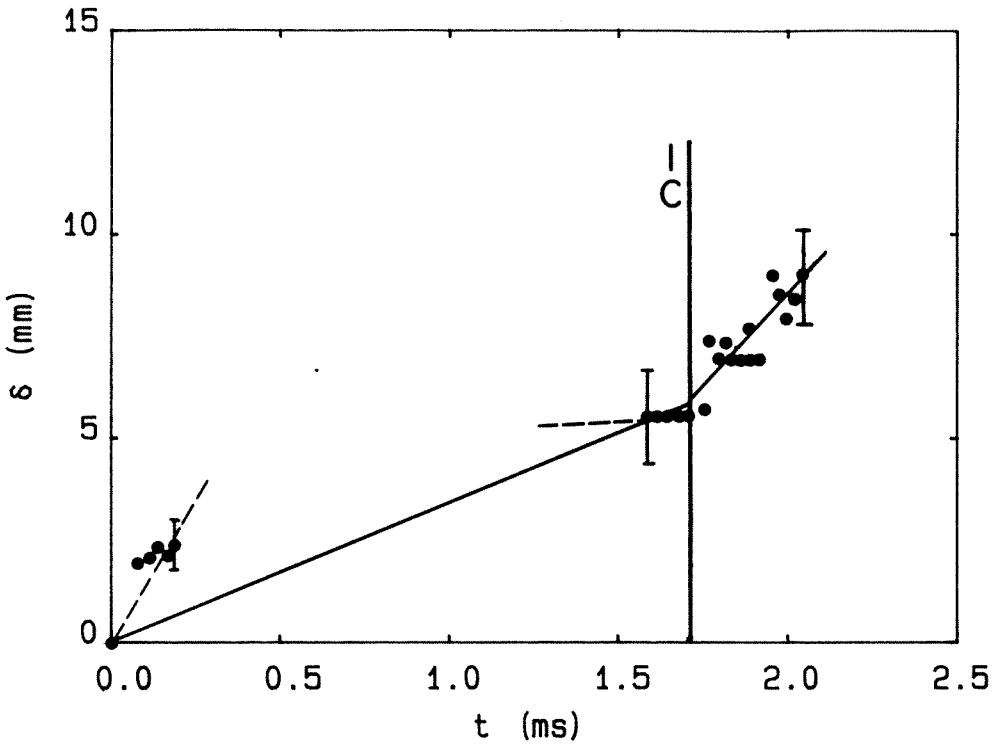

Figure 5.12 Time evolution of the thickness of the TMZ for the plane discontinuous interface between air and helium. M_s = 1.30, 1.32, close end wall and long time configurations. —— :average incident shock growth, reshock growth. --- : upper bound to early time growth, local incident shock growth.

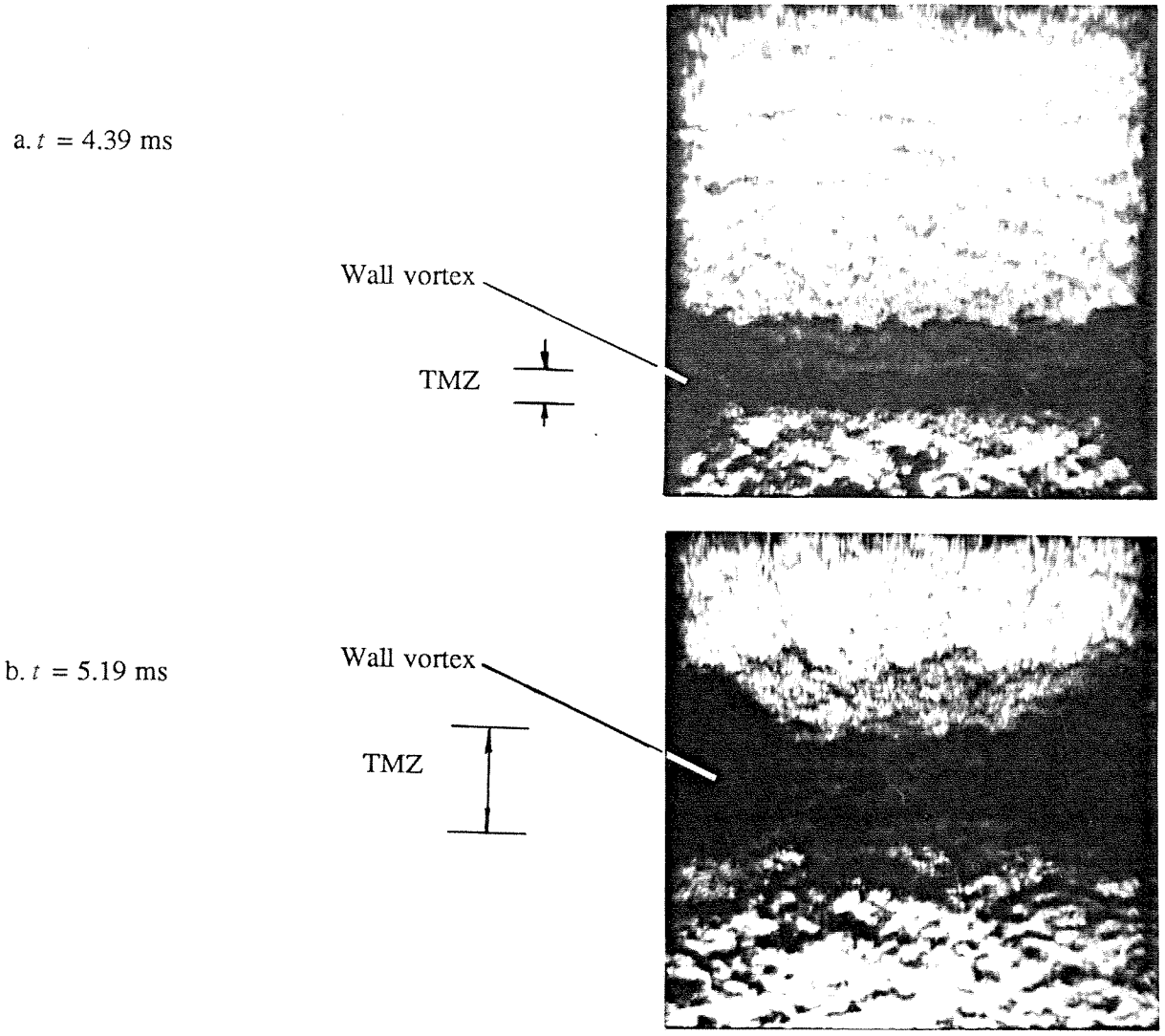

Figure 5.13 Richtmyer-Meshkov instability of a plane discontinuous interface between air and SF_6. M_s = 1.32, long time configuration.

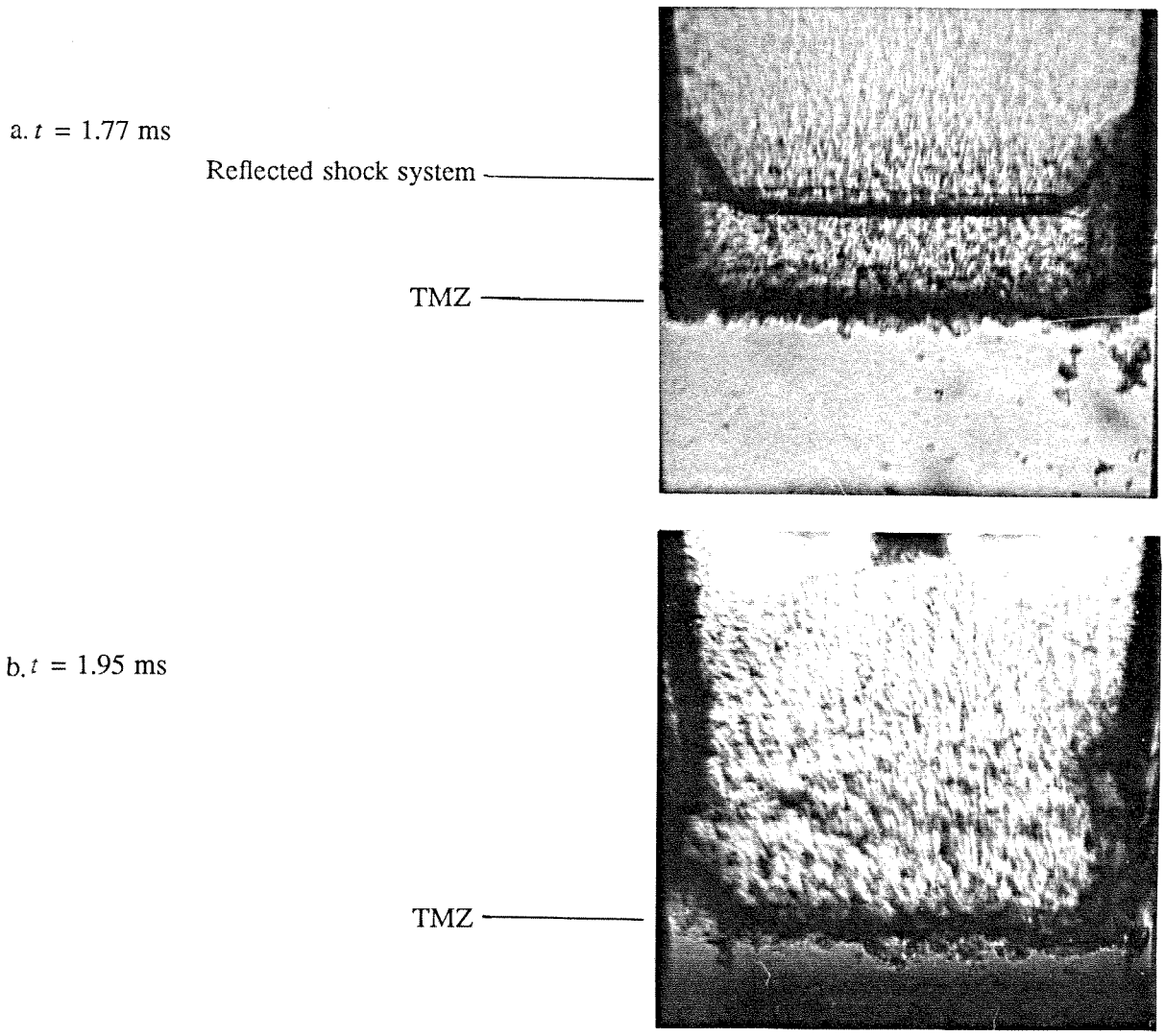

Figure 5.14 Richtmyer-Meshkov instability of a plane discontinuous interface between air and helium. M_s = 1.32, long time configuration.

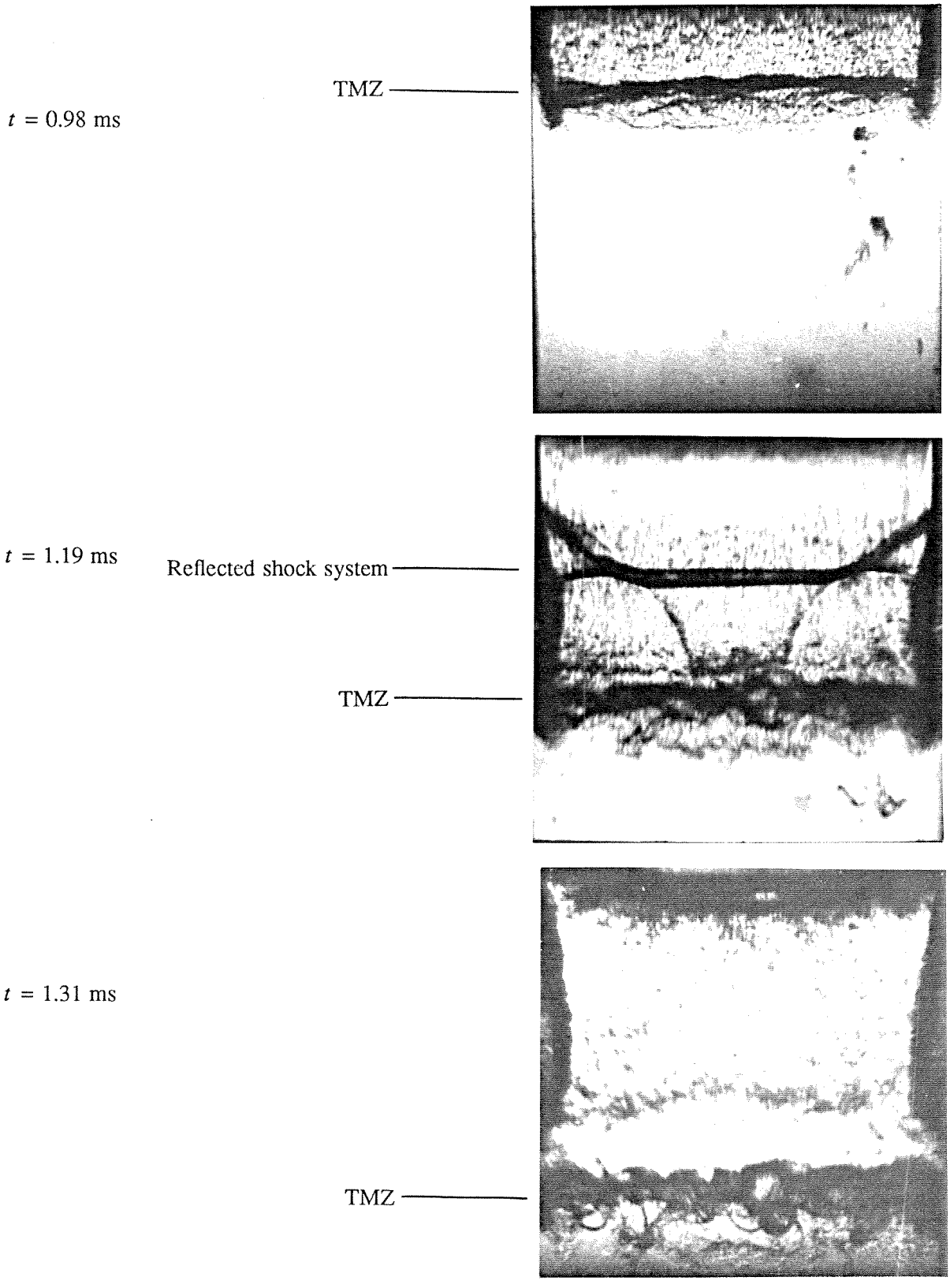

Figure 5.15a Richtmyer-Meshkov instability of a plane discontinuous interface between air and helium. M_s = 1.48, long time configuration.

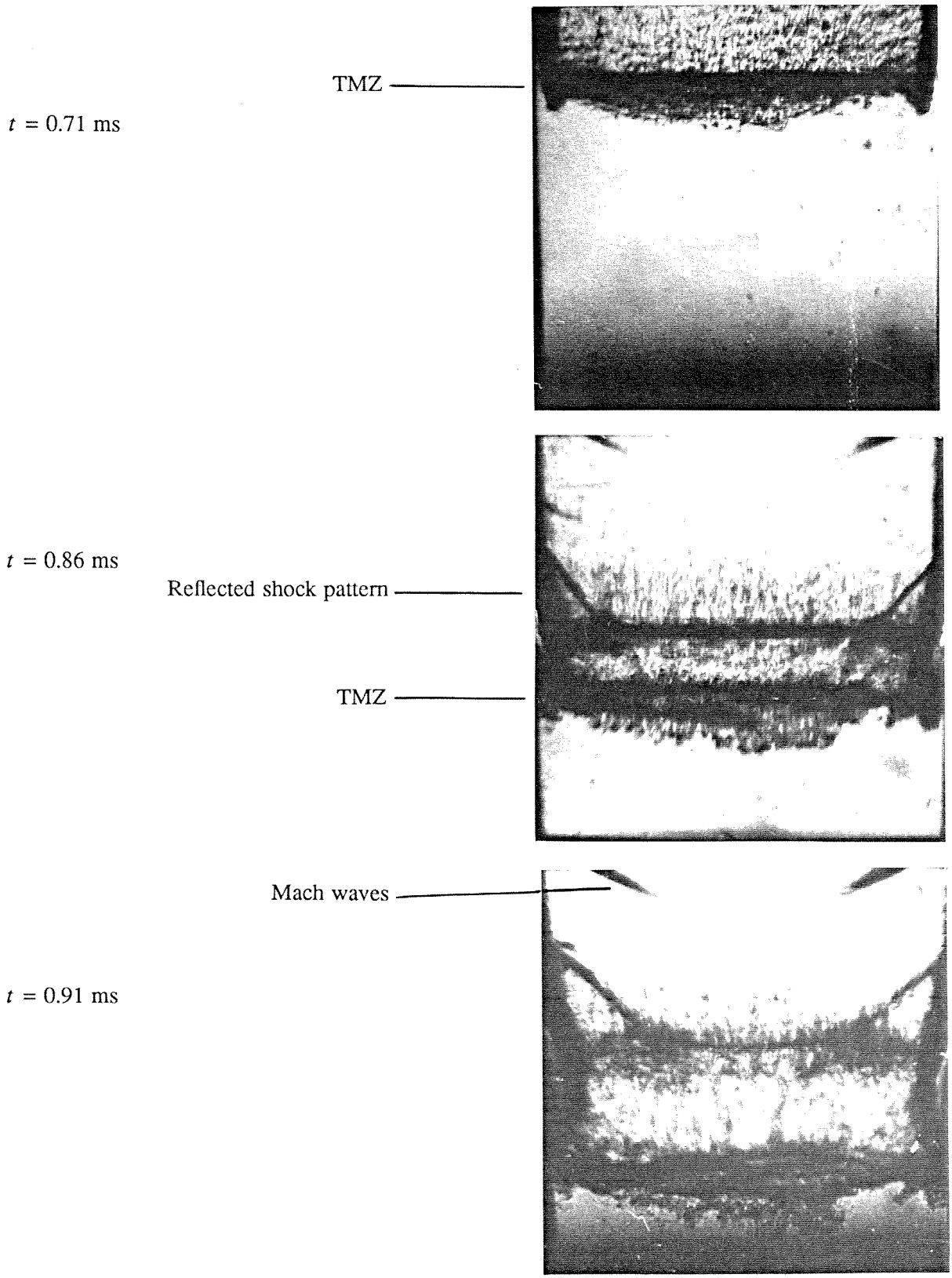

Figure 5.15b Richtmyer-Meshkov instability of a plane discontinuous interface between air and helium. M_s = 1.66, long time configuration.

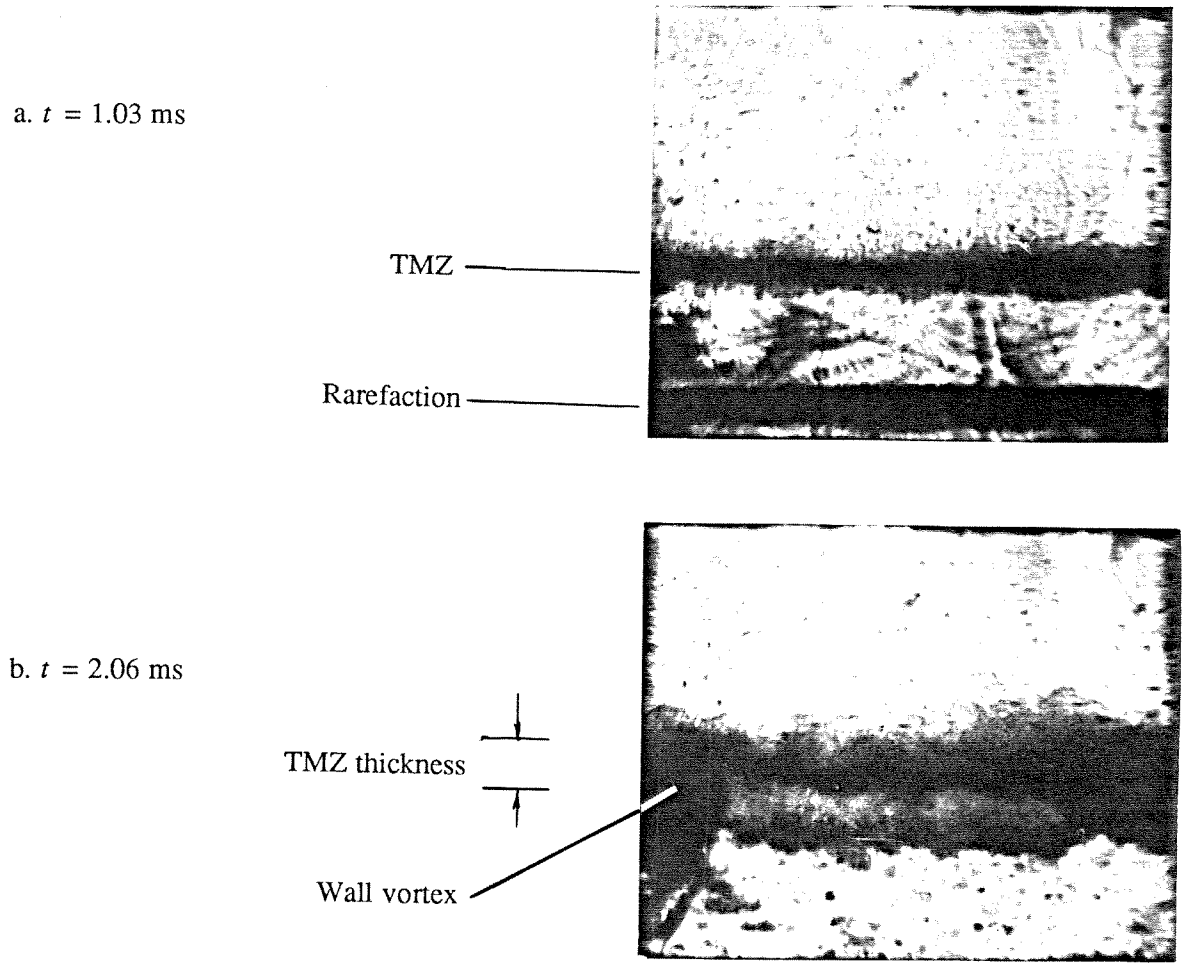

Figure 5.16 Richtmyer-Meshkov instability of a plane discontinuous interface between air and SF_6. M_s = 1.32, close end wall configuration.

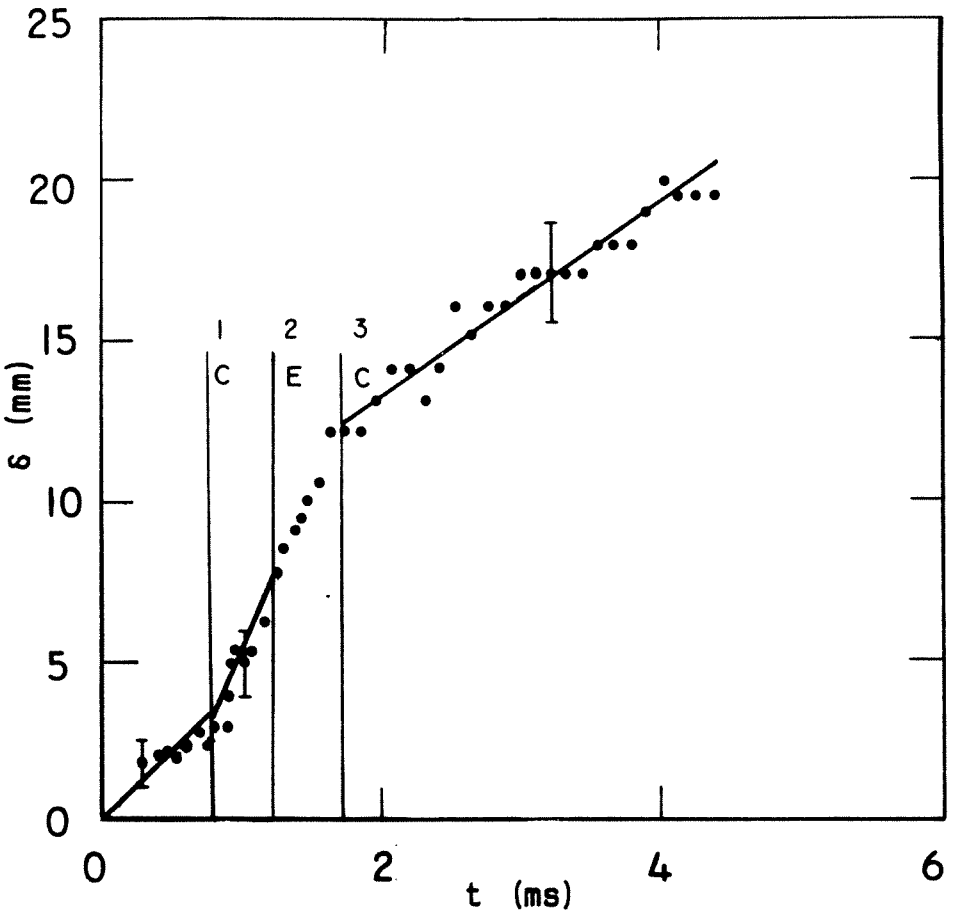

Figure 5.17 Time evolution of the thickness of the TMZ for the plane discontinuous interface between air and SF_6. M_s = 1.32, close end wall configuration.

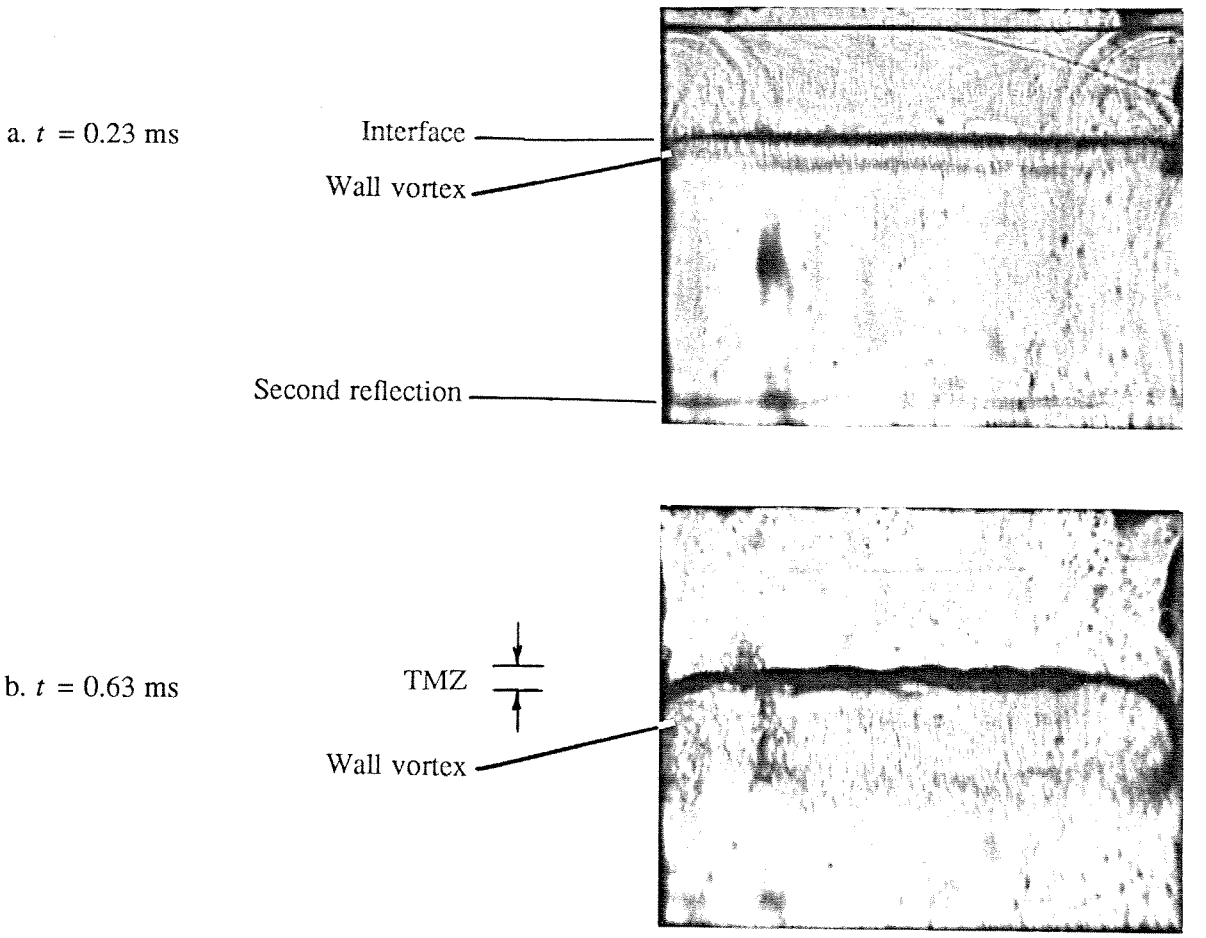

Figure 5.18 Richtmyer-Meshkov instability of a plane discontinuous interface between air and helium. M_s = 1.30, close end wall configuration.

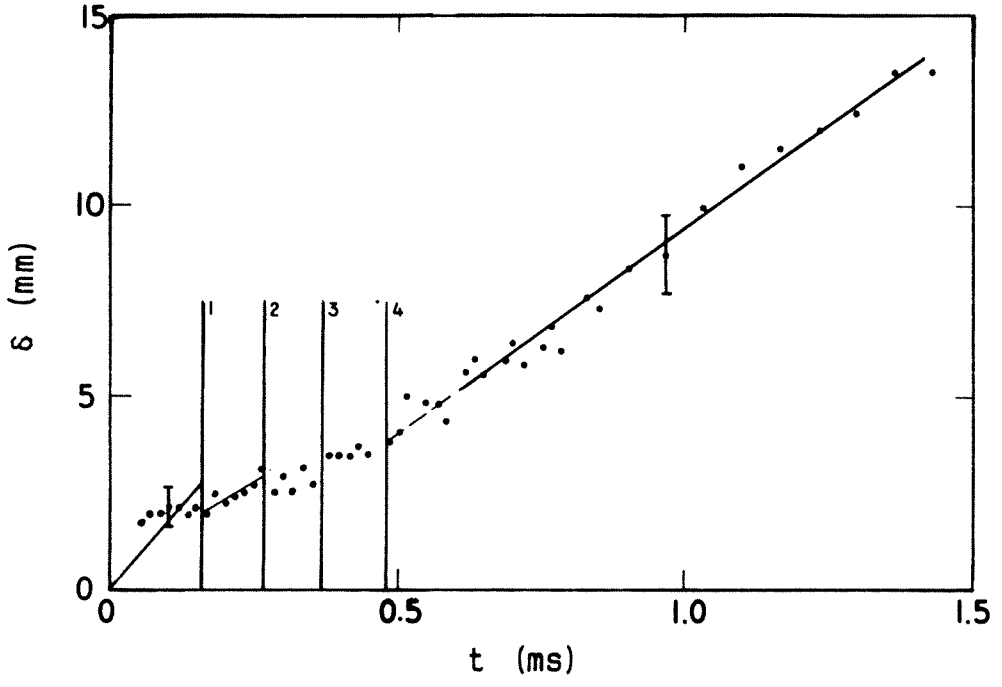

Figure 5.19 Time evolution of the thickness of the TMZ for the plane discontinuous interface between air and helium. M_s = 1.30, close end wall configuration.

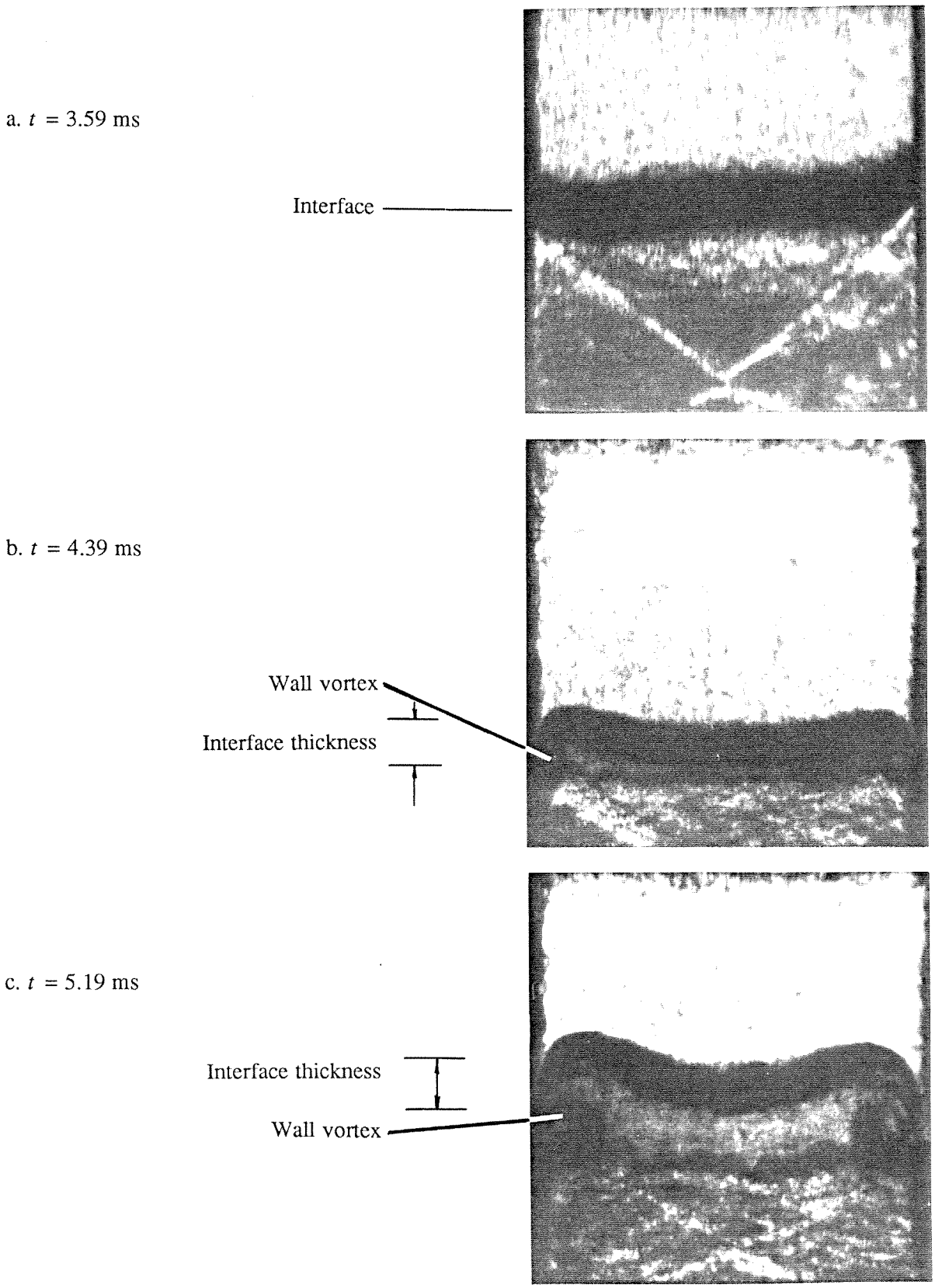

Figure 5.20 Richtmyer-Meshkov instability of a plane continuous interface between air and SF_6. M_s = 1.32, long time configuration.

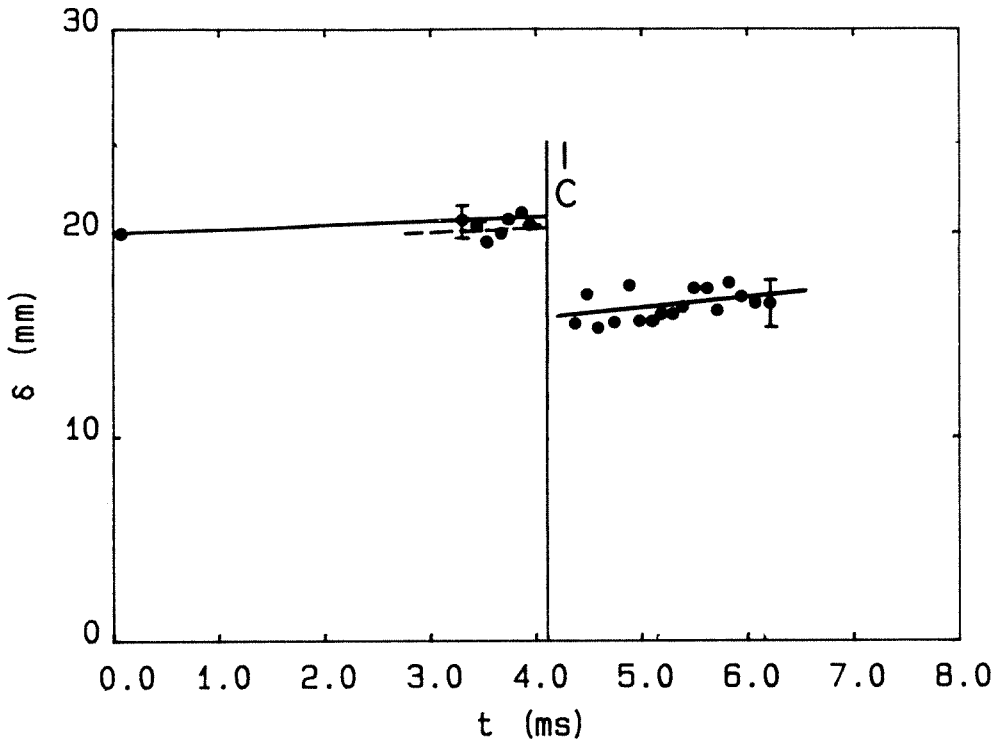

Figure **5.21** Time evolution of the thickness of the plane continuous interface between air and SF_6. M_s = 1.32, long time configuration. —— : upper bound to incident shock growth, reshock growth. – – –: local incident shock growth.

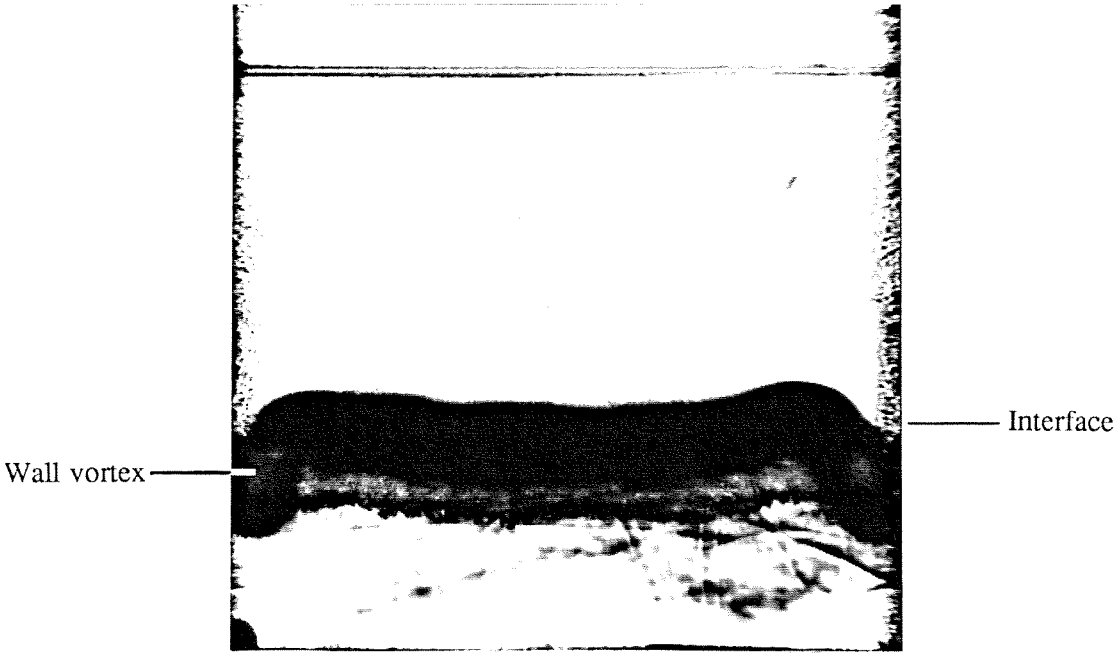

Figure 5.22 Richtmyer-Meshkov instability of a plane continuous interface between air and SF_6. M_s = 1.32, close end wall configuration, t = 1.91 ms. Note the SF_6-containing boundary layers visible on the side walls of the tube and the random acoustic field below the interface.

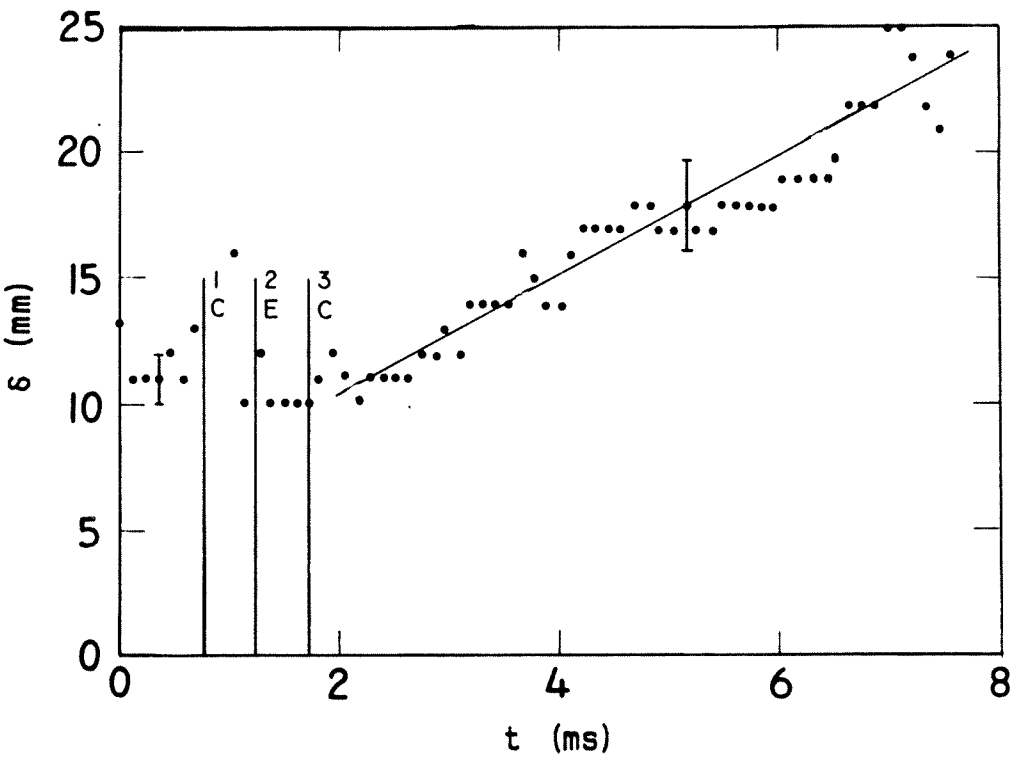

Figure 5.23 Time evolution of the thickness of the plane continuous interface between air and SF_6. M_s = 1.32, close end wall configuration.

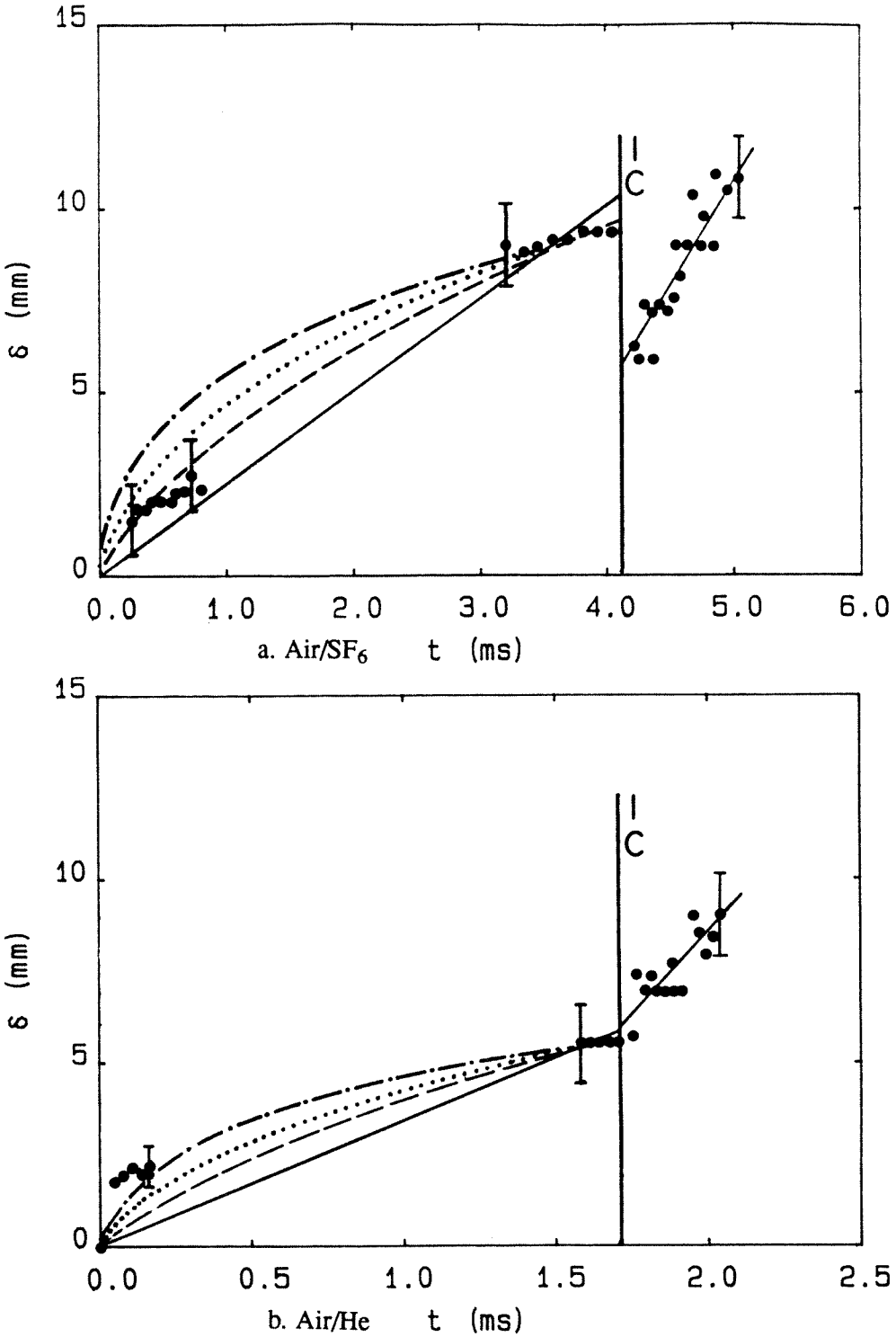

Figure **5.24** Time evolution of the thickness of the TMZ for two discontinuous interface experiments. Long time **and** close end wall configurations.
——: linear profile ($\alpha = 1$),– – –: $\alpha = 2/3$, ---- : $\alpha = 1/2$,–·– : $\alpha = 1/3$.

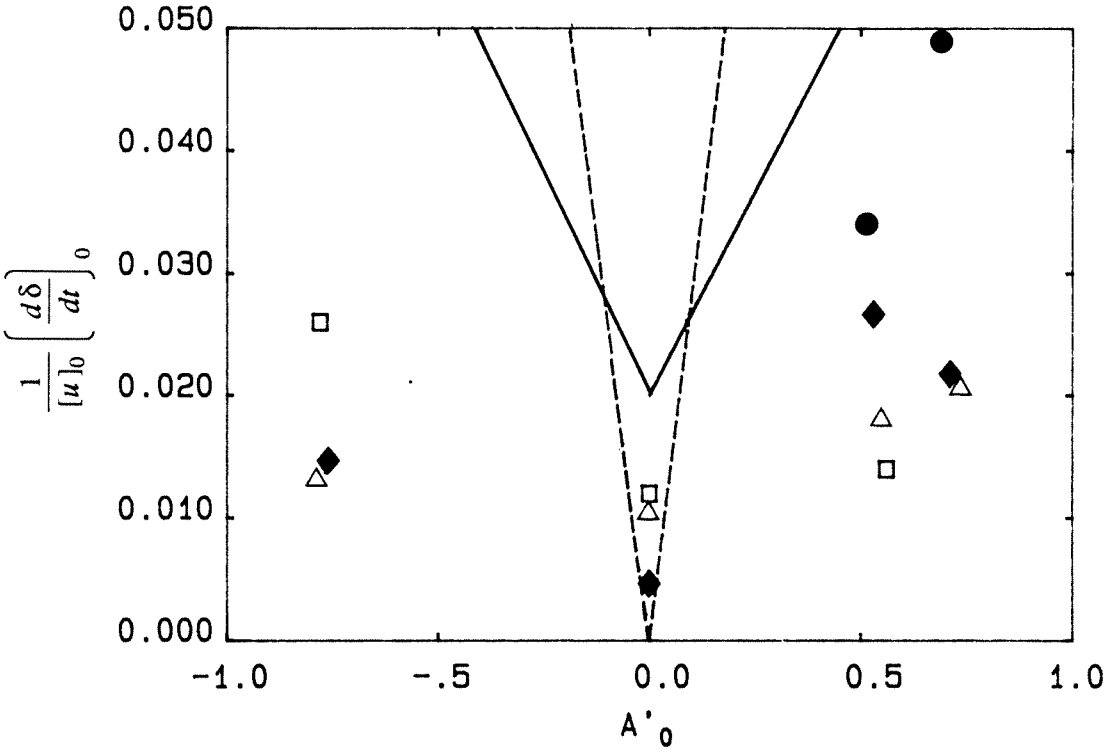

Figure 5.25 Correlation of average incident shock growth rates for the discontinuous interface experiments in the long time configuration.
Incident shock Mach number: ● : 1.12, ◆ : 1.32, △ : 1.48, □ : 1.66.
—— : Zaitsev *et al.* (1985), --- : Equation (3.23).

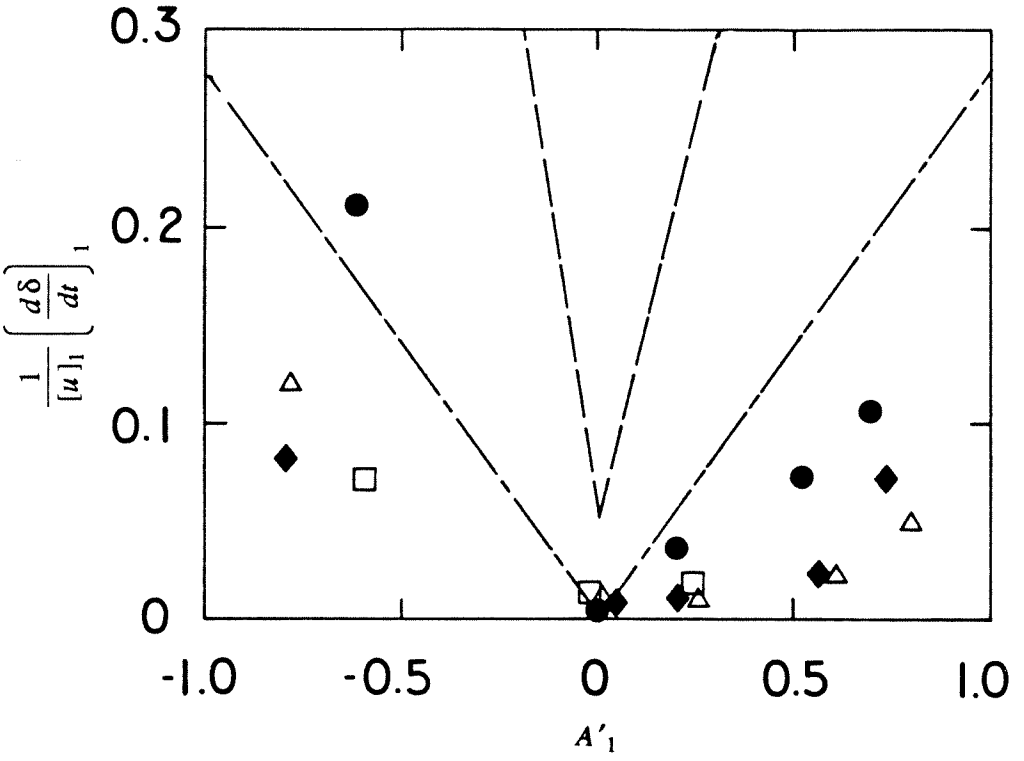

Figure 5.26 Correlation of reshock shock growth rates for the discontinuous interface experiments in the long time configuration. Incident shock Mach number: ●: 1.12, ◆: 1.32, △: 1.48, □: 1.66.— — : Zaitsev *et al.* (1985), —·— : Equation (3.23).

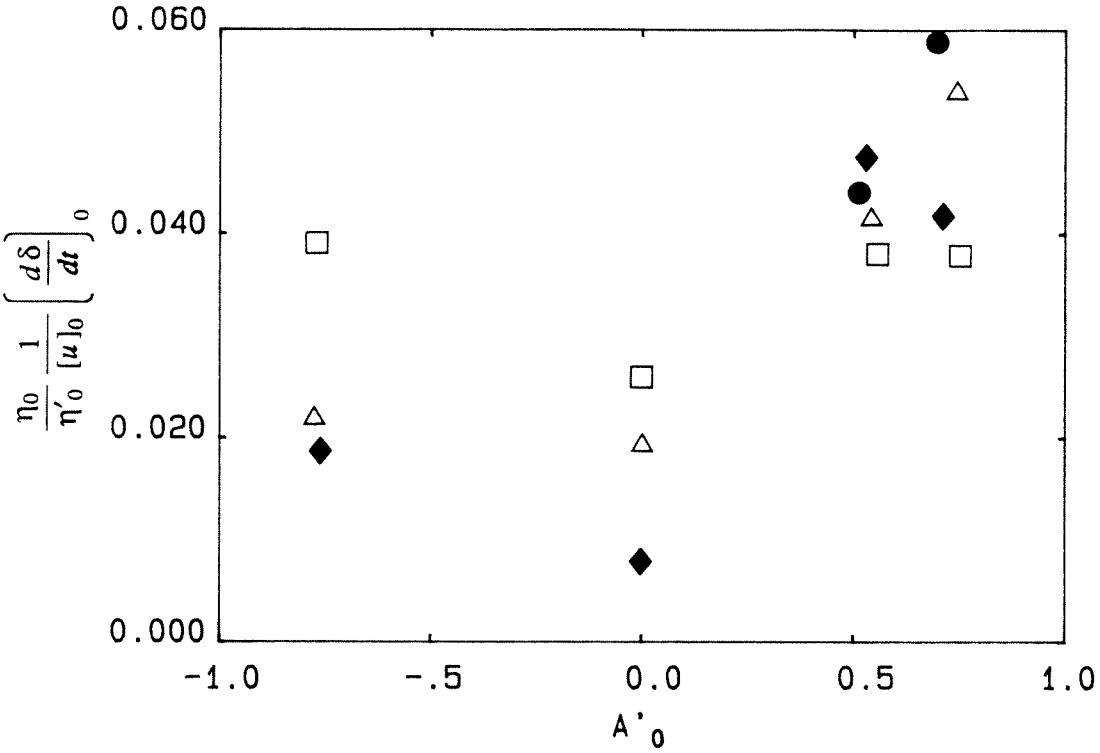

Figure 5.27 Correlation of average incident shock growth rates for the discontinuous interface experiments in the long time configuration. Incident shock Mach number: ●: 1.12, ◆: 1.32, △: 1.48, □: 1.66.

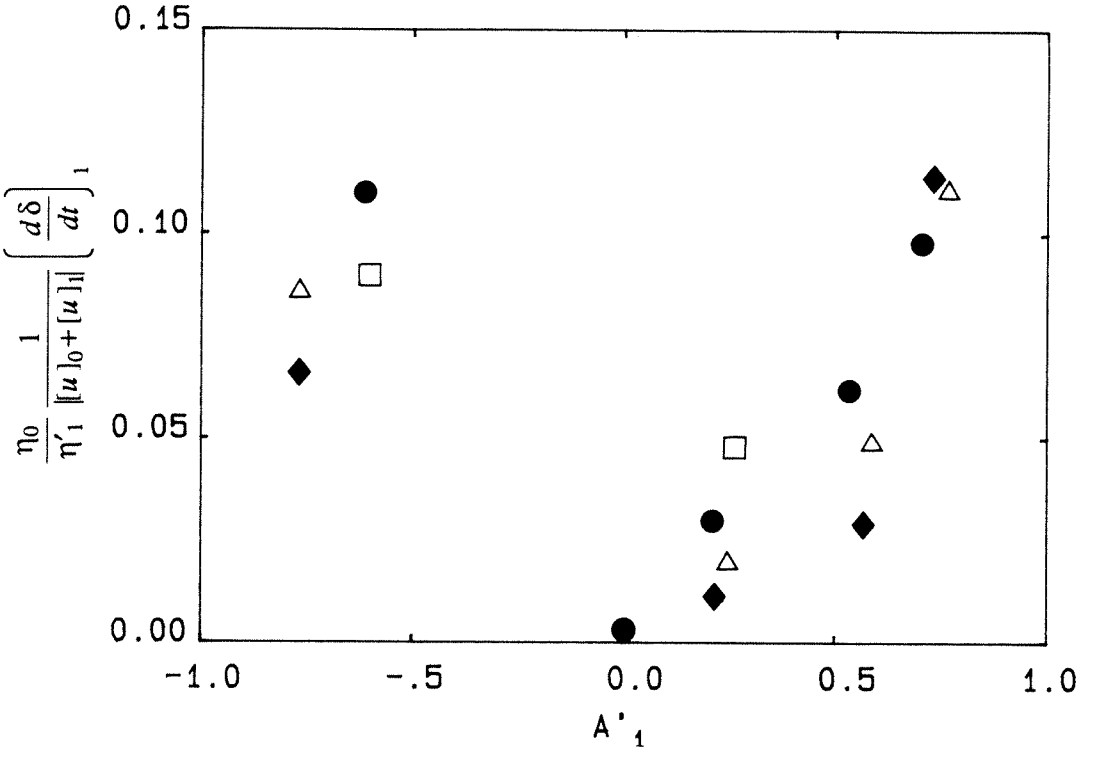

Figure 5.28 Correlation of reshock shock growth rates for the discontinuous interface experiments in the long time configuration. Incident shock Mach number: ●: 1.12, ◆: 1.32, △: 1.48, □: 1.66.

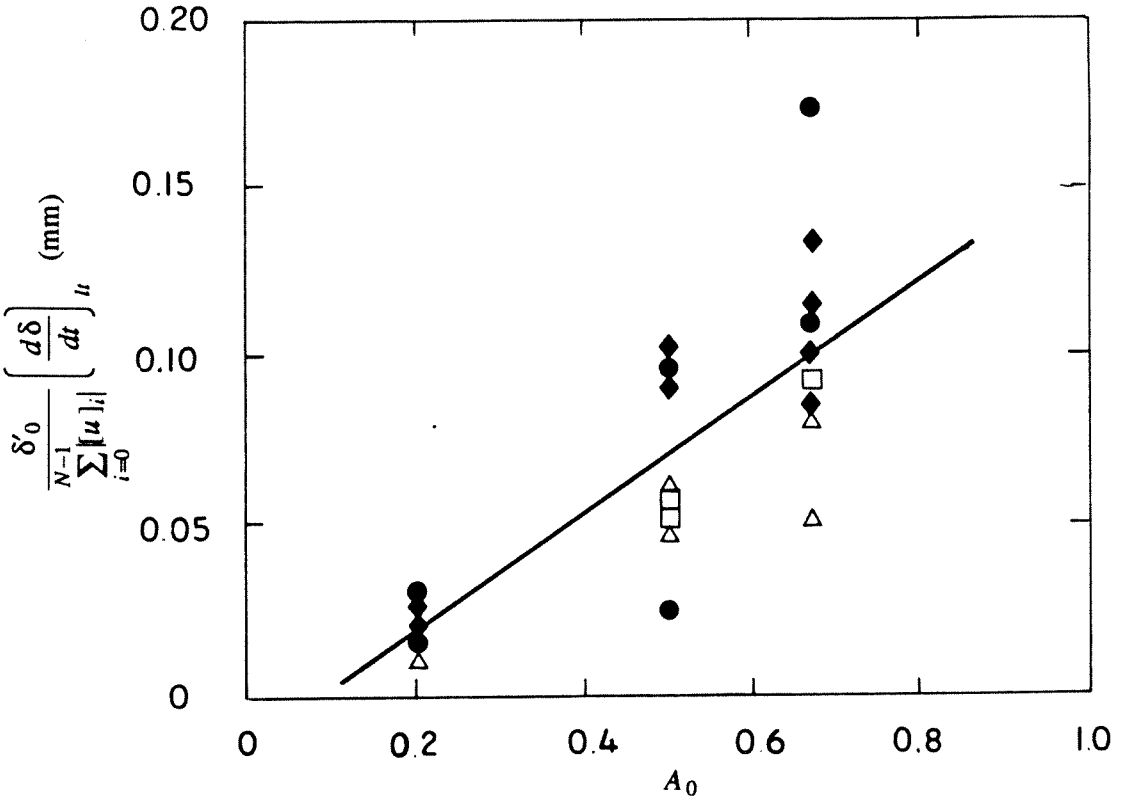

Figure 5.29 Correlation of late-time growth rates for the continuous interface experiments in the long time configuration. Incident shock Mach number: ●: 1.12, ◆: 1.32, △: 1.48, □: 1.66.

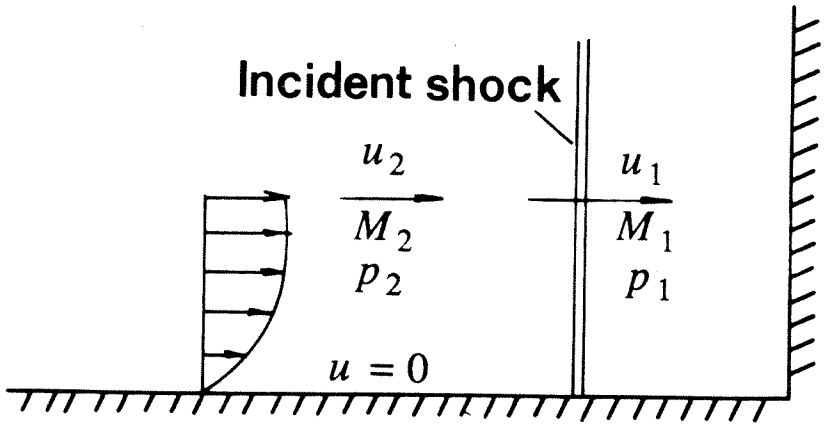

a. Shock incident to end wall.

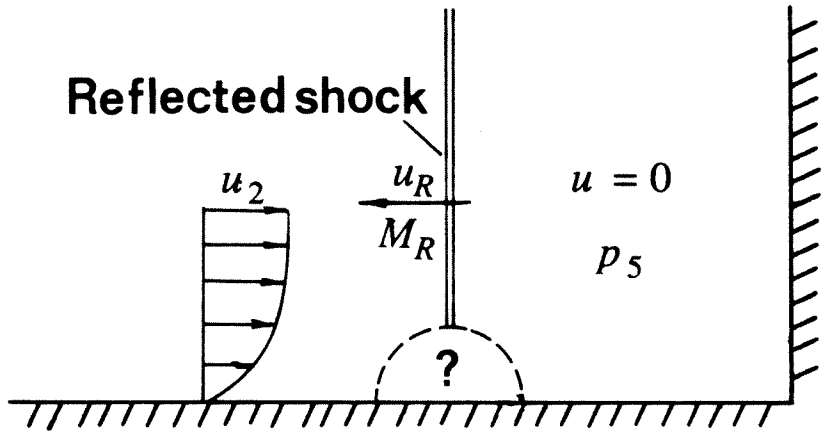

b. Interaction of reflected shock with boundary layer.

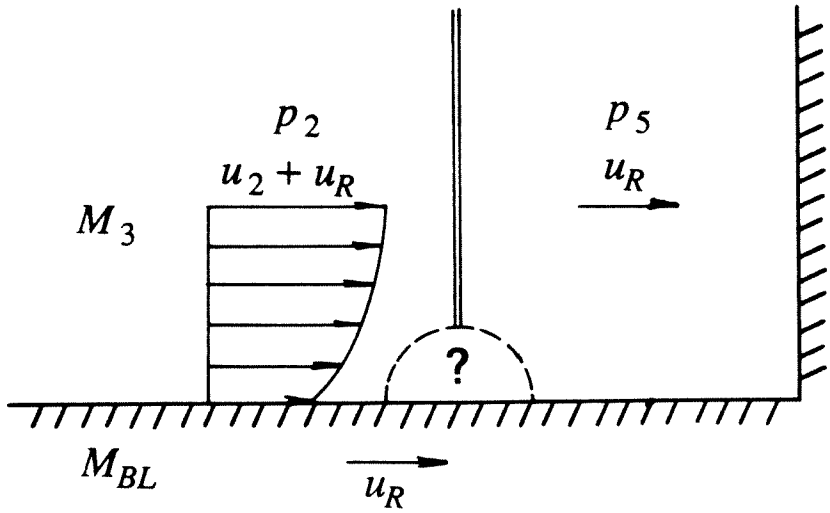

c. Interaction in shock-fixed coordinates.

Figure 6.1 Shock-boundary layer interaction (after Mark 1957).

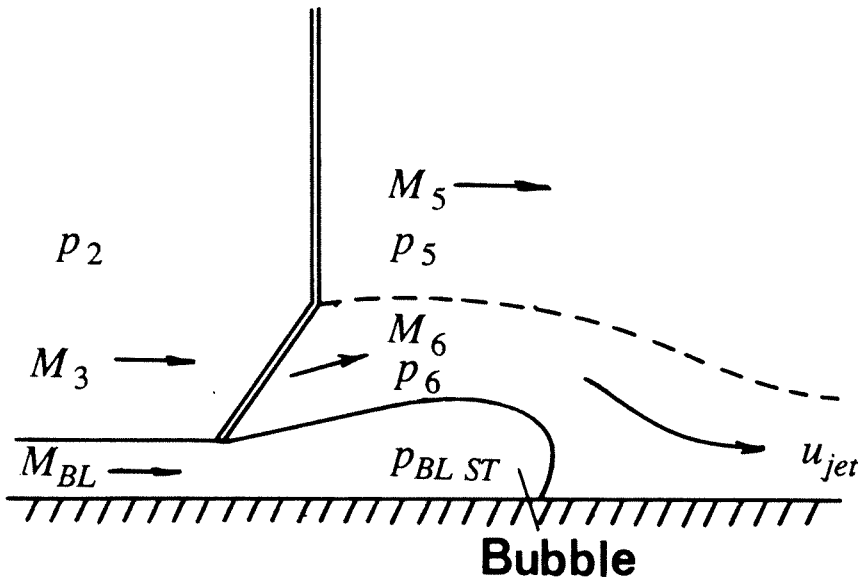

a. $M_6 < 1$.

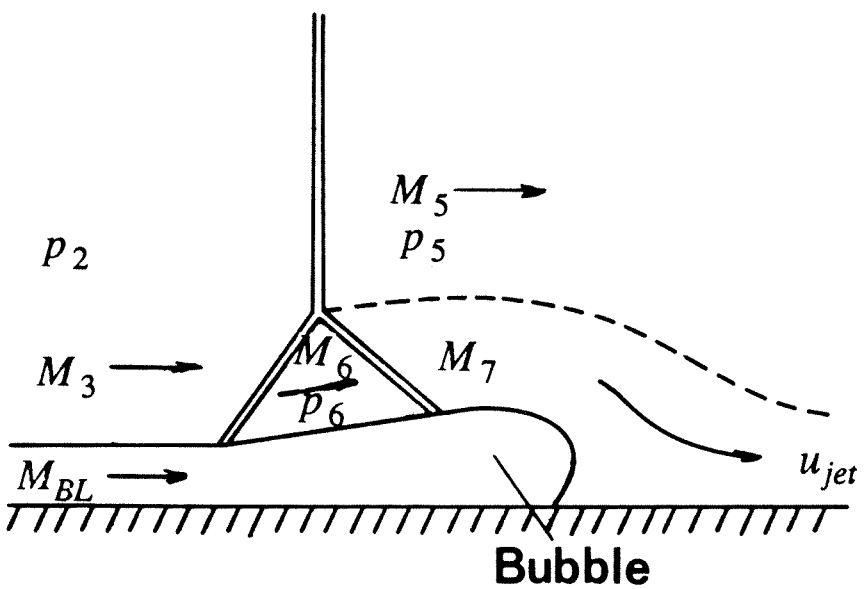

b. $M_6 > 1$.

Figure 6.2 Shock system over bifurcation bubble.

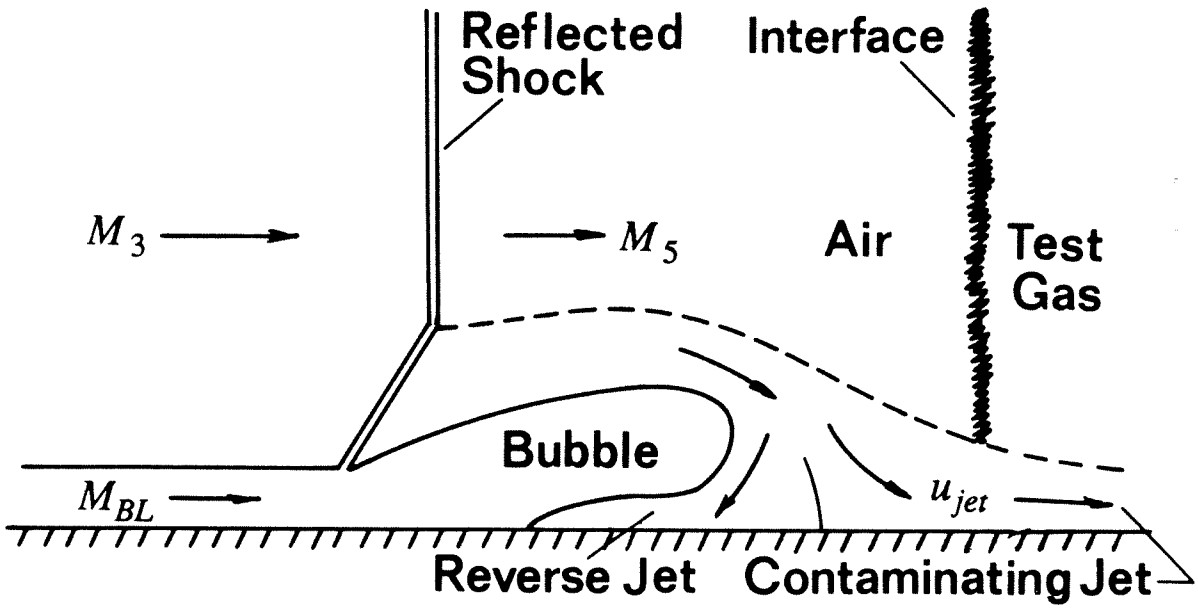

Figure 6.3 Formation of contaminating and reverse jets over bifurcation bubble after reshock crosses interface (adapted from Hess 1957).

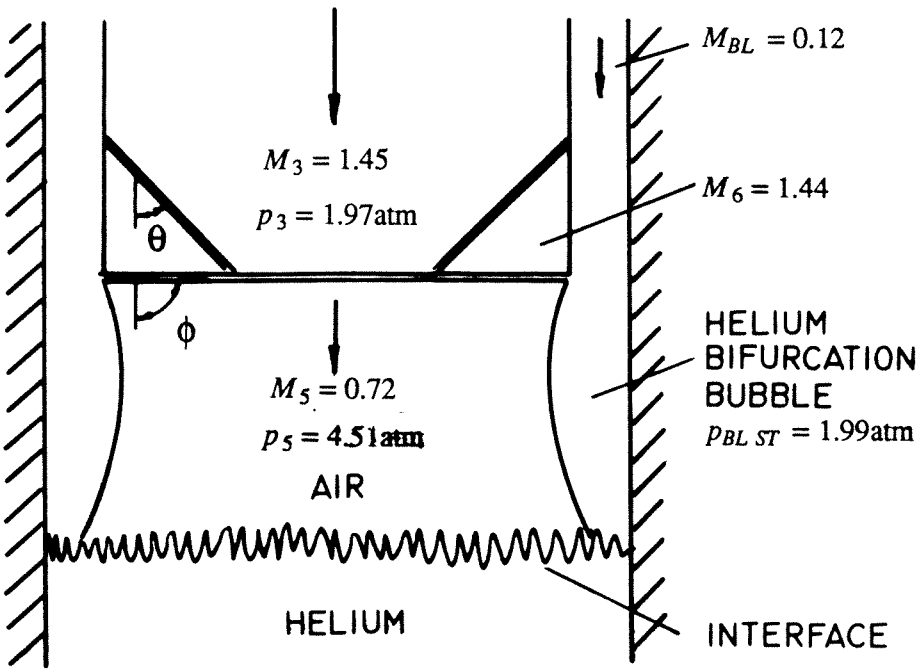

Figure 6.4 Construction for bifurcation wave pattern above interface (in shock-fixed reference frame). Air/He M_s = 1.66. θ = 44°, ϕ = 87°.

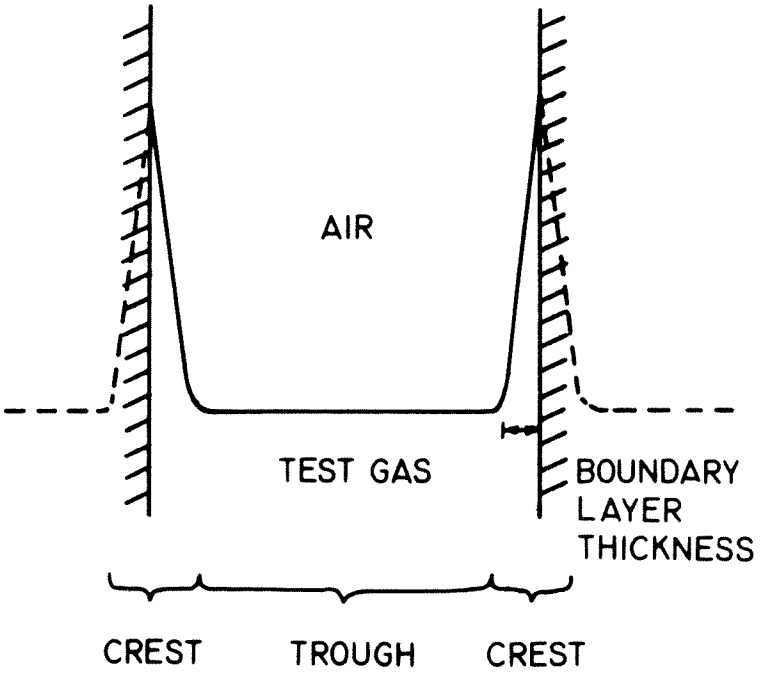

Figure 6.5 Shape of interface perturbation caused by boundary layers.

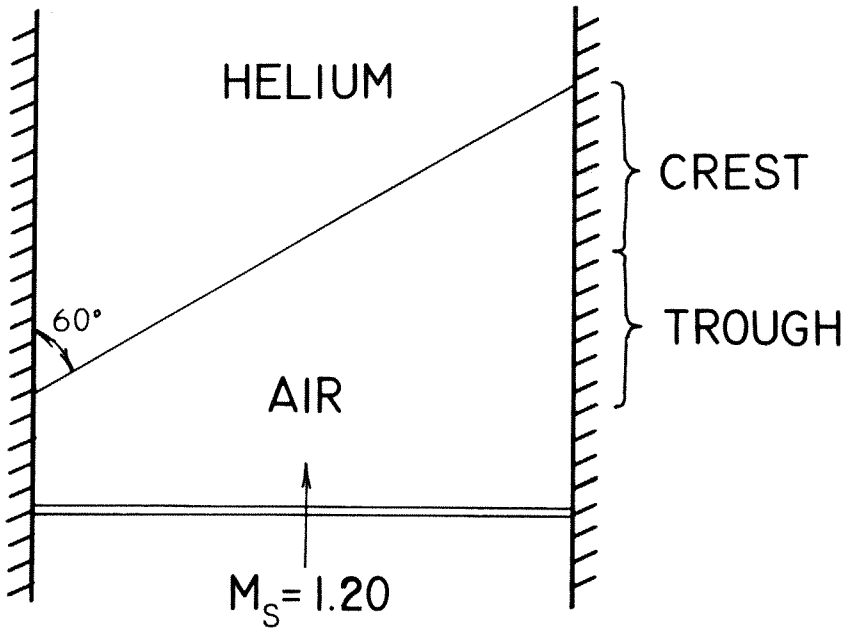

a. Initial configuration.

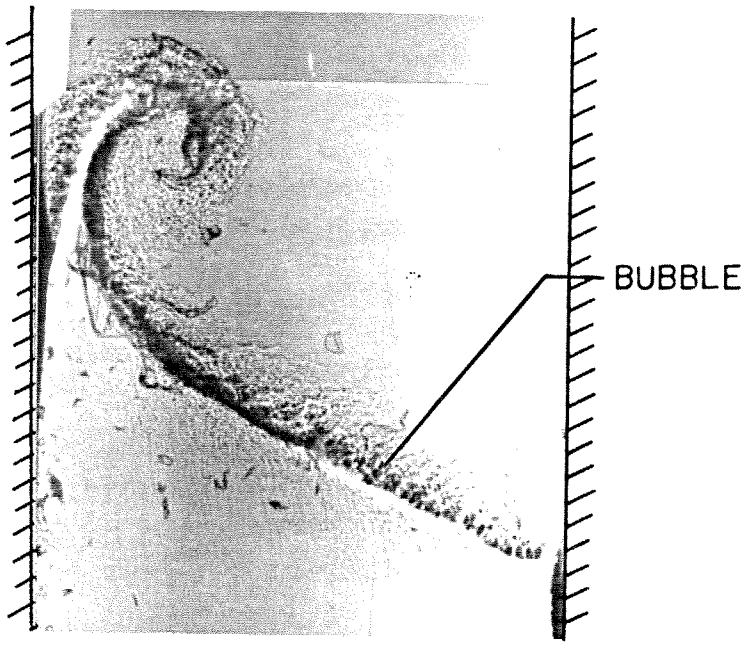

b. Interface at t = 0.77 for experiment of Haas (*cf.* Sturtevant 1988).

Figure 6.6 Formation of spike vortex from the interaction of a shock wave with an inclined heavy-light interface.

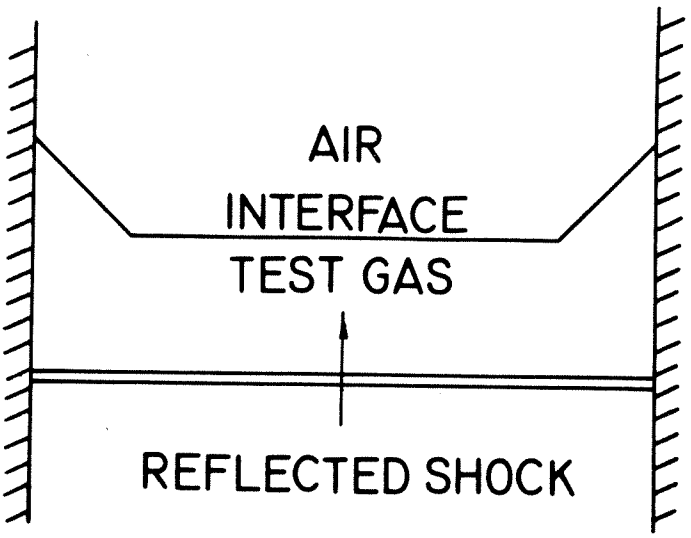

a. Interface perturbation before reshock.

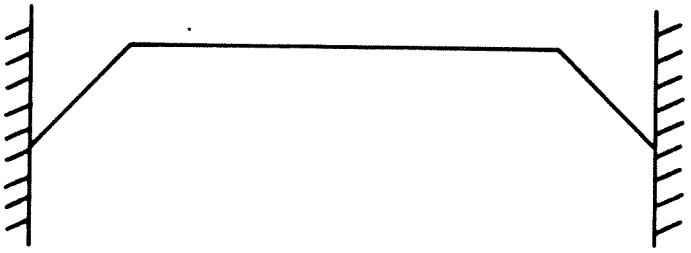

b. Phase reversal of perturbation.

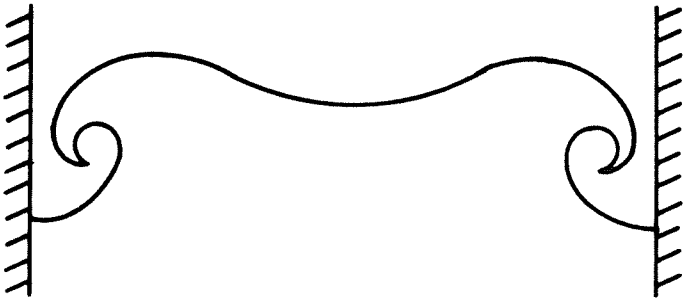

c. Roll-up of spike.

Figure 6.7 Mechanism of wall vortex formation.

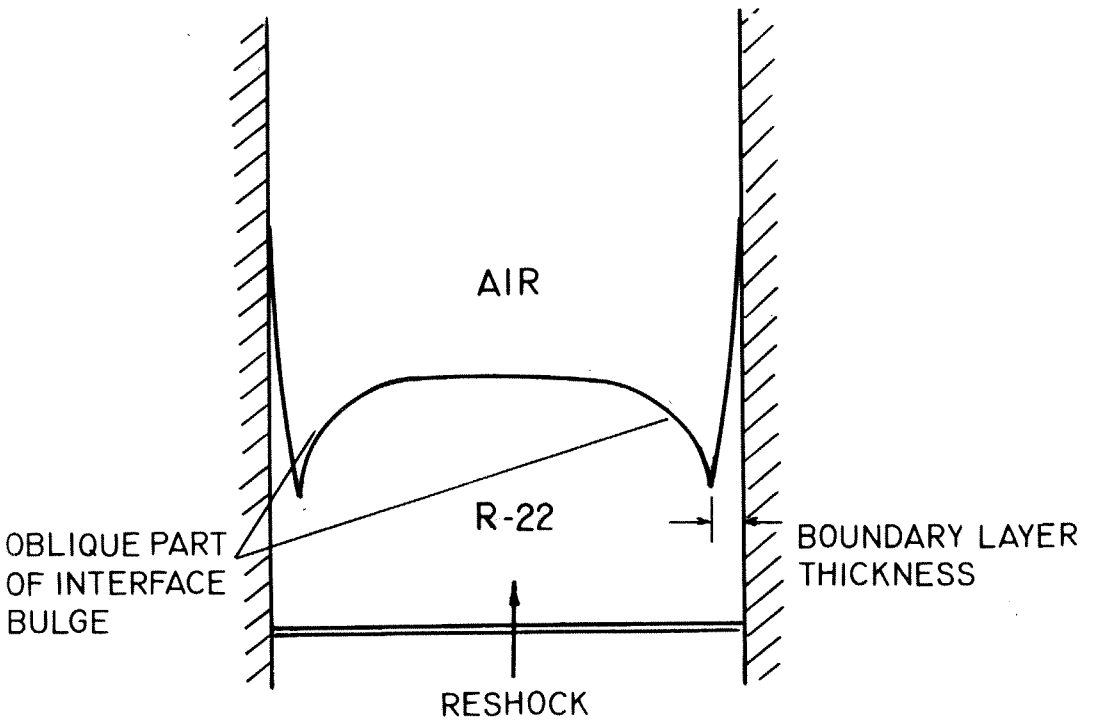

a. Perturbation obtained by a slight upward bulge on a light-heavy interface.

b. Formation of reverse wall vortex.
Air/R-22, M_s = 1.32, long time configuration.

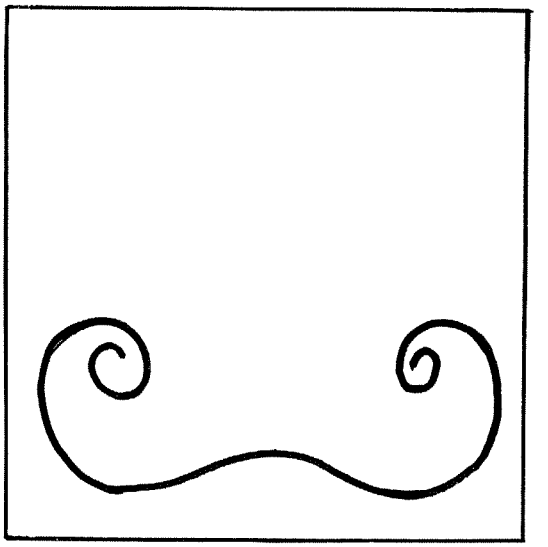

c. Schematic of reverse wall vortex

Figure 6.8 Reverse wall vortex.

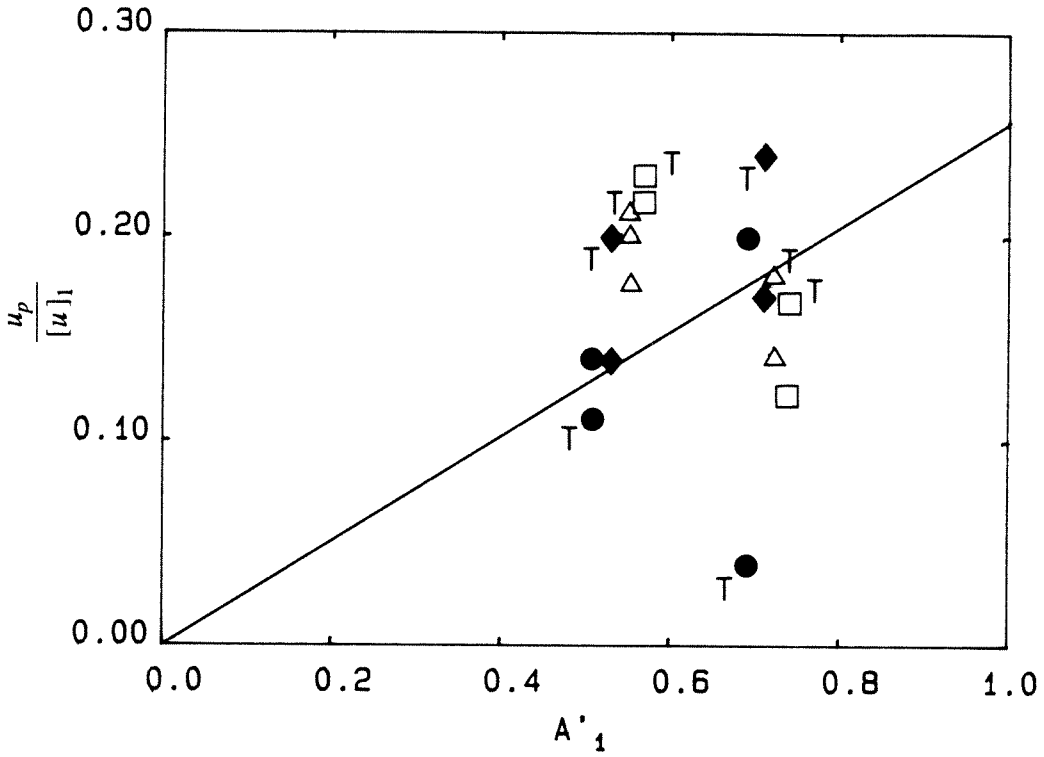

Figure 6.9 Wall vortex penetration speed, long time configuration.
Incident shock Mach number: ● : 1.12. ◆ : 1.32, △ : 1.48, □ : 1.66.
T: indicates the thicker interface for each
test gas at a given Mach number in Table 5.3.

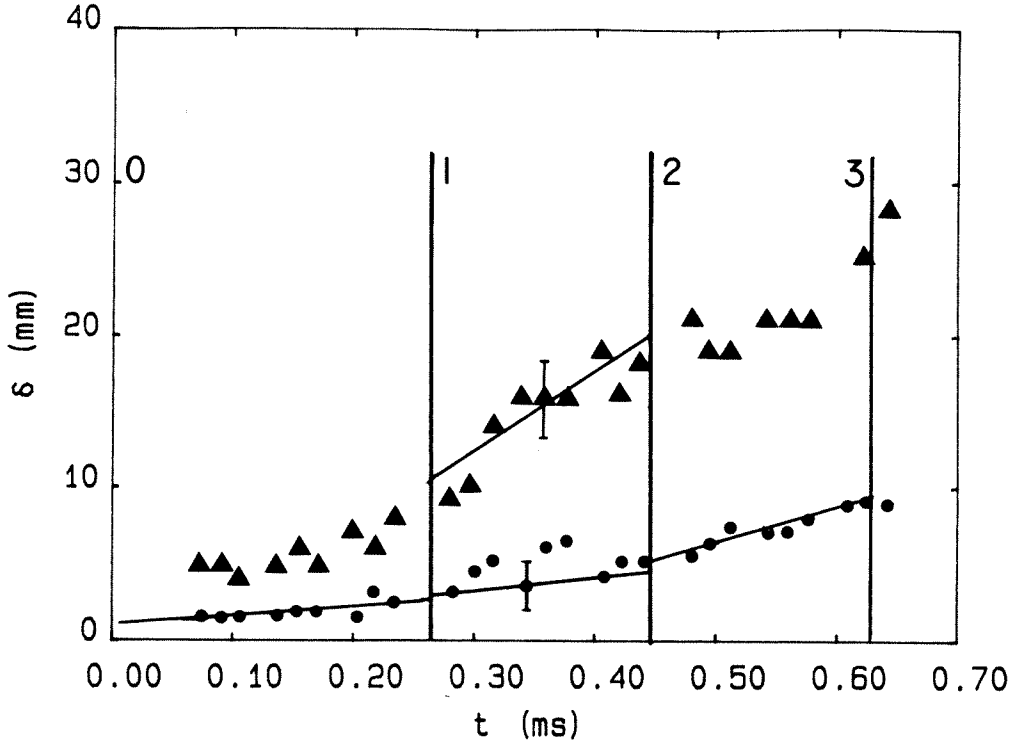

a. Present study: ● TMZ, ▲ wall vortex.

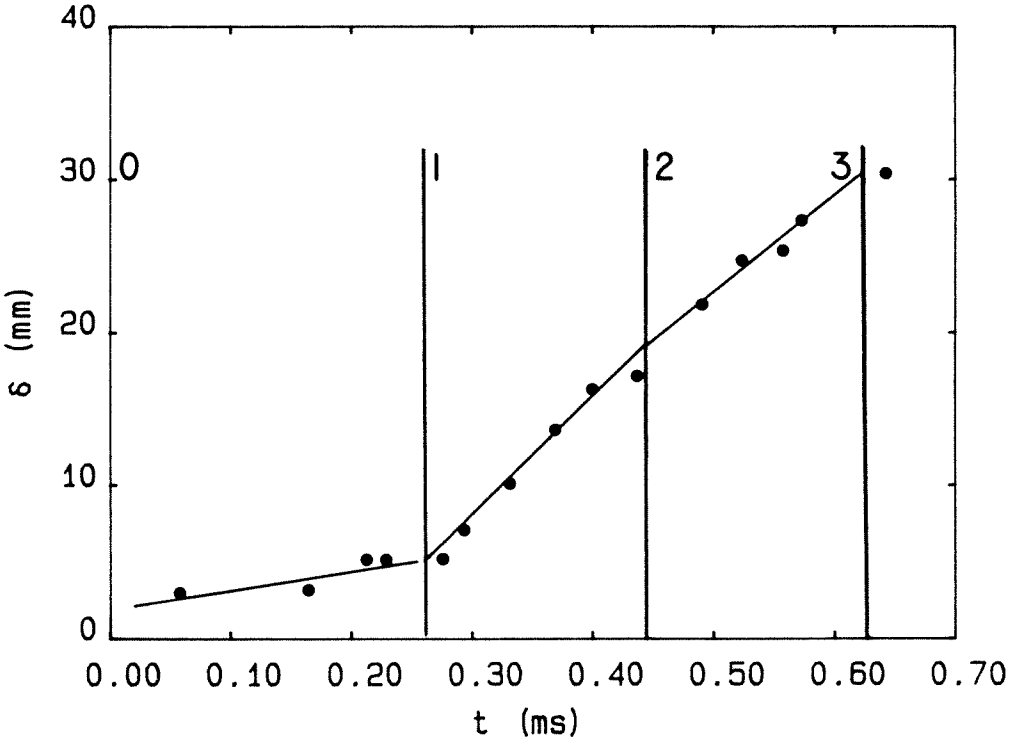

b. Andronov *et al.* (1976): ● TMZ.

Figure 6.10 Time evolution of the thickness of the TMZ for the plane discontinuous interface between air and helium, M_s = 1.30.

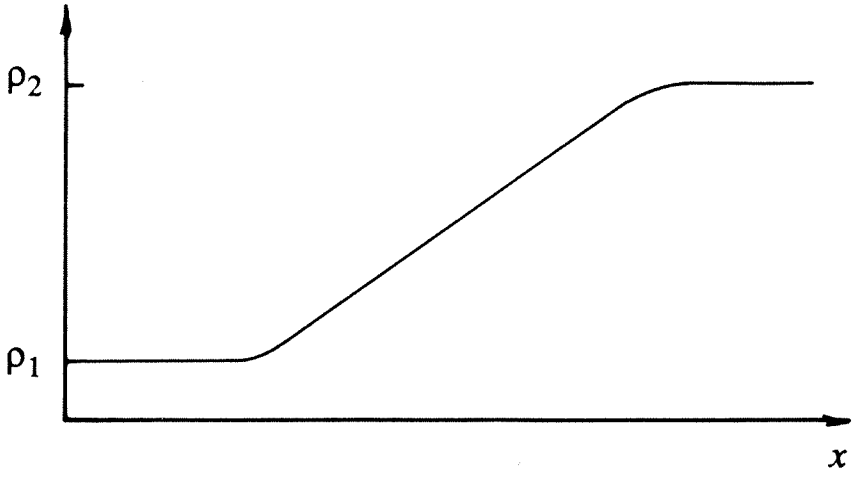

a. Actual density profile at interface.

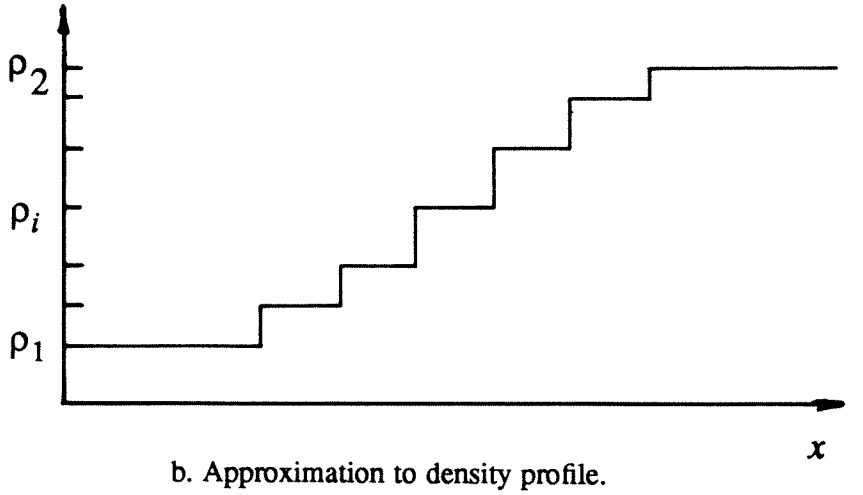

b. Approximation to density profile.

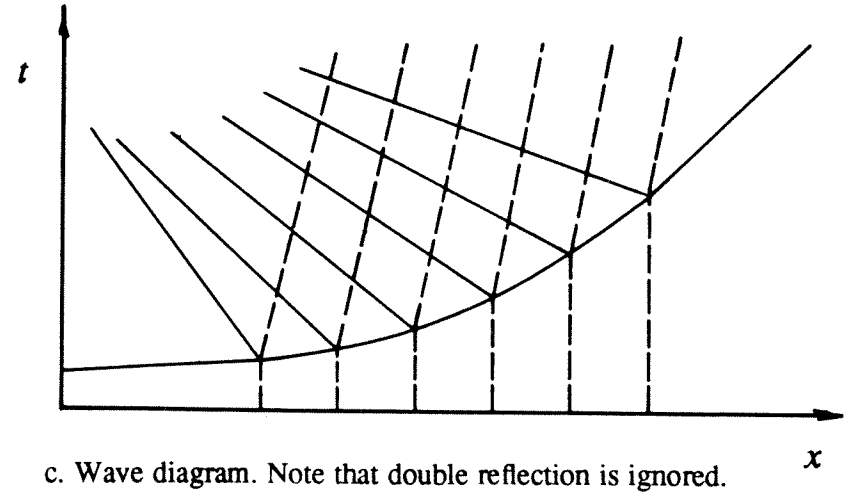

c. Wave diagram. Note that double reflection is ignored.
— waves —— interfaces

Figure 6.11 One-dimensional wave propagation in non-uniform media (from Chisnell 1955).

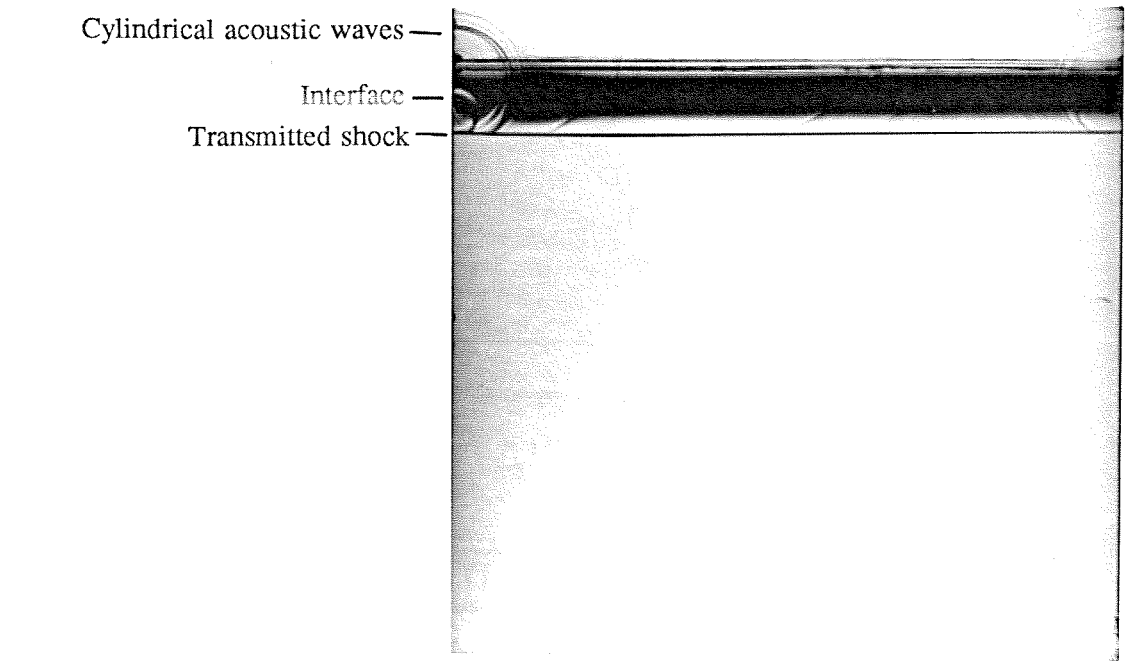

a. t = 0.04 ms

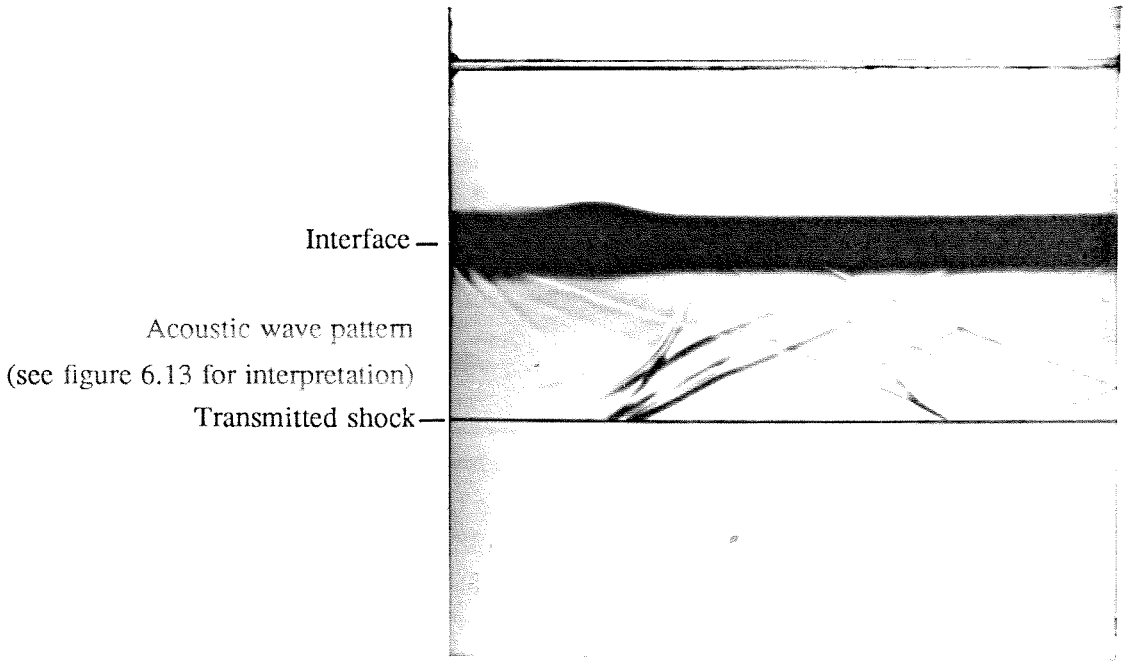

b. t = 0.27 ms

Figure 6.12 Wave pattern resulting from the refraction of a M_s = 1.32 shock wave at an air/SF_6 interface.

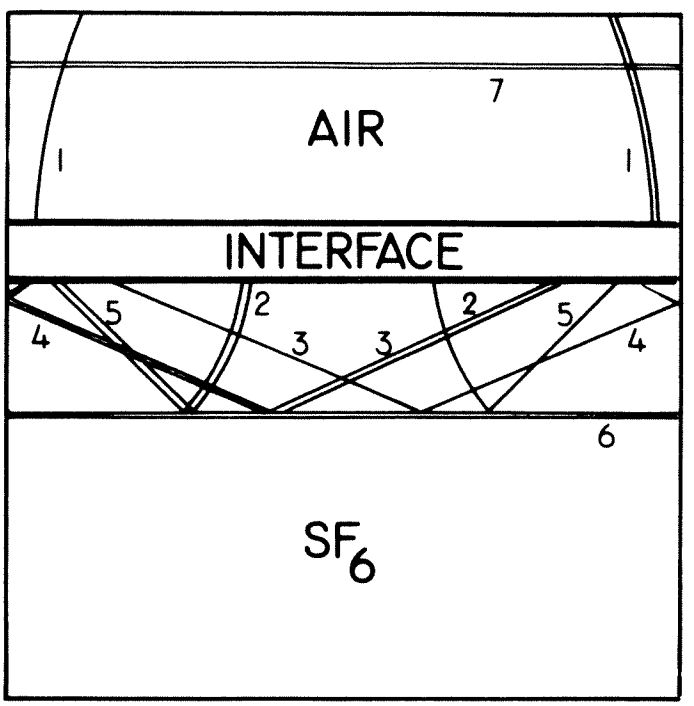

Figure 6.13 Wavefront construction for the interaction of a M_s = 1.32 shock wave with an air/SF_6 interface. 1. Cylindrical fronts in air. 2. Cylindrical fronts in SF_6. 3. Precursor waves in SF_6. 4. Reflection of precursor off transmitted shock. 5. Reflection of cylindrical fronts off transmitted shock. 6. Transmitted shock. 7. Grease marks left on window by sliding plate.

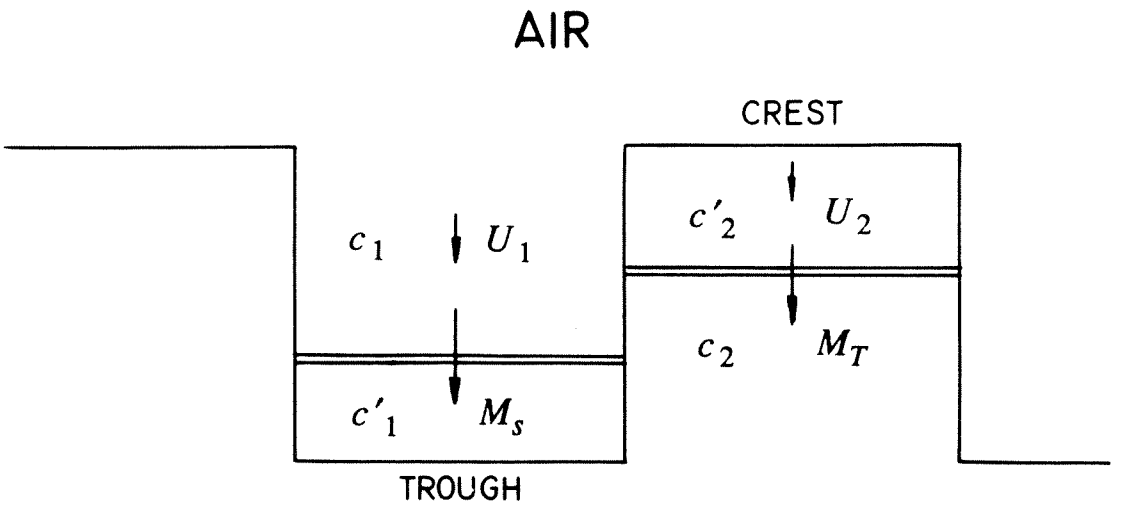

a. Light-heavy configuration.
$\Delta u_{max} = U_1, M_{rel} \equiv U_1/c_2$

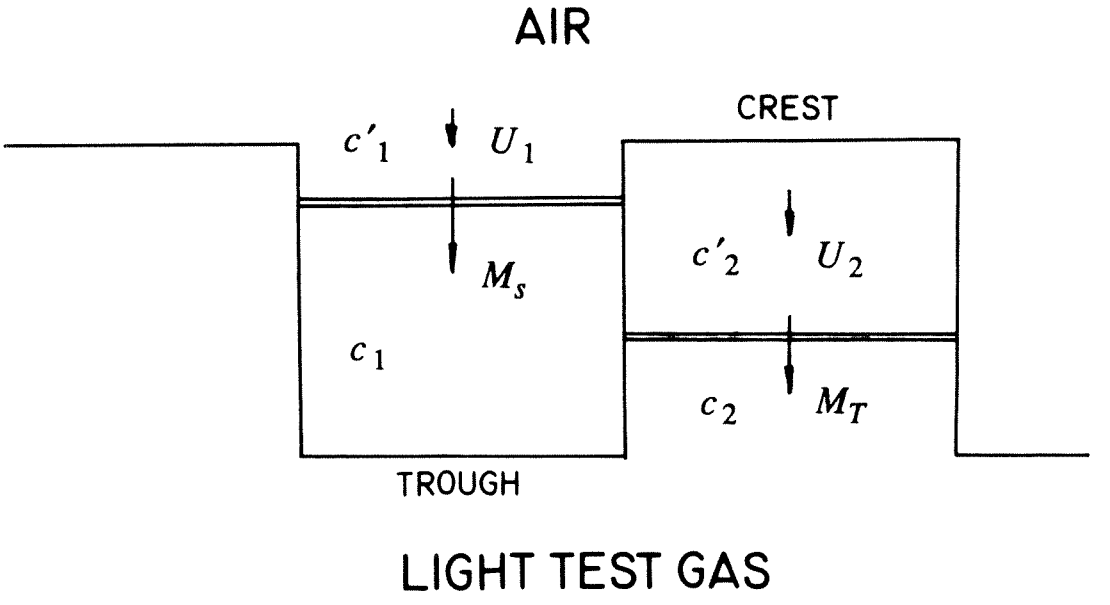

b. Heavy-light configuration.
$\Delta u_{max} = U_2, M_{rel} \equiv U_2/c_1$

Figure B.1 Definition of maximum relative Mach number M_{rel}.

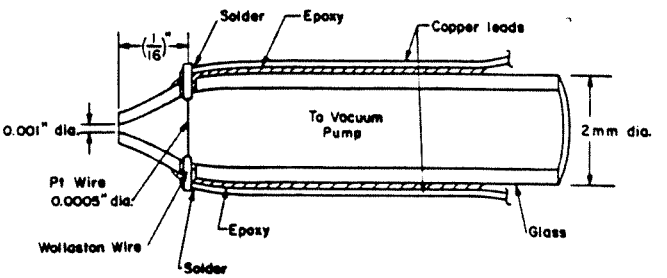

Figure C.1 Schematic of Brown-Rebollo probe.

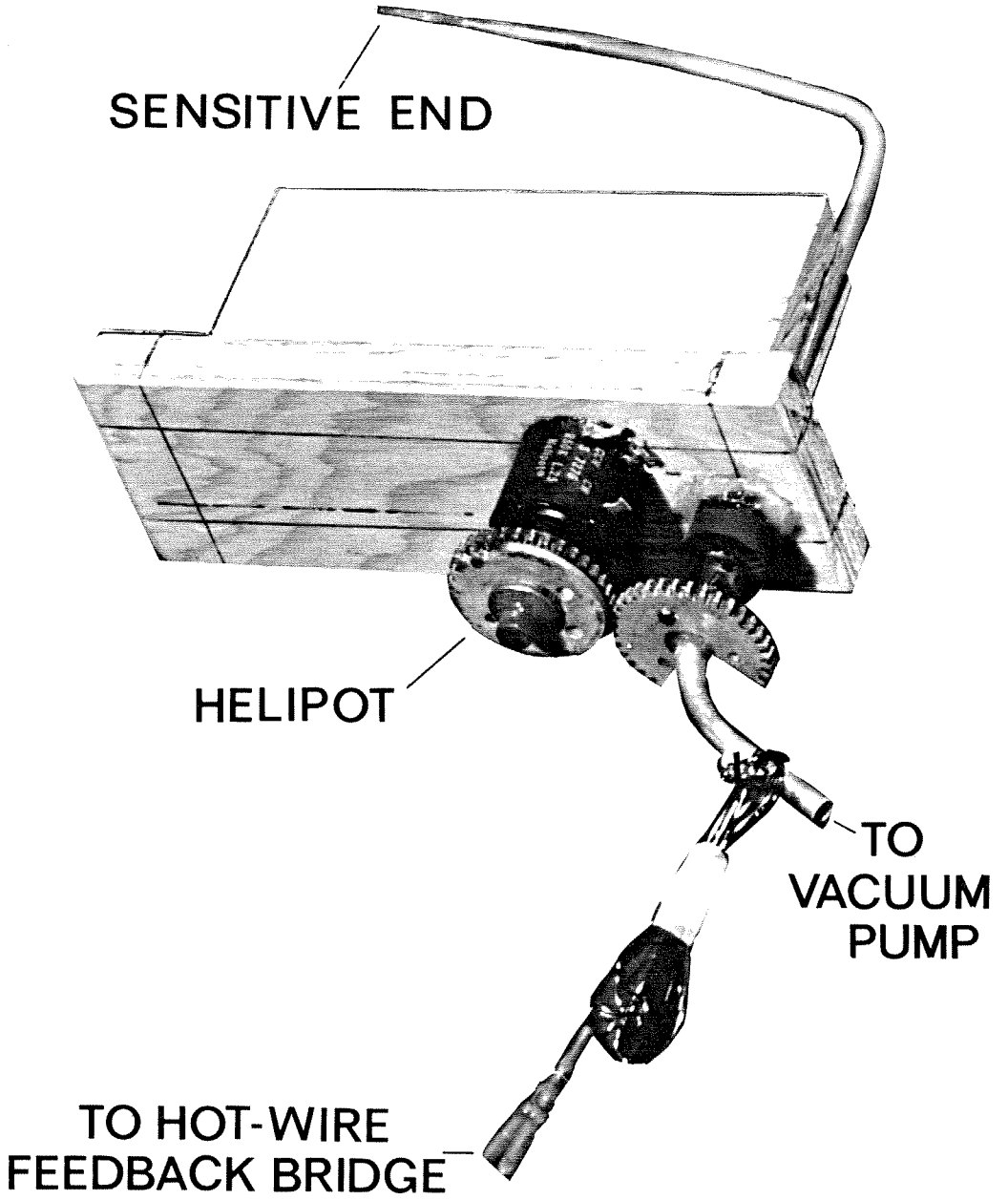

Figure C.2 Sampling probe assembly.

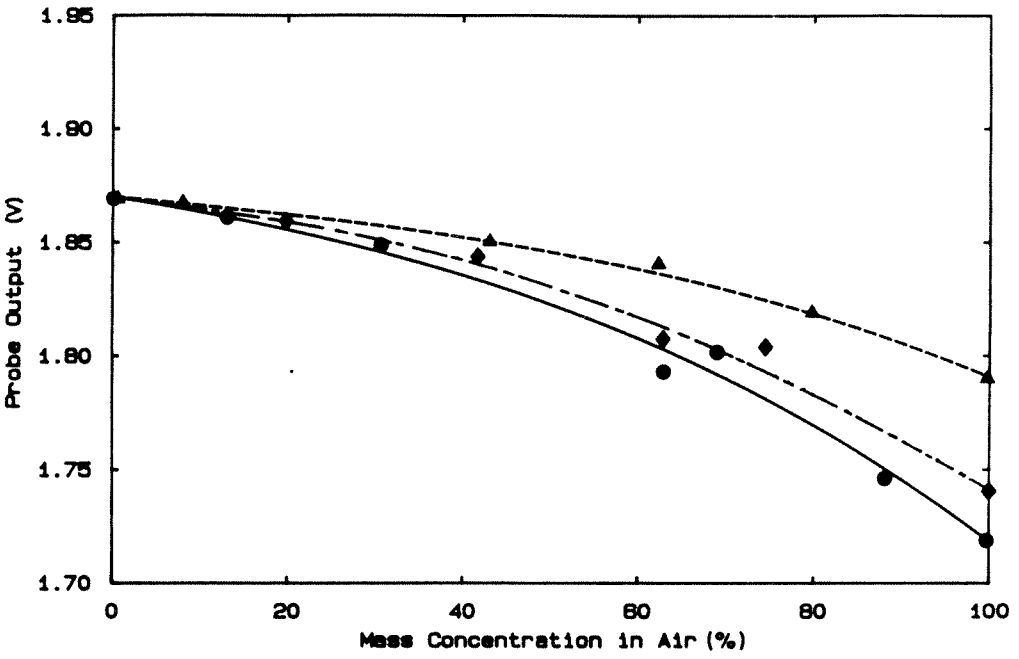

Figure C.3 Probe calibration.

● : air/SF_6, ◆ : air/R-22, ▲ : air/CO_2

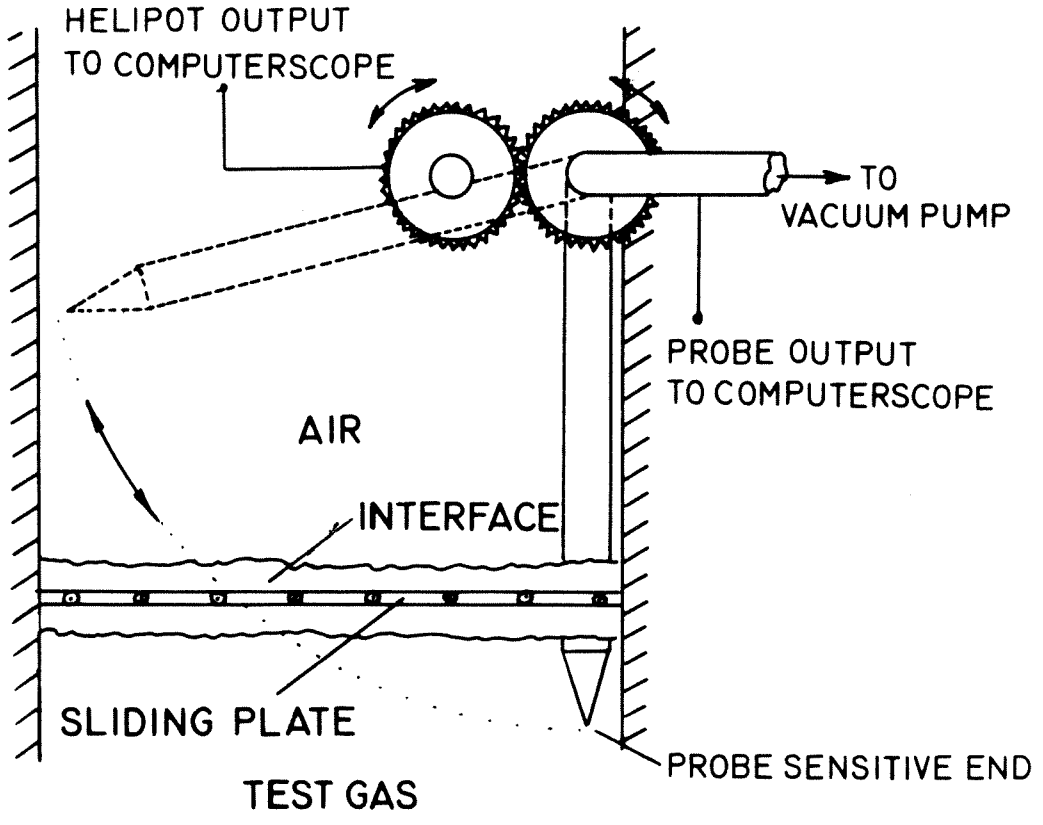

Figure C.4 Experimental arrangement for probe sampling of continuous interface. The plate slides out of the plane of the page.

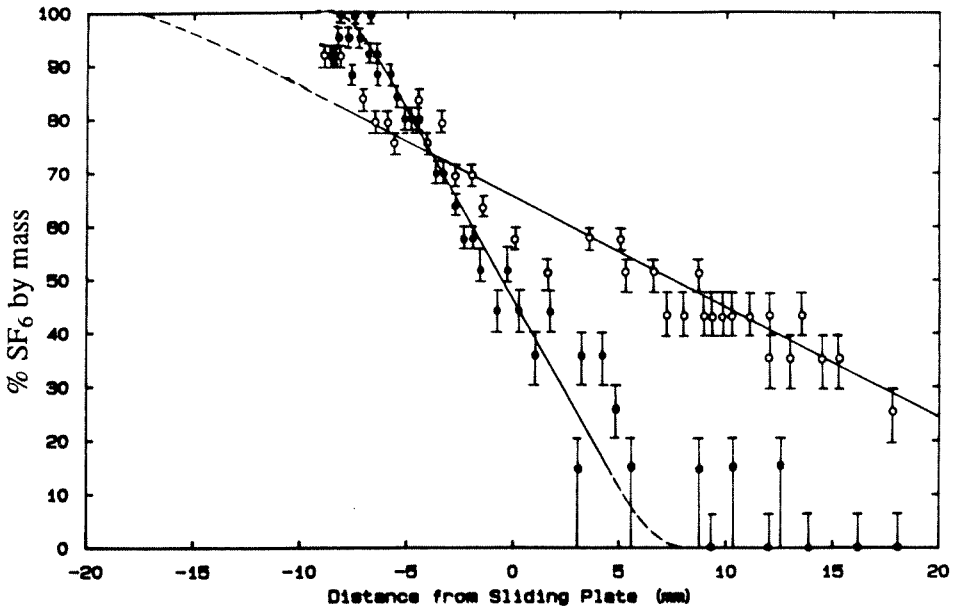

Figure C.5 Interface composition profile, air/SF_6.
● : t = 0.4 s, ○ : t = 10.2 s

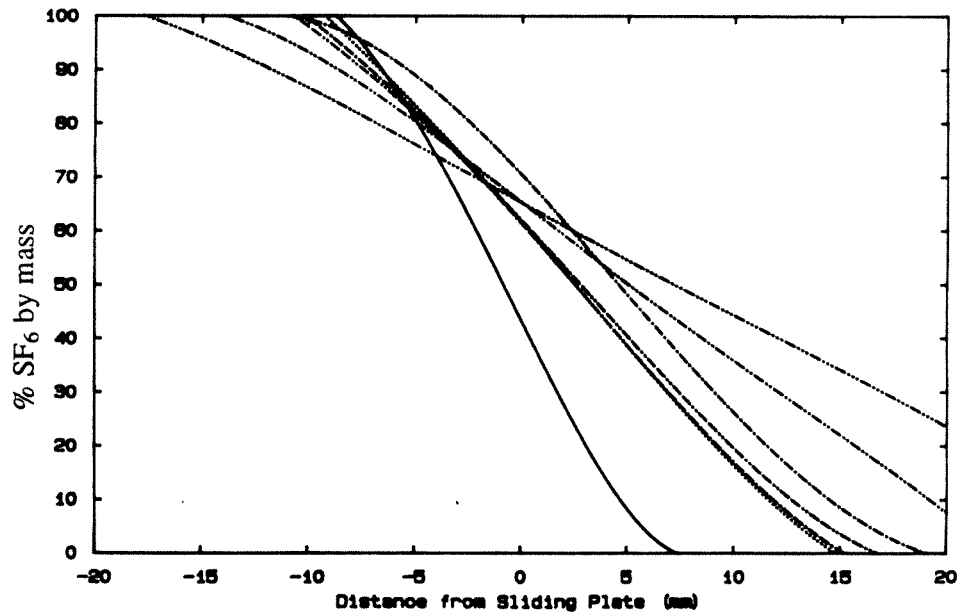

Figure C.6 Interface composition profile, air/SF_6.
— : t = 0/4 s, ····· t = 2.0 s, -·-·- : t = 3.5 s, - - - : t = 4.9 s,
—·— : t = 6.2 s, —·· — : t = 7.7 s, - - -·- : t = 10.2 s

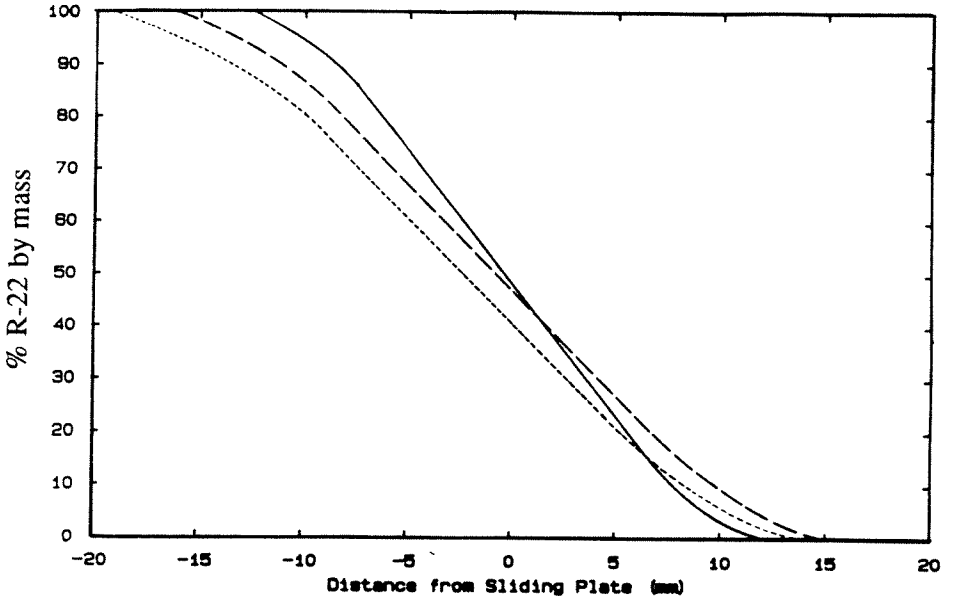

Figure C.7 Interface composition profile, air/R-22.
—: t = 0.4 s, – – : t = 4.0 s, - - - - : t = 8.0 s

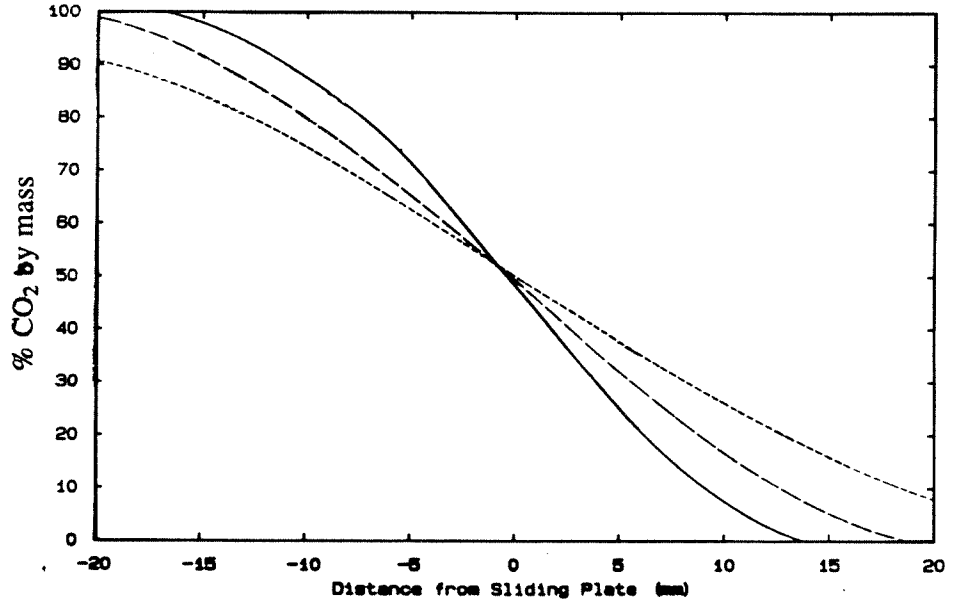

Figure C.8 Interface composition profile, air/CO_2.
—— : t = 1.6 s, – – t = 4.0 s, - - - - t = 6.0s

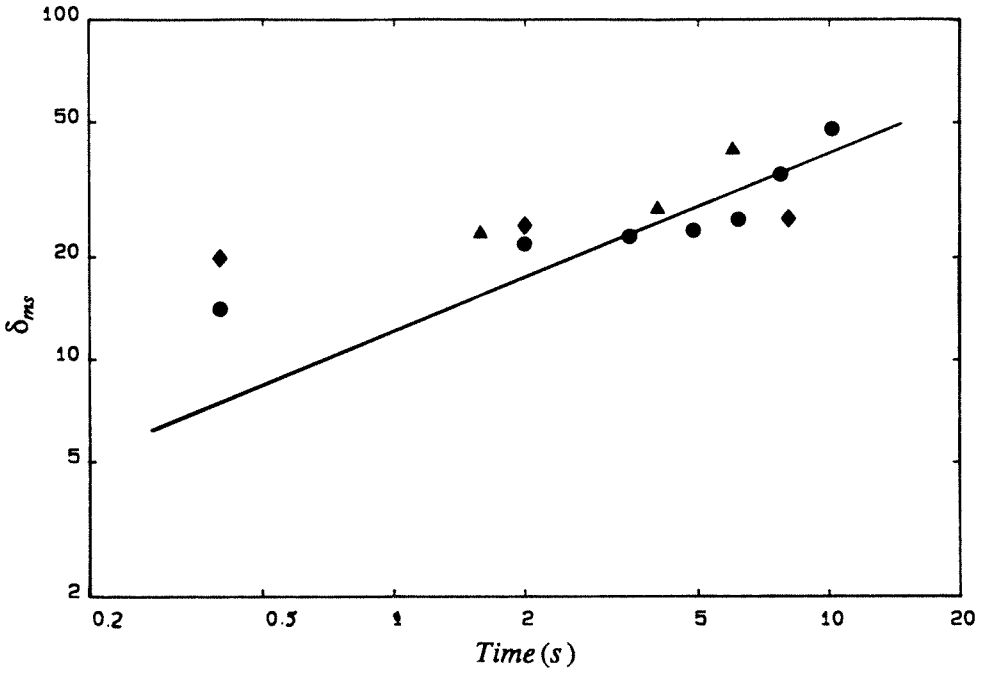

Figure C.9 Maximum slope thickness vs time.
● : air/SF_6, ◆ : air/R-22, ▲ : air/CO_2
—— : 1/2 slope line

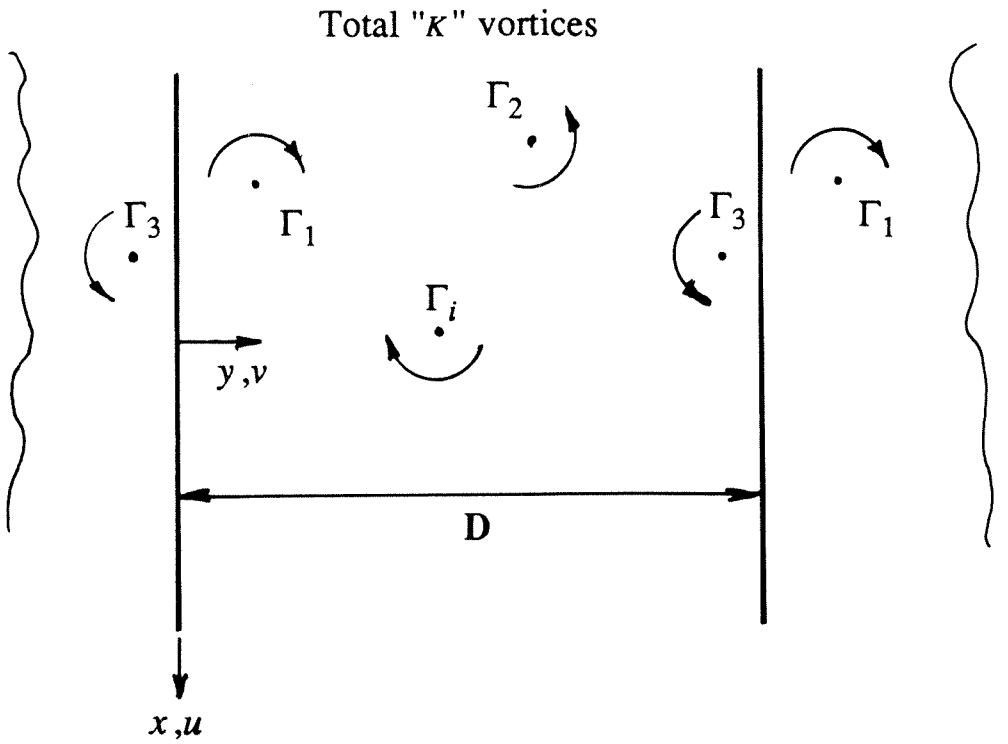

Figure D.1 Infinite system periodic in the y-direction, consisting of periodic cells of width **D** each with "K" vortices.

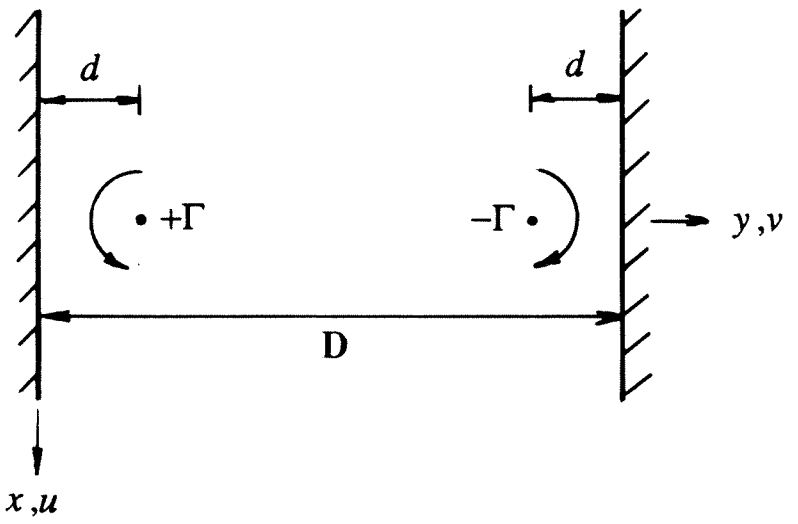

Figure D.2 Schematic of configuration used to estimate the strain induced by wall vortices.

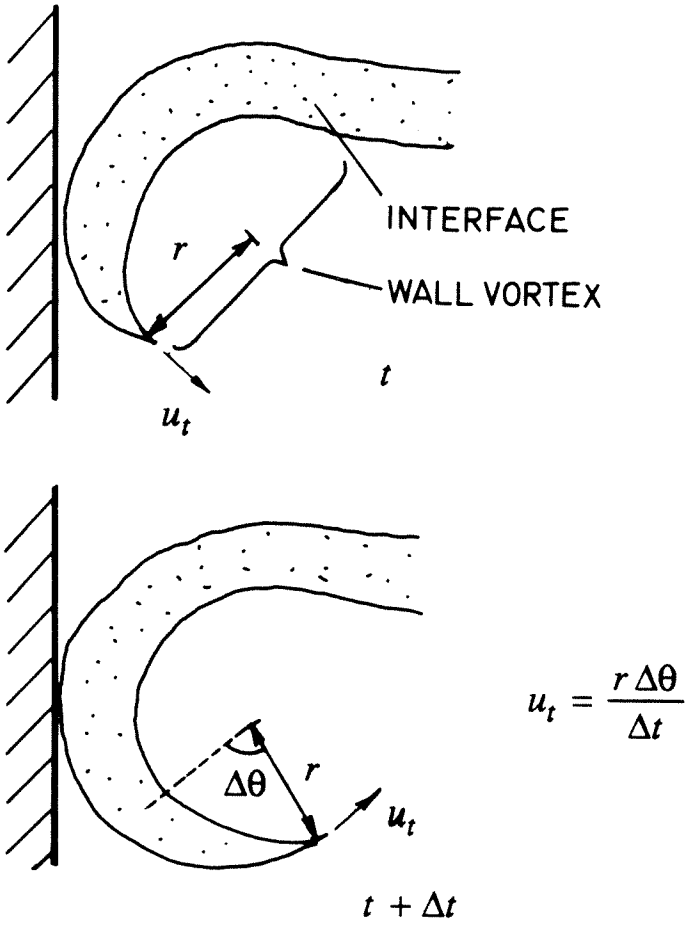

Figure D.3 Evaluation of tangential velocity of a wall vortex.